Calibration of Wide Field Imagers - The SkyDICE Project

P.-F. Rocci

THESE DE DOCTORAT
UNIVERSITÉ PIERRE ET MARIE CURIE

Spécialité: Physique

École doctorale : La Physique de la Particule à la Matière Condensée - ED389

réalisée

LPNHE

présentée par

Pier-Francesco ROCCI

pour obtenir le grade de :

DOCTEUR DE L'UNIVERSITÉ PIERRE ET MARIE CURIE

Sujet de la thèse :

Calibration of Wide Field Imagers: The SkyDICE Project

soutenue le 4 Novembre 2013

devant le jury composé de :

M.	Massimo Della Valle	Rapporteur
M.	Laurent Derome	Rapporteur
M.	Rémi Barbier	Examinateur
M.	Pascal Vincent	Président de Jury
M.	Nicolas Regnault	Directeur de Thèse

Contents

List of Figures

List of Tables

per me si va ne la città dolente,
per me si va ne l'eterno dolore,
per me si va tra la perduta gente.
(D. Alighieri / Inferno - Canto III)

No hay méritos morales o intelectuales. Homero compuso la Odisea;
postulado un plazo infinito, con infinitas circunstancias y cambios,
lo imposible es no componer, siquiera una vez, la Odisea.
(J. L. Borges / El Inmortal)

Remerciements

Tout d'abord je veux remercier mon Director de thèse, Nicolas Regnault, pour m'avoir suivi pendant tous les trois ans de travail jusqu'aux moment plus dure de la rédaction de ce manuscrit, et pour ses précieux conseils.

Un remercient à Laurent Le Guillou et Kyan Schahmaneche pour vôtres support scientifique et aide pendant toutes les étapes du projet SkyDICE et pour m'avoir supporté en Australie.

Je remercie tout l'ensemble du personnelle LPNHE sous le nom de son Director Reynald Pain. Un remerciement particulier au groupe Supernovae et à l'équipe technique du laboratoire qui ont permis la réalisation physique de SkyDICE (Merci Philippe Repain pour ton aide pendant l'installation!).

Je remercie encore le jury de thèse: les rapporteurs Massimo Della Valle et Laurent Derome, et les examinateurs Rémi Barbier et Pascal Vincent.

Un énorme merci à mes co-bureau présents et passés: Laura Zambelli (et ses plants), Augustin Guyonnet, Arnaud Canto, Mathilde Fleury (et son thé), Patrick El-Hage (et ses vidéos YouTube) et au dernier arrivé (University of Sussex Proud!) Ayan Mitra. Bonne chance à tous pour vos thèses et/ou vos carriers future.

Encore, Bonne Chance tous les souteneurs du 2013 pour vos PostDocs! Je voudrais même remercier le Pole Emploi français pour son soutien financier pendant les prochaines mois (vive le chômage!).

Je veux remercier tous mes amis parisiennes avec les quels ma vie n'aurait pas été la même.

Enfin tout cela n'aurait pas été possible sans le soutien de ma famille depuis le début et qui a été toujours présent dans cette aventure magnifique (Vi Voglio Bene!).

Un ringraziamento particolare va a te Mara, grazie per il tuo sostegno e la tua dolcezza, grazie per essermi stata vicino anche nei momenti più difficili. Senza te quest'avventura non sarebbe stata la stessa.

Introduction

Between 1999 and 2001, three measurements changed Cosmology forever: the discovery of Cosmic Acceleration (Perlmutter et al. 1998; 1999, Riess et al. 1998, Schmidt et al. 1998) indicated that the density of the Universe is dominated by some kind of repulsive Dark Energy (of unknown nature), the measurement of the first acoustic peak in the CMB temperature anisotropy spectrum (de Bernardis et al. 2000) combined with the precise determination of H_0 (Freedman et al. 2001) gave strong constraints on the flatness of space-time. These measurements contributed to solve the persisting disagreements between the observations that were favouring a low density of matter, and theoretical motivations for a higher-density (critical) Universe. It favoured the emergence of the Standard Model of Cosmology (Λ-CDM) that describes nearly all of today's observations with only a handful of free parameters (Planck Collaboration et al. 2013b). Cosmology has now entered an era of precision measurements, and the goal of observations is now to hunt for "tensions" within the cosmological model.

The case of Supernova cosmology is very characteristic of this situation. The measurement of luminosity distances to SNe Ia as a function of their redshift allowed one to discover (with less than 100 supernovae) the acceleration of cosmic expansion. Today, SNe Ia are still the most sensitive probe to w, the Dark Energy equation of state parameter, and growing number of SNe Ia are being detected and studied by several Collaborations all over the world, in order to pin down the value of w, and to start ruling out Dark Energy models. The precision on w is now as low as 7% (Howell et al. 2009, Conley et al. 2011, Sullivan et al. 2011) with nearly 1000 SNe Ia in the Hubble diagram. Unfortunately, the measurement is now dominated by systematic uncertainties, the dominant source of systematics being the photometric calibration of the imagers used to measure the SN Ia fluxes.

So, this work is about photometric calibration. This is a rather esoteric subject, which is seldom chosen by PhD students. But the thing is that, to improve on the current results, astronomers have no choice but to revisit the ancient calibration schemes. Since 2005, most Dark Energy Collaborations (with the invaluable help of the HST calibration program) have launched ambitious calibration efforts, redefined primary standards and metrology between those standards and their science images and push down their error budget well below 1% (e.g. Betoule et al. 2013). One suspect however, that these techniques, which rely on observations of stellar calibrators, will not allow one to reach the calibration requirements of future surveys. For this reason, several groups in the world are working on experimental laboratory sources, that would allow one to inject very well characterised light into the telescope optics and derive, from these measurements, the telescope throughput as a function of wavelength.

Since 2007, LPNHE cosmology group has been involved in the construction of a spec-

trophotometric calibration system for the last generation of wide field imagers (Barrelet and Juramy 2008). In particular, the team has designed and built two devices: SnDICE (Supernovae Direct Illumination Calibration Experiment) and SkyDICE (SkyMapper Direct Illumination Calibration Experiment), the first installed in the enclosure of the Canada France Hawaii Telescope (CFHT) on top of Mauna Kea, and the other in the dome of SkyMapper (Siding Springs Observatory, NSW, Australia).

This thesis is about SkyMapper. I started my PhD a few months after the SkyDICE project was funded. I was involved in nearly all stages of the project, in particular the integration and the calibration of the device on our test bench, as well as the installation and commissioning at Siding Springs. I then spent my third year analysing the commissioning data.

This memoir is organised as follows. In chapter 1 I described the standard model of Cosmology, with particular attention on the cosmological probes. I then (chapter 2) describe the experimental context of this thesis: SkyMapper, the stellar calibration techniques and their limitations and I review the main instrumental calibration projects. In chapters 3 I discuss the design and implementation of the SkyDICE calibration source. Chapters 4, 5 and 6 present the central part of my work: the calibration and characterisation of the source on our spectrophotometric test bench. In chapter 7 I describe the installation of the device on site, and the pre-analysis of the commissioning data I did then. Finally, in 8, I present the method developed to constrain the SkyMapper passbands, from series of calibration observations, I test it on a simulation, and I estimate the uncertainties that will affect our result.

Chapter 1

Modern Cosmology

At the end of the XIXth century our knowledge about the Universe outside the solar system was limited. Essentially our Galaxy, the Milky Way, was all we knew about Universe and Cosmology.

A theory to construct a real model of the Universe only came out with Einstein in 1917 and the publication of Theory of General Relativity (Einstein 1917); the first model of the Universe studied by Einstein static and uniform. We have to wait for the work of Freidmann (Friedmann 1922), Lemaitre (Lemaître 1927), and later De Sitter (Einstein and de Sitter 1932), to see a first theory where the Universe is dynamic and expanding. Around the same time Edwin Hubble made distance measurements of nearby galaxies, and discovered that Universe was in fact expanding. The publication of the famous Hubble's law in 1929 (Hubble 1929), can be seen as the birth of modern Cosmology.

In the 1930s, observations of the nearby clusters by Zwicky (Zwicky 1937), proved that the galaxy halos were surrounded by something invisible, a type of matter that could only be inferred from its gravitational effect; today, astronomers call this dark matter.

In 1998, two independent teams, working on supernovae projects, published observations of distant type Ia supernovae (Riess et al. 1998, Perlmutter et al. 1999), that indicated that the Universe was not only expanding but also that this expansion was accelerating. This milestones opened the way to the re-introduction of something that Einstein believed was his worst error: the cosmological constant.

After this brief history of modern cosmology we are going to focus on the basic concepts and equations used. In particular in §1.1 and §1.2 we describe the general principles behind modern Cosmology and the Λ-CDM model (also namely Concordance Model). Then, in the second part of the chapter, §1.3 and §1.4, we talk about Hubble's law, the expansion and the discovery of acceleration. Moreover, we define the most important cosmological probes that astronomers use to constrain models, with particular attention on type Ia supernovae. Finally, in the third part of the chapter §1.5 and §1.6, we talk about the dark side of the Universe with the actual hypothesis for dark energy and dark matter.

1.1 The Cosmological Principle

In 1543 Nicolaus Copernicus died and the same year one of the miles stone of human thinking the *De Revolutionibus Orbium Coelestium* were published. This book contained the seed of modern cosmology, known as the Copernican Principle. In a few words it says that our planet Earth is not at the centre of the Universe neither in a special position, this idea opened a new point of view about our Solar system and Universe.

To be more precise, Copernicus put the Sun at the centre of the Universe (and we know now this is not more true), but the power of this revolution was to eliminate the centrality of human being from science, in other words: *there is not special observer*. At the same time the works of Galileo and Newton, generalised in the past century with the introduction of General Relativity of Gravity, lead the way to the cosmology as we know it. A contemporaneous version of the Copernican Principle is the Cosmological Principle. In a simple way can be written as (Rowan-Robinson 1996):

«The Universe as seen by fundamental observers is homogeneous and isotropic»

This simple and pedagogic statement implies more profound meanings. First, *homogeneous*, means that every observer sees the same image of the Universe or, more simply, there is no special places in the Universe (see figure 1.1).

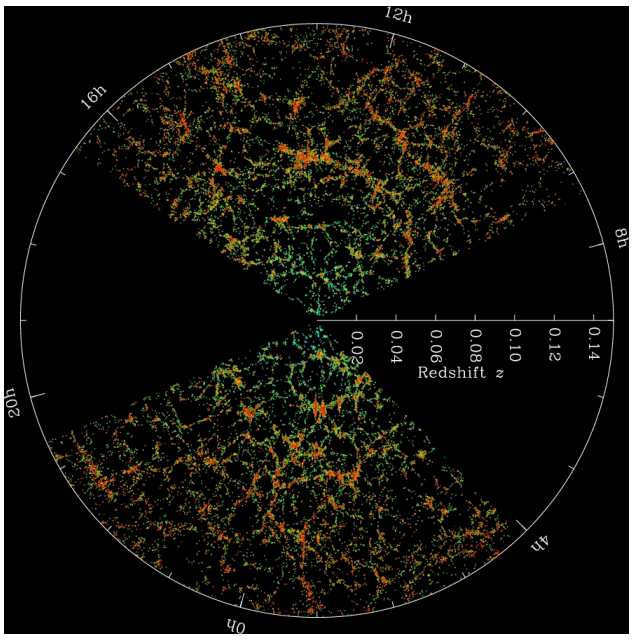

Figure 1.1: *Map of the distribution of galaxies. Earth is at the centre, and each point represents a galaxy. Galaxies are coloured according to the ages of their stars. The outer circle is at a distance of two billion light years (Blanton M. and SDSS Collaboration 2008).*

The second terms, *isotropic*, means that the Universe looks the same for every observer. There is not preferential direction or, in other way, an observation evidence taken from

different positions in the Universe must be the same. The two terms homogeneous and isotropic are distinct but related, a Universe that is isotropic from any two locations must also be homogeneous.

Until now the cosmological principle is consistent with observations taken in all the wavelengths, from radio to gamma rays. One of the best proof about the isotropy of the universe is the measurement of the Cosmic Microwave Background (CMB) done by COBE (Mather et al. 1990; 1994), WMAP and PLANCK (see fig. 1.2). For example, the map from WMAP 7 years describes an uniform microwave background with a temperature of $T_0 = 2.72548 \pm 0.00057$ K and oscillations less than 10^{-5} (Fixsen 2009).

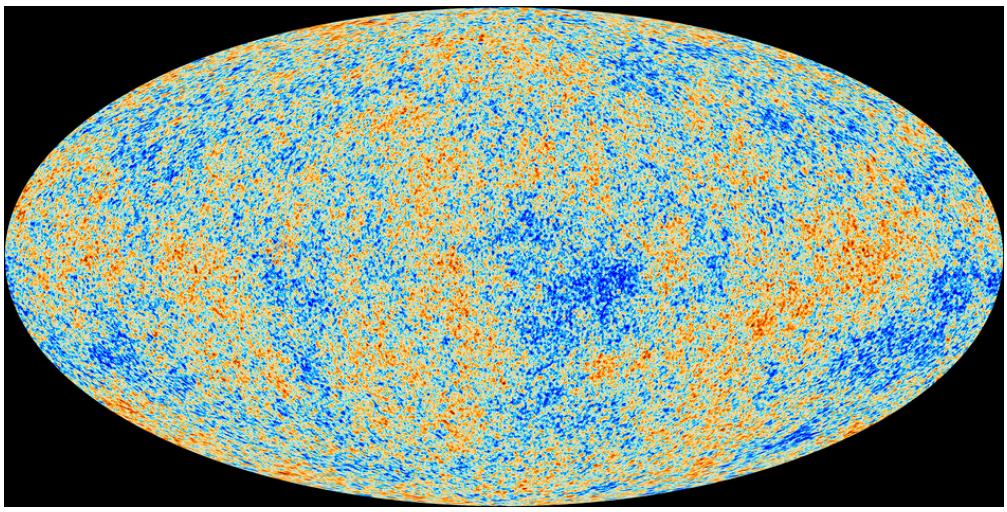

Figure 1.2: *This is a detailed all-sky picture of the Universe created from PLANCK data. The image reveals old temperature fluctuations that correspond to the seeds that after became galaxies, (Planck Collaboration et al. 2013a).*

1.2 Shape and Matter of the Universe

We now briefly describe the metric in a homogeneous and isotropic Universe, the connection between geometry, mass and gravity (Einstein equations), and the solution of the Einstein equations within this metric, the Friedmann equations.

1.2.1 Friedmann-Lemaitre-Robertson-Walker Metric

The Friedmann-Lemaitre-Robertson-Walker metric (FLRW) describes an expanding, homogeneous, isotropic Universe:

$$ds^2 = -cdt^2 + a^2(t)\left[\frac{dr^2}{1-kr^2} + r^2 d\theta^2 + r^2 sin^2\theta\phi^2\right] \tag{1.1}$$

where the spherical polar coordinates $r - \theta - \phi$ describe the spatial dimensions, while the ds is the space-time distance corresponding to a shift dt in time and a shift dr, $d\theta$ and $d\phi$

in space. The metric contains two unknown quantities, the scale factor $a(t)$ (see §1.2.3) and the curvature k. The latter is a constant, derived from observations, and the metric is qualitatively different depending on the value of k: every positive, zero or negative value corresponds to a possible geometry of the Universe,

$$\mathsf{k}\begin{cases} = 0, \text{ zero curvature: Euclidean Flat Universe} \\ > 0, \text{ positive curvature: Spherical Closed Universe} \\ < 0, \text{ negative curvature: Hyperbolic Open Universe} \end{cases} \tag{1.2}$$

Recent measurements of the cosmic background anisotropies (see (Hinshaw et al. 2012) or (Planck Collaboration et al. 2013b)), show that curvature k is close to 0. meaning our actual Universe has an euclidean geometry. This metric is one of the possible exact solutions of the Einstein's field equations.

1.2.2 Einstein Equations

Those equations are the mathematical core of the Theory of General Relativity (GR), published in 1915 (Einstein 1915). In GR the gravity is caused by the curvature of the space-time, curvature induced from the presence of matter in the space-time structure. One of the most important assumption of the theory is the *Equivalence Principle*, which is a generalisation of the the *Galilean Principle of Relativity* for non-inertial systems. Roughly speaking the principle says that the laws of physics experience by observers on a gravitational field are the same of the those in inertial systems. One of the direct derivation of this postulate are the equivalence of the gravitational mass and the inertial mass. Coming back on Einstein equation, its last version can be written as:

$$G_{\mu\nu} = \mathcal{R}_{\mu\nu} - \frac{1}{2} g_{\mu\nu} R - \Lambda g_{\mu\nu} \tag{1.3}$$

where $G_{\mu\nu}$ is:

$$G_{\mu\nu} = \frac{8\pi}{c^4} G T_{\mu\nu} \tag{1.4}$$

On the right hand side $T_{\mu\nu}$ is the *energy-momentum tensor* representing the properties of matters in the Universe. On the left hand side is the expression of the *geometry of the space-time*. More precisely, $\mathcal{R}_{\mu\nu}$ is the Ricci's tensor, $\mathcal{R}$ is its trace and most important $g_{\mu\nu}$ is the metric tensor directly connected with the metric geometry of space-time from the equation $ds^2 = g_{\mu\nu} dx^\mu dx^\nu$. The symbol Λ is the cosmological constant; previously insert by Einstein for the Steady-State model and then resurrected by modern Cosmology to account for the dark energy part (see §1.5).

Because of the lack of space in this work, we can schematically resume the meaning of this equation as follow (Liddle and Loveday 2009):

Curvature <–> Matter

as J. Wheeler said: *Matter tells Space-Time how to curve, Space-Time tells matter how to move.*

One last point: eliminating matter (right hand side equal to zero) from the equation is not enough to remove curvature. This is consistent with the fact that from observations effect of the gravitational field still present in the vacuum around astronomical objects.

1.2.3 Friedmann-Lemaitre Equations

Before the discovery of the expansion of the Universe, Friedmann in 1922, and Lemaitre in 1927 found from Einstein equation a model of the Universe homogeneous, isotropic, and expanding. Two independent equations were found. The first one derived from the $(0,0)$ component of the Einstein's equations is:

$$\left(\frac{\dot{a}}{a}\right)^2 + \frac{k}{a^2} = \frac{8\pi G}{3}\rho + \frac{\Lambda}{3} \tag{1.5}$$

the second one comes from the (i,i) trace of the Ricci's tensor:

$$2\frac{\ddot{a}}{a} + \left(\frac{\dot{a}}{a}\right)^2 + \frac{k}{a^2} = -8\pi G p + \Lambda \tag{1.6}$$

The terms ρ and p are respectively the density and pressure of the matter contained in the Universe. The first equation describes the expansion rate of the Universe from the parameter $\dot{a}$. Combining the two equations 1.5 and 1.6, we get the term of the acceleration of the Universe:

$$\frac{\ddot{a}}{a} = -\frac{4\pi G}{3}(\rho + 3p) + \frac{\Lambda}{3} \tag{1.7}$$

Studying these equations for different initial conditions we have three majors solutions:

$$a(t) \begin{cases} = \pm t^{2/3} : \text{matter domination} \\ = \pm t^{1/2} : \text{photons domination} \\ = e^{\pm t\sqrt{\frac{\Lambda}{3}}} : \text{dark energy domination} \end{cases} \tag{1.8}$$

the scale factor $a(t)$ is a function that describes the variations of the Universe at different time of its history. In §1.3.1 we are going to discover that this parameter is directly connected with the expansion rate of the Universe and the concept of redshift.

1.3 The Accelerating Universe

In 1917, Slipher discovered that galaxies were moving away us (Slipher 1917); but it was the work of Hubble (Hubble 1929), measuring the redshifts of nearby galaxies and discovering the law that has his name, to show the expansion of the Universe. Here we describe the Hubble's law and redshift in §1.3.1, then we define cosmological parameters in §1.3.2. Finally we show recent progresses made by the discovery of the acceleration of the expansion done in 1998 by two teams leading by S. Perlmutter, and B. Schmidt, H. Riess.

1.3.1 Hubble's Law

The linear proportion of the velocity recession of galaxies (and more generally for every astronomical object) and its distance is called the Hubble's law and can be written as:

$$v = H_0(t) \cdot d \tag{1.9}$$

where $H_0(t) = \frac{\dot{a}(t)}{a(t)}$ is the expansion rate of the Universe. The constant is called Hubble's constant and it has an actual value of (Planck Collaboration et al. 2013b):

$$H_0 = 68.0 \pm 1.4 \quad km \cdot s^{-1} \cdot Mpc^{-1}$$

By measuring the redshift of galaxies, Hubble was able to achieve this result, although finding a value for the Hubble constant 10 times larger than obtained by modern measurements. When a galaxy moves away from us, taking his spectra, we can see that the wavelength is stretched to the redder part of the spectrum. More precisely, if we call λ_e the wavelength emitted by the source and λ_o the light seen by an observer, we have:

$$\frac{\lambda_o}{\lambda_e} - 1 = \frac{a(t_o)}{a(t_e)} - 1 = z \tag{1.10}$$

z is what we call the redshift of the object. Using the FLRW metric and co-moving coordinates (equation 1.1), we can write the redshift as a function of the scale factor $a(z)$:

$$a(z) = \frac{1}{z+1} \tag{1.11}$$

this equation connects the scale factor a with the redshift of object. That means if we look an object at high redshift, for example $z = 1$, we are looking at the Universe how was in the past when its dimension were $a = 1/2$, roughly half the dimension of now. The scale factor says us that galaxies are not simply moving away from us only because of their proper motions, but it is all the space-time that is expanding.

1.3.2 Cosmological Parameters

Defining cosmological parameters is the first step towards testing theoretical model with the observational data. In this sense, cosmological parameters are a series of numbers which describe the detailed properties of our Universe such as density of matter. Using the Freidmann equations 1.5, 1.6, 1.7, we can extract the definition of the first of these parameters, the *critical density* ρ_c:

$$\rho_c = \frac{3H^2}{8\pi G} \tag{1.12}$$

the critical density is the density of the Universe that corresponds to a flat euclidean geometry of the space-time, the actual value is $\rho_c = 1.88 \cdot 10^{-26} h_0^2 \cdot kg \cdot m^{-3}$. Extracting the

different components inside the Friedmann equation, we can redefine the density parameter as follow:

$$\Omega_M = \frac{\rho_M}{\rho_c} \tag{1.13}$$

is the density parameter for matter components of the Universe,

$$\Omega_r = \frac{\rho_r}{\rho_c} \tag{1.14}$$

is the density parameter for the radiation component of the Universe,

$$\Omega_\Lambda = \frac{\Lambda}{3H^2} \tag{1.15}$$

is the density parameter for the cosmological constant (dark energy), and:

$$\Omega_k = \frac{\rho_k}{a^2 H^2} \tag{1.16}$$

describe the geometry of the Universe. Putting these four parameters together we can rewrite the Friedmann equation 1.5 in a simple form:

$$1 + \Omega_k = \Omega_M + \Omega r + \Omega_\Lambda = \Omega \tag{1.17}$$

This equation links explicitly the curvature of the Universe (the left hand side of the equation), with the density of single components (the right hand side). A universe with $\Omega = 1$ is flat, while $\Omega < 1$ ($\Omega > 1$) means a closed (open) Universe.

Another important parameter is the *deceleration parameter* that can be evaluated from Friedmann equations 1.5 and 1.6 as:

$$q(z) = -\frac{\ddot{a}(t)}{a(t)H^2} = \frac{1}{2}\sum_i \Omega_i(z)[1 + 3w_i(z)] \tag{1.18}$$

We have rewritten the equation in terms of the new parameters $\Omega - i$ and w_i, where the latter is the *equation of state (EoS) parameter* $w = \frac{p}{\rho}$.

1.3.3 The Acceleration of Expansion

The expansion rate of the Universe would be expected to be slowing down due to the gravitational force between galaxies opposes to the expansion; in another way the expansion of the Universe should be decelerating. But in 90s, two different groups published results about the studies of distant type Ia supernovae (Perlmutter et al. 1998; 1999, Riess et al. 1998, Schmidt et al. 1998), indicating that the expansion of the Universe was accelerating. Measuring their redshift, they discovered that the supernovae were more faints (distant) that could be expected from a matter dominated Universe. This meant that at some point in the history of the Universe, the expansion has started to accelerate, see fig. 1.3. As a consequence a Universe characterised by low density matter can be described in terms of

an equation of state often expressed as $p = w(z)$, where $w(z) = w_0 + w_a(z)/(1+z)$ (e.g. Chevallier and Polarski 2001, Linder 2003)

consequence of that is a Universe with less matter density, lead by fluid with negative pressure. Nowadays, comparing different studies, we are able to say that almost $\sim 68,3\%$(Planck Collaboration et al. 2013b), of the observable Universe is made by this unknown kind of energy, namely dark energy.

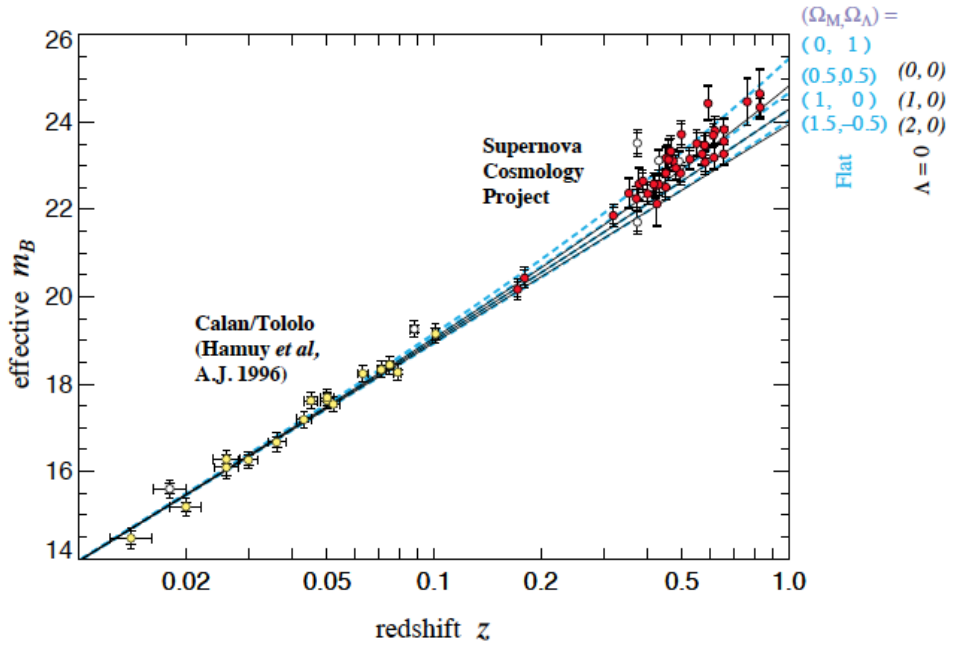

Figure 1.3: *Hubble diagram for 42 high-redshift SNe Ia from the Supernova Cosmology Project, and 18 low-redshift SNe Ia from the Calan/Tololo Supernova Survey, after correcting both for the light-curve width-luminosity relation (Perlmutter et al. 1999).*

1.4 Observational Cosmology

To evaluate the view of the Universe that until now we have described, we need a way to measure its main parameters (§1.3.2), in order to confirm or reject the model. In these last years lots of progresses have been made in astronomy thanks to the advantage of the new satellites mission (i.e., HST, FERMI, PLANCK), and new sensible and big ground based telescopes (i.e., CFHT, VLT, KECK). In this section we show some of the most important probes in observational cosmology that put strong constrains in the Λ-CDM Model. In particular in §1.4.1 we describe the Cosmic Microwave Background, in §1.4.2 we talk about Baryonic Acoustic Oscillations, in §1.4.3 we briefly describe Large Scale Structures, and finally in §1.4.4 we talk about type Ia supernovae.

1.4.1 Cosmic Microwave Background (CMB)

The CMB is the relic radiation from the young Universe after the Big Bang. It is the dominant form of radiation in the present Universe and extremely close to isotropy, meaning that the radiation received from all direction is more or less identical. The origin of the CMB falls in the early stage of the evolution of the Universe, at a time corresponding to a $z \sim 1000$, when the temperature was cooling down sufficiently to allow electrons and nuclei to bound together and form stable atoms; the average temperature was $T \sim 3000$ K. At that time the Universe made the transition from opaque to transparent lead photons to propagate freely.

Technically, two separate physical processes were taking place around the formation of the CMB. One is *recombination*, and it is referred to the phenomena where electrons and nuclei could combine together and form atoms ($t \sim 380000$ years after the Big Bang). The other effect is the *decoupling*, and it is the time when the photons can fly freely (it happened shortly after the recombination). The CMB was discovered in 1965 by Penzias and Wilson (Penzias and Wilson 1965, Wilson and Penzias 1967).

After the decoupling, the Universe continued to expand and photons continued to redshift. This expansion increased their wavelength about one thousand time, putting them into the microwave part of the electromagnetic spectrum. The spectrum of the CMB is a thermal spectrum with an actual temperature of roughly $T_0 \simeq 2.73$ K, and it is one of the most accurate measurements in Cosmology. One of the most important features of the CMB are the little fluctuations in temperature. This anisotropies are the signature of the density fluctuations of matter at the time of recombination and they are absolutely important in order to form the structures that we see in the present Universe. Since before the discovered by COBE in 1992 (Smoot et al. 1992), lots of studies have been made to constrain and understand anisotropies of the CMB. The main quantity to be measured is the radiation angular power spectrum, known as C_l:

$$C_l = \sum_{m=-l}^{l} |a_{lm}|^2 \tag{1.19}$$

where a_{lm} is the amplitude of spherical harmonics of temperature fluctuations, describe by the following equation:

$$\frac{\Delta T}{T}(\theta, \phi) = \sum_{m,l} a_{lm} Y_{lm}(\theta, \phi) \tag{1.20}$$

Because of the angular distribution of fluctuations depending on the geometry of the space-time, from the power spectrum we can have information about the real geometry of the actual Universe. The first peak of this spectrum (see fig. 1.4), corresponds to temperature fluctuations at the time of the recombination, and in the case of a flat Universe this peak is roughly at $l \sim 220$ (l is the multipole momentum, connected with the angular size by $\theta \simeq \pi/l$). The last result from PLANCK analysis (Planck Collaboration et al. 2013b), comes

out with a value of the dark energy density parameter Ω_Λ:

$$\Omega_\Lambda = 0.686 \pm 0.020 \tag{1.21}$$

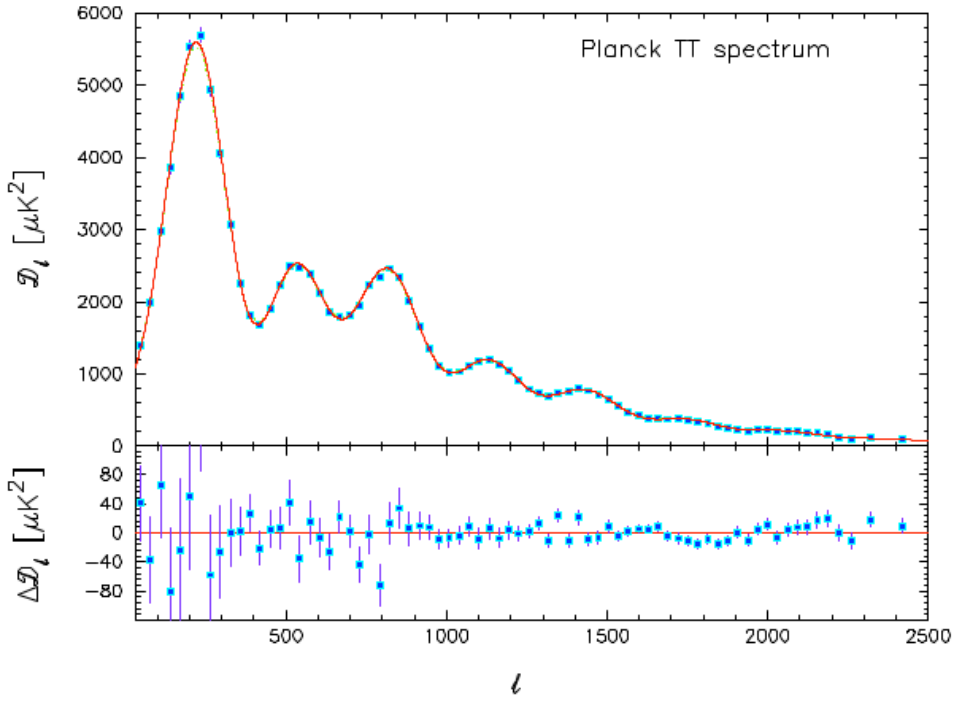

Figure 1.4: *Planck TT power spectrum. The points in the upper panel show the maximum-likelihood estimates of the primary CMB spectrum. The red line shows the best-fit base CDM spectrum. The lower panel shows the residuals with respect to the theoretical model (Planck Collaboration et al. 2013b).*

1.4.2 Baryonic Acoustic Oscillations (BAO)

In the last years, the acoustic peaks in the cosmic microwave background power spectrum (BAO) have emerged as one of the strongest cosmological probes. Before of the period of decoupling, baryons (read neutrons, protons and electrons) interact strongly with photons, this interaction creating a strong pressure force. In the region of high matter density, gravity tried to draw the baryons in, while the pressure offered a opposite force; these two factors created oscillations analogous to acoustic waves in a medium (while the radiation dominated, the speed of sound at these condition was really high $v \sim c/\sqrt{3}$).

The scale of these oscillations is set by the acoustic horizon at the time of recombination, defined as the co-moving distance travelled by sound waves between their creations and the time of the recombination, in numbers:

$$s = \int_0^{t_{rec}} c_s(1+z)dt = \int_{z_{rec}}^{\infty} \frac{c_s}{H(z)}dz \tag{1.22}$$

where c_s is the speed of sound defined by the ratio from the baryonic density and the density of photons at that time. Density perturbations on larger scales lead to oscillations in a longer time scale because of the proportional relation between their period and the length scale of the Universe. This relation shows us the fact that BAO can be used as "standard ruler" for length scale in cosmology: the length of this standard ruler can be measured by looking at the large distant scale structures as cluster of galaxies. In particular resolving the equation 1.22 gives us where to look for them, at $s \simeq 150$ Mpc.

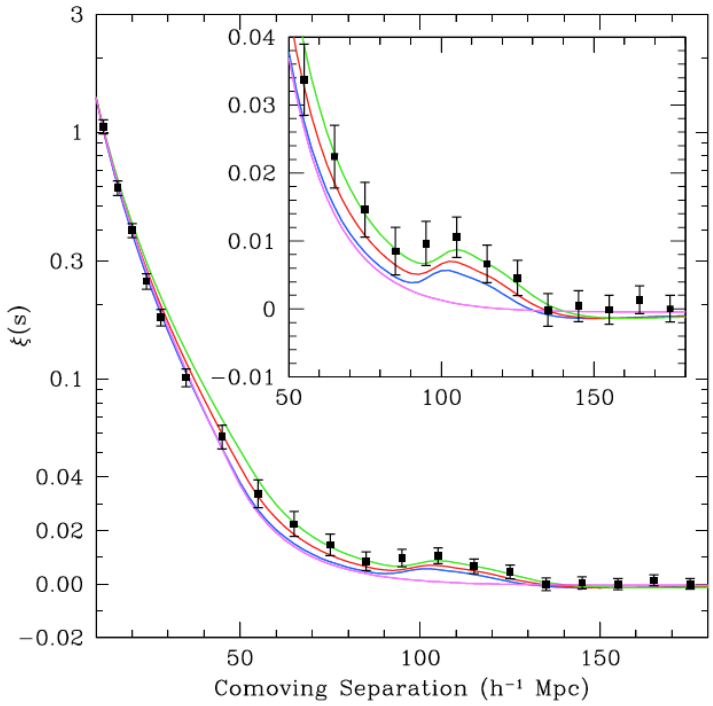

Figure 1.5: *The large-scale redshift-space correlation function of the SDSS LRGs sample. The models are* $\Omega_m h^2 = 0.12$ *(green),* 0.13 *(red), and* 0.14 *(blue), all with* $\Omega_b h^2 = 0.024$ *and* $n = 0.98$*. The magenta line shows a pure CDM model with* $\Omega_m h^2 = 0.105$ *(Eisenstein et al. 2005).*

Because of perturbations from dark matter are dominants compared to the baryonic ones, the peak in the correlation function is smaller and the acoustic signatures are fainter than the CMB signal. It is necessary to probe large structures of matter to find this signature; the magnitude of this volume is $1h^{-3}\text{Gpc}^3$.

The first detection of BAO peak was found in 2005 (Eisenstein et al. 2005). To measure BAO they used sample of Luminous Red Galaxies (LRGs) taken from the Sloan Digital Sky Survey (SDSS). The correlation function is showed in the fig. 1.5; in that figure we can see a little peak at $100h^{-1}$ Mpc. The position and intensity of the peak is strictly correlated to the density of baryons, meaning that it is possible to examine the amount of the ordinary matter in the Universe and, comparing that with theoretical predictions from WMAP 9 years (Hinshaw et al. 2012) and Hubble Space Telescope (HST) (Riess et al. 2009), we obtained a

value for the total density Ω_{tot}:

$$\Omega_{tot} = 1.0027^{+0.0039}_{-0.0038} \tag{1.23}$$

This result is confirmed by the seven years analysis of the SDSS data (Kazin et al. 2010). The detection of the BAO peak is direct demonstration of the Big Bang model and the early evolution of the Universe at the epoch of the recombination and decoupling; the value found from SDSS analysis is in accord with a $z \simeq 1000$.

1.4.3 Large Scale Structures (LSS)

The various forms of structures we observe today in the universe are collectively referred to LSS. Observations of these structures provide us important constrains on the cosmological model since they are believed to trace regions with over-density in the early Universe after the epoch of inflation. There are several ways to measure them, but the two most important are cluster counts and the weak gravitational lensing.

Galaxy Clusters

Clusters of galaxies have a long history as cosmological probes, beginning with the first discovery of dark matter (Zwicky 1937), through study of cluster of galaxies, and then providing evidence for a low matter density distribution (White et al. 1993). These discoveries came from observations of the properties of individual systems. But we know now that also the population of clusters as a whole contains lots of cosmological information.

The number of galaxy clusters in the local Universe measures the size of the density perturbations on a scale corresponding to the cluster mass. The way on which the number of clusters change with distance give us the changing-rate of the density perturbations. This rate depends on the total density of matter, but also on properties of the dark energy. The measurement of the spatial density and distribution of galaxy clusters is sensitive to dark energy through the angular-diameter and distance-redshift relation. To do that astronomers use several observables, either separately or combined, to infer the number and galaxy cluster mass function: direct counting, through the X-ray emission of the hot cluster gas (Mantz et al. 2008), although Sunyaev-Zeldovich and optical surveys are also making significant progress in that field.

In the Λ-CDM model, the number density of dark halos as a function of redshift can be compared with the number obtained in the large cluster surveys. The relation between galaxies cluster and its mass distribution can be written as:

$$\frac{d^2N(z)}{dzd\Omega} = \frac{d_M(z)}{H(z)} \int_0^{\inf} f(O,z)dO \int_0^{\inf} p(O|M,z)\frac{dn(z)}{dM}dM \tag{1.24}$$

where $f(O,z)$ is the observable redshift dependent selection function, $dn(z)/dM$ is the co-moving density of dark halos, and $p(O|M,z)$ is the probability that a halo of mass M at redshift z is observed as a cluster with observable O. This equation is sensitive to cosmology by the co-moving element $d_M^2(z)/H(z)$ and the growth structure term $dn(z)/dM$, which depends on the primordial spectrum and density perturbation.

Gravitational Lensing

Another method to study the large scale structures as galaxy clusters is to use the well known gravitational lensing effect. The light deflection caused by the gravitational potential of the cluster of galaxies, creates a distortion of the images of galaxies behind the lens. This kind of distortion allows us to measure the geometry and, overall, the distribution of total dark matter with its evolution in time. The observed shape of distant galaxies become slightly distorted as light from them passes through foreground mass structures. The distortion pattern depends then on the distances to the source and lens as well as its mass, being thus both a geometrical (distance-redshift) and mass distribution probe. This lensing signal that induces an observable ellipticity (cosmic shear) in the background galaxies has been detected (Bacon et al. 2000, Hoekstra et al. 2006), and wide field galaxy surveys are now being carried out (e.g. Fu et al. 2008), to improve the quality of this cosmological probe.

1.4.4 Type Ia Supernovae (SNe Ia)

A supernova is the phenomenon that occurs when a star ends its life in a violent explosion. This is one of the most energetic events in the universe, creating a new short-lived object in the sky, that outshines its host galaxy during a time of few weeks (≈ 30 days). Supernovae play a central role creating elements heaver than Fe, and distributing these elements through space; more important, their extreme intrinsic luminosity make supernovae observable up to cosmological distances and a standardisable object to constrain dark energy equation.

Historically, supernovae classification has been based on their spectral features. Minkowski divided them into two groups (Minkowski 1941), depending on the existence of hydrogen lines on their spectra at maximum light: type I supernovae do not show hydrogen lines, whether type II supernovae do. This division was later extended by Filippenko (Filippenko 1997) and Turatto (Turatto 2003), as it became noticeable that there were more spectral and photometric differences inside each group (see fig. 1.6). Furthermore, SNe Ia present an overall homogeneous spectroscopic and photometric behaviour, contrary to the other types. Those evidences are connected with the different physical mechanisms of origin between the SNe Ia and all the other SNe.

Assuming that a supernova originates from a single stellar object, two physical mechanisms can explain the observed energy amount: the release of the nuclear energy by an explosive reaction (thermonuclear supernovae), or a gravitational collapse of a massive star ($> 8M_{\odot}$), through the creation of a neutron star or a black hole (core-collapse supernovae).

Type Ia Supernovae as Standard Candles

Observationally, SNe Ia are defined as supernovae without any hydrogen lines in their spectrum, but with a broad silicon absorption line, $Si-II$, at about 400 nm. The progenitor is believed to be a binary system in which a CO white dwarf (no hydrogen layer), accretes material from a companion star (SD, single degenerate system), or possibly another white dwarf (DD, double degenerate system). The process continues until the mass of the white dwarf approaches the Chandrasekhar limit, at which point a thermonuclear explosion is triggered.

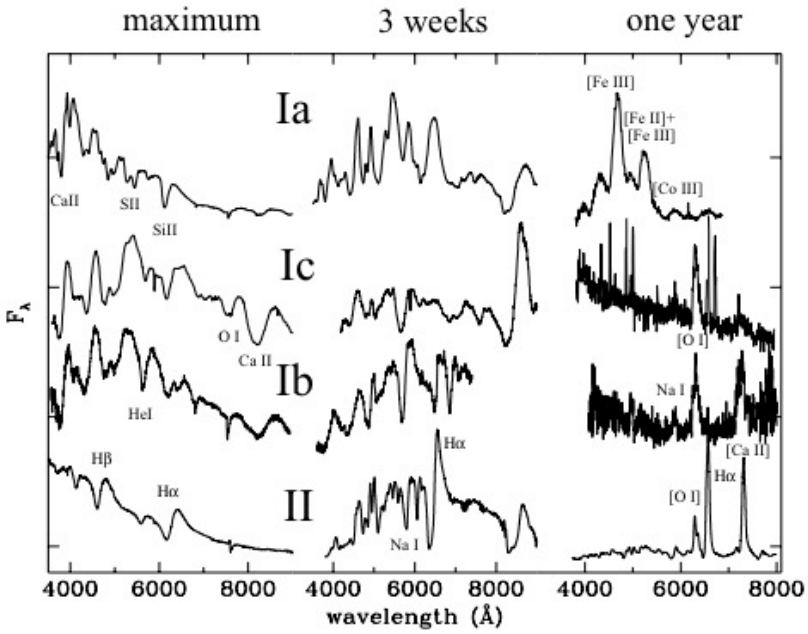

Figure 1.6: *Spectra of SNe at maximum, three weeks, and one year after. The representative spectra are those of SN1996X for type Ia, of SN1994I (left and centre) and SN1997B (right) for type Ic, of SN1999dn (left and centre) and SN1990I (right) for type Ib, and of SN1987A for type II (Turatto 2003).*

The fact that all SNe Ia have a similar mass explains their consistent properties. They are very homogeneous in luminosity, colour and spectrum. Only a small, correlated variations of these quantities are observed.

In 1992 Phillips (1993) discovered, for nearby SNe Ia, a correlation between their intrinsic brightness at maximum light and the duration of light curve. After that SNe Ia started to be largely observed, and it was clear that a correlation existed between the peak luminosity and the decline rate of their light curve. By applying an empirical correction model to the absolute magnitude of SN (Hamuy et al. 1996), they found a good linear relation between peak and decline-rate, which allowed to push down the dispersion of SN Ia distance estimates to $7 - 10\%$.

In the 1990s, other standardisation and correction methods were created: the MLCS (Riess et al. 1996), and stretch methods (Perlmutter et al. 1997, Goldhaber et al. 2001), using supernovae light curve shape templates (see fig. 1.7); the C12 method for the "brighter-bluer" relation (Wang et al. 2005); the MLCS2k2 (Jha et al. 2007) and SALT/SALT2 methods (Guy et al. 2005; 2007), using both light curve shape and colour parameters.

While light-curves are determined with photometric measurements in several broadband filters (i.e., SDSS *ugriz* filters), spectroscopy near maximum light allows us to (1) identify the SN Ia among all the discovered transients, and (2) at the same time determining its redshift. The key feature of the spectrum is the $Si - II$ absorption line, whose its detection identifies the SN as a type Ia, and its position determines the redshift.

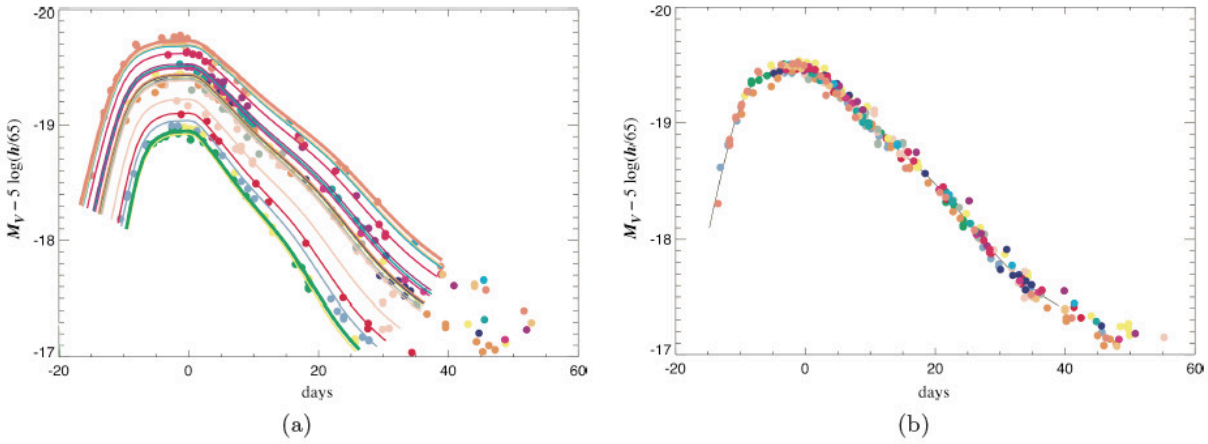

Figure 1.7: *Calan/Tololo nearby Supernovae absolute magnitudes in V band, (a) - as observed and (b) - after correction using the stretch parameter (Kim et al. 1997).*

1.4.5 Measuring Distances in Cosmology

Measuring distances in Cosmology is a complicated task. We need to know precisely the flux of the object, the redshift, and fundamental parameters as the Hubble constant H_0. For an object of intrinsic luminosity L, and a measured energy flux F, one can define the luminosity distance d_L to the object, trough the inverse square law. This luminosity distance is defined as:

$$d_L(z) = \sqrt{\frac{L}{4\pi F}} = (1+z)r(z) \tag{1.25}$$

where $r(z)$ is the co-moving distance to an object at redshift z,

$$r(z) = \int_0^z \frac{dz'}{H(z')} = \int_{1/(1+z)}^1 \frac{da}{a^2 H(a)} \quad (k=0) \tag{1.26}$$

$$r(z) = |k|^{-1/2}\chi\left[|k|^{1/2}\int_0^z \frac{dz'}{H(z')}\right] \quad (k \neq 0) \tag{1.27}$$

and where $\chi(x) = sin(x)$ for $k > 0$ and $sinh(x)$ for $k < 0$.
Specialising to the flat model and constant w,

$$r(z) = \frac{1}{H_0}\int_0^z \frac{dz'}{\sqrt{\Omega_M(1+z')^3 + (1-\Omega_M)(1+z')^{3(1+w)} + \Omega_r(1+z')^4}} \tag{1.28}$$

here Ω_M is the present fraction of critical density in non-relativistic matter, and $\Omega_r \sim 0.8 \times 10^{-4}$ represents the small contribution to the present energy density from radiation and relativistic neutrinos. In this model, the dependence of cosmic distances upon dark energy is

controlled by the parameters Ω_M and w. The luminosity distance is related to the distance modulus μ by:

$$\mu(z) \equiv m - M = 5\log_{10}\left(\frac{d_L}{10pc}\right) = 5\log_{10}\left[\frac{(1+z)r(z)}{pc}\right] - 5 \tag{1.29}$$

where m is the apparent magnitude of the object (proportional to the *log* of the flux) and M is the absolute magnitude (proportional to the *log* of the intrinsic luminosity). "Standard Candles", objects of fixed absolute magnitude M as SNe Ia, and measurements of the logarithmic energy flux m constrain the cosmological model and thereby the expansion history through this magnitude-redshift relation, known as the Hubble diagram (see figure 1.8). Expanding the scale factor around its value today, the distance-redshift relation can be written in its historical way:

$$H_0 d_L = z + \frac{1}{2}(1 - q_o)z^2 + ... \tag{1.30}$$

The expansion rate and deceleration rate today appears in the first two terms of its taylor expansion. This expansion, only valid for $z \simeq 1$, is of historical utility; it is not more useful today since objects as distant as redshift $z \sim 2$ are being used to probe the expansion history. However, it illustrates the general principle: the first term on the right hands side represents the linear Hubble expansion, and the deviation from a linear relation (starting from the second term), reveals the deceleration.

Another way to measure distances is trough the angular-diameter distance relation d_A, a distance inferred from the angular size $\delta\theta$ of a distant object of fixed diameter D is defined by:

$$d_A \equiv \frac{D}{\delta\theta} = \frac{r(z)}{(1+z)} = \frac{d_L}{(1+z)^2} \tag{1.31}$$

The use of "Standard Rulers" (objects of fixed intrinsic size), provides another means of probing the expansion history, again through $r(z)$.

Measuring Distances Using SNe Ia

As we know from §1.4.4 SNe Ia can be used as "standard candles" to measure luminosity distances. These distances are determined from the measurement of their *restframe* magnitude at the SN peak of luminosity in the (restframe) B band. As the rest-frame magnitude of supernovae is not directly observable, we need to infer it from the observer frame light curves, using a spectrophotometric model of the SN.

Many empirical SN Ia models have been built to fit SN light curves (see §1.4.4 and its references). For example, the SALT2 light curve fitter is a package developed at LPNHE (Guy et al. 2007), for the analysis of the SNLS (SuperNova Legacy Survey) dataset. This model allows us to estimate the rest-frame B-band magnitude (noted $m_B^\star$) of a SN Ia at a given redshift from its (observer frame) light curve, along with other observables, such as the light curve decline rate (or equivalently, its stretch (s), and the *rest-frame colour*, c, of

the object. Building upon the "brighter-bluer" and "brighter-slower" relations, we define the "standardised" distance modulus:

$$\mu = m_B^\star - M + \alpha \times (s-1) - \beta \times c \tag{1.32}$$

where the so-called "standardisation parameters", α and β describe the slope of the brighter-slower and brighter-fatter relations.

The cosmological parameters are determined by minimising the χ^2 function:

$$\chi^2 = \sum_i \frac{\mu(M,\alpha,\beta) - \mu(z,\Omega_M,w,\ldots)}{\sigma_i^2} \tag{1.33}$$

where $\mu(M,\alpha,\beta)$ is the observed distance modulus defined in equation 1.32 and $\mu(z,\Omega_M,w,\ldots)$ the cosmological model prediction. In practice, the (average) absolute magnitude M of SNe Ia is totally degenerate with the Hubble constant. Both parameters are grouped into one single nuisance parameter which is fit along with the cosmology and then marginalised over. Same thing for the standardisation parameters, α and β which are also fit and marginalised over. See (Sullivan et al. 2011, Conley et al. 2011) for details.

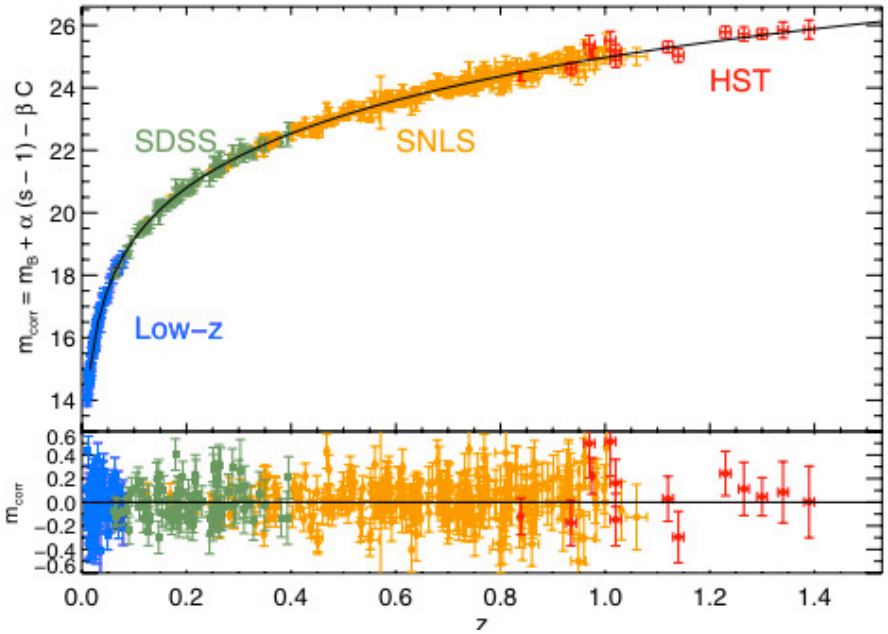

Figure 1.8: *Hubble diagram of the same combined Low-Z, SDSS, SNLS and HST sample. The residuals from the best fit are shown in the bottom panel (Conley et al. 2011).*

Figure 1.8 shows the latest Hubble diagram published by SNLS (Conley et al. 2011). It contains a sample of 472 SNe Ia at different redshifts, from low to the 14 high-redshift taken by HST. Constrains on the w parameter are shown in figure 1.9 as a function of the Ω_m density parameter. Supernova results combined with the BAO and CMB data give an value

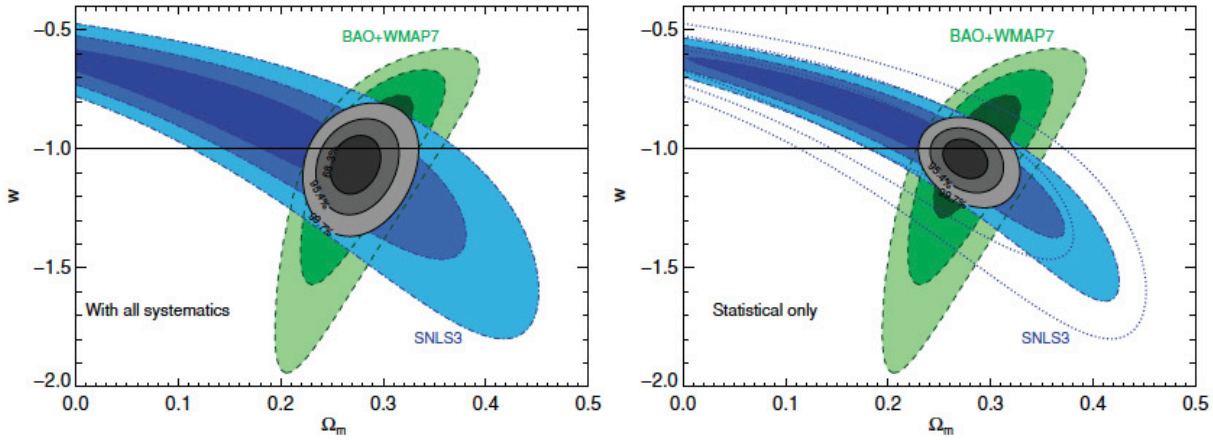

Figure 1.9: *Statistical joint constraints on Ω_M, w, flat cosmological models (including systematics), CMB and BAO. The common contours (grey), constrain models close to a cosmological constant (Sullivan et al. 2011).*

of $w = -1.068 \pm 0.08$ stat + syst. Such a value is compatible with what we would expect from a cosmological constant. The corresponding confidence contours in the plane $\Omega_M - w$ are shown on figure 1.9. From this same figure, it is clear that systematic uncertainties represent at least half of the total error budget.

The statistical and systematic uncertainties affecting this measurement are analysed in detail in Conley et al. (2011). As of today, the error budget is dominated by the systematics, the main contributions being (1) photometric calibration (2) uncertainties carried by the SALT2 light curve models (due to the finite size of the training sample) (3) uncertainties due to a un-completeness of the SNe Ia samples (Malmquist bias) and (4) uncertainties of astrophysical origin, such as a correlation between the SN and its host galaxy.

1.5 Dark Stuff

Observations have confirmed that the expansion of the Universe is accelerating under the influence of a repulsive form of energy, dark energy, that built two-thirds of the Cosmo ($\sim$ 68.3%), $\sim$ 26.8% seems to be dark matter, and roughly $\sim$ 4.9% normal (baryonic) matter (fig. 1.10). Here we describe briefly some of the most plausible ideas about the dark problem. We spend only few lines with the description of the dark matter problem because is not the object of our work and then we come up in more detail with some hypothesis for the explanation of the dark energy problem.

1.5.1 Dark Matter

It is almost universally accepted that a large part of the Universe is filled with a material that can be see only by its gravitational effects. As we told in the introduction, dark matter was suggested by Zwicky in the 30s, studying the nearby Coma galaxy cluster. Comparing

the motion of galaxies with their total mass, he discovered that the velocity in the outskirt of galaxies did not decrease as we expect if the total amount of mass would have been only the visible one. Nowadays is widely accepted that this kind of unknown matter, called dark matter, plays a key role in the Concordance Model, allowing the total baryonic and non-baryonic matter to form the cosmological structures and cluster of galaxies that we see today. We know that a very little percentage of dark matter is normal baryonic matter, as red-brown dwarf stars and planets, interstellar material, dust and diffuse gas. But it counts only for 0.5% of the total, so what is the rest? The most common accepted theories to describe dark matter the Hot Dark Matter and Cold Dark Matter model.

First the weak hypothesis: hot dark matter. A classical candidate is the neutrino particle. Neutrino is an extraordinary weakly interacting particle, coming in three types, each believed to have a particular mass. At the moment the possibility of only a hot dark matter Universe is ruled out by observations, but there is still a little possibility that the total dark matter is a mix of hot and cold weakly "particles".

Nowadays, the most accepted dark matter candidate is the second one: Cold Dark Matter (CDM) particles. In that sense is now used within the Λ-CDM model. Two main types o candidates are considered: the WIMPs and the Axions. Weakly-interacting massive particles are motivated by super-symmetry, which is not yet confirmed and it regarded as a property of modern standard model of particle theory, where axions are particles proposed to explain why particles and anti-particles are similar properties.

1.5.2 Dark Energy

Since the discovery of the cosmic accelerating expansion, cosmologists around the world have tried to describe the force responsible for the acceleration: it accounts for the majority of the cosmic energy density, it is gravitationally repulsive, it does not appear to cluster in large structures, and it is stretching "space-time" apart. It is beyond the scope of this work to describe all the theory behind dark energy hypothesis, instead we give only a glimpse into the subject choosing three of the most accepted ideas: the cosmological constant, the scalar field hypothesis, and finally the modified gravity.

Cosmological Constant and Vacuum Energy

The cosmological constant was introduced by Einstein himself in order to modify GR equations and account for a static Universe. After the discovery of expansion, this constant disappeared from cosmology models for years until 1998. This constant appears to perfectly fit the Einstein equation, and in that sense one can expects such a term because it is indistinguishable from the contributions as gravitational source of what we call *zero-point energy* (vacuum energy), expected in quantum field theories.

Vacuum energy is one of the most puzzling candidate. GR requires that the stress-energy of the vacuum takes the form of a constant metric tensor, $T^{\mu\nu}_{vac} = \rho_{vac} g^{\mu\nu}$. Without entering into a mathematical discussion we can prove that the vacuum energy has a pressure equal to minus its energy density, $p_{vac} = -\rho_{vac}$. That means the vacuum energy is equivalent to a cosmological constant. Problems come when we tried to compute the value of the vacuum

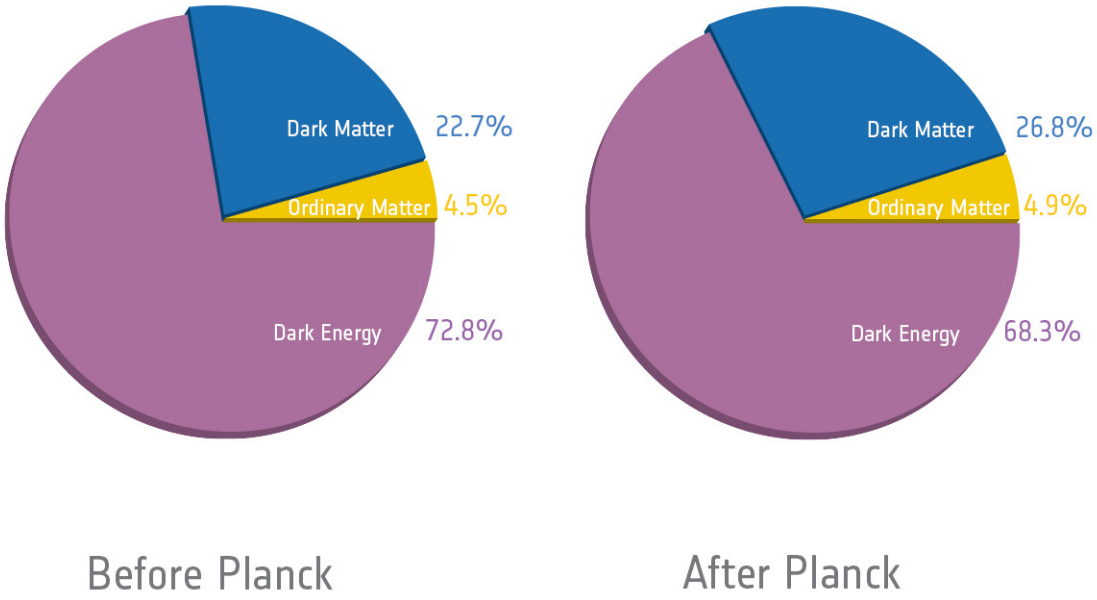

Figure 1.10: *After Planck the baryonic matter counts for* 4.9% *of the total. Dark matter gives the rest* 26.8%*; this matter has only been detected indirectly by gravity effect. The rest is composed of dark energy, that acts as a sort of an anti-gravity force (ESA/Planck Collaboration 2013).*

energy density. To illustrate the magnitude of the problem, we can write the general equation for the density energy of the vacuum:

$$\rho_{vac} = \frac{1}{2} \sum_{fileds} g_i \int_0^{\inf} \sqrt{k^2 + m^2} \frac{d^3k}{(2\pi)^3} \simeq \sum_{fields} \frac{g_i k_{max}^4}{16\pi^2} \tag{1.34}$$

where g_i is the degree of freedom of the field and k_{max} is an imposed cutoff of the momentum. If the energy density contributed by just one field, then the cutoff k_{max} must be < 0.01 eV: below any energy scale thought. Taking the cutoff to be the planck scale ($\simeq 10^{19}$ GeV), then quantum field theory does not work more using a classical space-time metric, then the zero-point energy density would exceed the critical density by some 120 orders-of-magnitude. This very large discrepancy is known as the cosmological constant problem (Weinberg 1989).

Scalar Field

Vacuum energy does not vary with space-time. However, if we introduce a degree of freedom, namely a general scalar filed ϕ, we can make vacuum energy dynamic (Wetterich 1988, Frieman et al. 1995, Zlatev et al. 1999). Just for the completeness we give the equation of a typical scalar field dark energy equation of state:

$$w = \frac{-1 + \dot{\phi}^2/2V}{1 + \dot{\phi}^2/2V} \tag{1.35}$$

where $\dot{\phi}^2/2$ is the kinetic energy and V is the potential energy. When $\dot{\phi}^2/2V \ll 1$, then $w \simeq -1$, and the scalar field becomes a varying vacuum energy. Different scalar field can be classified as *thawing* and *freezing* (Caldwell and Linder 2005). In *thawing* models, the field is frozen by a friction term, and it acts as a vacuum energy; when the time evolves and expansion rate drops a certain value, the field roll out and w evolves away from -1. In *freezing* models, field rolls out more slowly as time goes on.

Scalar fields might be solve the problem introducing a degree of freedom in the equation but this contribution costs the raise on new unexpected problems, such as the correlation between the accelerating expansion and the primordial inflation.

Modified Gravity

A very different approach involves a modification of Einstein equations and theory of gravity itself. Assuming that we can still described space-time by a metric, to change GR directly we need to step: a new version of the Friedmann equations (section §1.2.3), and a modification of equations that govern the evolution of LSS. A number of ideas have been explored until now, motivated by $> 5D$ dimensional theories and string theory (Deffayet 2001), or by modifications of the GR Lagrangian itself (Hu and Sawicki 2007). We can easily change the Friedmann equation maintaining the Concordance Model valid at early times (from Big Bang to the CMB anisotropies and structure formation); the only request is that the new Friedmann equations must reduce to the GR standard form for $z \simeq 1$. If we consider the model of (Dvali et al. 2000), which arises from a 5-dimensional gravity theory and has a 4D Friedmann equation:

$$H^2 = \frac{8\pi G\rho}{3} + \frac{H}{rc} \tag{1.36}$$

where rc is a length scale related to the 5-dimensional gravitational constant. As the energy density in matter and radiation ρ, becomes small, there is an accelerating solution, with $H = 1/rc$. From the viewpoint of expansion, the additional term in the Friedmann equation 1.36, has the same effect as dark energy which evolves from $w = -1/2$ (for $z \gg 1$) to $w = -1$ in the distant future. Unitl now there are no evidence that this model is consistent with observations (Gregory et al. 2007).

1.6 Open Problems

All the knowledge learnt until now is summarised what is called the Standard Model of Cosmology, or Λ-CDM model. This theory describes us the geometry and dynamics of an expanding Universe, described by the GR equations and the FLRW metric; the Universe is flat ($k = 0$ and $\Omega_{tot} = 1$), and had inhomogeneities in the density perturbations, which are responsible for structures that we see today, as predicted by the inflation theory (Guth 2004). The total energy density of the universe is divided into three major parts (see fig. 1.10): 4.9% by the baryon energy density, constraint by the big bang model of primordial nucleosynthesis. 26.8% by a non-baryonic matter (dark matter). The rest 68.3% is describe by a cosmological constant Λ representing a dark energy model with $w = -1$.

Those model predictions and assumptions are currently well constrained by observational data. As we said there are tentatives of explanation without solution (i.e., vacuum energy explanation has a difference of 120 orders of magnitude between the quantum mechanics prediction and the measured values). Another problem is the so-called *coincidence problem* (Frieman et al. 2008): why is $\Omega_M + \Omega_\Lambda \simeq 1$ precisely today, after an expansion of several billion years? If Ω_M decreases with time and Ω_Λ remains constant, why has the cosmological constant begin to dominate only now? All these questions have no answers yet.

7

Chapter 2

Instrumentation for Cosmology

We now present the context of this thesis. In 2006, the LPNHE Cosmology Group was contacted by Pr. B. Schmidt, the initiator of the SkyMapper project (and co-discoverer of the accelerated expansion of the Universe). Pr. Schmidt suggested that we collaborate on the analysis of the supernovae that would be discovered by SkyMapper. As photometric calibration was becoming an important issue, the group proposed to contribute to the project a calibration source that would be used to monitor the transmission of SkyMapper.

The project was named SkyDICE, and presented to the EMERGENCE program of Université Pierre et Marie Curie (UPMC). It was accepted and funded by UPMC, and I was hired, as a PhD student, to work on the construction, calibration and commissioning of the source. In what follows, we will first present the SkyMapper telescope (§2.1) for which the SkyDICE source was built. Then, we will present the main motivations for trying to improve so aggressively the calibration of wide field imagers (§2.2), and we will discuss the current techniques, based on observations of stellar calibrators. Finally (§2.3), we review the relatively new field of instrumental calibration, to which SkyDICE belongs.

2.1 The SkyMapper Southern Survey (S3)

SkyMapper is one of a new generation of dedicated wide-field survey telescopes based at the Siding Spring Observatory (see fig. 2.1)[1]. The telescope has been operating since 2010. The goal of the survey is to obtain a complete map of the southern sky at small redshift ($z < 0.1$), unfortunately it has not yet started due to instrumental problems. The facility operates in an automated way and requires minimal support. The telescope is controlled on remote with an scheduling and data quality system. Data is transferred via a fast network to the ANUs Supercomputing Facility where the data reduction pipeline resides. When ready, SkyMapper will do the multi-colour and multi-epoch Southern Sky Survey, called S3.

[1] see http://rsaa.anu.edu.au/observatories/siding-spring-observatory

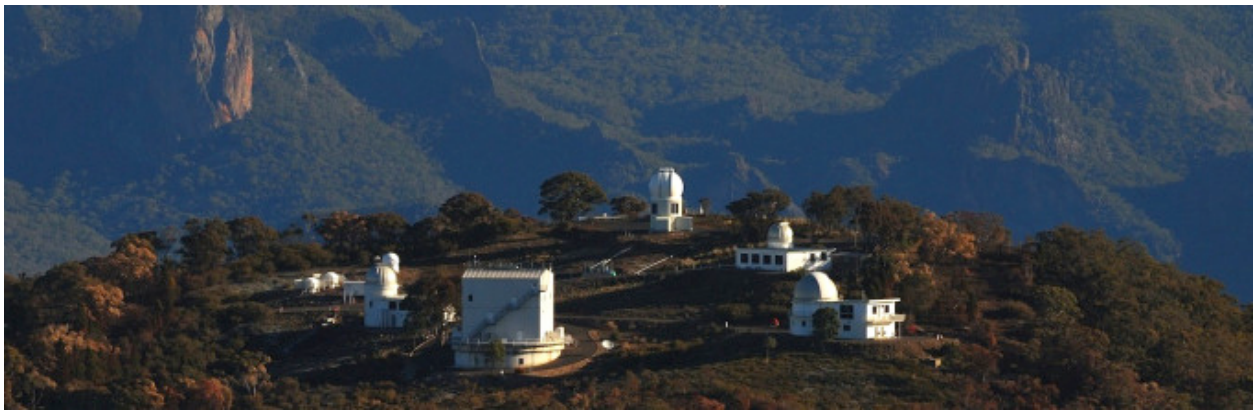

Figure 2.1: *Arial view of the Siding Spring Observatory (SSO). SkyMapper is the one at the top of the mountain in the centre (Siding Spring Observatory 2012).*

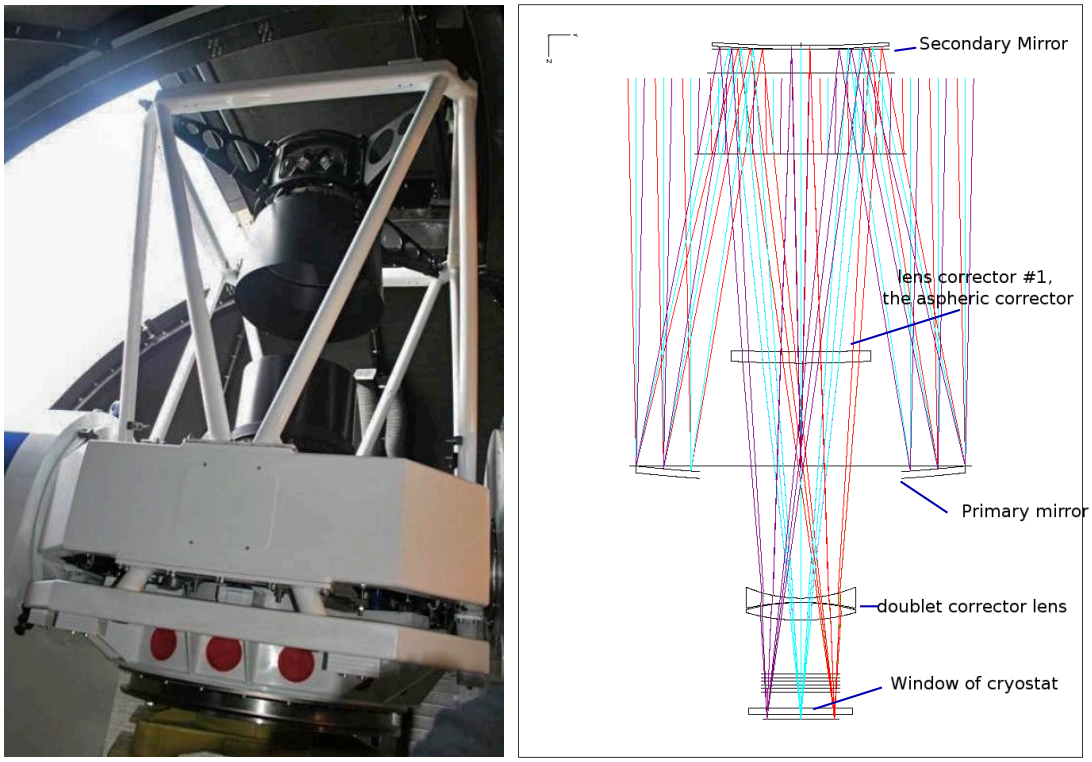

Figure 2.2: *(Left) - Image of the SkyMapper telescope inside the dome. (Right) - Overview of the optical design of the telescope.*

2.1.1 Optical Design

The SkyMapper telescope optics was designed by Electro Optics Systems (Australia)[2]. It has a 1.35 m primary mirror and a large 0.69 m secondary mirror. This results in a collecting area equivalent to an un-obstructed aperture of 1.13 m, see figure 2.2. The telescope is a modified Cassegrain, optimised for wide-field observations between 340 nm and 1000 nm.

The structure design is really compact. The primary mirror is an Astro-Sital Glass Ceramic made by LZOS (Russia)[3]. The secondary mirror is carried on an actuated hexapod mount that allows for $tip - tilt$, $x\&y$ and telescope $focus$. The telescope control system uses the hexapod to adjust for gravity induced flexure and focus change due to temperature. The three transmissive corrector elements are anti-reflection coated and is composed of fused Silica to maximise the UV response. The telescope can point to ± 3 arcsec and track to 0.5 arcsec RMS for ~ 5 minutes. Both of the telescope principal axes are driven by direct on-axis DC ring motors and direct on-axis incremental encoders.

2.1.2 SkyMapper Camera

The SkyMapper focal plane is built with a mosaic of 32 CCDs resulting in a total of 268 Mega pixels, with high speed device controllers, and low noise readout (Keller et al. 2007). The imager has been designed at ANU Astronomy department (Granlund et al. 2006). Due to the large focal plane, the instrument is heavy for the size of telescope: fig. 2.3 shows the auto-guider, science filters and the focal plane imager with the CCD mosaic. The Imager vacuum jacket is at the centre, capped in a helium cryostat. The shutter is above the vacuum jacket window. The shutter is composed of two blades that form a moving slot of variable width to provide uniform exposure of the focal plane. The shortest exposure is about 1 ms and exposure homogeneity is 0.3% at 100 ms exposure (Reif et al. 2004). The vacuum jacket window is 25 mm thick fused Silica with an antireflection coating. A uniform flow of dry air is passed over this window to prevent condensations.

SkyMapper has 6 interchangeable filters (u, v, g, r, i, z) similar to those used in the SDSS project, each one is 309×309 mm and 15 mm thick. The filter set is constructed of coloured glass where possible. Coloured glass filters show a better homogeneity across the focal plane than can be currently achieved with multi-layer interference filters. The filter glass was made by Macro-Optica (Russia), and Schott (Germany). Only the r and i band filters have additional short wave-pass coatings to define the total bandpass (Bessell et al. 2011).

The CCD Mosaic

The SkyMapper Imager CCD mosaic is a 4×8 array of E2V[4] CCD44-82 detectors. Each CCD detector has 2048×4096, 15 μm squared pixels. The deep depletion device is back-illuminated. They have a good quantum efficiency in the range of $350 - 950$ nm (fig. 2.4), and low readout noise.

[2] see http://www.eostech.com
[3] see http://lzos.ru/en/
[4] see http://www.e2v.com/

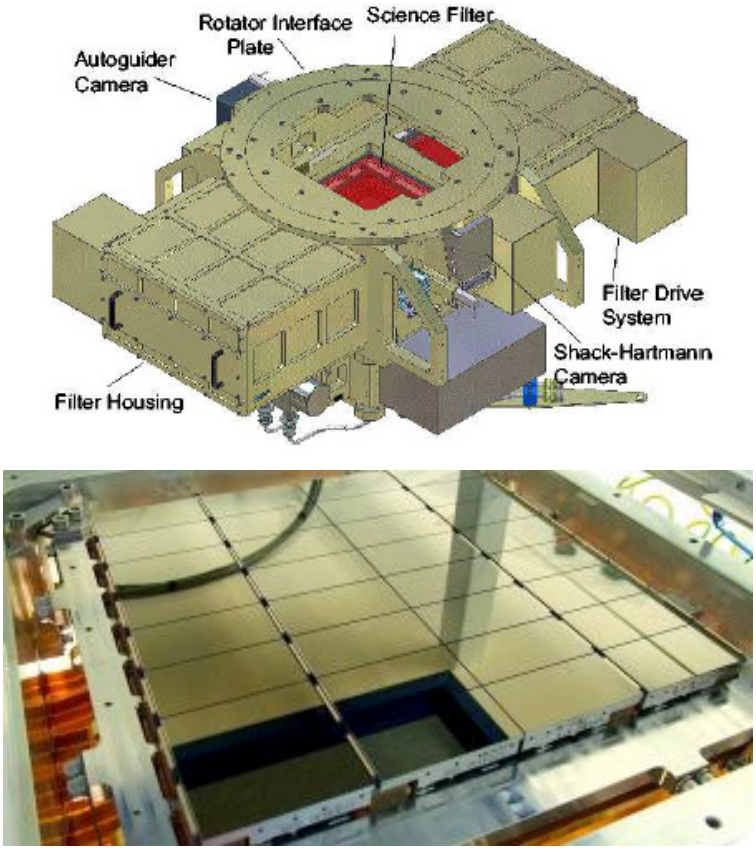

Figure 2.3: *(Top) - Design of the SkyMapper imager system as seen from above. (Bottom) - The CCD mosaic of the SkyMapper wide field camera (Siding Spring Observatory 2012).*

All 32 CCDs are carried on a 10 mm thick carrier plate. Its surface is uniform with a factor to 10 μm. The aim for focal plane flatness is to match the single pixel geometric depth of field in the $f/4.78$ beam of ± 32 μm. The inner two rows of CCDs are put together with a 1.5 mm gap between the rows and a 0.5 mm gap between columns. This assembly gives a filling factor of $\sim 91\%$.

CCDs Controller

The wide field imager uses a custom version of the 16-channel STAR-GRASP controller developed for Pan-STARRS (Onaka et al. 2006). A hybrid 300MHz CPU FPGA is used in the controller for the digital signal processing. The controller has different Gigabit ethernet ports for a rapid readout, which enables the camera to easily meets a reading in ~ 20 s. Both detector controllers are connected to a single server computer that transfers data to local storage. The server is commanded by the Computerised Instrument Control And Data Acquisition system - CICADA (Young et al. 1999), built by ANU for all SSO instruments. Finally, the Telescope Automation and Remote Observing System - TAROS (Wilson et al.

2005), controls CICADA to configure the instrument and acquire the required exposure.

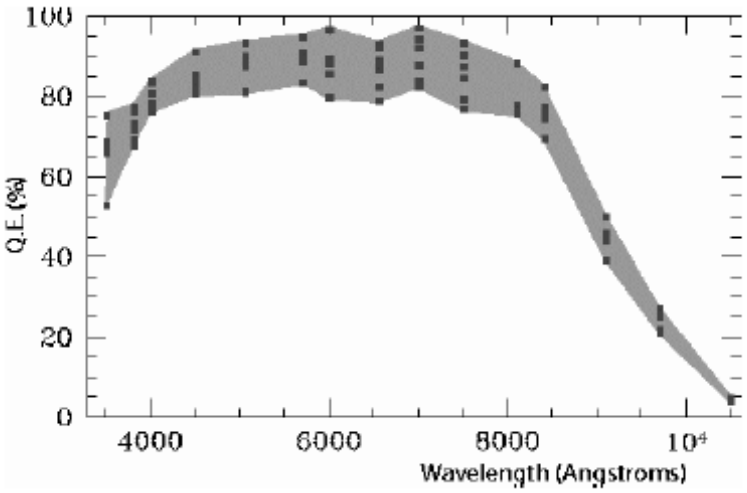

Figure 2.4: *Spectral response of SkyMapper science CCDs (Keller et al. 2007).*

2.2 Photometric Calibration

We now turn to the problematic of photometric calibration, the core of this thesis work. We discuss briefly the motivation for improving the flux calibration of future imagers. We then present successively the standard calibration techniques, based on the observation of standard stars. In a last section, we present the current efforts, inside the community, to develop an alternate calibration chain, anchor on the modern flux metrology techniques.

2.2.1 Motivations for Photometric Calibration

The measurement of the cosmological parameters, in particular, the Dark Energy Equation of state parameter with Type Ia Supernovae is now dominated by systematic uncertainties. The good news, however, is that the dominant (by far) contribution to the systematic error budget is the photometric calibration of the imagers, used to follow the flux of the SNe Ia. Improving the precision of the recent SNLS measurement of w (e.g. Conley et al. 2011, Sullivan et al. 2011) requires improving the accuracy of the calibration of MegaCam.

Why is photometric calibration so important in SN cosmology ? Let's have a look at figure 2.5. It shows the spectra of several supernovae at different redshifts. The cosmological information is extracted from the comparison of the *restframe* flux of the nearby and distant supernovae, i.e. the integral of an (arbitrary) reference region of the spectrum. In general, one choose the restframe-B band (the spectral regions overlined in blue on the figure).

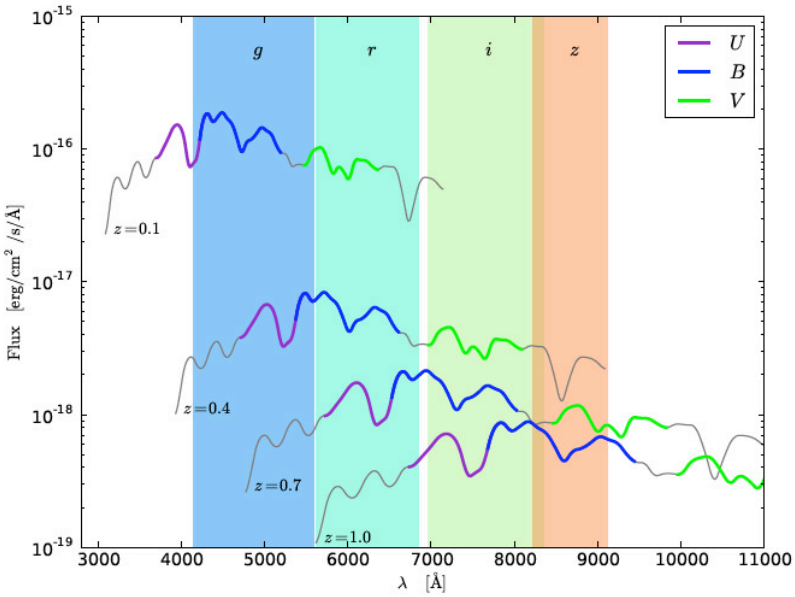

Figure 2.5: *SN Ia spectra at various redshifts. The shaded areas represent the imager passband. The distance estimate is generally chosen as the integral of the SN spectrum in the rest-frame B-band (Regnault 2013).*

The shaded areas on the figure represent the imager passbands. What the observer actually measures are the integrals of the SN spectra in those passbands. From these measurements, the core of the cosmology analysis consists in (1) infering the SN restframe B-flux from the observer frame measurements (using a spectrophotometric model of the supernovae) and (2) intercalibrating the fluxes measured in the bluer and redder bands of the imagers.

This intercalibration step is essential as the SN restframe B-band flux is not inferred from the same imager passbands, depending on whether the SN is nearby or distant. Hence, any error on the intercalibration of the telescope passbands will translate into a redshift dependent bias on the SN distance estimates, and therefore, into a bias on the cosmological measurements.

As we see, what is essential for supernova cosmology, is to make sure that the fluxes measured in the blue and red bands of the imagers are measured in the *same* units. On the other hand, it is not necessary to perform an accurate absolute calibration of the instrument, since the cosmology is actually insensitive to the absolute flux scale.

The traditional flux calibration techniques in use today are based on the observations of absolute stellar spectrophotometric standards. In the next section, we review the main standards in use today.

2.2.2 Primary Standards

Vega The α Lyrae star has been the primary standard for years. In the 60s and 70s, there have been many attempts to calibrate its spectrum using laboratory sources (see Hayes 1985;

and references therein). The precision of the flux standards was not what it is today, and the precision on the (relative) colour calibration is estimated to be of about 1%.

Unfortunately, Vega is too bright and cannot be observed with large telescopes. For example it is about 10,000 times brighter than the magnitude 10 stars that themselves can be observed only by defocussing the telescope and reducing the exposition to a fraction of a second. As a consequence, people have been relying on increasing long and complicated metrology chains (e.g. Landolt (1992) → Landolt (1983) → Landolt (1973) → Johnson and Morgan (1953)) to tie their science images to the flux scale of Vega (which they could not observe themselves). This metrology chain is today considered as broken (Regnault et al. 2009, Betoule et al. 2013).

DA White Dwarfs Model Another approach, first proposed to Finley and Koester (Finley and Koester 1991) is to rely on primary standards whose spectral energy distribution (SED) can be modelled. In particular, hot DA (pure hydrogen) white dwarfs have reputedly a simple atmosphere that contains only pure hydrogen, and very few heavier elements. As a consequence, modelling their atmosphere relies on the physics of only one element (H) and one can predict their SED with a good accuracy.

Several stellar atmosphere codes are in use today: ATLAS (Kurucz 1993) calculates a 1D, plane-parallel, horizontally homogeneous stellar atmospheres, in radiative and hydrostatic equilibrium (LTE). TLUSTY (Hubeny and Lanz 1995) makes essentially identical assumptions for NLTE atmospheres, PHOENIX (Hauschildt and Baron 1995) is a multi-purpose stellar atmosphere code, developed initially for modelling novae and supernovae.

The most interesting feature of stellar models is that they depend on a very small number of parameters, specifically, the temperature of the star, its surface gravity and its metallicity. These parameters can be inferred from the profile of the spectral lines of the stars (e.g. for white dwarfs, the Balmer lines). As a consequence, they can be estimated from high-resolution spectroscopy of a few selected spectral features, and then injected into the model that predicts the entire SED of the star, from the far-UV to the infra-red.

CALSPEC The need for high-accuracy flux standards, valid from the far-UV to the infra-red has become stronger and stronger, with the advent of the Hubble Space Telescope (HST). For this reason, the HST community started implementing the program described above in the early 1990's.

This calibration program is now called CALSPEC [5] and its goal is to define an accurate "white dwarf flux scale" and to establish a set of spectrophotometric standards anchored on this flux scale. The program has selected 3 white dwarfs as primary standards candidates, derived synthetic SEDs using the TLUSTY model atmosphere code, and used them to calibrated the HST instruments, notably the STIS spectrograph (in the visible), and NICMOS the NIR spectro-imager. These two instruments have been used in turn to expand the HST flux scale to a larger number of fainter objects that can be observed with large modern telescopes.

[5] see http://www.stsci.edu/hst/observatory/cdbs/calspec.html

As of today, CALSPEC seems to be the only set spectrophotometric standards with a traceable calibration chain. As a consequence, most cosmological surveys than need an accurate calibration are anchored on the white dwarf flux scale.

However, the CALSPEC flux standards are themselves affected by uncertainties, which have two origins. First, there are uncertainties which are related to the finite repeatability of HST, in particular due to the fact that due to a finite pointing precision, even with a large slit, the flux losses affecting a same star vary from one epoch to another. These uncertainties can be estimated from repeated measurements of a same object (e.g. Regnault et al. 2009). They are of a few mmags, and decrease with the number of epochs.

Another source of uncertainty come from the stellar atmosphere models. Indeed, even DA white dwarfs are complex objects, and the modeling systematics that affect the CALSPEC flux scale are actually difficult –if not impossible– to estimate with precision. Accepted values are in the range 3 mmag $< \sigma_{g-z} <$ 8 mmag.

The calibration of SNLS and SDSS As an example, the SNLS and SDSS supernova surveys, the two major contributors to the SN Ia Hubble diagram have invested a lot a effort into anchoring their calibration on the HST flux scale (Holtzman et al. 2008, Regnault et al. 2009). Until recently, their uncertainty budget was dominated by the sophisticated calibration chain they had to set up in order to link their science observation to the CALSPEC standards. In 2010, the two surveys joined forces and launched an ambitious intercalibration program. In particular, they managed to build four redundant calibration chains from their respective science images to a series of CALPSEC stars. This allowed them to push the uncertainty of the transfer of the CALSPEC flux scale to the survey images down to unprecedented levels of ~ 3 mmags (Betoule et al. 2013), on par with the CALSPEC error budget. As a result, it is now time to start challenging the HST flux scale if we want to improve further the calibration of future surveys.

2.3 Instrumental Calibration

Despite tremendous progress, we see that the accuracy of the fundamental flux standards is still slightly uncertain, this uncertainty being itself uncertain ($\sigma_{g-z} \sim 3-8$ mmag). This was not a problem when the calibration of wide field instruments by uncertainties in the metrology chain, linking the primary standard to the science images. It is starting to be a problem now that these uncertainties are as low as ~ 3 mmag.

In this context, several groups have proposed alternatives to the current stellar calibration techniques. In particular, they have proposed to build upon the new detector based flux metrology techniques, accurate at the 0.1%-level and to anchor the flux calibration of modern instruments to the calibration chain developed and maintained at NIST (Larason and Houston 2008).

2.3.1 Metrology Chain

Before the introduction of Silicon photodiodes, instrumental calibration were performed using Pt or Cu ovens emulating blackbody radiation. These calibrators were heavy, difficult to control and were precise at the 1-2% level. Everything changed with the advent of Silicon photodiodes, which are small, stable, compact and inexpensive detectors, sensitive from the UV to the near-IR with an average accuracy of $\sim 0.2\%$. At about the same time, the NIST flux metrology chain evolved, from source based standards (i.e. ovens) to detector based standards (figure 2.6).

The new primary standard maintained at NIST is an electrical substitution cryogenic radiometer, called the Primary Optical Watt Reference (POWR Houston and Rice 2006). POWR is used to calibrate a laser source called SIRCUS (Brown et al. 2006). The SIRCUS calibration is then transferred to a set of photodiodes. Finally the calibration carried by these photodiodes is then finally transferred to the client photodiodes at the Spectral Irradiance Facility (SCF), which operates a large set of lamp and monochromator based sources. The reported accuracy of POWR is of a few 10^{-4}. The accuracy of the client photodiode calibration if of about 0.2% in the visible and almost 1% in the UV and the near-IR.

Several photodiodes are used to disseminate the NIST calibration. We use the Hamamatsu S2281[6], which is a large area photodiode, with a good sensitivity from the UV to the near-IR. Today, almost all proposed alternatives to stellar calibration (including our project) anchor themselves to the calibration chain represented on figure 2.6, and implement the two steps represented on figure 2.7. In the remaining of this section, we review some of these projects.

2.3.2 Instrumental Calibration Projects

ACCESS

The Absolute Colour Calibration Experiment for Standard Stars ACCESS (Kaiser et al. 2010), is constructing a small rocket telescope of ~ 40 cm, equipped with a low-resolution spectrograph. The goal is to calibrated the telescope+spectrograph ensemble directly at the SIRCUS facility and observe, during a series of flights a handful of bright stars $0 < V < 10$ in the $350 - 1700$ nm range. The targeted accuracy should be $\lesssim 1\%$. ACCESS have chosen to use a rocket borne telescope to reach an altitude of > 100 km in order to avoid the absorption lines from OH radicals, those lines affecting in particular near-IR observations. It also allows them to avoid UV absorption from the atmosphere. The target stars have been selected using two criteria: either they have been already used as primary standards by previous surveys (this is the case for bright historical standards, such as Vega or Sirius), and they possess a simple atmosphere, with as few absorption features as possible.

As the ballistic flights are short (400 sec of usable time), the target stars are all very bright. As a result, ACCESS will rely heavily on HST observations, to bridge the gap between the $0 < V < 10$ magnitude range and the $V > 15$ range that can be observed with modern telescopes.

[6] see http://www.nist.gov/calibrations/

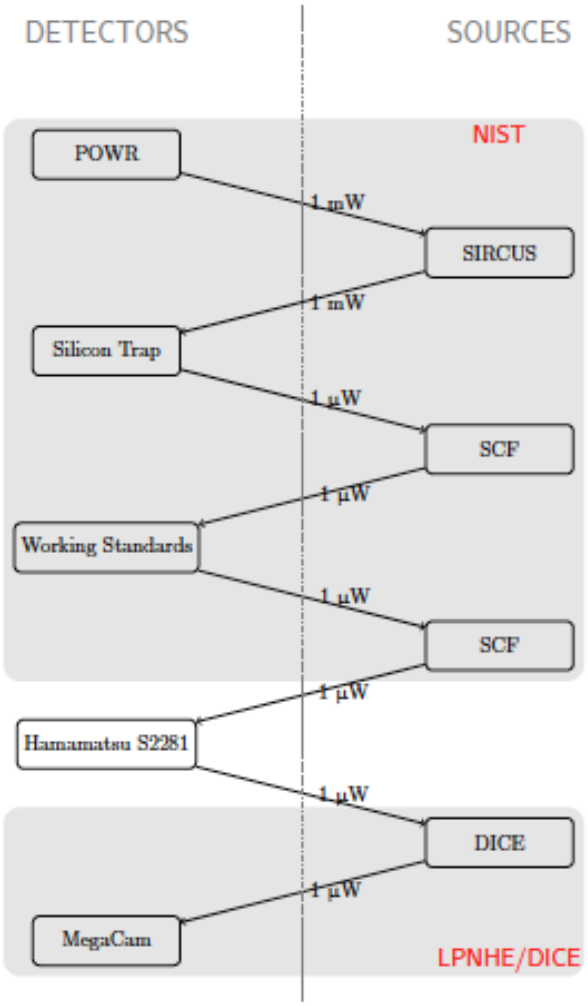

Figure 2.6: *NIST metrology chain (Regnault 2013).*

NIST Standard Star Network

NIST institute is funding a similar project but with a small (10-cm) ground based telescope, equipped with a spectrophotometer, (called AESoP) (McGraw et al. 2012). The plan is to calibrate the telescope+instrument together, using an artificial source (calibrated at NIST), and to monitor the telescope + atmosphere system using another distant calibrated source. The goal of the project is to establish a series of spectrophotometric standard stars, characterised with an accuracy of $\sim 1\%$. Again, these are bright stars, in the $0 < V < 5$ magnitude range.

In any case, with the help of HST, both projects will permit a direct comparison of the HST and NIST flux scales, which is an invaluable piece of information. However, they will not relieve survey calibrators from monitoring their instrument (in particular their passbands).

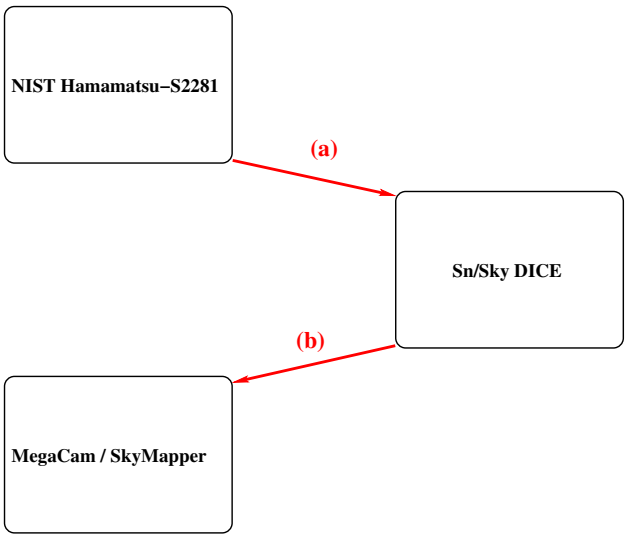

Figure 2.7: *DICE metrology chain.*

SDSS Calibration

The main purpose of system described in Doi et al. (2010) and installed on the SDSS 2.5 m telescope at Apache Point Observatory is to measure the imager passbands "in situ", and to monitor them over the life of the survey. The source is a lamp coupled to a monochromator and an integrating sphere. The flux is monitored in real time by a calibrated Hamamatsu photodiode. The source hits the camera from a position close to the cryostat window. Several measurements campaigns have been conducted to measure the SDSS passbands, as well as the passbands of the auxiliary "Photometric Telescope" which is used to complement the SDSS observations with calibration patches.

Wavelength uncertainties are dominated by the monochromator resolution (± 3 Å), and by the fact that the system can not reproduce the exact beam geometry and angular distribution. An important result of this calibration system is the demonstration of a slow degradation in the imager response during its life-time, directly affecting the accuracy of photometric measurements. The work also demonstrated that telescope passbands are not stable as we thought, and that ageing comes out as a major problem for calibration in the era of 0.1% accuracy. A regular precision monitoring of the telescope response must be implemented if one seeks to do precision cosmology with future surveys.

ESSENCE and PanSTARRS

The device designed and built by the Harvard team led by C. Stubbs (Stubbs et al. 2010), is composed of a large flat field screen fed with a tuneable laser, and monitored in real time by an Hamamatsu Si photodiode calibrated at NIST. This light source illuminates the telescope aperture, generating a diffuse and uniform illumination on the focal plane. Demonstrators were installed at the Blanco 4.2 m telescope (Cerro-Tololo) to calibrate the Mosaic-II imager, and at the PanSTARRS telescope (Hawaii) to calibrate the 3 sq. deg. Giga pixel camera.

The wavelength uncertainties of filters are of about 2 Å, which fit very well with general specifications for current dark energy surveys. This project is slightly more advanced that its competitors, as it has been able to compare directly its instrumental calibration with a stellar calibration. However, they observed a disappointing 5% discrepancy between both, which they attribute to systematic errors affecting their flux measurements. Several sources of systematics have been found that dominate their error budget. The non perfect uniformity of the screen and pollution of the calibration frames by stray light are two of the most important ones.

The DICE Experiment

All systems describe above are only a part of the next generation of calibrators that will be installed on modern telescopes and future survey projects. There even more projects that we did not talk about, like the DECCal calibrator (Rheault et al. 2010), built for DEC (Dark Energy Camera).

Our laboratory (LPNHE), proposed a new light source design, based on LEDs (Barrelet and Juramy 2008). It was called Direct Illumination Calibration Experiment (DICE). As of today, two demonstrators have been built and installed, one at the Canada France Hawaii Telescope (Hawaii - USA), and the other in the enclosure of the SkyMapper Telescope at Siding Spring Observatory (Australia). These two systems are the core of the next part of the thesis. In the next chapter we discuss the design and implementation of SkyDICE, the second generation light source.

Chapter 3

The DICE Calibration System

The goal of the DICE system (Direct Illumination Calibration Experiment), is to calibrate wide field imagers with a precision of a few per mil. A first demonstrator, called SnDICE (Supernova DICE), was designed and built in 2007, then installed in 2008 at the Canada France Hawaii Telescope (CFHT). A twin copy was also built, so that we could test and monitor the device in our laboratory over long durations. For a detailed description of the SnDICE project see the thesis work of Guyonnet (2012) and Villa (2012).

In 2011-2012, a second generation instrument, called SkyDICE (SkyMapper DICE), was built and installed at the Siding Spring Observatory inside the enclosure of the SkyMapper telescope (see section §2.1 on chapter 2). The design of SkyDICE is very similar to that of SnDICE, besides a few key improvements that were added from the lessons learned operating SnDICE.

In this chapter we describe the principles that have guided the design of the DICE calibration source (§3.1 and §3.2), and we give an overview about the physics of our source of calibration. We then describe the internals of DICE systems, with a particular emphasis on SkyDICE in§3.3. Finally, in §3.4, we introduce the Data Acquisition System (DAQ), and we describe how SkyDICE is interfaced with the telescope control system.

3.1 Goals of the DICE system

DICE was designed with three goals in mind. First, we wanted to build a stable source that would allow us to monitor the imager, follow the small fluctuations of the readout gains, and also follow the slower degradation of the telescope throughput. Second, we wanted to be able to monitor the telescope passbands, in particular, to detect any alteration of the passband fronts. Finally, we wanted to anchor the calibration of the telescope to the modern flux metrology chain defined by the Institutes of Standards, and maintained primarily by NIST.

3.1.1 Monitoring

On most imager, the gains of the CCD readout chain are not perfectly stable, and display fluctuations at a level of $1 - 2‰$. Gain variations are easily absorbed into the imager zero points, which are determined nightly with observations of stable stellar calibrators. On wide field imagers, though, they have an impact on the flat field solution. With the advent of segmented CCDs which are read through multiple readout channels, there is a stronger incentive to monitor the gains in real time, with a dedicated instrument.

Also, the thought-put of a telescope degrades slowly over time, because of dust deposits on the optical surfaces (especially the mirror) and normal ageing of the optical coatings. Several authors have reported significant changes of the effective passband of their telescope (e.g. Doi et al. (2010), Betoule et al. (2013)). Again, the calibration requirements on modern imagers make it necessary to follow precisely these degradations.

3.1.2 Flat-Fielding

Another problem is the control of the uniformity of the imager photometric response as a function of the position on the focal plane. This can be seen in the MegaCam CCDs mosaic, where the difference between the centre of the focal plane and corners are of about $\sim 10\%$ (Betoule et al. 2013). Much of these non-uniformities are due to flat pollution by stray-light. In practice, they are mapped using dithered observations of dense stellar fields. But this approach costly in terms of observation time, and the technique is very sensitive to image quality and absorption variations along the dithering sequence. Mapping these effects with a controlled illumination, which would permit to distinguish between direct light and stray light would be extremely helpful.

3.1.3 Flux Calibration

Now, the main goal of DICE is the flux calibration of the broadband imagers used to measure the SN Ia luminosity distances. More precisely we want to secure the inter-calibration of the effective passbands of the telescope. As discussed in chapter 2, it is a fundamental ingredient of SN Ia cosmology. The techniques in use today rely on *stellar models*, and an important on-going project in the community is to anchor the flux calibration of modern telescopes on the flux metrology chain maintained at NIST.

DICE is therefore a light source designed to transfer the flux calibration carried by a calibrated light detector (a photodiode calibrated at NIST) to another light detector (the focal plane of the telescope).

Figure 3.1 summarises our goals regarding flux calibration. First, we need to follow precisely the relative normalisation of the telescope passbands (the blue arrows). These normalisation however are not enough, as the shape of the telescope passbands, in particular, their positioning is wavelength may evolve with time. As a consequence, we also need to monitor, at the very least, the absolute positions of the filter cutoffs (the red arrows). The are the main calibration variables we want to extract from DICE calibration frames.

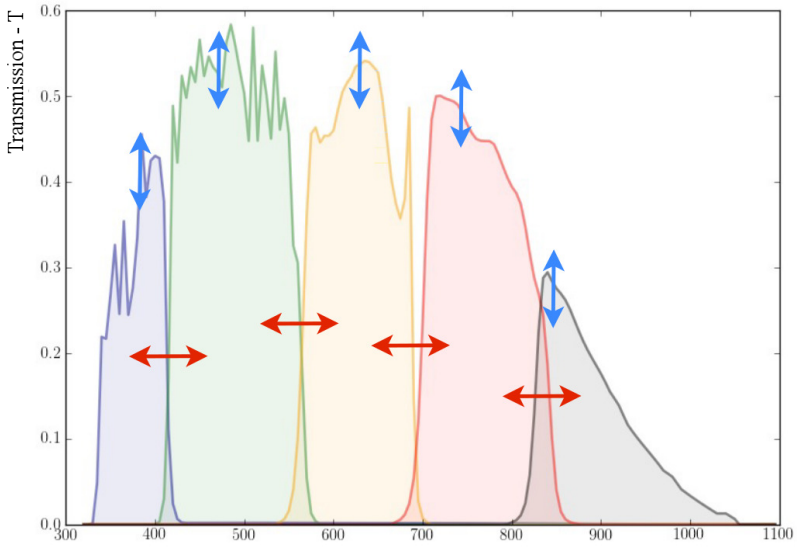

Figure 3.1: *Calibration variables monitored by DICE: passband normalizations and filter cutoffs.*

3.2 Design Principles

In this section we discuss the ideas that have guided the design of DICE. In particular we describe the calibration beam, the stability requirements of the source, and the choice of the light emitters.

3.2.1 DICE Calibration Beam

Beam Geometry Ideally, a calibration device should mimic as much as possible the science objects under study. Since a supernova survey is dealing with point sources (supernovae and field stars), we should try and generate quasi-parallel beams, covering the entirety of the primary mirror (see figure 3.2). Such a beam would result in a spot on the focal plane, and we could use the photometry code in production in the survey photometry pipeline to estimate its flux, thereby avoiding the systematic errors that arise from using different flux estimators.

Unfortunately, it is very difficult to emulate a good artificial star, especially in the small volume of a telescope enclosure. As a consequence, we opted for a totally different design.

The DICE calibration beam is presented on figure 3.2. DICE is a point source, placed at a finite distance to the telescope entrance pupil. As can be seen, the DICE beam is the conjugate of the typical science beam. What is emitted is a conical (divergent) beam, and the optics transforms it into a quasi-parallel beam, that generates a quasi-uniform illumination on the focal plane. The aperture of the beam is chosen taking into account the field of view of the imager, the goal being to illuminate quasi-uniformly the focal plane. For example for the SnDICE version, because MegaCam has a FoW of about 1 sq. deg., we opted for an

aperture of the beam of about $\simeq 2°$. The FoW of SkyMapper is bigger and this fact drove us to adopt an aperture $\simeq 3.2°$.

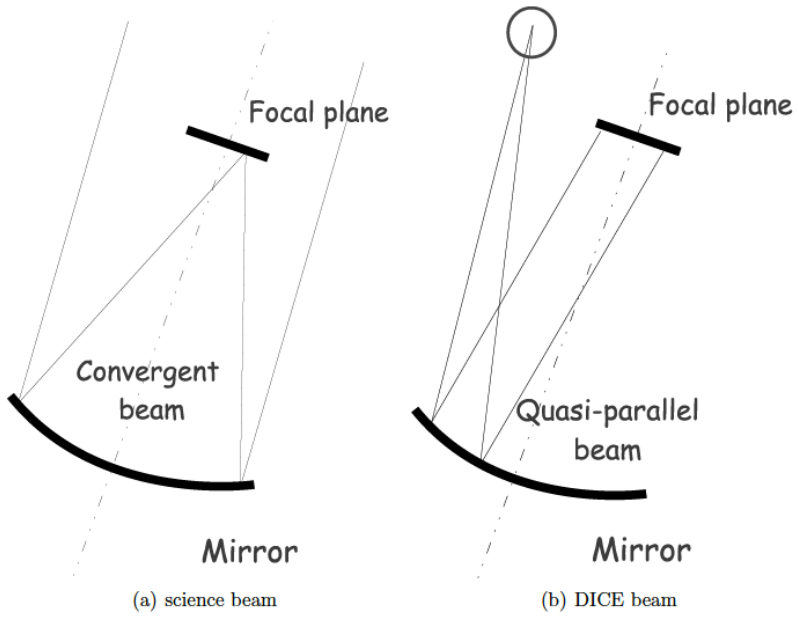

(a) science beam (b) DICE beam

Figure 3.2: *(Left) - Standard telescope illumination with a point source. (Right) - DICE calibration beam (Regnault et al. 2012).*

As shown on figure 3.2, the calibration beam is radically different from the science beam. In particular, the angular distribution of the light rays that hit the various optical surfaces is not comparable. It also differs from the beams generated by alternate devices designed by other groups who use a diffusive screen to re-emit the light is all directions (Stubbs et al. 2010, Rheault et al. 2010). We adopted this beam design for at least two reasons.

Direct Illumination First, this light beam is extremely simple to generate. It requires just a point source, and some baffling to shape a conical beam. In particular, no intermediate optical elements (monochromator, folding mirror etc.) subject to ageing need to be placed between the light emitter and the telescope entrance pupil. This design is extremely simple, easy to implement, easy to maintain, and reduces greatly the number of optical surfaces to monitor over the life of the source.

Beam Model Another nice property of the beam is that it is compact, easy to characterise with a photodiode, and easy to model. Furthermore, the structure of the beam is much simpler than that of the science beam, in the sense that each pixel sees photons that came through a unique path. In other terms, there is a one-to-one relationship between the focal plane elementary surface elements and the calibration beam elementary solid angles. It is therefore quite simple to predict the focal plane illumination at position $\boldsymbol{x}$, $\phi(\boldsymbol{x})$, once one

knows the beam radiant intensity, $\mathcal{B}(\boldsymbol{u})$ (i.e. the power emitted per unit solid angle in direction $\boldsymbol{u}$:

$$\phi(\boldsymbol{x}) = \mathcal{B}(\boldsymbol{u}) \times \mathcal{T}(\boldsymbol{x}) \times \left|\frac{\partial \boldsymbol{x}}{\partial \boldsymbol{u}}\right| \tag{3.1}$$

$T(\vec{x})$ is the imager response function at position $\vec{x}$, and $\left|\frac{\partial \vec{x}}{\partial \vec{u}}\right|$ is the geometrical response of the optical system. The latter can be calculated using a ray-tracing model of the optics (see e.g. appendix A).

3.2.2 Light Emitters

Narrow-spectrum light emitting diodes (LED) were chosen as light emitters. LEDs are known to be extremely stable, as long as they are fed with stable currents. It it is relatively easy today to build current sources stable at a few 10^{-5} over a temperature range of a few degrees, therefore, with some care, it is relatively easy to build a LED-based light source that can deliver very stable beams over long durations.

Light Emitting Diodes

A LED is a particular type of diode that uses a physical phenomenon called electroluminescence. Some kind of materials, typically doped semiconductors, when they are stimulated with an electrical power source, emit light in a narrow range of wavelengths; this phenomenon occurring at room temperature. This is possible because of the radiative recombination that occurs inside the depletion zone of the *pn* junction of the semiconductor.

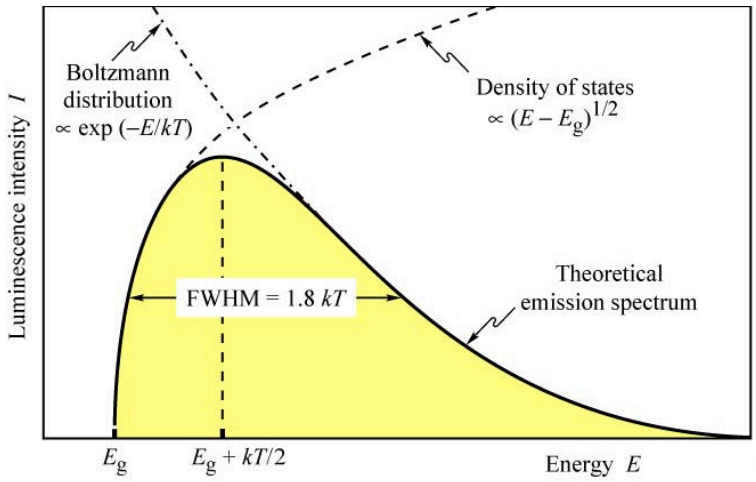

Figure 3.3: *Theoretical emission spectrum of a LED, see Schubert (2007).*

Generally, radiative recombination happens in every semiconductors but the distinction from a possible light emitter and a simple semiconductor is given by the their type of gap. The are two possible gap: an *indirect gap* (i.e., the *Si*) where the radiative recombination is mediated by phonons of the lattice structure producing no emissions, and *direct gap* where

the radiative recombination creates a photon that can easily escape from the material. The latter is the kind of gap that we want to create light emitting diodes.

This emission of light is caused by the injection of electrons through a direct polarised *pn* junction of the LED. The emission of photons is created when the energy of the polarisation is equal to the energy gap of the semiconducting material.

At that moment holes of the *pn* junction are radiatively recombined with electrons, creating photons with the same energy of the energy gap. A LED stimulated by an external current, can create a spontaneously emission of photons. The equation that governs the typical $I - V$ characteristic of a LED is the modified Shockley equation:

$$I - \frac{(V - IR_s)}{R_p} = I_s e^{(V-IR_s)/(n_i kT)}$$

where R_s and R_p are parasitic resistances, due to imperfection or non-radiative recombination, I_s is the saturation current, and n_i is the *ideality factor* and it generally spams from a 0 to 2. For a perfect diode $n_i = 1$. For the current work we also need to understand the shape of the LED spectrum. Without entering inside the argument, we just need to remind us the spectrum created by a LED. As we can see from the figure 3.3, a general LED spectrum is the product of two main physical distributions: one is the Boltzmann distribution and the other is the density of states for carriers inside the junction. The emission intensity I depends on the Density of State of electrons (holes) inside the junction well represented by the law $N(E) \propto \sqrt{E - E_g}$, where E_g is the energy gap of the junction, and is limit by the Boltzmann Distribution $\propto e^{-E/kT}$. The intensity and shape is directly depending to the average temperature and to the current injected in the *pn* junction. Moreover the medium peak wavelength of the spectrum (the central colour), slightly changes with the temperature and current.

Wavelength Coverage

LEDs do not emit monochromatic light. The typical FWHM of a LED spectrum is of about $\delta\lambda/\lambda \sim 5 - 7\%$ (i.e. 20-nm to 50-nm). This means that we need 20 to 25 LEDs to cover the entire visible spectrum (from 350-nm to 1100-nm). On figure 3.4, we show the sampling that could be obtained with the first DICE prototype, built for MegaCam (figure 3.4a). We also show, for comparison, what could be achieved four years later for SkyDICE, the second prototype built to calibrate the SkyMapper imager (figure 3.4b). As can be seen, the diversity of LEDs available on the market improved very significantly in the interval between both projects. Today, combining the catalogs of the three main LED manufacturers, it is possible in theory to cover the entire spectral range of silicon imagers, with about 1 LED every 5-nm.

The LEDs was were selected for SkyDICE are listed in table 3.1. A similar table with the SnDICE LEDs can be found in Guyonnet (2012) and Villa (2012).

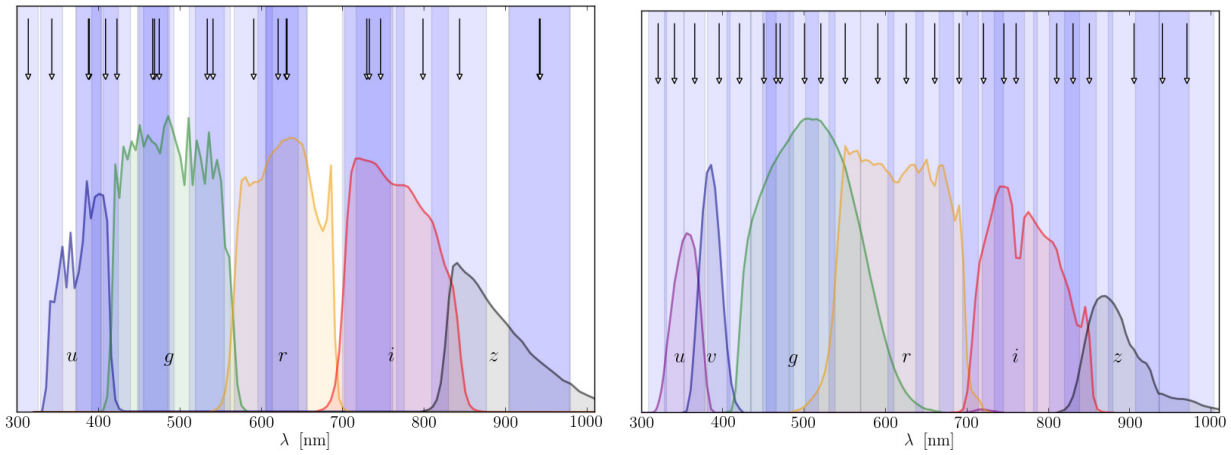

(a) MegaCam passband coverage (SnDICE) (b) SkyMapper passband coverage (SkyDICE)

Figure 3.4: *(Left) - MegaCam passband sampling by SnDICE. (Right) - SkyMapper sampling with SkyDICE LEDs.*

Sensitivity to temperature

LEDs come with just one caveat: their emission properties vary with temperature. As temperature increases, the LED emission efficiency drops by up to 0.5%/°C, and the mean wavelength of the emitted light shifts red-wards by about 0.1 Å/°C. As will be seen in chapter 4, these variations are generally linear and always extremely reproducible. As a consequence, once each emitter has been well characterised, one only needs to implement a real time follow-up of the source temperature to account for these effects.

3.3 Description of the DICE Device

We now describe the implementation of DICE, in particular the mechanical layout of the system, as well as its control electronics. We wanted to build a source that would be modular and easy to install, with a stable and robust current generator. In what follows we will describe the main parts of the system: the source and its mount (§3.3.1 and §3.3.2), the calibration LED channels (§3.3.3), the off-axis control photodiodes (§3.3.4), the artificial planet system (§3.3.5), the backend electronics (§3.3.6) and finally, the offline control photodiodes (§3.3.7).

3.3.1 Mechanical Layout

A DICE source an assembly of anodised aluminium blocks, each pierced with 25 holes to let the light through. In particular the blocks are identical and they permit to have a modular system able to be configured for different telescopes and configurations. SnDICE is made of 8 of those blocks. SkyDICE which generates a wider beam is shorter and is made of 5 blocks

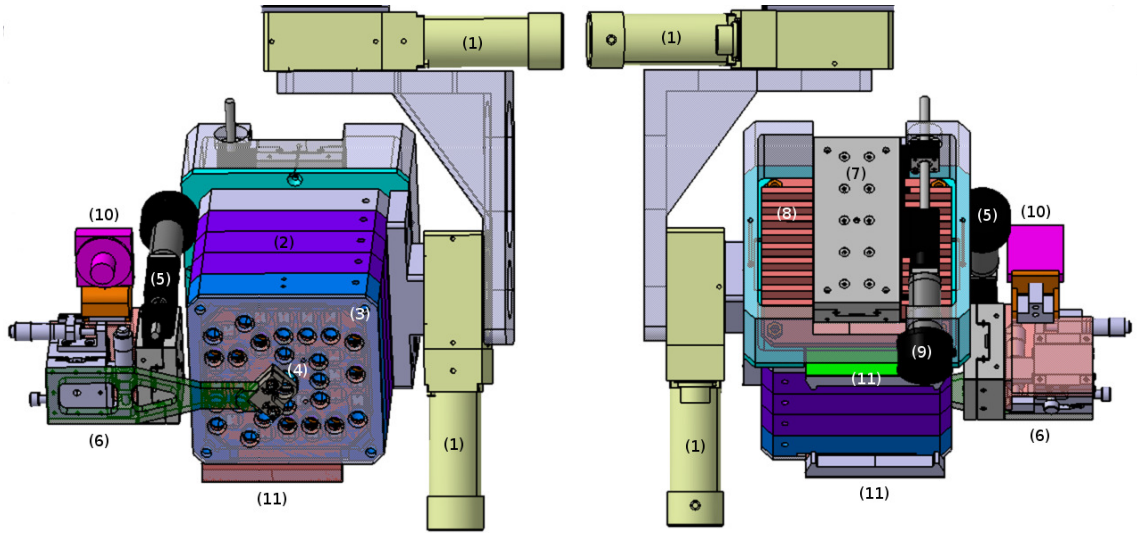

Figure 3.5: *3-dimensional view of the illumination system. Two DC-MOTORS (1). The LED head (2). The front face of the device (3) displays* 24 *holes. The lens is mounted on a tip-tilt support (4). A linear motor (5) permits to shift the lens along the optical axis to adjust the focus. The lens arm is mounted on a manual X-Y plate (6). The planet LEDs are mounted on a board (7) placed behind the radiator (8). This board can slide linearly (9). A webcam (10) is mounted on the device. The LED and control photodiodes are mounted on two boards located on the back and front of the device. These board are connected to the backend electronics with two flat cables (11).*

only.

Figures 3.5 and 3.6 show the mechanical layout of the SkyDICE source. This LED-head is a $13 \times 15 \times 22.7$ cm box, hooked on a motorised structure, itself attached to one of the telescope dome arch-beams. It can rotate around two axes, so that its optical axis can be aligned with the telescope axis. The full device, including the cables has a total weight of $\sim$ 15 kg. The head itself, with the small auxiliary motors that control the position of the planet-LED weights $\sim$ 8 kg.

The LEDs are located on the back of the device. They are glued to a radiator whose main function is to thermalise them. The calibration beams exit through $\varnothing$ 9-mm apertures located on the front face of the source. This design permit to generate conical beams, whose aperture is determined by the distance between the LEDs and the front face. The additional elements that can be seen on figure 3.5 are described in the next sections.

Figure 3.6: *Overview of the LED head components. From left to right: (1) - planet lens arm (2) - lens; manual tip-tilt lens support (3) - manual X-Y support (4) - webcam (5) - planet focus DC motor (6) - LED head font panel (7) - photodiode board (8) - mask elements (9) - LED head elements (10) - holes (notice the 10 µm planet hole at the centre) (11) - LED board and radiator (12) - planet LED support (13) planet LED DC motor.*

3.3.2 Mount System

During operations, the DICE system scans a selected fraction of the telescope primary mirror. This is done by moving simultaneously the telescope and the LED head between exposures.

The illumination system may be rotated around an altitude axis and an azimuth axis using two remote-controlled DC motors (AXMO 16200ENS001)[1]. The mount itself has an L-shape made of aluminium, holding the two motors and attached to a ELCOM$^{\text{ő}}$ structure, finally fixed to the dome. The position and orientation of the rotation axes have been chosen to minimise the torque-force on the motor axes. The LED head is balanced with the vertical axis, so that the residual torque force is almost zero. On the horizontal axis we have detected a small residual torque, but it does not add errors on motors control.

The system needs to cover approximately a range of $\sim 20°$ in azimuth and $\sim 15°$ in altitude. Motor stops are implemented, in order to reduce the range of possible orientations and errors from users and to give us a origin position for both axes. Since there is no reason to drastically limit the device motion, we target a range of $180°$ in azimuth and $[-80° ; +25°]$ in altitude.

The isotropic beams are generated by $\varnothing$ 5 mm holes placed in front of each LED. The light propagates from the LED board to the front side through ~ 150 mm long tubes drilled in the LED head structure. As we said before different masks are superimposed in every blocks to shape the beam and to eliminate any possible stray light. The front side aperture of each channel is 9 mm hole. For the SkyDICE version the beam has an aperture $\theta \simeq 3.42°$ and covers a solid angle $d\Omega = 0.0028$ sr. Finally, a radiator is fixed on the back of the LED-head, directly connected with LED board. This simple system is used to cool down the temperature of LEDs.

3.3.3 Calibration Beams

Figure 3.7 presents a sketch of the LED beam seen from the inside of the device. From right to left we have the LED board where diodes are physically mounted. The light generated passes through a first mask: this mask has the role to eliminate stray light from the LED board, and to shape the beam.

An anodised mask pierced with $\varnothing$2-mm holes (one for each LED) is inserted just after the LED board, in order to prevent stray light pollution. After this first mask, the beam passes in different aluminium blocks. These blocks are anodised and painted in black to eliminate parasite light and internal reflections. Furthermore, anodised, circular masks are inserted between the aluminium blocks, to help shaping the beam and eliminate stray light.

Each hole has an elongated shape (13×23 mm). This permits to place an off-axis control photodiode in each LED channel, in order to monitor in real time the light delivered by the source. These photodiodes are built to provide us with an independent measurement of the flux delivered by LEDs.

At first order, LEDs are Lambertian emitters. The beam that comes out of the LED board is quasi-Lambertian, but nevertheless presents small fluctuations of $\sim 1\%$. Those

[1] see http://www.axmo.fr/

variations has created by:

1. residual stray light,
2. small imperfections on the holes shape,
3. imperfect centring of the LEDs, during the soldering procedure.

3.3.4 Off-Axis Control Photodiodes

Another component of the DICE project are the off-axis control photodiodes. These electronics devices are necessary to monitor the flux of LEDs during operations. This task is extremely important because, as we said, the beam is not perfectly uniform and the intensity varies with temperature. As we will see in chapter 5, monitoring the beam before it hits the mirror and the focal plane of the telescope, help us to control the stability of each source.

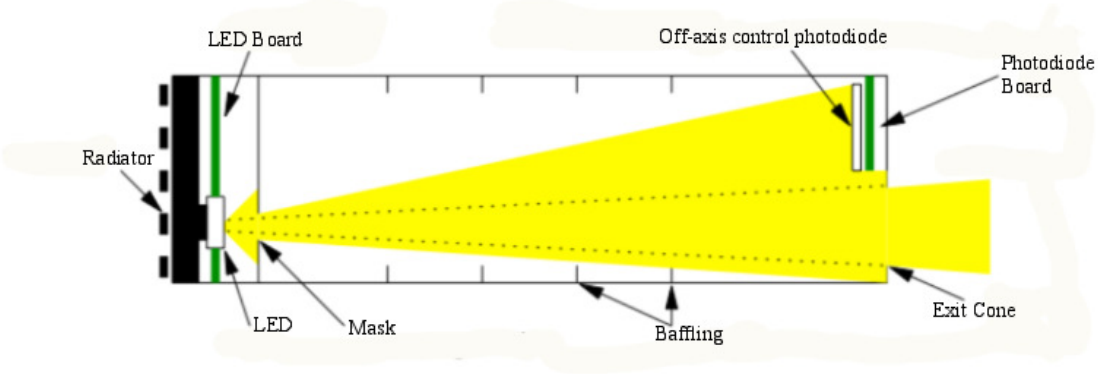

Figure 3.7: *Layout of the LED beam projection inside the DICE system.*

For our purpose, we adopted a set of 24 Hamamatsu S2387 *Si* photodiodes[2], with a passband from 320-nm to 1100-nm. These are multipurpose photodiodes with a good efficiency (especially in the UV) and a small temperature coefficient along all the passband. Finally, all 24 LEDs are mounted on a front-end board connected to the electronics of control by a flat and flexible cable.

3.3.5 The Artificial Planet

As the calibration beam is compact and illuminates only a small fraction of the mirror, it is necessary to control the alignment of the telescope and the source. This is done with a special pencil beam generated with a white LED, and called the *artificial planet*. Such a

[2]see http://www.hamamatsu.com/us/en/product/category/3100/4001/4103/S2387-1010R/index.html

LED Type	$\langle\lambda_p\rangle$	I_{max}^{vendor}	SkyMapper Passband	LED Number
UVTOP315-FW-TO39[a]	320 nm	20 mA	u	8
UVTOP335-FW-TO39[a]	340 nm	20 mA	u	21
APG2C1-365-S [a]	365 nm	350 mA	u, v	2
APG2C1-385[a]	385 nm	350 mA	u, v	23
APG2C1-395[a]	395 nm	350 mA	v, g	3
APG2C1-420[a]	420 nm	350 mA	v, g	22
LD W5AM[b]	450 nm	500 mA	g	4
LB W5SM[b]	465 nm	500 mA	g	17
LV W5AM[b]	512 nm	500 mA	g, r	5
LT W5SM[b]	525 nm	500 mA	g, r	24
LT W5AM[b]	550 nm	500 mA	g, r	6
LY W5SM[b]	590 nm	500 mA	g, r	20
LA W5SM[b]	625 nm	500 mA	g, r	7
APG2C1-660[a]	660 nm	500 mA	g, r	18
APG2C1-690[a]	690 nm	500 mA	r	1
APG2C1-720[a]	720 nm	500 mA	r, i	16
APG2C1-760[a]	760 nm	500 mA	i	15
APG2C1-810[a]	810 nm	500 mA	i, z	10
APG2C1-830[a]	830 nm	500 mA	i, z	19
APG2C1-850[a]	850 nm	500 mA	i, z	12
SFH421[b]	880 nm	100 mA	z	13
APG2C1-905[a]	905 nm	500 mA	z	9
APG2C1-940[a]	940 nm	500 mA	z	14
APG2C1-970[a]	970 nm	500 mA	z	11
Planet LEDs				
APG2C1-365-S [a]	365 nm	350 mA	u, v	
APG2C1-395[a]	395 nm	350 mA	v, g	
LB W5SM[b]	465 nm	500 mA	g	
LY W5SM[b]	590 nm	500 mA	g, r	
ZW W5AM[b]	*white*	500 mA	u, v, g, r, i, z	29
LA W5SM[b]	625 nm	500 mA	g, r	
APG2C1-720[a]	720 nm	500 mA	r, i	
SFH4230[b]	850 nm	1000 mA	z	
APG2C1-940[a]	940 nm	500 mA	z	

[a] - UV and IR LEDs, see http://www.roithner-laser.com/.
[b] - Visible and IR Golden Dragon, see http://www.osram-os.com/osram_os/en/.

Table 3.1: *SkyDICE LEDs. The table shows the type, the central wavelength, the maximum current and the corresponding SkyMapper filters.*

beam results in a spot on the focal plane, and the position on this spot tells us about the angle between the planet beam and the telescope optical axis.

To generate the pencil beam we use a smaller (⌀10 µm) mask, to emulate a point source, and we place a convergent lens in front of the mask (at the focal distance). This generates a quasi-parallel beam, as shown on figure 3.8. The quality of the spot we obtain is quite good: $\sim$ 250 pixels for SnDICE (Guyonnet 2012, Villa 2012; and), $\sim$ 100 pixels for SkyDICE (see chapter 7).

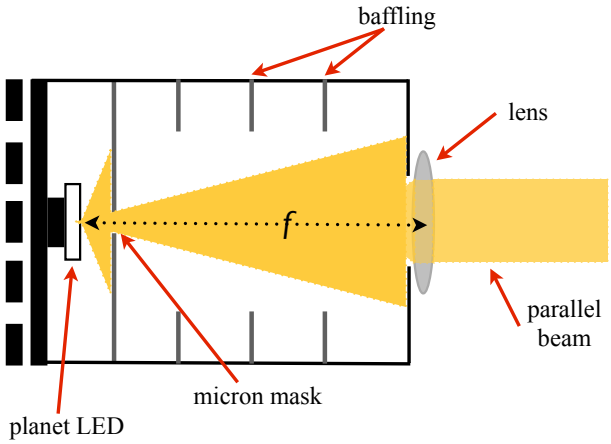

Figure 3.8: *Sketch of the artificial planet source path.*

In the SnDICE experiment, when analysing the planet images we discovered that the spot was followed by a set of ghosts due to reflections from filters glass and correction lenses (see figure 3.9). We found that these ghosts could be used to estimate the reflectivity of the various optical surfaces, hence to estimate the level of contamination of the calibration frames by ghosts.

Pushed by this idea, we decided that we would equip SkyDICE with a new planet system which could generate light at various wavelengths, so that we could test the reflectivity of the optics over the full optical wavelength range. We constructed a LED board with 9 different LEDs covering almost all the passband of SkyMapper camera (see table 3.1 at the end of the chapter). The LEDs are selected by translating the board using a small motor fixed on the back of the radiator.

An additional improvement of the system consisted in mounting the lens on a step motor, so that its position can be translated remotely. The idea was to be able to adjust the focal distance between the lens and the exit hole, and therefore to improve the quality of the planet spots. The planet system and the focus system are represented on figure 3.5.

3.3.6 Electronics

The electronics, in particular, the LED current generation system is the last critical part of the DICE system. It was entirely designed and built at LPNHE.

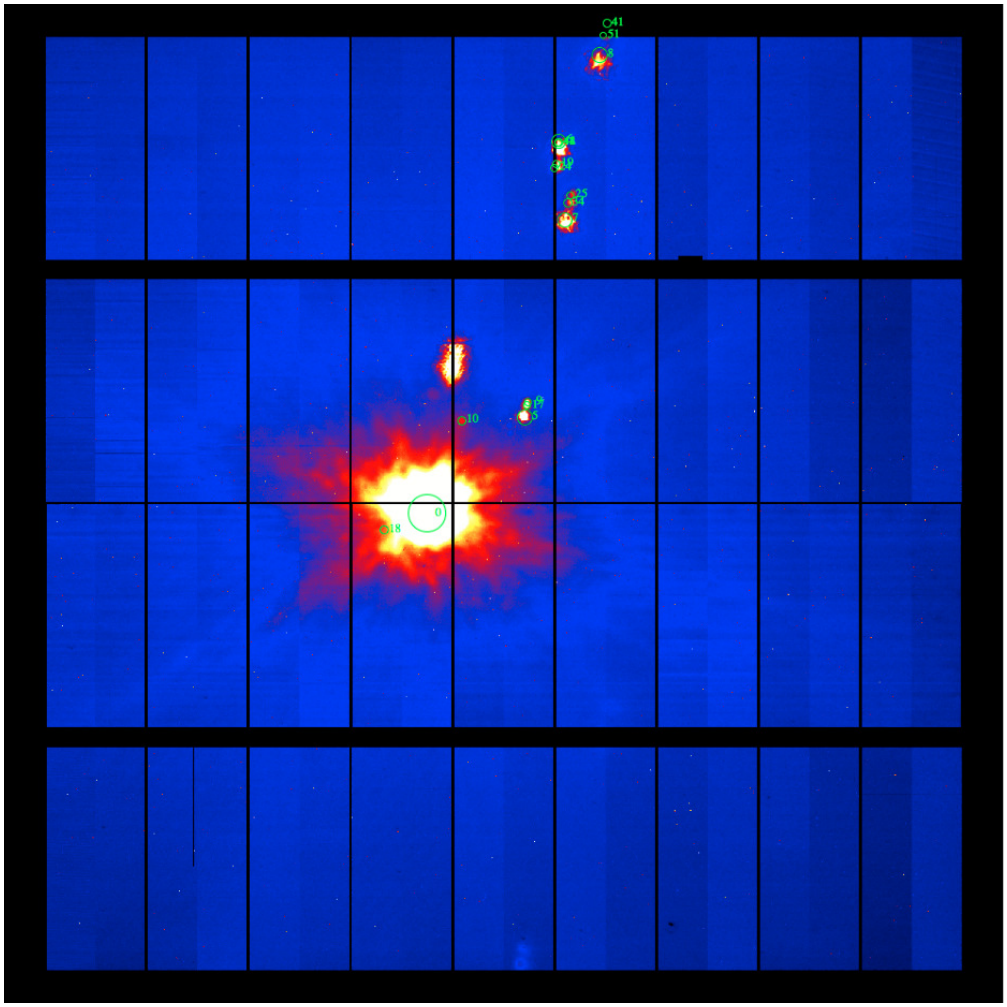

Figure 3.9: *Image taken from SnDICE data. We can clearly see the ghosts created by the primary and secondary reflections of the DICE source through optics and the filter of the CFHT telescope (Villa 2012).*

The electronics of DICE can be divided in two parts. First, we designed two passive boards that hold respectively the calibration LEDs (on the back of the device) and the off-axis control photodiodes (close to the front face). Figure 3.10 shows the LED board mounted in its crate. Second, the current generation system, and the control photodiode readout system are all implemented on an external board call the "backend board". This board is connected on one hand to the LED head with a flat cable, and on the other hand to a control PC, with a standard USB link.

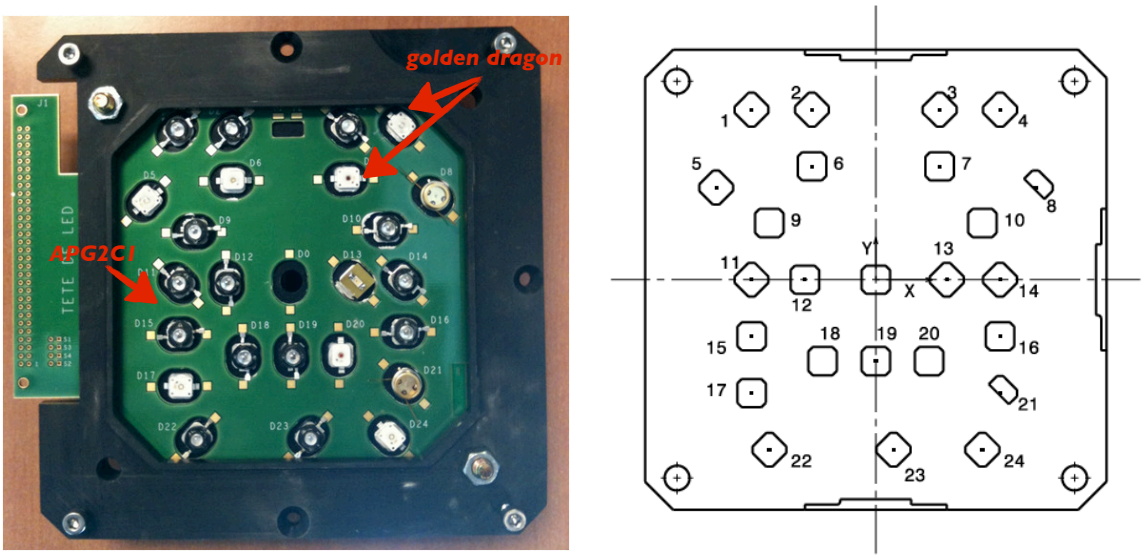

Figure 3.10: *(Left) - SkyDICE main LEDs board with all 24 sources positioned. The hole at the centre is the place of the artificial planet. (Right) - CAD drawing of the same circuit board.*

The backend board is equipped with a FPGA circuit, which allows it to interact with the control PC. It can set the level of the LED current, measure and digitise the current that passes through a given LED, measure and digitise other useful observables such as (1) the reference voltage of the circuit V_{ref}, (2) the backend temperature, (3) the temperature of the PT1000 thermistor mounted on the LED-head radiator, the off-axis control photodiode currents I_{phd}. The digits are stored on board in a 16MB buffer and sent on request to the control PC.

The most important part of the backend control circuit is the LED current generator (see figure 3.11). This current source has a stability of 10^{-4} over the all range of working temperature (usually $0 - 20$ °C) . Technically speaking is a transistor current source with a programmable voltage level. The stabilisation of the source is done by a negative feedback loop. The voltage level is sampled by another 16 bit ADC, directly implemented in the circuit. The accuracy of the backend control system gives an output LED flux with a stability around 10^{-5}.

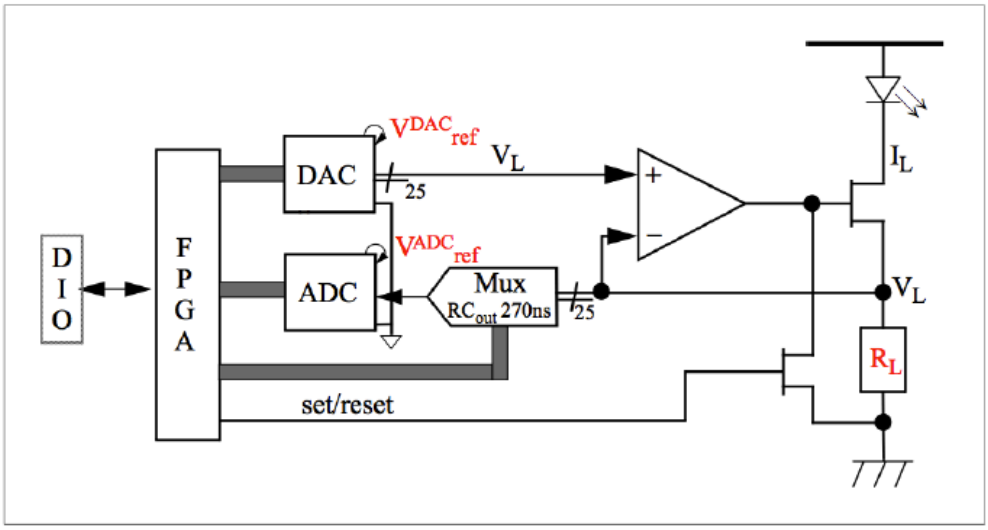

Figure 3.11: *LED current generator and its feedback circuit.*

3.3.7 Cooled Large Area Photodiode (CLAP)

DICE is constructed to be a very redundant device, with different levels of monitoring systems, but it lacks an external independent system that would monitor in real-time the light actually delivered by the source on the primary mirror. To close the chain, for both SnDICE and SkyDICE, we built an external device called CLAP. This system is an external calibrated photodiode mounted next to the primary mirror and used to control the flux that hits the mirror before it enters the optical path of the telescope.

The chosen device is an Hamamatsu S3477-04[3] photodiode coupled to a ultra-low noise current amplifier designed at LPNHE, and implemented as an ASIC. To increase its sensitivity, the photodiode is polarised in reverse and operated in photoelectric mode. It is coupled to a small Peltier effect, which allows one to operate it around -20°C, hence reducing very significantly the dark current when the photodiode is polarised in reverse. Then all the system is connected with a backend circuit which samples and digitises the signal. The CLAP module has been extensively used during the test-bench and stability tests. Several CLAP modules have been sold to others research group in Europe.

3.4 Data Acquisition System & Operation

Finally, we discuss the implementation of the SkyDICE Data Acquisition System (DAQ), and its interface with the SkyMapper DAQ (CICADA & TAROS protocol).

The control system is composed of three elements: the two boxes containing the LED head backend electronics and the CLAP control and sampling system, an external box containing the SkyDICE motor controllers, and two dedicated PC104s to control the whole system.

[3] see http://www.hamamatsu.com/jp/en/index.html

All the subsystems (LED and CLAP backends, and motor controllers) are connected to the PC104s through USB links. Those PCs communicate with the SkyMapper Data Acquisition System (DAQ) via an ethernet cable.

3.4.1 Data Acquisition (DAQ) Architecture

The diagram on figure 3.12 illustrates how the system works. There are two subsystems: the LED head system, attached to the telescope dome, and the CLAP subsystem, mounted on the telescope. Both are controlled with a PC104, connected to the SkyMapper DAQ with an ethernet link.

Each PC104 runs a dedicated server which interacts with the DAQ with a simple, high-level protocol (XML-RPC). The LEAD-head server controls the four motors (the alt/az rotation motors, and the planet LED and focus motors) and the LED backend electronics. A second server runs on the PC which operates the CLAP subsystem.

Both servers are under the control of the SkyMapper DAQ system (Young et al. 1999), which coordinates data taking. It executes orders sent through CICADA, such as (1) orientation of the LED head (2) LED current configuration and control (3) retrieval of the monitoring data (control photodiode fluxes, LED currents and temperatures).

3.4.2 Standard Operation Protocol

SkyDICE is built to work during day time. This model has two advantages: first we do not use the telescope night time which is expensive. Also, because calibration is done during the day, SkyDICE can have the full control of the telescope and take a larger amount of data.

In a typical calibration session the dome tracking system is disconnected and and the dome aperture closed. In the case of SkyMapper, all the surface of the telescope enclosure is covered by a grey foam but is not perfectly dark. As a consequence, there is some amount of stray light, which we have to account for, as will be discussed in chapter 7. Then we align the *SkyDICE + telescope* system to allow the LEDs source to point directly into the primary mirror. This alignment is done using the planet beam as a reference spot in the focal plane of the telescope. A perfect alignment is reached when the planet-spot is placed at the centre of the CCD mosaic. We then take exposures, altering the LED and the filters, and we store them into the main server of the SkyMapper telescope. Then we move again the telescope to cover a different area of the mirror and we take again a series of exposures. We iterate until the end of the run.

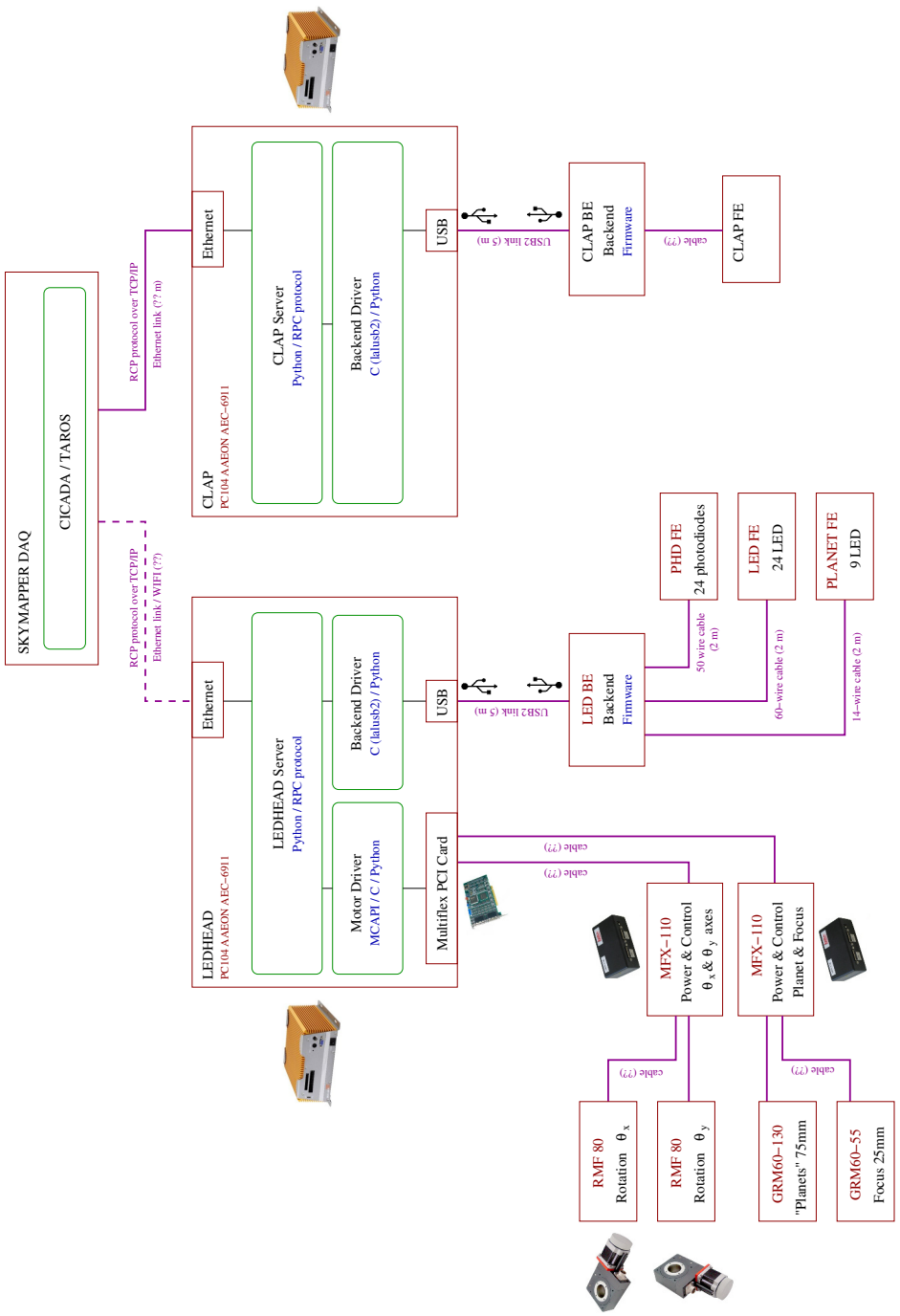

Figure 3.12: *Overview of the SkyDICE DAQ system. We can recognise on the left the LED-head subsystem, and on the right the CLAP subsystem. Both are linked directly with the CICADA/TAROS DAQ system of the SkyMapper telescope.*

Chapter 4

SkyDICE Test Bench

The main goal of the test bench studies is to transfer the calibration carried by the NIST photodiode to the light source. In practice, this means that we will characterise the emissivity of each LED using the NIST photodiode as our primary flux standard.

The physical quantity which describes the emissivity of a point source is its *spectral intensity*, $\mathcal{S}(\lambda, \vec{u})$. It is defined as the power emitted by the source, per unit wavelength and per unit solid angle (at a given wavelength λ and in a given direction $\vec{u}$). As the properties of many of the SkyDICE LEDs are sensitive to temperature, we expect $\mathcal{S}$ to be also a function of the temperature T of the source: $\mathcal{S}(\lambda, T, \vec{u})$.

In this chapter, we describe the measurements that will allow us later to build a model of the spectral emissivity of each LED. In the first section (§4.1), we define the spectrophotometric quantities we want to measure. We then describe the layout of the test bench (§4.2).

As I spend a significant fraction of my time automating the test bench, and getting it to work properly, I will describe in some detail the instrumentation, and the improvements I was able to obtain implementing a fully automated measurement protocol. In the second and third sections, §4.3 and §4.4, we present the test bench configuration for photometric and spectroscopic data taken during the 2012 calibration run. Finally we describe the *pre*-analysis study of the test bench data I did shortly after the data was taken. It is much more succinct than what will be presented in chapter 6 but gives a good sense of how the data looks like.

4.1 Definitions

$\mathcal{S}(\lambda, T, \vec{u})$ depends on 4 parameters. This is a lot, especially if we want to calibrate the source at several temperatures. For this work, we have assumed that the spectral intensity of all the LEDs which equip the DICE light sources can be written as:

$$\mathcal{S}(\lambda, T) \times \mathcal{B}(\vec{u}) \tag{4.1}$$

where $\mathcal{S}$ is the spectral intensity of the LED, in an (arbitrary) reference direction, while $\mathcal{B}(\vec{u})$ is a dimensionless function, which accounts for the variations of the beam intensity as

a function of the angle of emission. $\mathcal{B}(\vec{u})$ is normalised to 1 in the reference direction.

In what follows, we refer to $\mathcal{S}(\lambda, T)$ as the the LED "spectrum", keeping in mind that it is actually a spectral intensity. Following the usage in astronomy, we choose to express $\mathcal{S}$ in erg/s/Å/sr. The dimensionless quantity $\mathcal{B}(\vec{u})$ is called the "beam map". In the next sections, we report on the measurement of these two components.

There are two key quantities, the calibration of the light source is performed in two distinct steps. The beam maps $\mathcal{B}$ can be measured simply by intercepting the beam with a calibrated photodiode placed at a known distance from the source, and moved with respect to the source, in order to sample the whole beam. The measurement of $\mathcal{S}$ is a little more complex. We need to perform spectroscopic measurements, by inserting a monochromator between the source and the calibrated photodiode.

4.1.1 Beam maps

The radiant intensity of each calibration beam is mapped by moving the standard photodiode in a series of planes orthogonal to the Z-axis. These calibration sequences, called hereafter "photometric calibration sequences" are performed at about 10 to 15 different temperatures, ranging between $\sim$ 0°C to $\sim$ 20°C. They allow us to study how the intensity delivered by each LED varies with temperature and how the intensity varies with the direction of emission. They also permit to assess the stability of the source.

Since detailed beam maps are quite expensive ($\sim$ 30 to 60 minutes) to acquire, we optimise the photometric measurements as follows. In a first series of measurements, we concentrate on a few specific beam locations, keeping the photodiode fixed, while varying the bench temperature. These sequences, called "mini-maps", are targeted at measuring, for each LED, the relative variations of the LED emission with temperature.

We also realise maps of the LED beams, at two or three temperatures, keeping the temperature of the bench as constant as possible during data taking. From this data, we obtain fine grained maps of the beams, and we verify that these maps are stable with temperature. Such measurements are taken at several distances to the source, in order to verify the projectivity of the beam, and to check that we control the LED-source geometry well.

4.1.2 Spectra

In a second step, we insert a *Digikröm DK240* Czerny-Terner monochromator between the light source and the calibrated photodiode. The LEDs are then positioned in turn in front of the monochromator entrance slit, while the photodiode senses the output. These measurements are performed at about 10 distinct temperatures, between 0°C and room temperature.

The spectroscopic test bench is somewhat more delicate to operate. In particular, we need to control the wavelength calibration of the monochromator, as well as its transmission. On this point, we rely a lot on the work performed by A. Guyonnet who devoted a lot of energy to the precise calibration of our DK240. We ourselves checked our calibration by applying the procedure described in Guyonnet (2012).

4.1.3 On the choice of the LED currents

The flux emitted by a LED depends (generally linearly) on the current that traverses it. For some LEDs, the shape of the spectrum also depends slightly on the current, in particular, the position in wavelength of the spectrum peak. Mapping the spectral response of all LEDs as a function of the current value can be done with the test bench as it exists. However, this would require much more data, for little added value, as all LEDs are generally operated at the same current level. As a consequence, we define for each LED a nominal current, and the source is calibrated at those currents only.

The LED nominal currents are listed in table 4.1. They are chosen to obtain an illumination on the focal plane of the telescope of about 10^3 electrons per second, while avoiding saturation of the control photodiode placed inside the LED head (see table A.5 in the appendix A). As can be seen, all LEDs are operated at a low regime, at a fraction of the maximum intensity reported by the vendor.

In practice, the LED currents are a function of the LED forward tension V_{DAC} assigned by the DAC controller (see 3.11) and of a resistance R_L, which is different for each LED. The relation between the LED current and the DAC command is linear ($I_{led} = k_{led} \times I_{ADU}$). In the last column of table 4.1, we report the conversion factor k_{led} for future reference.

4.2 Test-Bench Overview

The general configuration of the test bench is shown on figure 4.1. There are three main elements:

[**A**] - the DICE LED-head is mounted on a computer controlled linear table, that can move in the X and Y directions (orthogonal to the Z-axis of the bench). Thus, the LED head can be moved automatically with a precision of $\sim$ 10 µm.

[**B**] - The calibrated photodiode which is used as our fundamental flux standard is mounted on an almost identical support, that can be moved in the X, Y and Z directions. The distance z between the photodiode and the LED-head can be varied.

[**C**] - A Digikrom DK240 monochromator can be placed between the LED-head and the NIST to perform spectroscopic measurements (see section §4.4.1 below for details).

[**D**] - Finally the NIST photodiode support is fixed in a z-axis motorised optical bench that can be moved with a precision of $\sim$ 10 μm. All the devices can be controlled remotely.

The test bench is installed inside a 2 m$\times$1.5 m$\times$3.5 m thermally-insulated dark enclosure. This enclosure (and the whole test bench) is not fully thermalised. Indeed, the insulation is not perfect, and more importantly the air conditioning system is not powerful enough to reach the low temperatures typical of what is measured at the summit ($T \sim 0$℃) everywhere in the enclosure. For those reasons, even after hours of operations, a gradient of temperature between the LED-head and the opposite side can still be measured. This is not really a problem, as we monitor in real time the temperatures of all the test bench devices. This is done using PT1000 thermistors (typical precision of 0.1℃), a Digisense[1] sensor (0.1 °C) and

[1] see http://www.coleparmer.com/

LED number	$\langle\lambda_p\rangle$ (nm)	k_{led} (mA/ADU)	I_{led} (mA)	$I_{sat}/I_{max}^{(DICE)}$ (mA)
01	690	$3.051944\ 10^{-3}$	3.1	50.0/ 50.0
02	367	$2.136363\ 10^{-3}$	10.7	35.0/ 35.0
03	395	$2.136363\ 10^{-3}$	10.7	35.0/ 35.0
04	451	$3.051944\ 10^{-3}$	3.1	15.3/ 50.0
05	512	$3.051944\ 10^{-3}$	3.1	15.3/ 50.0
06	525	$3.051944\ 10^{-3}$	3.1	36.6/ 50.0
07	625	$3.051944\ 10^{-3}$	3.1	21.4/ 50.0
08	320	$1.220778\ 10^{-3}$	6.2	20.0/ 20.0
09	906	$3.051944\ 10^{-3}$	3.1	36.6/ 50.0
10	810	$3.051944\ 10^{-3}$	3.1	21.4/ 50.0
11	959	$3.051944\ 10^{-3}$	3.1	42.7/ 50.0
12	849	$3.051944\ 10^{-3}$	3.1	30.5/ 50.0
13	735	$6.103888\ 10^{-3}$	6.2	30.5/ 100.0
14	950	$3.051944\ 10^{-3}$	3.1	50.0/ 50.0
15	763	$3.051944\ 10^{-3}$	3.1	30.5/ 50.0
16	720	$3.051944\ 10^{-3}$	3.1	36.6/ 50.0
17	464	$3.051944\ 10^{-3}$	3.1	9.2/ 50.0
18	659	$3.051944\ 10^{-3}$	3.1	50.0/ 50.0
19	831	$3.051944\ 10^{-3}$	3.1	21.4/ 50.0
20	593	$3.051944\ 10^{-3}$	15.5	50.0/ 50.0
21	338	$1.220778\ 10^{-3}$	6.1	20.0/ 20.0
22	415	$2.136363\ 10^{-3}$	2.1	35.0/ 35.0
23*	-	—	-	-
24	544	$3.051944\ 10^{-3}$	3.1	3.1/ 50.0

Table 4.1: *Typical SkyDICE LED currents and current upper limits. I_{led} is a nominal current defined for each LED. I_{sat} is the current level at which control photodiode starts to saturate. Finally I_{max}^{DICE} is the maximum current the backend electronics can deliver to the LED (it varies from LED to LED, as it is a function of the serial resistor R_L (see figure 3.11). (*) LED23 turned out to be faulty during the tests.*

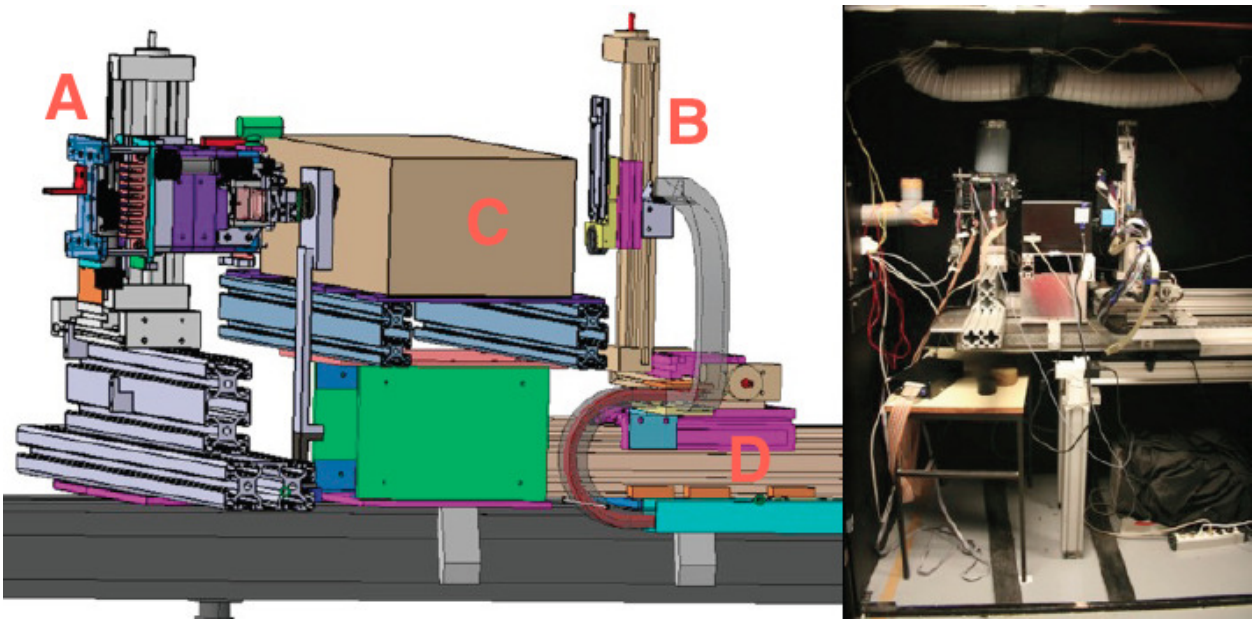

Figure 4.1: *(Left) - Test bench set up for spectrophotometric measurements, [A] the LED head with its support and [B] the NIST photodiode support, then in [C] we can see the monochromator and in [D] the optical bench. (Right) - A real picture of the set up used to take spectra with the SkyDICE system.*

two Lakeshore[2] sensors (0.001 °C).

At the precision level we target ($\sim 10^{-4}$), the system response may be sensitive to tiny details, such as the length of the cables. Therefore, we made sure that the system under tests was the exact same system that would be installed in the telescope enclosure. No hardware changes were allowed between the calibration run and the installation and commissioning of the device.

As described in the previous chapter, the LED head is controlled by an industrial computer (PC104), connected to the backend electronics. The DAQ program running on this system is very similar to the final program installed on site. The only difference is that, in its test bench version, this program also controls the various temperature sensors installed in the bench, as well as the Keithley pico-ammeter connected to the NIST photodiode. Another PC104 is dedicated to the control of the linear tables and moves on demand the LED head and/or the NIST photodiode with respect to each other.

4.2.1 The NIST Photodiode

As described above, the fundamental standard is a 1 cm^2 Silicon photodiode (Hamamatsu S2281[3]). This photodiode was calibrated at NIST (National Institute of Standards and Technology). The spectral response of the device, as reported by NIST, is shown on figure

[2] see http://www.spectralproducts.com/dk240

[3] see http://www.hamamatsu.com/us/en/index.html

4.2 along with its uncertainties. The photodiode is sensitive in the range of $200 - 1100$ nm. The average accuracy reported by NIST is of about $\sim 0.2\%$ from 430-nm to 950-nm. Note that NIST does not report on the full covariance matrix of the measurements. We suspect that a fraction of these uncertainties are correlated, however, we did not manage to get information from our contacts at NIST on this subject. We discuss this problem later in chapter 6.

As discussed in the previous chapter, a typical LED, operated in a low regime, emits intensities ranging from 0.1 - 0.5 mW/sr. In photometric mode, the NIST photodiode is typically placed at a distance of $\sim$ 1-m to 1.5-m from the source, and therefore covers a solid angle $\delta\Omega$ of a few 10^{-5} sr. As a consequence, the photodiode intercepts fluxes of a few nano-watts and generates photocurrents of a few nano-amperes. In spectroscopic mode, the flux that can be measured around the spectrum peak is of about 5% of that value. So, depending on the bench setup, we have to measure photocurrents of pA to nA. These low currents are measured with a Keithley 6514 feedback pico-ammeter, that can measure currents as low as $\sim 10^{-14}$ Ampere, two orders of magnitude smaller than our ordinary values.

Following the recommendations issued by NIST, the photodiode is operated in photo-voltaic mode, i.e. unbiased, at room temperature. The average dark current given by the constructor is of $10 - 100$ pA for a reverse voltage on the range $0.01 - 1$ V. This value agrees with what we measure using the Keythley pico-ammeter at standard condition $T_a = 25$℃, inside our dark-enclosure.

The connection between the photodiode and the measurement hardware is made by a metal shielded BNC connector. The metal shield is necessary to avoid any kind of electro-magnetic interference in the measurement. During the calibration runs, we discovered that the connection between the cable and the pico-ammeter itself was not properly shielded. This explains that the noise affecting some of the spectra is higher that it should be.

4.2.2 Test Bench Automation

To calibrate a LED, we need to acquire about 10 spectra, at different temperatures, plus a series of mini-maps, also at different temperatures, plus two to three fine grained maps. Therefore, a calibration run represents several days of data-taking, millions of data samples (essentially flux and temperature measurements) and dozen of small motions of the LED head and the photodiode relative to each other. It was therefore essential to optimise the automation of the test bench, in order to speed up data taking as much as possible. During the second year of my thesis, I spent several months working on this subject. The new DAQ system I wrote under the guidance of L. Le Guillou, is flexible and easy to deploy and to adapt to new instruments. It allowed us to increase the cadence and the repeatability of the measurements.

While designing the new system, we aimed for simplicity and robustness. As described above, the system is controlled with two industrial PC104. Those computers are directly connected to the bench devices through standard RS-232 serial ports. We have developed a generic interface to RS232 instruments in the python language, that can be adapted to virtually any lab instrument equipped with a serial port. The high-level control of the test

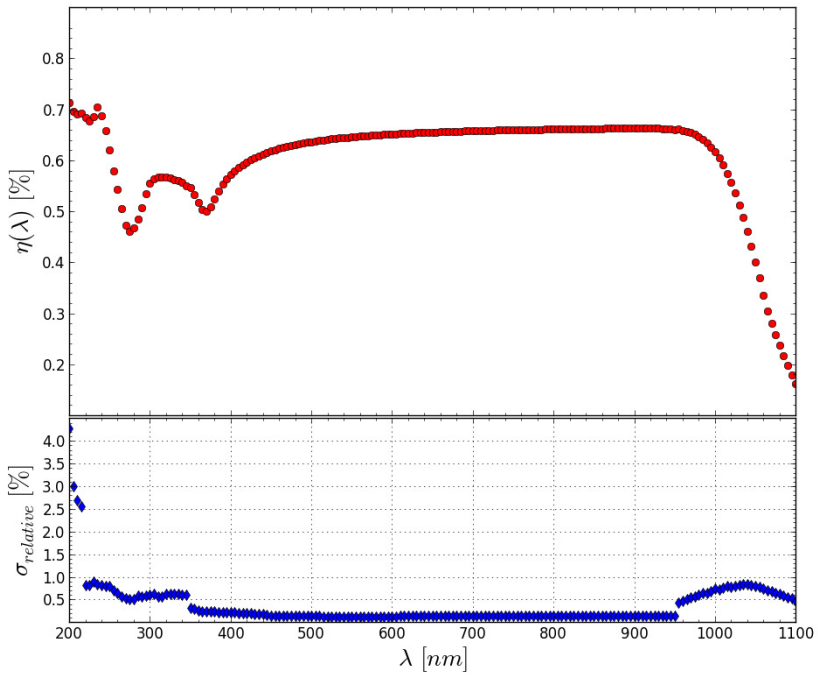

Figure 4.2: *Efficiency $\eta(\lambda)$ of the calibrated NIST photodiode (Hamamatsu S2281) used for our measurements. The associated average error $\sigma(\lambda)_{rel}$ given by the NIST is $\sim 0.2\%$.*

bench is therefore performed with a series of very simple, easy to maintain python scripts. The only manually controlled part is control of the climate chamber used to thermalised the test-bench for temperature driven measurements.

The data is stored in tables in ASCII format. It comprises flux measurements, along with meta-data, acquired at a lower cadence, necessary for the subsequent analysis. In a typical data file we store the description of the set up used during the run, the computer time in seconds (both PCs are synchronised), the LED input current, all the science data, like the measured NIST photodiode current and the off-axis control photodiodes current, the x, y, z position of the NIST photodiode and the LED-head (for photometric data), or the wavelength and measured currents (for spectroscopic data). Moreover, we record all temperatures from different thermistors, and the reference voltage of the backbend electronics (this latter used to recover temperatures from the PT1000 mounted and to check the system).

4.3 Photometric Test Bench

In order to calibrate our LEDs source we have to map the flux of every Lambertian beam at different distances and nominal currents, using our NIST calibrated photodiode. Fixing the position of the LED-head, the beam delivers an almost uniform illumination, the intensity of it depending as the inverse of the squared distance r and the I_{led}. The relation that allow

us to reconstruct the beam intensity and shape for every measurement is given by:

$$I_{PD} = I_{NIST} - I_{dark} = \mathcal{B}(\vec{u}; T) \times \delta\Omega \times \eta(\lambda) \tag{4.2}$$

where I_{PD} is the fraction of the photodiode current that corresponds to the signal we want to measure, i.e. the difference between the raw photodiode current I_{NIST} and the dark current I_{dark}. $\mathcal{B}(\vec{u})$ is the radiant intensity of the beam (in W/sr), $\delta\Omega$ is the solid angle subtended by the NIST photodiode at its current position ($\vec{u} \cdot d\vec{S}/r^2$), and $\eta(\lambda)$ is the efficiency of the NIST photodiode (in A/W).

As described above, the set up used for these measurements is similar to what is shown on figure 4.1, with the only difference that we have eliminated the monochromator. During a typical measurement session we turn on the LED at its nominal current, we record and fix the position of the LED-head, and we scan the surface of the beam using the mobile xy support of the NIST photodiode. The photodiode is moved in steps of 2-mm, in x and y, which allows us to over-sample the beam profile.

This measurement sequence is repeated for different z positions of the photodiode, placing it in turn 0./500./1000. and finally 1500.-mm away from the LED-head beam exit hole. As we measure the flux sensed by the calibrated photodiode, we also register (1) the flux sensed by the off-axis control photodiode placed behind the exit hole of the LED-head, the current actually injected into the LED (3) the temperature of the LED head (4) the temperature of the backend electronics and finally, the temperatures reported by the various sensors placed on the key test bench devices, such as the monochromator. We repeat this measurement sequence at different temperatures, using the climate chamber installed in the test bench.

Before and after each measurements we take a set of dark current samples. We need indeed to subtract the intrinsic dark current coming form the NIST photodiode. the dark current represents a small fraction of the raw signal ($\lesssim 0.1\%$), however, it has been found to be slightly variable as a function of time.

The main difficulty during these measurements is the control of the relative positions of the photodiode with respect to the source. Indeed, the main axes of the calibration beams are not perfectly orthogonal to the z-axis of the source, due to small misalignments of the LEDs themselves relative to the masks which define the conical beams. As a consequence, the map of each beam is measured relative to the position of the planet beam (i.e. the pencil beam which allows us later to reconstruct the position of the source relative to the telescope). The photometric data, complemented with additional data taken with a laser telemeter allows us to reconstruct a geometrical model of the LED head emission. This aspect of the analysis is not developed in detail in this memoir as I have not explicitly worked on it.

4.3.1 Data Set

The photometric data have been taken during Mars and May of 2012, just before shipping the LED source to Australia. We started with initial checks during which we discovered and solved problems related to the shape of the beams themselves (due to a faulty mask). We also adjusted the current of a few LEDs (LED02, LED08 and LED21, a UV LED) form their initial values, listed in table 4.1, because their measured flux turned out to be too

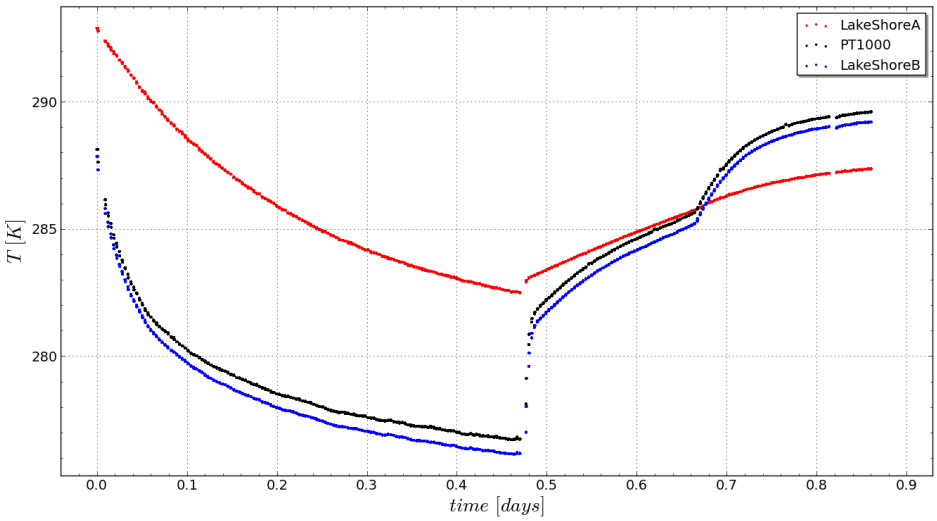

Figure 4.3: *The plot shows the temperature of LEDs (PT1000), the average temperature of the test bench (LakeshoreA), and the temperature of the radiator (LakeshoreB) versus the time for all mini-maps taken in the run of 13th May 2012. As we aspect that the PT1000 and the Lakeshore probe are in good agreement. However, values of the LakeshoreA are different due to the temperature gradient inside dark-enclosure.*

weak. Then, over a few days, we took several sets of maps and mini-maps, at different temperatures.

The analysis of the maps themselves is not presented in this memoir. We have rather concentrated on the analysis of the mini-maps, which allowed us to check the stability and the repeatability of our photometric calibration chain, and to control the linearity of the LED response. In figure 4.5, we show the profile a complete beam map. We discovered that some LEDs display a small bump at the centre of the beam, probably due to the shape of the LED emission zone, and the packing chosen by the constructor. This effect has already seen with SnDICE, the early DICE prototype (Guyonnet 2012), and (Villa 2012).

The last photometric data was taken on May 13th 2012. Figure 4.3 shows the temperature ramp of the calibration run, during which we took the reference set of mini-maps. The content of the dataset is summarised on figure 4.4 and in table 4.2. As can be seen, this is a rich dataset, that spans all temperature ranges, from about 4℃ to room temperature. With some more time, we may have been able to go down to 0℃. However, these temperatures seems to be rarely attained at Siding Springs observatory, hence, we decided to stop our temperature descent slightly above that point.

4.4 Spectroscopic Test Bench

We now turn to the description of our work on the spectroscopic measurements. These are an essential piece of information to characterise the LED radiant intensities. In the spectroscopic

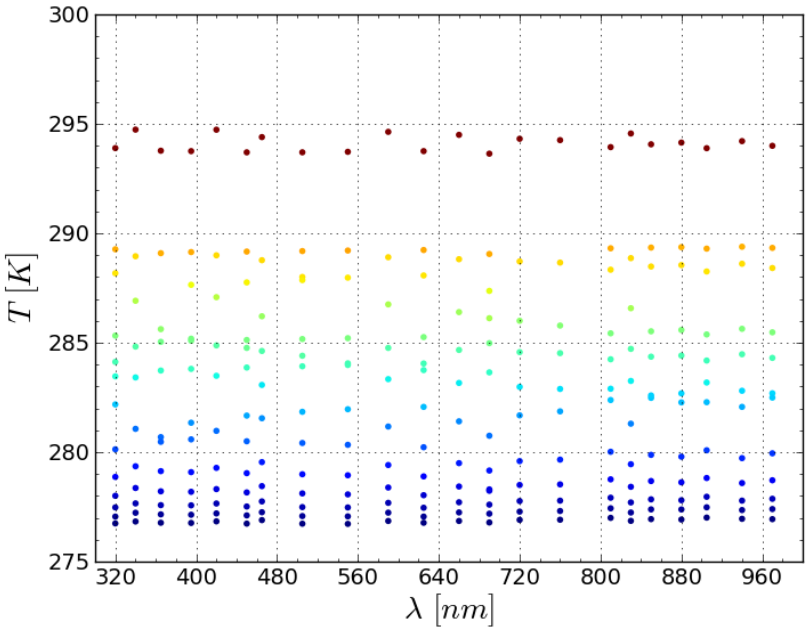

Figure 4.4: *We show all the temperatures reached during the full set of measurements for all LEDs. The average range is from* ~ 275 *to* ~ 295 *K.*

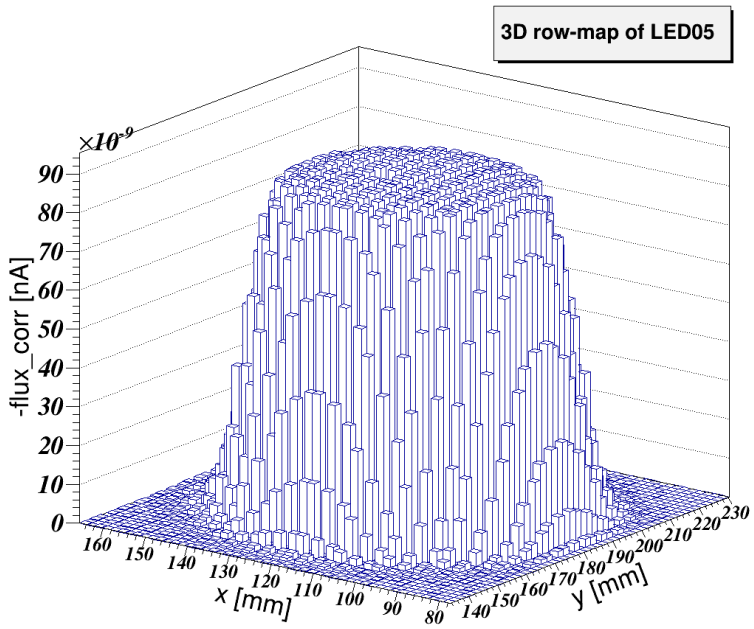

Figure 4.5: *An example of the beam map produced by the LED05* ($\langle \lambda_p \rangle = 512$ *nm) of the SkyDICE source at room temperature. This is a row map where we only subtracted the dark current contribution from the NIST.*

LED Number	$\langle\lambda_p\rangle$ (nm)	I_{led} (ADU) /(mA)	Maps #	z (mm)	(x_{ref}, y_{ref}) (mm)	Accuracy (A)
01	690	1000/3.1	7	0/-500/-1000/-1500	100, 175	2E-7
02	367	10000/21.4	7	" "	100, 150	2E-7
03	395	5000/10.7	7	" "	110, 125	2E-7
04	451	1000/3.1	7	" "	110, 100	2E-7
05	512	1000/3.1	7	" "	125, 180	2E-7
06	525	1000/3.1	7	" "	125, 160	2E-7
07	625	1000/3.1	7	" "	125, 125	2E-7
08	320	10000/12.2	7	" "	125, 80	2E-7
09	906	1000/3.1	7	" "	130, 160	2E-7
10	810	1000/3.1	7	" "	110, 140	2E-7
11	959	1000/3.1	7	" "	160, 170	2E-7
12	849	1000/3.1	7	" "	150, 160	2E-7
13	735	1000/6.2	6	" "	160, 120	2E-7
14	950	1000/3.1	6	" "	160, 100	2E-7
15	763	1000/3.1	6	" "	165, 170	2E-7
16	720	1000/3.1	6	" "	165, 100	2E-7
17	464	1000/3.1	6	" "	185, 175	2E-7
18	659	5000/15.5	7	" "	170, 155	2E-7
19	831	1000/3.1	6	" "	165, 145	2E-7
20	593	5000/15.5	6	" "	175, 110	2E-7
21	338	10000/12.2	6	" "	185, 100	2E-7
22	415	1000/2.1	6	" "	200, 170	2E-7
23*	-	-	-	-	-	-
24	544	1000/3.1	6	" "	200, 110	2E-7

Table 4.2: *SkyDICE photometric data sample taken during the* 13 *of May 2012 run. We represent the current I_{led} used, the wavelength of the LEDs, the distance from the* 0 *point of the test bench z axis, points representing the rough centre of each beam (x_{ref} and y_{ref}) and the chosen range for the pico-ammeter. (*)LED23 is faulty.*

configuration of the test bench, we insert a monochromator between the source and the NIST photodiode. The photodiode current is then given by:

$$I_{PD} = I_{NIST} - I_{dark} = \mathcal{S}(\lambda; T) \otimes \mathcal{W}_{mono}(\lambda) \times \mathcal{T}_{mono}(\lambda) \times \eta(\lambda) \tag{4.3}$$

where I_{PD} is the photodiode current minus the dark current, $\mathcal{W}_{mono}(\lambda)$ is the transfer function of the monochromator, $\mathcal{T}_{mono}(\lambda)$ is the transmission of the monochromator as a function of the wavelength, and finally the $\eta(\lambda)$ is the efficiency of the NIST photodiode. Our goal is to reconstruct and model the spectral intensity of each LED, $\mathcal{S}$, the I_{PD} from the photodiode measurements, knowing the transfer function of the monochromator and its transmission.

As mentioned already, one of the disadvantages of LEDs is the fact that their peak wavelength is temperature dependent: typical LEDs display a small shift of their peak of about 1Å/K (or less) up to 5Å/K. Of course, this has to be taken into account if we want to construct a good calibrator, and we need to build a temperature-dependent model of the LED spectral intensities. Again, we will therefore need to take calibration data over a wide range of temperatures, with the additional burden of monitoring the monochromator's temperature in additional to all the other sensors.

To do those type of measurements we need to add the monochromator to the photometric configuration as showed on figure 4.1 at the beginning of this chapter. The monochromator is the most important element. Before discussing the data taken, in the next section we are going to describe basic principles of function of the Digikrom DK240 monochromator. Then we spend some words about its calibration (for more details see the thesis work of Guyonnet (2012)).

4.4.1 The Digikrom-DK240 Monochromator

The monochromator used for the spectral calibration is a Czerny-Turner Digikröm DK240 (Spectral Products [4]) device, of focal length 240 mm, and equipped with a triple grazing system (figure 4.6). The gratings are controlled by a microprocessor-driven stepper motor, itself controlled by software through a universal serial port RS-232. The width of the entrance and the exit slits are also controlled by software. They can be set from 10 µm to 3000 µm.

The transmission of a typical monochromator depends on the diffraction properties of the grating system and on the reflectivity of the mirrors. To calibrate our spectra, we need to know the transmission of the monochromator, as well as its transfer function (which depends on the slit aperture). For the Digikröm DK240, the transfer function is a trapezoid, whose width depends on the width of the entrance and exit slits. If both slits are open at 625µm, it is well described by a triangle of FWHM 2-nm. On figure 4.6 we show a plot of this typical transfer function for this particular monochromator.

We also need to calibrate the spectra in wavelength, i.e. to control the relation between the position of the grating system and the exit wavelength. In practice, the monochromator comes with a default calibration which is reputedly stable. The DICE team has nevertheless

[4] http://www.spectralproducts.com

checked it extensively over the last years Guyonnet (see 2012). Before taking the spectroscopic data described below, we have applied the wavelength calibration protocol described in the reference above.

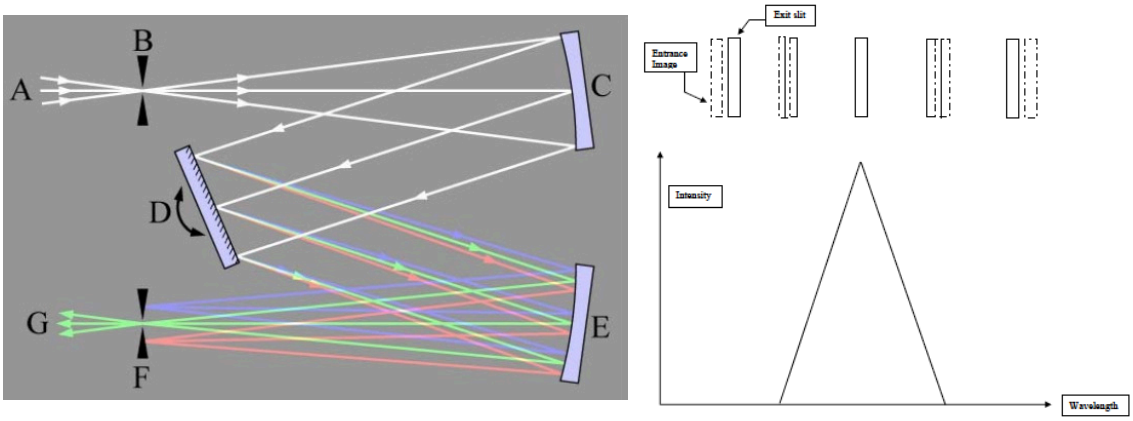

Figure 4.6: *(Left) - Optical design of a "Czerny-Turner". The illumination source [A] passes through the entrance slit [B]. The amount of light energy available for use depends on the intensity of the source in the space defined by the slit. The slit is placed at the focus of a curved mirror [C]. The collimated light is diffracted from the grating [D] and then is collected by another mirror [E] which refocuses the light, now dispersed, on the exit slit [F]. A rotation of the dispersing element causes the band of colours to move relative to the exit slit, so the desired entrance slit image is centred on the exit slit. (Right) - The Diagram shows the typical triangle-shape transfer function for the Digikröm DK240 when the entrance slit and exit slit have the same aperture.*

Principles of the Monochromator

A typical monochromator is designed to select a narrow band of wavelengths from some incoming radiation. The typical response function is a triangular profile, peaking at the selected wavelength. As the monochromator is an essential component of the spectral bench, we will briefly describe below how it works.

If we consider an uniform and point-like source at the entrance slit of the monochromator as represented in figure 4.7, then we can write the electric field diffraction as the product of two main components: the diffraction term produced by one of the grating grooves and the interference term of the whole grating system:

$$E_{tot}(\alpha_x, \alpha_y, \theta, \lambda) = E_{diff}(\alpha_x, \alpha_y, \theta, \lambda) \times E_{interf}(\alpha_x, \theta, \lambda) \tag{4.4}$$

where the meaning of the variable can be understood looking on figures 4.7 and 4.8 left. We can recognise the incident angle i_x of the wavelength coming form the first convex mirror and the reflection angle α_x, the tilt angle $\theta$of the grating system, the Ebert angle α that

represents a fixed angle between the two mirrors and the grating system (the value for our monochromator is 18.7°), and the blaze angle ϵ that is the angle between the grating plane and the single grating groove.

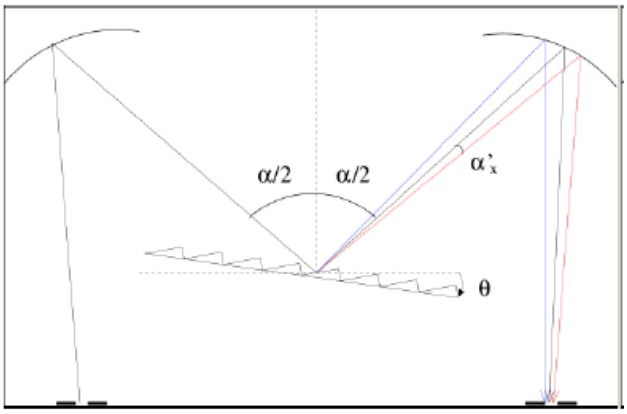

Figure 4.7: *Optical path of a monochromator. The mirror-grating system splits a polychromatic point-like source in the different wavelength components.*

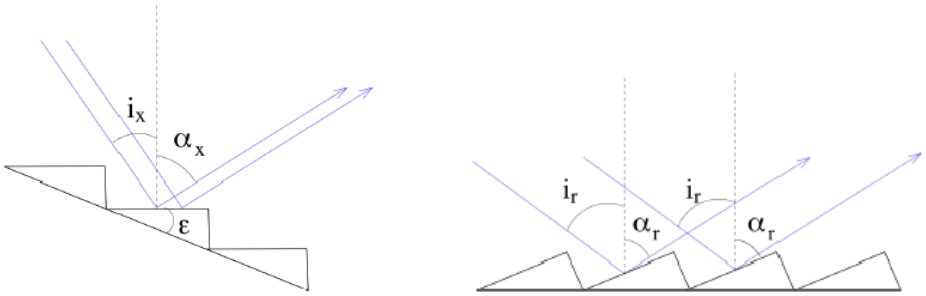

Figure 4.8: *(Left) - Single diffraction path. Here $\epsilon = \theta$ is the grating inclination. (Right) - Interference between two grating grooves.*

From this angles we can define $i_x = \alpha/2 - \epsilon - \theta$ and $\alpha_x = \alpha/2 + \epsilon + \theta + \alpha_x^{'}$ and finally we can write the diffraction term E_{diff} of the equation 4.4 it can be explicitly written using the following equation:

$$E_{diff}(\alpha_x^{'}, \alpha_y, \theta, \lambda) = E_0 sinc\left(\frac{\pi d}{\lambda}\left[2cos(\frac{\alpha}{2})sin(\theta+\epsilon)+cos(\frac{\alpha}{2}+\theta+\epsilon)sin(\alpha_x^{'})\right]\right)\times sinc\left(\frac{\pi h}{\lambda}sin(\alpha_y)\right) \tag{4.5}$$

The second term is the interference between two grating grooves. We can calculate this term as the difference between two incident rays on two different grating grooves . Looking on figure 4.8 right, we can define the angle α_r and i_r with the similar meaning of the i_x

and α_x of the last equation 4.5. Then with the same substitutions we can finally write the interference term E_{interf}:

$$E_{interf}(\alpha_x^{'}, \theta, \lambda) = \frac{sin(\frac{N\pi d}{\lambda}[2cos(\frac{\alpha}{2})sin(\theta) + cos(\frac{\alpha}{2} + \theta)sin(\alpha_x^{'})])}{sin(\frac{\pi d}{\lambda}[2cos(\frac{\alpha}{2})sin(\theta) + cos(\frac{\alpha}{2} + \theta)sin(\alpha_x^{'})])} \tag{4.6}$$

From equation 4.5 and 4.6 one can evaluate the term of the transmission for the central wavelength, T_{mono} given by the following expression:

$$T_{mono}(\lambda_c) = A_0 \times sinc\Big(\pi cos(\epsilon) - \frac{\pi d}{\lambda} 2cos(\frac{\alpha}{2})sin(\epsilon)\sqrt{1 - \frac{\lambda^2}{4d^2cos^2(\frac{\alpha}{2})}}\Big)^2 \tag{4.7}$$

This equation is used with the expression of I_{PD} given before to reconstruct the spectral energy distribution of every LED.

Transmission of the Monochromator

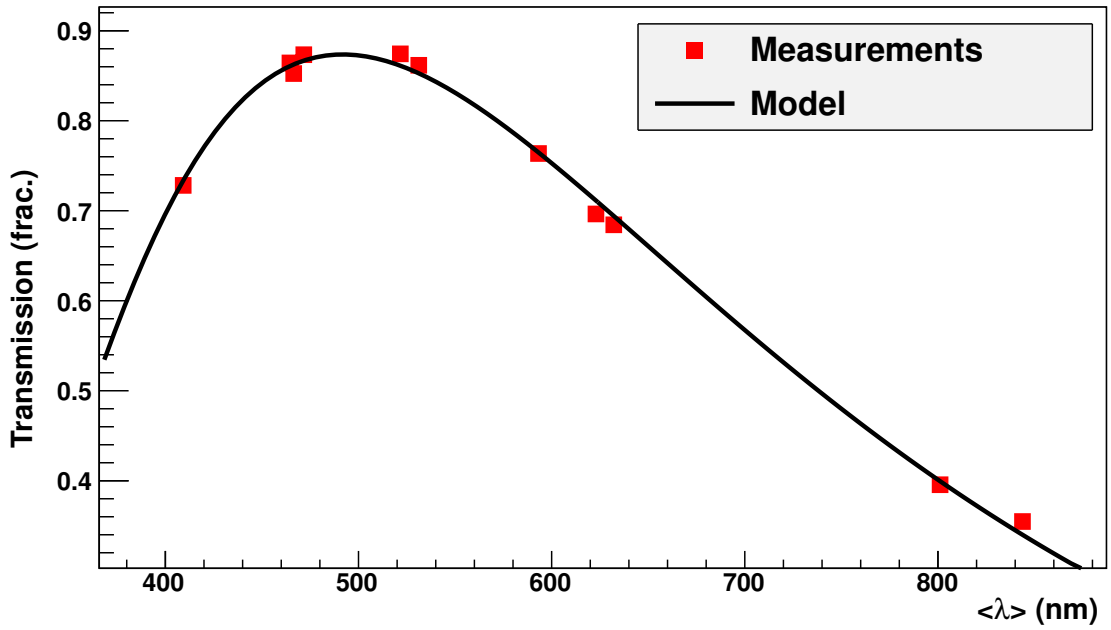

Figure 4.9: *Measurement of the monochromator transmission using the LED head itself (Guyonnet 2012).*

The transmission of our DK240 monochromator is studied in detail in (Guyonnet 2012). The classical way to measure the transmission of a monochromator is to manufacture a monochromatic source with a auxiliary monochromator, characterise it with the photodiode, and then insert the monochromator under study between the monochromatic source and the photodiode. Was was done instead it to manufacture a narrow spectrum source delivering a

Grating #	$\Delta\lambda_{gr}$ (nm)	$\beta_{gr} = d\Delta\lambda/dT$ (nm/°C)
1	+0.154 ±0.246	-0.002499 ±0.0023
2	+0.020 ±0.059	-0.002526 ±0.0016
3	-0.008 ±0.096	-0.002654 ±0.0022

Table 4.3: *Wavelength dispersion offset for the three grating configuration measured at* $T_a = 25°C$ *with the their temperature dependence (Guyonnet 2012).*

quasi-pencil beam, slightly smaller than the entrance slit, by placing a mask in front of the LED head. Then, measurements were performed with and without the monochromator and the results were used to constrain the relation 4.7 above (figure 4.9).

Wavelength Calibration of the Monochromator

The procedure use to calibrate the DK240 is the following. The monochromator is configured with exit and entrance slit positioned at 625µm. Then, several different primary spectral sources are placed in front of the entrance slit: a low pressure Cadmium lamp, a Sodium lamp and a polymetallic lamp.

The Sodium and Cadmium lamps have spectra that contain known doublets at known wavelength distance. Measuring this doublets with different grating configuration and at different dark-enclosure temperature, one can evaluate the dispersion of the monochromator. Measuring the positions of known spectral lines allows one check the wavelength calibration of the monochromator.

One last point. Because what we want to calculate is the spectral energy distribution $\mathcal{S}(\lambda, T)$ as a function of temperature, we need to keep in mind that even the grating system of the monochromator is weakly sensitive to a gradient of temperature. The sensitivity of the monochromator response to temperature has been studied in Guyonnet (2012). It is well described by a linear law:

$$\Delta\lambda = \Delta\lambda_{gr} + \beta_{gr}(T - T_a) \tag{4.8}$$

and table 4.3 shows the coefficients that have been determined.

Finally, the uncertainty of the monochromator wavelength calibration (taking into account this temperature sensitivity) has been estimated in detail in (Guyonnet 2012). It is summarised on figure 4.10. As can be seen, it is of about 0.1-nm w on the entire visible wavelength range.

4.4.2 Data Set

The spectroscopic dataset has been acquired in April 2012. In an initial phase, we have checked the monochromator calibration, and performed initial tests. In particular, we have decided to add additional temperature sensors, notably two Lakeshore[5] temperature moni-

[5]see http://www.lakeshore.com/

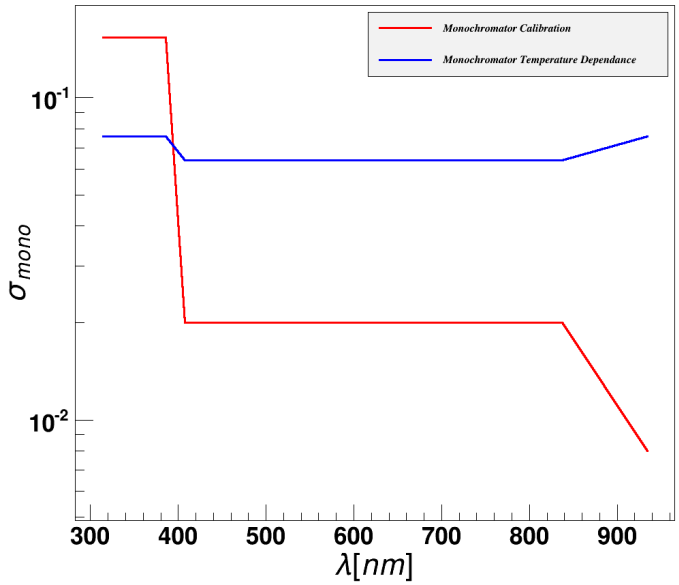

Figure 4.10: *The figure presents the wavelength dispersion σ_{mono} and its temperature dependence (Guyonnet 2012).*

tors, so that we could follow the temperature of the monochromator and to obtain a redundant measurement of the LED temperatures during the tests.

We also worked on optimising the configuration of the Keithley 6514 pico-ammeter. It was initially programmed to take itself several measurements, average them and report on the mean and the variance. In this configuration, it became clear that the measurement noise was under-estimated, probably because a good fraction of the noise power was peaking at lower frequencies (in particular the 50 Hz). We therefore decided to take about 20 single measurements for each point of the spectrum. This would be slower, but would allow us to gather more statistics and to obtain a correct estimate of the measurement noise.

The final spectroscopic dataset was taken on April 26th and 27th. The monochromator slits were open at 625µm, the pico-ammeter configured as said above. Several spectra were first acquired for each LED, with the grating the most adapted to the LED wavelength. On April 27th, we turned on the cooling system and started ramping down from room temperature to 0°C, while taking data. Figure 4.11 shows the temperature variations reported by several of our probes during this run. The probe labeled "PT1000" is mounted inside the LED board of the SkyDICE-head, while the others three sensors are mounted respectively on the radiator of the LED board, on the monochromator (Lakeshore probe A) and on the optical bench (Digisense sensor).

Figure 4.12 illustrates the range of temperatures reached from the all data run taken during the April period. We can easily see that we sampled all the possible temperature values for every LED of the SkyDICE system. This range of temperatures in agreement with

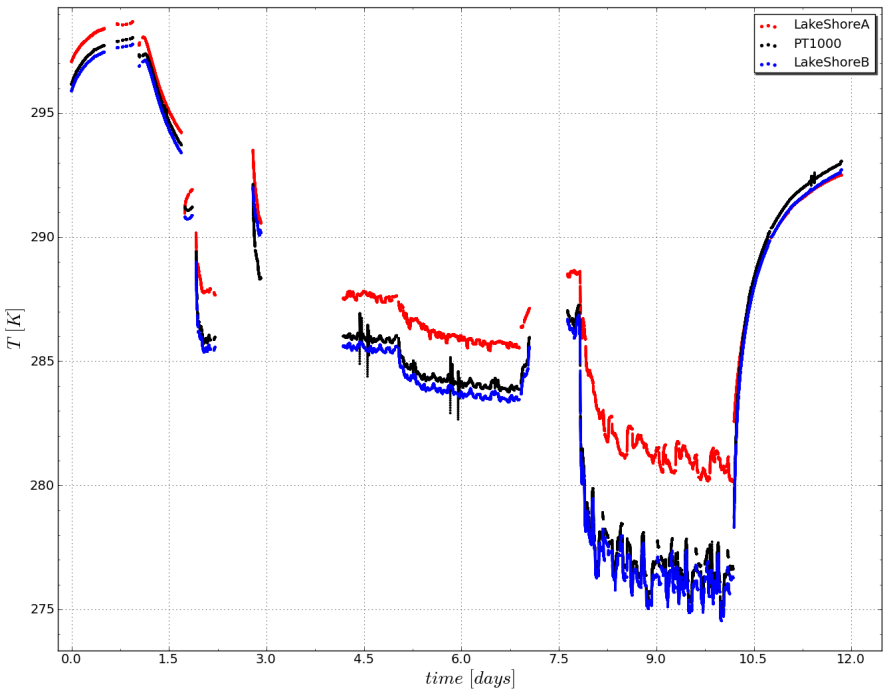

Figure 4.11: *The plot shows the temperature of LEDs (PT1000), the average temperature of the monochromator (LakeshoreA) and the temperature of the radiator (LakeshoreB) vs. the time for all data taken in the last two runs of 26 and 27 April 2012. As we aspect the PT1000 and the LakeshoreB probe are in good agreement. However, the values of the LakeshoreA are slightly higher due to the temperature gradient.*

what we expect to measure inside the enclosure of the SkyMapper telescope during a full year. The full dataset is summarised in table 4.4. Again, it is very rich, and will allow us to model the LED emission from almost 0 ℃ to room temperature (see chapter 6).

4.5 Pre-Analysis of the Test Bench Dataset

During data taking, and shortly afterwards, I conducted several quick analyses in order to assess the quality of the data that was on disk. The goal was also to prepare the commissioning of the device on site. These studies are much less sophisticated than what will be presented in chapters 6 and 8. However, they give a good sense of how the data looks like. For this reason, I will summarise them here. It can be seen as an overview of the test bench dataset.

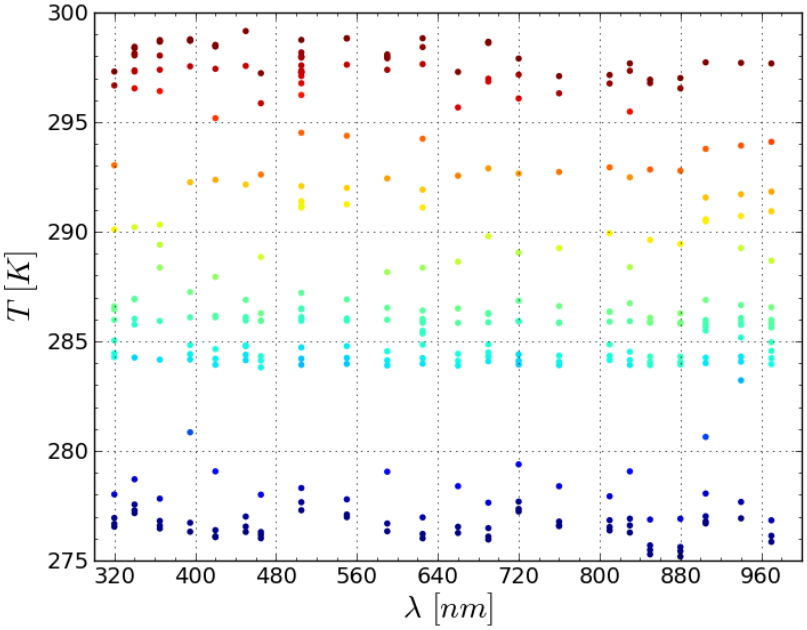

Figure 4.12: *A plot with temperatures reached during the full set of spectra measured. The average range is from* ~ 275 *to* ~ 300 *K.*

4.5.1 Photometric Mini-maps

The main purpose of the mini-maps is to normalise the LED emission, and to measure the relative variations of the LED flux as a function of temperature. In this section, we describe the preliminary analysis of the reference photometric dataset, taken on the 13th of May 2012. The only pre-processing was only the subtraction of the dark current. Also, we did not re-evaluate the noise.

Our main goal here is to study the variations of the LED flux with temperature. In particular, we want to evaluate (1) how large the effect is and (2) whether it is well described with a linear law, or whether we have to resort to a quadratic function for some LEDs. Another goal is to check that in each calibration channel, the control photodiode works as expected, and that the flux registered is nicely correlated with what is measured with the NIST photodiode.

The dependence of the LED flux is parametrized with a linear law which is is fitted on the data using the standard least square method. The estimated slopes a_0 and reference fluxes ϕ_0 can be found in table 4.5, where $\mathrm{d}\phi_{iphd}/dT$ refer to the off-axis control photodiode data, while the $d\phi_{NIST}/dT$ refers to the NIST photodiode data.

All control photodiodes have been found to work properly. In particular, they give results which are consistent with what is measured with the NIST photodiode. This is clearly apparent for example on figure 4.13, which shows on the x axis the $d\phi_{NIST}/dT$ parameter of the NIST photodiode, and on the y axis the $d\phi_{phd}/dT$ of the off-axis photodiode parameter. As we see, the slopes are perfectly correlated ($\rho \simeq 0.99$).

LED Number	$\langle\lambda_p\rangle$ (nm)	I_{led} (ADU)	Spectra #	Grating position	Slits (μm)	Accuracy (A)
01	690	1000/5000	17	2	625.0	2E-9
02	367	5000/10000	14	1	625.0	2E-9
03	395	5000	11	2	625.0	2E-9
04	451	1000/5000	15	2	625.0	2E-9
05	512	1000/5000	18	2	625.0	2E-9
06	525	1000/5000	15	2	625.0	2E-9
07	625	1000/5000	17	2	625.0	2E-9
08	320	5000/10000	15	1	625.0	2E-9
09	906	1000/5000	17	3	625.0	2E-9
10	810	1000/5000	14	2	625.0	2E-9
11	959	1000/5000	16	3	625.0	2E-9
12	849	1000/5000	14	2	625.0	2E-9
13	735	1000/5000	16	2	625.0	2E-9
14	950	1000/5000	15	3	625.0	2E-9
15	763	1000/5000	14	2	625.0	2E-9
16	720	1000/5000	14	2	625.0	2E-9
17	464	1000/5000	14	2	625.0	2E-9
18	659	5000/5000	13	2	625.0	2E-9
19	831	1000/5000	14	2	625.0	2E-9
20	593	5000	12	2	625.0	2E-9
21	338	5000/10000	13	1	625.0	2E-9
22	415	1000/5000	13	2	625.0	2E-9
23*	-	-	-	-	-	-
24	544	1000/5000	13	2	625.0	2E-9

Table 4.4: *SkyDICE spectroscopic data sample taken during the* 26 *and* 27 *of April run.* I_{led} *is the nominal current in ADU for this run. Grating position is the chosen set up for the monochromator: in particular* 1 = 1200 *groove/mm,* 1 = 600 *groove/mm* 1 = 300 *groove/mm. (*)LED23 seems to be faulty.*

During these tests, it was established that LED23 does not work (it was probably broken during its soldering on the LED mother board). We also detected that the flux delivered by LED17 (a UV LED) is unstable flux for all input currents.

In most cases, as expected, the flux decreases as a function of temperature (see e.g. table 4.5 as well as figures 4.14 (LED03) and 4.15) (LED07). The measured slopes are in accordance with what is expected from the constructor data-sheets. The variations are linear for all LEDs, with residuals in the range 0.2-0.3%.

For two LEDs, i.e. LED05 (figure 4.16) and LED24 (figure 4.17), the flux has been found to *increase* as a function of temperature. This probably related to the fact that these LEDs

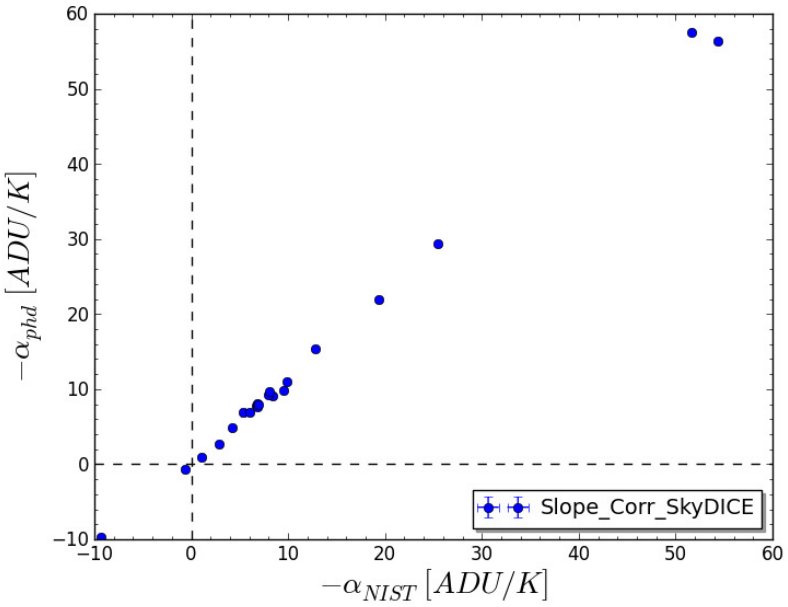

Figure 4.13: *The correlation between the NIST and the off-axis control photodiodes slope parameters for all studied LEDs.*

are operated at a very low current, at the limit of the operating range recommended by the constructor. The effect actually disappears if we increase the LED current. This is not a real problem for the calibration analysis and for the correct functioning of the DICE system. What it is important instead, is the stability of the behaviour of the source.

The slopes discussed in this section have been found to be reproducible from one run to another. The study of the source stability is the subject of chapter 5. We now know that we have a source that works, that seems to be stable, and whose flux varies linearly as a function of temperature. We now turn to the description of the spectral dataset.

4.5.2 Pre-Analysis of the Spectroscopic Dataset

We now discuss the final spectroscopic data sample, taken on the 26th and the 27th of April 2012 (see table 4.4 for details).

The total number of spectra taken were 401 with an average of 17 spectra for each LED. After a quick check we decided to use only 323 spectra of the 401 for the analysis and modelling. This happened because we observed a displacement of few millimetres of the LED-head working position, probably caused by the displacement of the y axis motor of the SkyDICE support. The 78 "bad" spectra display a significantly lower intensity profile compared with what was expected. However, the shape of the spectra was still good.

As for the photometric data, we needed to measure and subtract the dark current from the raw photodiode current measurements. To do that we took an amount of 100 measurements before turning on each LED, and after turning it off. The dark current varies slightly as a

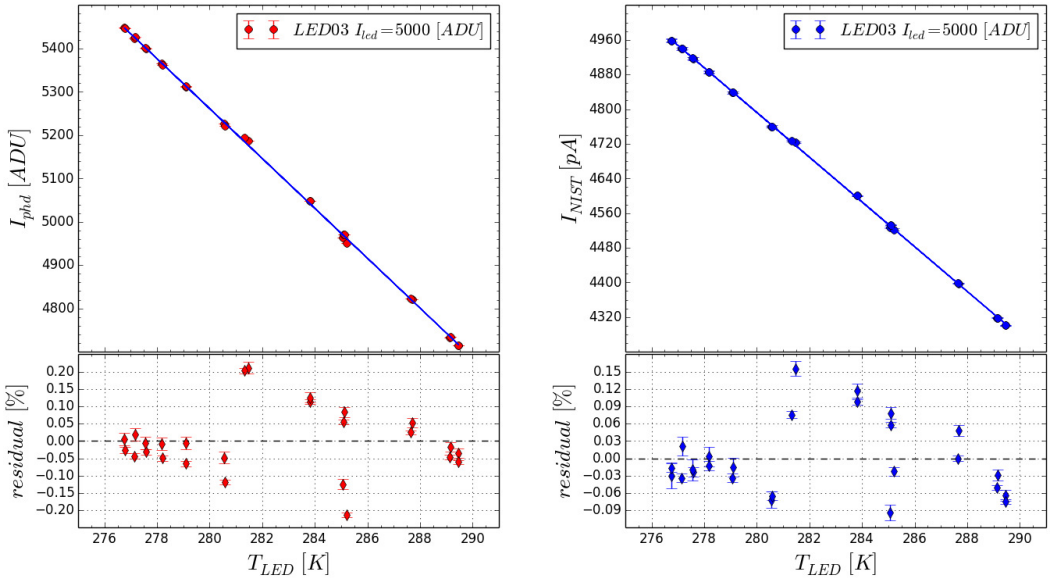

Figure 4.14: *Linear fit of the LED03 (*395 *nm). In the left is shown the data plus the fit obtained for the off-axis control photodiode, where in right side we presents the same results for the NIST photodiode. The two fit are in good agreement.*

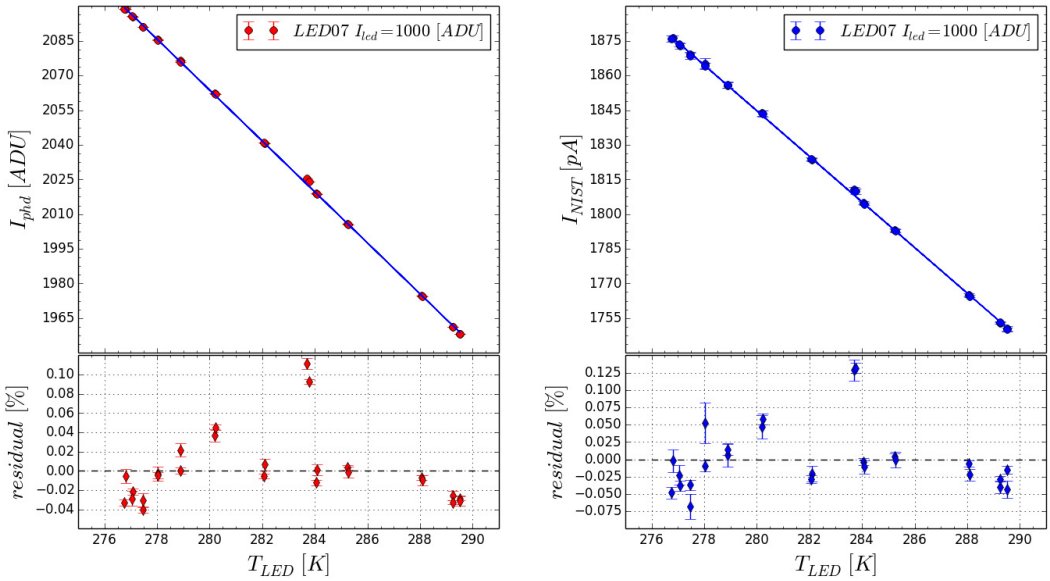

Figure 4.15: *For the red LED07 (*625 *nm), the result is in good agreement with what we expect from the constructor data-sheets. Again the flux decrease as the temperature increase.*

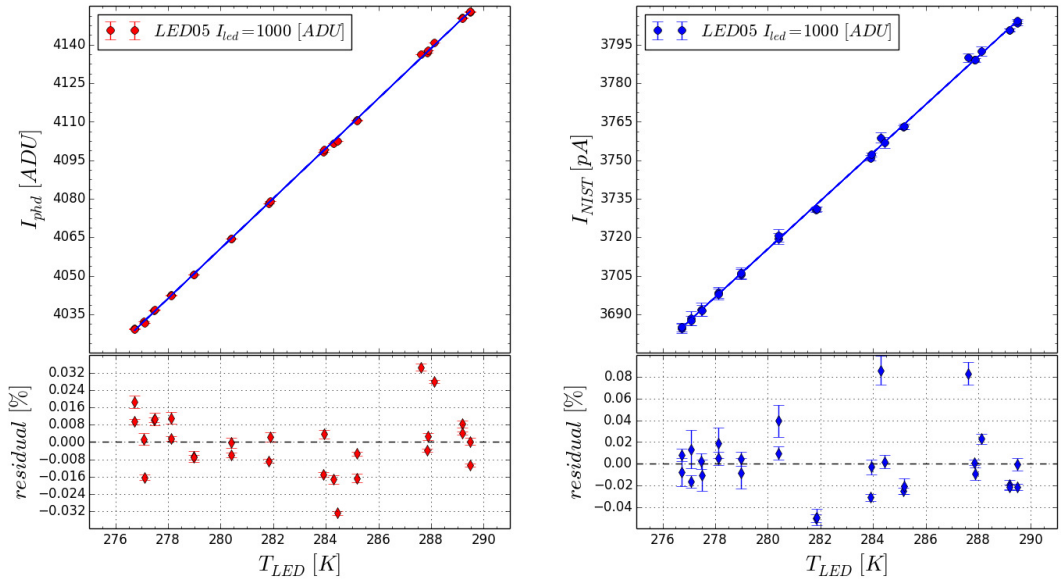

Figure 4.16: *The same plot but for the LED05 (505 nm) at 1000 ADU. In that case it is clear the strange behaviour that affect the LED at low current. The average flux increase as the temperature increase, instead decreasing as we expected from the data-sheets of the constructor. This effect disappears as soon as we augment the forward current of the device.*

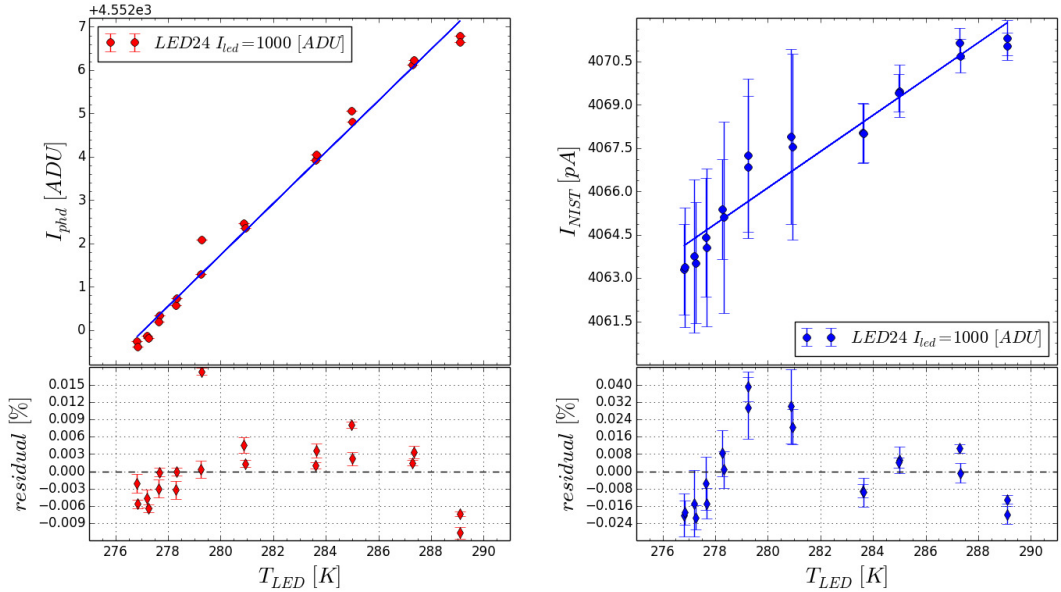

Figure 4.17: *We obtain the same result of LED05 for the LED24 (528 nm). Both are green LEDs.*

LED number	I_{led} (ADU)	$d\phi_{phd}/dT$ %/K	$d\phi_{NIST}/dT$ %/K
1	1000	-0.491 ± 0.002	-0.477 ± 0.004
2	10000	-2.193 ± 0.006	-2.214 ± 0.005
3	5000	-1.278 ± 0.004	-1.257 ± 0.003
4	1000	-0.132 ± 0.003	-0.120 ± 0.004
5	1000	0.233 ± 0.001	0.246 ± 0.005
6	1000	-0.414 ± 0.001	-0.404 ± 0.001
7	1000	-0.575 ± 0.002	-0.574 ± 0.002
8	10000	-0.353 ± 0.010	-0.350 ± 0.010
9	1000	-0.477 ± 0.002	-0.480 ± 0.003
10	1000	-0.213 ± 0.001	-0.187 ± 0.035
11	1000	-0.355 ± 0.003	-0.368 ± 0.002
12	1000	-0.323 ± 0.002	-0.313 ± 0.005
13	1000	-0.640 ± 0.001	-0.636 ± 0.002
15	1000	-0.172 ± 0.001	-0.168 ± 0.007
16	1000	-0.431 ± 0.001	-0.472 ± 0.003
18	5000	-0.459 ± 0.002	-0.455 ± 0.003
19	1000	-0.375 ± 0.003	-0.377 ± 0.003
20	5000	-0.291 ± 0.003	-0.282 ± 0.004
21	10000	-0.763 ± 0.004	-0.765 ± 0.008
22	1000	-0.617 ± 0.003	-0.600 ± 0.004
24	1000	0.013 ± 0.001	0.015 ± 0.003

Table 4.5: *The table contains the slope parameters from the least-square fit of the control photodiode current and the NIST current, measured during the 26 and 27 of April run. The only missed value is the LED17 because of an instability of the flux at low forward current, and the LED14 because the fit did not converge.*

function of time, and we interpolate linearly between the measurements in order to account for this. The average intensity of the dark current is at the level of $10^{-13} - 10^{-14}$ A, more that three orders of magnitude lower than the typical intensity of a spectrum from IR to UV.

Spectra Features

Let's first have a look at the spectral diversity of our LED sample. In the following figures we show examples of spectra taken from UV to near IR LEDs, along with a zoom on the spectrum peak. The y axis is the NIST photodiode current measured by the Keythley pico-ammeter (with caliber 10^{-9}). On the x we plot the wavelength λ, in nm.

We start with two UV LEDs LED03 (395 nm) and LED08 (320 nm) represented on figures 4.18 and 4.19 respectively. LED03 is an APGC1-395 UV single chip, with a spectrum that displays a small bump around $405 - 410$ nm. We notice the variation of the total LED

flux as a function of temperature. However, the variations of the *shape* of spectrum as a function of temperature seems to be weak. In particular, we do not observe any significant shift with wavelength.

LED08 is a UVTOP315-FW-TO39. As this LED is further in the UV, it is also much weaker, with measured currents around 32 pA (which explains that the spectrum is somewhat noisier). It displays however a spectrum which is similar as that of LED03 but without any unusual features.

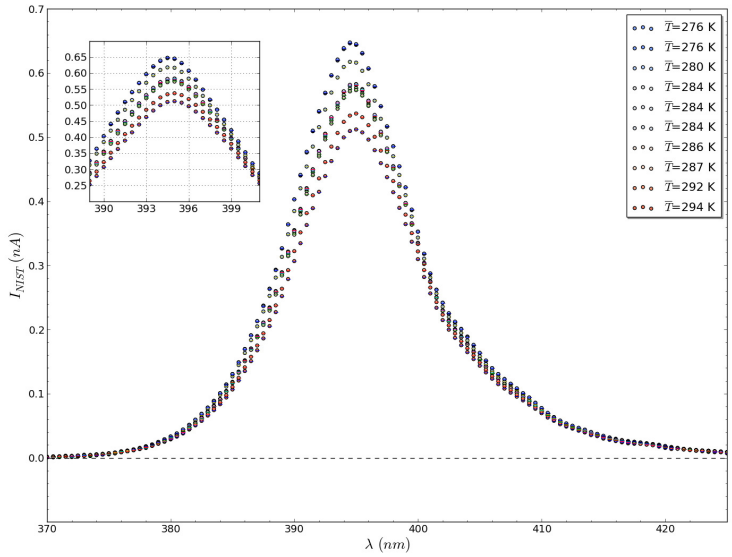

Figure 4.18: *Spectra of the UV LED03 ($\langle\lambda_p\rangle = 395$ nm). The shape of the spectrum still the same over the temperature, only the flux decrease as the temperature increase. There is also al small shift on the central wavelength of the spectrum.*

We now move to the visible part of the spectrum. The next LED represented is the green LED05 with $\langle\lambda_p\rangle = 512$ nm. It is a Golden Dragon LV W5AM LED, a green diode made with a $ThinGaN$ semi-conductor, which displays a broad asymmetric spectrum. This LED has already been encountered in the previous section: it is, along with LED24, the one whose flux increases with temperature when operated in sub-regime. On figures 4.20 and 4.21 we present spectra of LED05 taken with two different forward currents, respectively $I_{led} = 1000$ ADU and 5000 ADU. In both cases the device works in the sub-regime region. On the first plot, the LED flux increases as a function of temperature, on the second, the LED is operated at a higher current, its flux decreases with temperature, and the temperature sensitivity seems to be weaker.

This effect is unexplained at the moment, neither data-sheets from the constructor, nor literature do report any indication of this behaviour at low forward current. For our purpose, what it is important is that (1) the flux varies linearly with temperature and that (2) the spectrum shape varies as little as possible with temperature. From the test bench data we

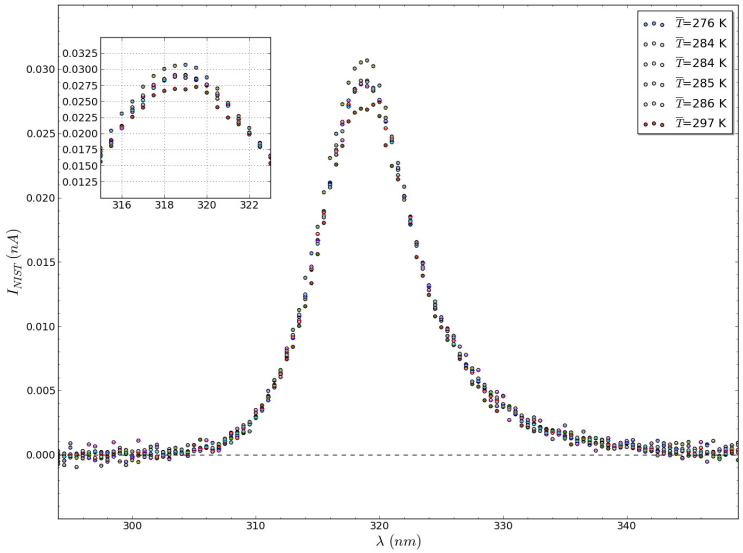

Figure 4.19: *Another UV LED, this time the LED08 ($\langle\lambda_p\rangle = 320$ nm) at different temperature. In this case the intensity of the current I_{NIST} is really weak, ~ 32 pA, as we expected for UV LEDs. This resulting on a really noisy spectrum.*

have discussed so far, this seems to be the case.

Finally, we take a look at the LEDs that emit in the redder part of the spectrum, for example LED07 ($\langle\lambda_p\rangle = 625$ nm), and the near IR LED10 ($\langle\lambda_p\rangle = 810$ nm) whose spectra are shown on figures 4.22 and 4.23 respectively. The first one is a Golden Dragon LA W5SM, and the second is an APG2C1-810 near-IR LED. Here the situation is more complex. Both LEDs show a normal behaviour regarding the flux vs. temperature variations. However, they display a strong wavelength shift with temperature that can be clearly seen on the figures.

Wavelength vs. temperature

We now move to a more quantitative study of the LED spectral dependence with temperature. We will estimate the variations of the average LED wavelength as a function of temperature.

In this *pre*-analysis we did not normalised the flux spectra using information from beam map measurements. What we done is essentially a first level parametrisation of the wavelength variation using as a model a simple linear law:

$$\langle\lambda(T_{led})\rangle = a_0 \Delta T_{led} + \langle\lambda_0\rangle \tag{4.9}$$

where $\langle\lambda(T_{led})\rangle$ is the wavelength of our NIST photodiode, a_0 is the slope of the linear law, $\Delta T_{led} = T_{led} - T_0$, with $T_0 = 293.15$ K, and finally $\langle\lambda_0\rangle$ is the intercept equal to value of the wavelength at the temperature T_0. For each LED, we estimate the first moment of each of the spectra, and we fit the law by minimising a χ^2.

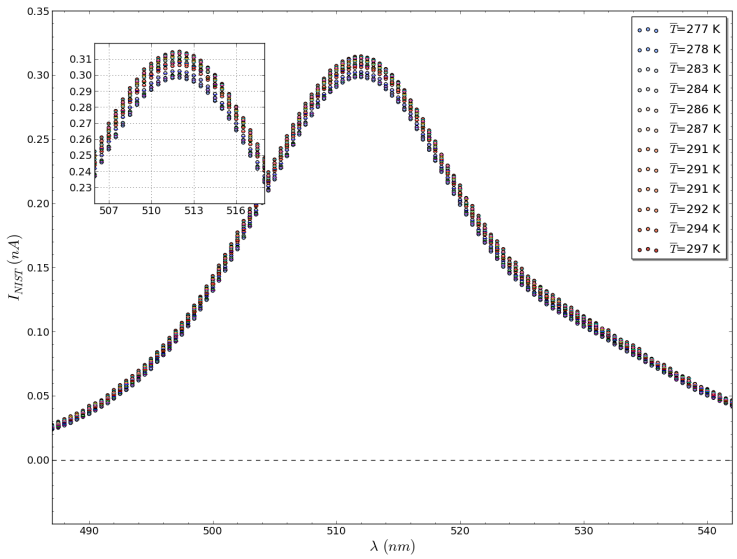

Figure 4.20: *Spectra of the green LED05 ($\langle\lambda_p\rangle$ = 512 nm). This spectrum shows a small bump at high wavelength, but in that case, due to a too few current, the LED works at sub-regime and shows an increase of the the measured current I_{NIST} as the temperature increase. The wavelength is almost not shift along all temperatures range.*

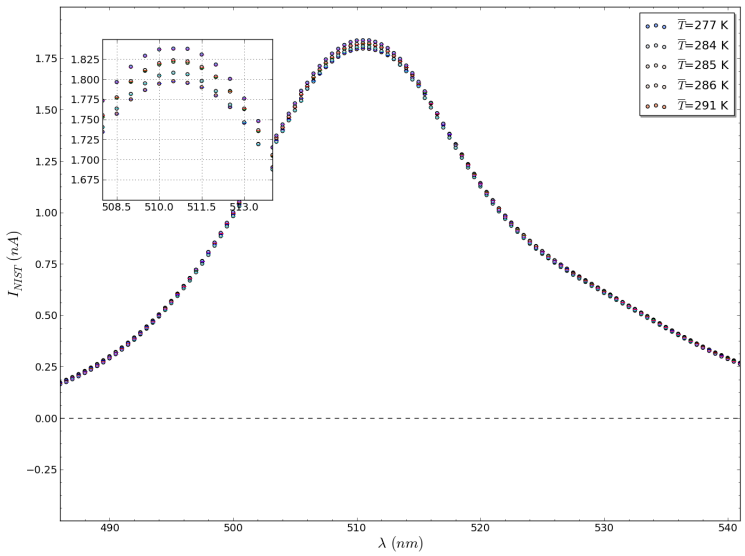

Figure 4.21: *The same LED05 but with an higher forward current. In that case the LED works properly, showing a decrease of the flux as the temperature increase.*

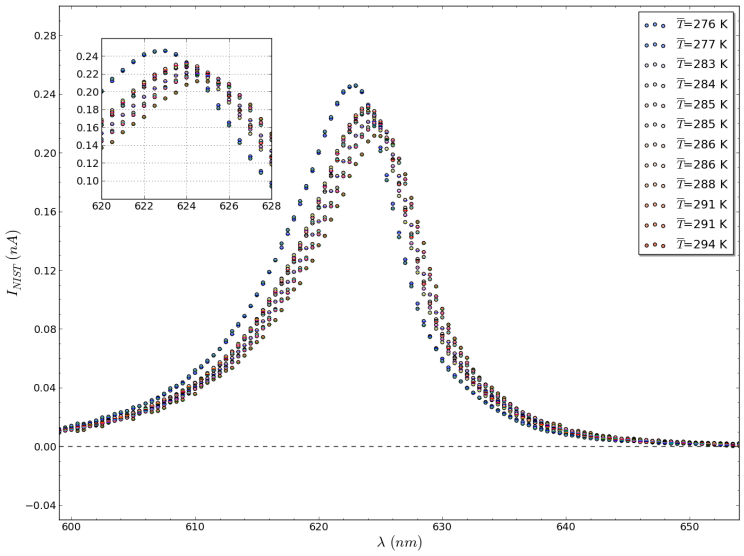

Figure 4.22: *Spectra of the red LED07 ($\langle\lambda_p\rangle$ = 625 nm). In that case not only the flux decrease, but it is evident that the all the spectrum shift with its central wavelength.*

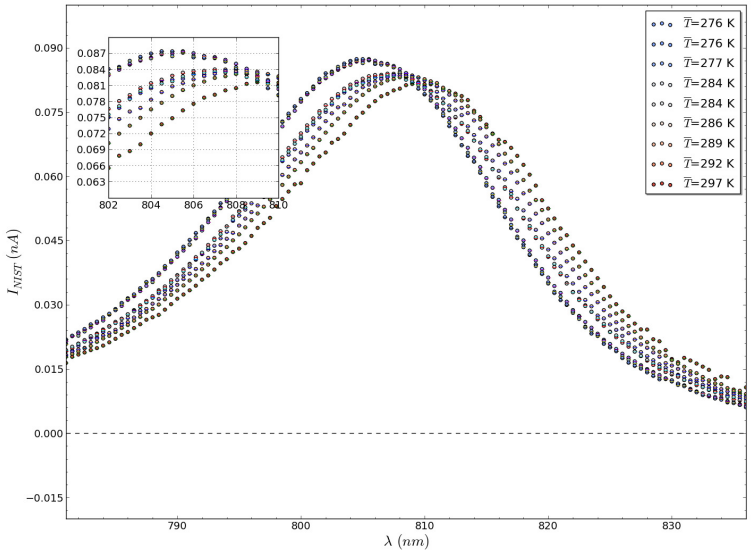

Figure 4.23: *For spectra of the near-IR LED10 ($\langle\lambda_p\rangle$ = 810 nm) the behaviour is similar to the red LED07 shown on figure 4.22.*

The results are presented in table 4.6. In this table we do not report results for LED23 because it is broken, LED17 (a green LED), because the flux was too unstable due to the small forward current. Also LED14 (a IR LED) is not shown because we got too few temperature measurements and the fit did not converge properly.

Most LEDs display the same behaviour: their spectrum becomes slightly redder as the temperature increases. However, the intensity of the effect varies greatly from one LED to another.

UV LEDs

We start, as the section above, with the result from from the LED03, presented on figure 4.24. What we see in that case is a small positive temperature dependence of the wavelength, this is the case also for the LED02 at 5000 ADU forward current. Those values contrast with the one obtained for LED02 at 10000 ADU and for the slope obtained with the LED08. The explication is probably due to a lack of data in temperature for those last two LEDs.

Visible LEDs

The result from the fit of LED05 is shown on figure 4.25. This time, as we expected looking its spectrum on figure 4.20 and 4.21, the temperature dependence is almost null. The average wavelength maintains the same value along all DICE working temperature. We obtained the same result for the LED24, with a small value of $d\langle\lambda\rangle/dT = 0.009$. A small temperature dependence is found for almost all LEDs in the visible.

Red and near-IR LEDs

In the case of red and near IR LEDs we obtained a different result. As we shown on figure 4.26 and 4.27, it is clear a strong temperature dependence on wavelength. Almost all LEDs give value of the slope $d\langle\lambda\rangle/dT$ in the range of $0.1 - 0.3$ nm per degree Kelvin. This value is much bigger compared with visible and UV LEDs.

All this spectroscopic *pre*-analysis has been taken in account as a starting point for the most difficult task of modelling and normalising the spectral energy distribution $\mathcal{S}(\lambda; T)$.

4.6 Test Bench Systematics

We end this chapter with a discussion on the uncertainties that affect our test bench measurements. These uncertainties will become sources of systematic errors when the calibrated source is operated in the telescope enclosure. At the moment, we have identified two main sources of systematics. First, our knowledge of the monochromator transmission and wavelength calibration, which may respectively distort or shift in wavelength our estimates of the LED spectra. Second, the uncertainties affecting the efficiency of the NIST photodiode. We discuss both below.

LED number	I_{led} (ADU)	$\langle\lambda_p\rangle$ $[T \simeq 300K]$ (nm)	$\langle$FWHM$\rangle$	$d\langle\lambda\rangle/dT$ (nm)/K
1	1000	690	23.6	0.141 ±0.009
	5000		23.4	0.144 ±0.001
2	5000	367	10.2	0.002 ±0.018
	10000		10.1	-0.019 ±0.016
3	5000	395	13.8	0.018 ±0.002
4	1000	451	21.9	0.014 ±0.003
	5000		22.6	0.011 ±0.004
5	1000	512	28.0	-0.003 ±0.002
	5000		28.7	0.001 ±0.003
6	1000	525	34.4	-0.019 ±0.009
	5000		34.3	-0.013 ±0.002
7	1000	625	13.9	0.099 ±0.006
	5000		14.0	0.108 ±0.001
8	5000	320	10.2	-0.016 ±0.047
9	1000	906	66.7	0.136 ±0.027
	5000		65.8	0.127 ±0.002
10	1000	810	31.5	0.176 ±0.012
	5000		31.2	0.180 ±0.003
11	1000	959	17.6	0.290 ±0.019
	5000		20.7	0.273 ±0.004
12	1000	849	33.6	0.192 ±0.011
	5000		33.3	0.206 ±0.008
13	1000	735	24.6	0.151 ±0.003
	5000		25.2	0.159 ±0.004
14	5000	940	67.5	0.173 ± 0.003
15	1000	763	27.4	0.164 ±0.010
	5000		27.2	0.171 ±0.004
16	1000	720	25.9	0.138 ±0.012
	5000		25.8	0.157 ±0.006
18	5000	659	21.2	0.144 ±0.004
19	1000	831	32.1	0.195 ±0.009
	5000		31.9	0.211 ±0.009
20	5000	593	16.7	0.101 ±0.004
21	5000	338	12.6	0.018 ±0.036
	10000		12.3	0.052 ±0.031
22	1000	415	13.8	0.008 ±0.008
	5000		13.9	0.011 ±0.006
24	1000	544	43.8	0.009 ±0.005
	5000		41.7	0.010 ±0.005

Table 4.6: *The table show the full list of the slope parameter found using the linear fit discussed in §4.5.2.*

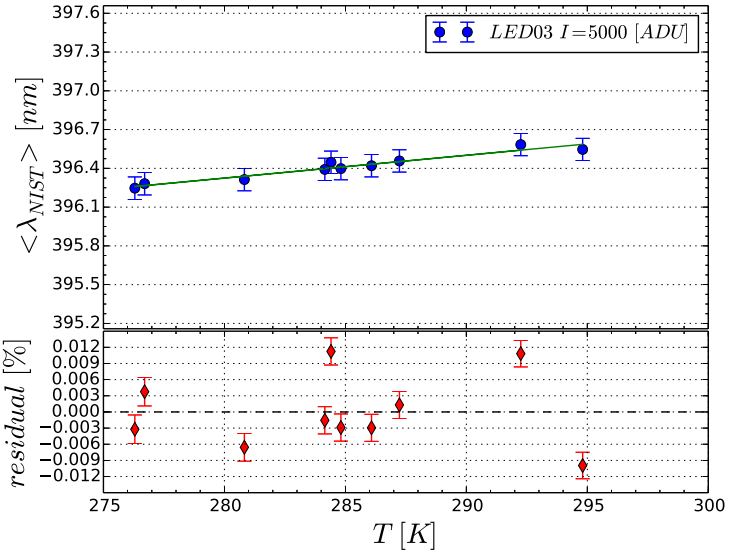

Figure 4.24: *The plot represents the average wavelength computed from the NIST photodiode measurements for the LED03. We fit data with a linear law as a function of the temperature. The plot below show the small residual from the original data.*

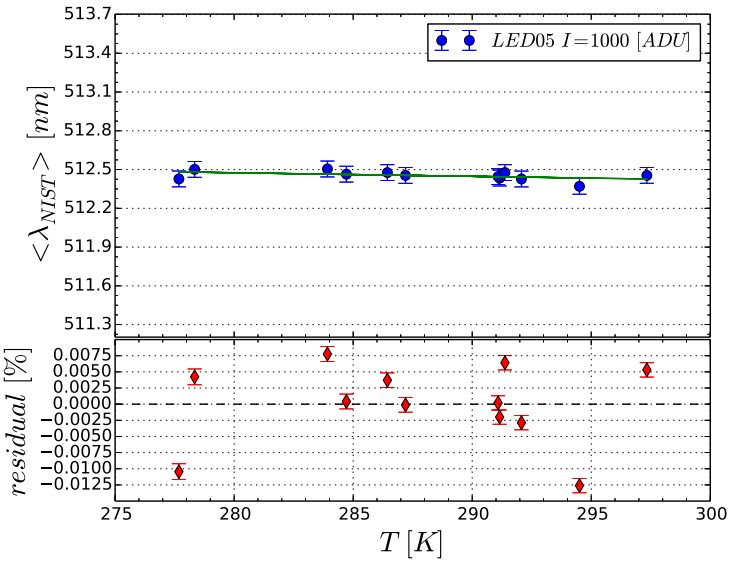

Figure 4.25: *Here is fit drawn for the LED05. In that case the wavelength is weakly dependents by the temperature.*

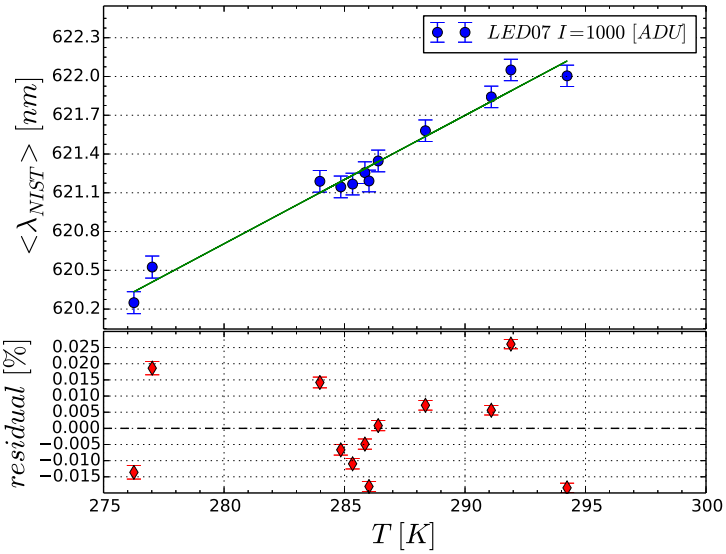

Figure 4.26: *The fit for the red LED07. The temperature dependence in that case are strong.*

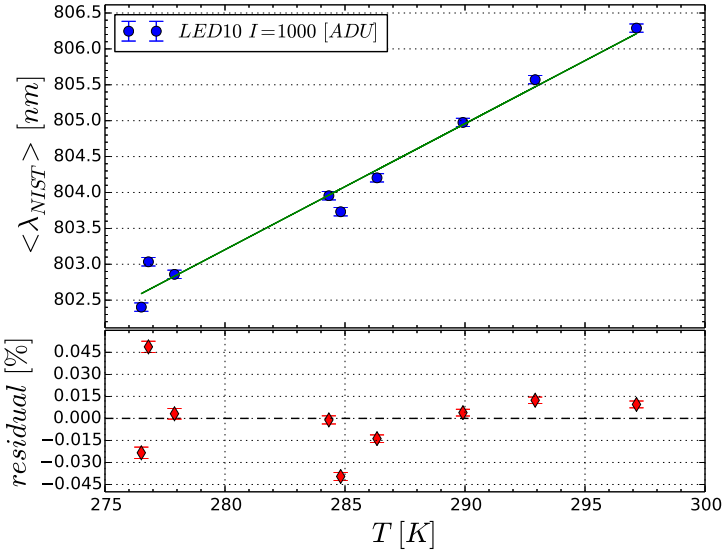

Figure 4.27: *The fit for the near-IR LED10. As the LED07 the temperature dependence is strong for near-IR LEDs.*

4.6.1 Monochromator

The key point here is the control of the monochromator calibration. We have checked (1) the wavelength calibration of the monochromator (2) its transmission $\mathcal{T}_m(\lambda)$ and (3) its spectral response, $\mathcal{W}_m(\lambda)$.

- The wavelength calibration of the device is checked (at several temperatures), using a series of calibration lamps, notably sodium lamp, and a polymetallic lamp. We obtain from this dataset a correction to the calibration given by the manufacturer. This correction does not exceed 0.1 nm in amplitude. We find a small linear dependance of the wavelength calibration with temperature, of about $0.1nm/°C$ which is taken into account. Overall, the uncertainty on the monochromator calibration never exceeds 0.1 nm.

- The transmission of the monochromator, $\mathcal{T}_m(\lambda)$, is measured at several discrete wavelengths. For Czerny-Turner designs, it is relatively easy to compute the shape of $\mathcal{T}_m(\lambda)$, as a function of two specific angles: the so-called Ebert angle α_E, which depends on the optical design of the device, and the blaze angle ϵ_{blaze} of the grating i being used. Fitting this model on the measurements, we are able to reproduce the values of α_E and ϵ_{blaze} with a precision of 1% and 0.3% respectively. We use the continuous models fitted on the data as our estimates of the monochromator transmission (see figure 4.9). At first order, $\mathcal{T}_m(\lambda)$ depends only on ϵ_{blaze}. The error on the monochromator transmission is then estimated by propagating the uncertainty on the blaze angles. On figure 4.28 we show the (normalised) transmission of the three gratings. We also show how it varies as a function of ϵ_{blaze}.

  Note that although the shape of $\mathcal{T}_m(\lambda)$ is well constrained, its absolute normalisation is affected by an uncertainty which is small but difficult to assess. This uncertainty depends primarily on the the absolute vertical centring of the LED head with respect to the entrance slit of the monochromator.

- Finally, the shape of $\mathcal{W}_m(\lambda)$ is set by the respective widths of the entrance and exit slits. For this work, we have chosen to open both slits at 0.625-nm, which results in a triangular-shaped spectral response of FWHM 2-nm.

4.6.2 NIST photodiode

The calibration of the NIST photodiode is itself uncertain. NIST provides its clients with an error budget, as shown on figure 4.2. NIST reports typical uncertainties of 0.2% in the visible ($400\ \lambda < 950\ \lambda$) which goes up to 1% in the UV- and the near-infrared.

Unfortunately, no information is available on how these uncertainties are correlated. We expect a fraction of the error budget to be wavelength-dependent, and since we are primarily interested in the *relative* inter-calibration of the passbands, it is essential for us to account for the off-diagonal terms of the NIST uncertainties. As of today, we have not been able to

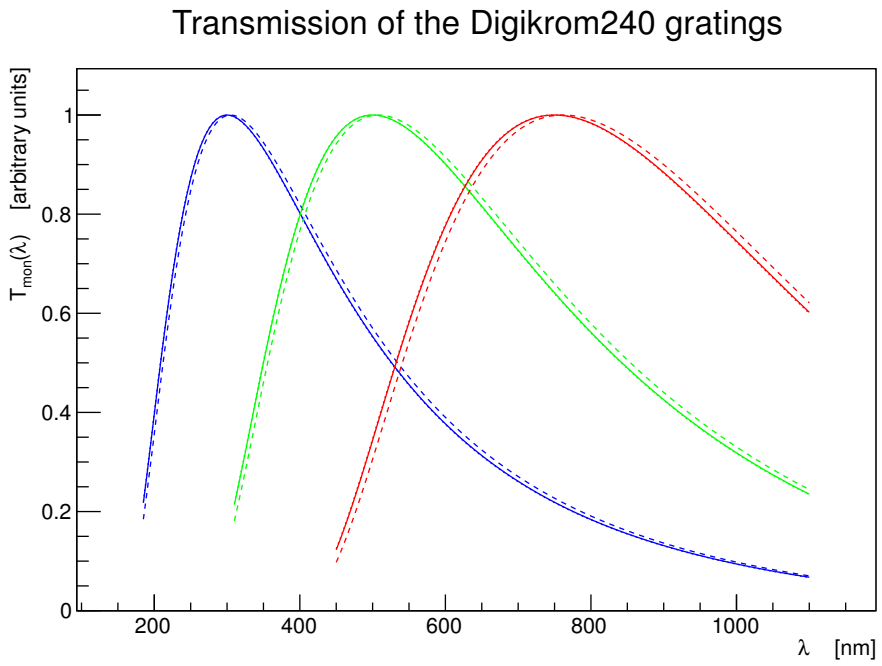

Figure 4.28: *Digikrom240 transmission for the 3 gratings used in the measurements.*

obtain this information from our contacts at NIST. As a consequence, we choose to build two different error budgets, depending on how we interpret the NIST uncertainties.

In the "best case" scenario, we assume that the NIST uncertainties are all positively correlated. In other words, what is uncertain is the global flux scale, but the slope of the photodiode response is very well known. For us, this would be an excellent situation: we are primarily interested into calibrating passbands, and we do not seek to perform an absolute calibration of the image response. The uncertainty on the global flux scale (about 0.2% according to NIST) cancels out as we compare the bands with each other.

In the "worst case" scenario, we assume that a fraction of the NIST uncertainties are correlated in such a way that distant passbands are negatively correlated. In other terms, there is a "colour uncertainty" in addition to a grey scale uncertainty. This may be modelled by two noise terms α_{NIST} and β_{NIST}, affecting the determination of the NIST efficiency estimate:

$$\eta_{NIST}(\lambda) = \eta_{\text{true}}(\lambda) \times (\alpha_{NIST}\ (\lambda - \langle\lambda\rangle) + \beta_{NIST} + 1) \tag{4.10}$$

From this, one can easily express the uncertainty on η_{NIST} as a function of $\sigma_{\alpha_{NIST}}$ and $\sigma_{\beta_{NIST}}$, and choose the latter terms so that we stay compatible with the uncertainties reported by NIST (see figure ??). The impact on these two scenarios on our determinations of the telescope passbands is detailed in chapter 8.

All the test bench uncertainties studied so far are listed in table 4.7. They will be further discussed in the next chapters.

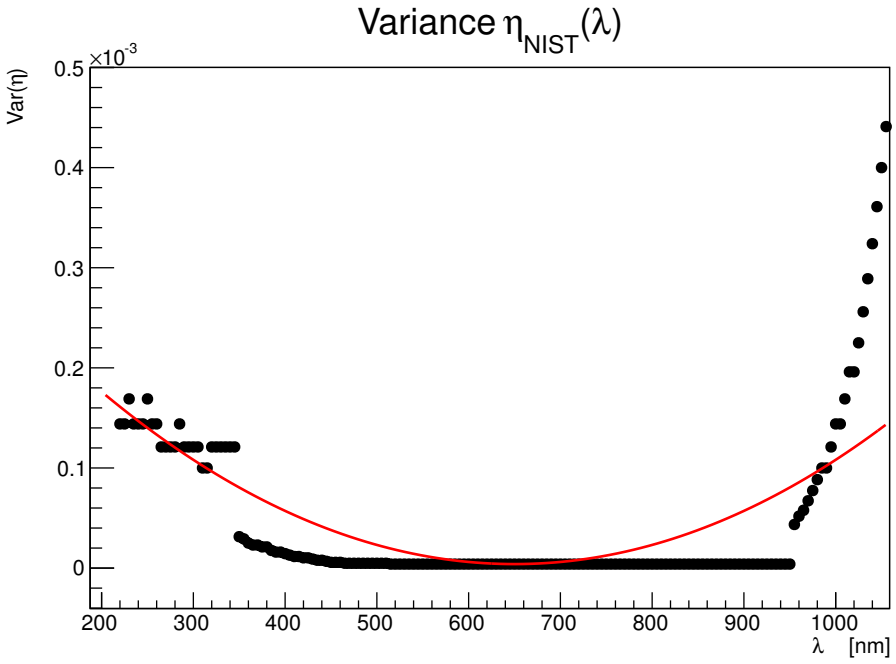

Figure 4.29: *Variance of the NIST efficiency $\eta(\lambda)$.*

	$1-\sigma$ uncertainty	Comment
Monochromator		
Wavelength calibration	0.1 nm	
α_{Ebert}	1°	
ϵ_{blaze} (grism #1)	0.17°	$\langle\lambda_{led}\rangle < 450$ nm
ϵ_{blaze} (grism #2)	0.28°	450 nm $< \langle\lambda_{led}\rangle < 750$ nm
ϵ_{blaze} (grism #3)	0.43°	$\langle\lambda_{led}\rangle > 750$ nm
Calibrated photodiode		
α_{NIST}	2.9 10^{-5} nm^{-1}	From the calibration uncertainties provided by NIST.
β_{NIST}	0.002	

Table 4.7: *Summary of the test bench systematics.*

Chapter 5

Stability Study

If we want to achieve the ‰ target, the first requirement is the stability and repeatability of our calibration source. Following that demand, the stability of a the whole DICE system, *LEDs source + backend electronics + off-axis control photodiodes*, has been checked.

As the stability studies typically require very long (weeks) acquisition sequences, this work has not been performed on the original SkyDICE instrument, but rather on a spare source, equipped with similar LEDs and connected to a replica of the SkyDICE backend electronics.

In fact, we have seen in the previous chapter that a DICE source cannot be intrinsically stable, at least for one good reason: it is not kept at constant temperature while all LEDs display a temperature dependence of their emission. Therefore, our goal is not to see whether the source is stable or not, but whether we can *predict* the relative flux variations of the source, using various monitoring data, the question being how well our predictions match the observed flux variations.

There are two types of monitoring data. First, we have our records of the LED temperature, and of the current actually injected into the LED. Second, we have direct flux measurements by the off-axis control photodiodes which are placed in each LED channel. In what follows we will first use the first set of metadata, to see how well we can predict the flux variations with these alone. Then, we will roll out the off-axis measurements, in order to see whether they increase our ability to understand the variations of the source emissions.

This chapter is divided in four sections: we first (§5.1) describes the test bench set up and the type of data that was acquired. We then discuss (§5.2) a stability analysis using the current and temperature records only. Then, we will estimate in (§5.3) the improvements obtained by adding the measurements performed with off-axis control photodiodes. Finally, in §5.4, we give some details on the result of a spatial relative stability analysis of LED beams, and its uniformity.

5.1 Data Set

The Spare Source Because of the impossibility to use directly the SkyDICE device, the measurements has been performed using a spare LED-head. This source had been built a few

LED number	LED type	SkyDICE type	λ_{peak} (nm)	I_{max} (mA)	Beam shape	I_{led} (ADU)
01	SMC	-	805	50.0	Lambertian	6000
02	Golden Dragon	yes	633	35.0	Lamb.	10000
03	Golden Dragon	-	472	35.0	Lamb.	4000
04*	-	-	-	-	**planet led channel*	-
05	SMC	-	951	50.0	Lambertian	6000
06	APG2C1	yes	721	50.0	Lamb.	14000
07	Golden Dragon	-	535	50.0	Lamb.	8000
08	SFH	yes	880	20.0	Lamb.	12000
09	APG2C1	-	763	50.0	Lamb.	8000
10	Golden Dragon	yes	463	50.0	Lamb.	6000
11	APG2C1	yes	831	50.0	Lamb.	3000
12	APG2C1	-	656	50.0	Lamb.	14000
13	Golden Dragon	-	526	100.0	Lamb.	4000
14	400/420	-	407	50.0	Lamb.	6000
15	Golden Dragon	yes	851	50.0	Lamb.	3000
16	400/420	yes	422	50.0	Lamb.	14000
17	APG2C1	-	908	50.0	Lamb.	5000
18	Golden Dragon	yes	633	50.0	Lamb.	6000
19	Golden Dragon	yes	623	50.0	Lamb.	8000
20	Golden Dragon	yes	593	50.0	Lamb.	14000
21	APG2C1	-	959	50.0	Lamb.	14000
22	APG2C1	yes	688	50.0	Lamb.	14000
23	Golden Dragon	yes	464	35.0	Lamb.	10000
24	UV	yes	342	50.0	Lamb.	14000

Table 5.1: *LEDs list for the spare LED-head device used in this analysis with the SkyDICE LEDs identification. I_{max} represents the maximum DAC value available for the input current (corresponding to $DAC_{max} = 16384$). I_{led} is the DAC current value used in this experience.*

years before, along with the early DICE prototypes. It has been retrofitted with a modern electronics, and equipped with the same type of LEDs used for SkyDICE. The goal was to obtain a device as similar to SkyDICE as possible, and also to build an upgraded calibration source that would be ready to use with any imager. Table 5.1 lists all the new LEDs, that are mounted on the spare source.

Test bench configuration We used a bench set up very similar to the one used by SkyDICE to measure beam maps; the LED-head is fixed in a central position, parallel to the z-axis of the test bench, then the NIST photodiode is moved around its xy plane at a fixed z-distance from the LED-head. To ensure a good signal to noise ratio, we chose a value of the input current I_{LED} corresponding to $\sim 80\%$ of the off-axis photodiodes saturation.

As described in the previous chapters, the temperatures of all devices were monitored during data taking. The LED temperature is measured with a PT1000 sensor, soldered on the LED radiator, complemented with a Lakeshore probe, located inside the radiator. Other temperatures control were performed at the backend box level, and from another Lakeshore-probe mounted inside the dark-enclosure. As we have seen before (see chapter 4), those temperatures are in good agreement even though, as we expect, a small temperature gradient exists from the LED-head and the dark-enclosure temperatures due to a not perfect thermal-insulation of our test bench.

To simplify the operations we decided to run at room temperature, without varying the temperature of the bench. The temperature range probed during data taking is smaller ($\sim$ 5℃) but representative of what can be measured in the SkyMapper dome over similar durations.

Dataset Since the DICE sources are installed almost permanently in the telescope enclosure, we wanted to test their behaviour over long durations (i.e. weeks, at least). As a consequence, we ran data taking session over 3 weeks, from 03/05 to 27/05 of 2013.

During these runs, we performed continuing flux measurements, using all LEDs at a specific input current. At the end of the run we obtained almost 37 small beam maps for each LED. In the end, every LED had been turned on for almost 24 hours in accumulated illumination beam. This value may be considered small compared to the average life time of a LED, but we have to keep in mind that the DICE LEDs are used only for the time of an exposure (generally < 1 min) during a flat-fielding session with SkyMapper (or MegaCam).

5.2 Stability Analysis

To reduce and analyse data obtained from the 3 weeks run, we implemented a pipeline to process the data sample. Before and after every beam map, the dark current was measured. Again, the interpolated linearly between dark current variations, and these interpolated values were subtracted from the original signal. At this stage, we found that the overall dispersion of the LED flux measurements, using only data uncorrected for temperature or LED current variations was about 5×10^{-3}, well above the target of 10^{-4}.

LED flux vs. temperature The spare head is equipped with LEDs of the same model as those which equip SkyDICE. However, as there are variations between the properties of LEDs of the same model, the first step is to study again the dependence of the LED fluxes as a function of temperature. The approach has already been described in the previous chapter, and is not discussed again here. We model the LED flux variations with a linear law:

$$\phi_{led} = a_0 \Delta T_{led} + \phi_0 \tag{5.1}$$

which is fit on the data. For all LEDs, we find that the flux varies linearly with temperature over the temperatures range tested.

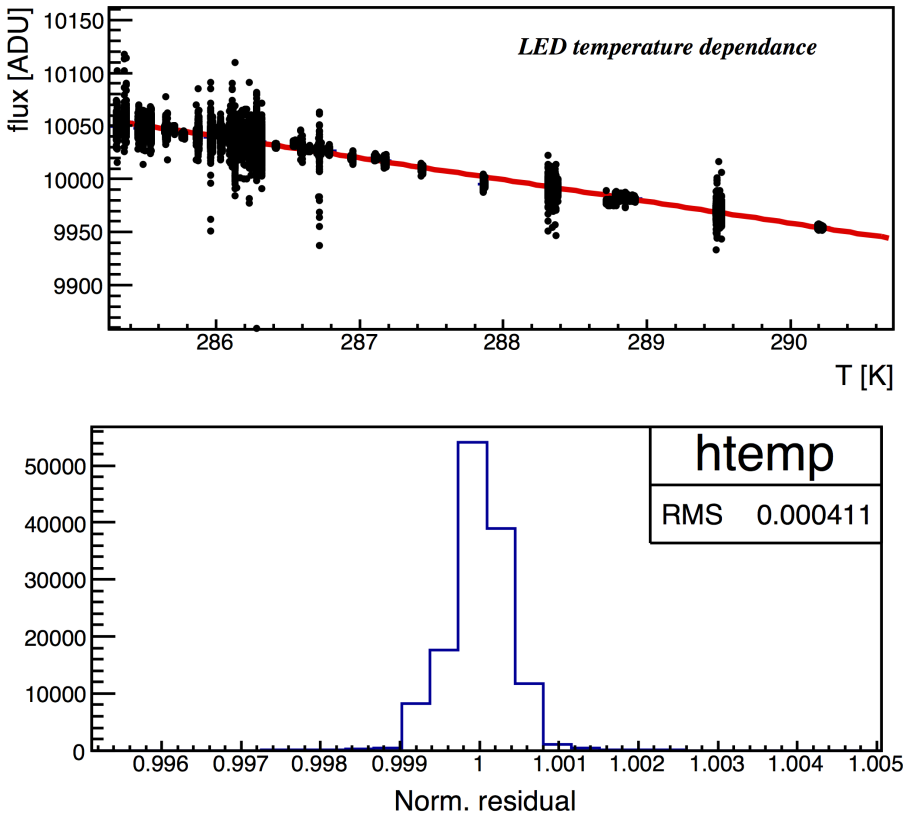

Figure 5.1: *(Up) - The plot shows the dark corrected flux contribution of the LED23 ($\langle\lambda_p\rangle$ = 464 nm), as a function of the temperature measured by the Lakeshore-probe. The response is linear over all range of measured temperatures. The flux variations are due to readout noise coming from the not perfect shielded Keithley-NIST connection and from electromagnetic interference generated inside the cable. (Bottom) - This figure shows the residual distribution from the linear law fit (red line). Here the RMS represents the relative uncertainties and its value is* $\sim 4 \cdot 10^{-4}$.

Figure 5.1 represents what was obtained for one of the 23 LEDs, LED23 with a $\langle\lambda_p\rangle$ centred at 463 nm. As we can see from the distribution of the residuals (bottom figure), the RMS is around $4 \cdot 10^{-4}$. The small variations of the flux are due to readout noise coming from the Keithley pico-ammeter NIST connection. We also discovered a small electromagnetic interference in the signal recorded by the Keithley.

Unfortunately, all LEDs are not as stable as LED23. Figure 5.2 shows the stability of all 23 LEDs. As can be seen, the average value is of about $1.6 \cdot 10^{-3}$. This value is not far from our target of 10^{-4} but is still disappointing. The temperature alone does not allow us to predict the variations of the source at the precision level we would like to attain.

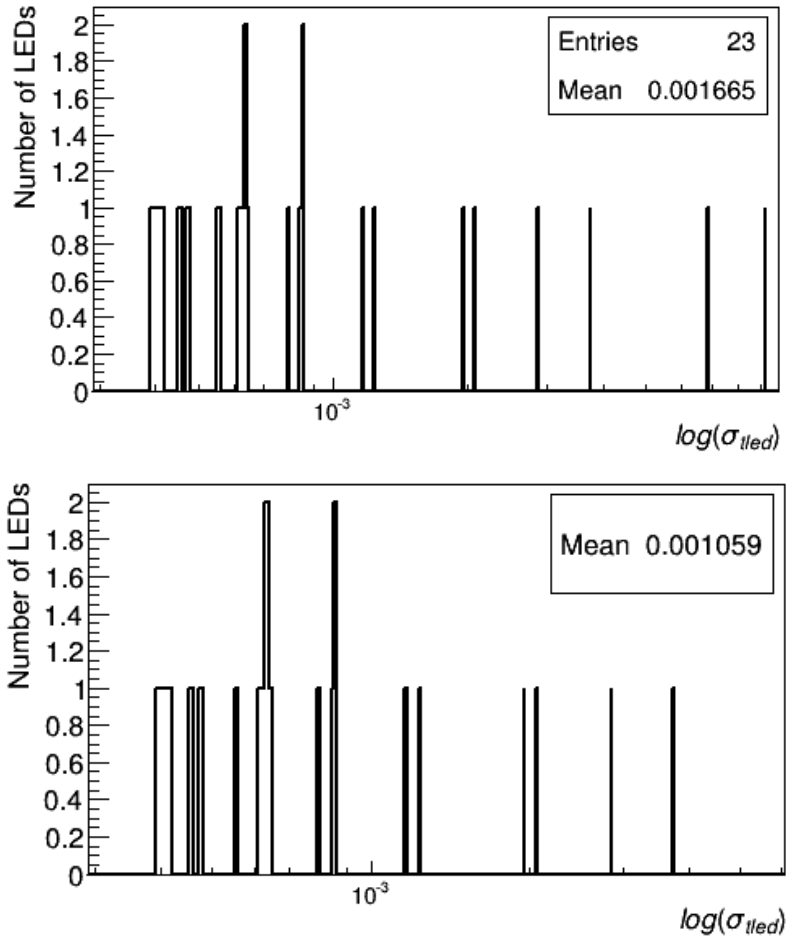

Figure 5.2: *The plot shows the dispersion of the flux when the flux follows a linear law only function of the T_{led}. The computed average value for all 23 LEDs is around $1.6 \cdot 10^{-3}$. The second plot is the same when we do not consider the worst two LEDs.*

5.2.1 Flux Variations versus backend Temperature

So, we need other observables to standardise our source. It is illuminating to take a look at figure 3.11 of chapter 3, which describes the circuit that generates the LED current. As we can see from that circuit, there are three main components that are sensitive to temperature variations: the DAC and ADC devices, the LED itself, and the load resistance R_L, directly connected with the DAC circuit, and linked to the LED forward voltage by the Ohm law $V_{led} = R_L \cdot I_{led}$.

Variations of temperature can cause small changes on the value of resistance R_L in the circuit that can directly affect the input current generated by the forward voltage V_{led}. If we call T_{be} the temperature of the backend electronics, T_{led} the LED temperature (the Lakeshore-probe measurement), and I_{led} the current that varies itself due to resistance R_L variations, then, we may insert all these new parameters T_{be} and V_{led} in our analysis and obtain a better model of the source fluctuations. The fact that backend electronics (and the voltage V_{led})

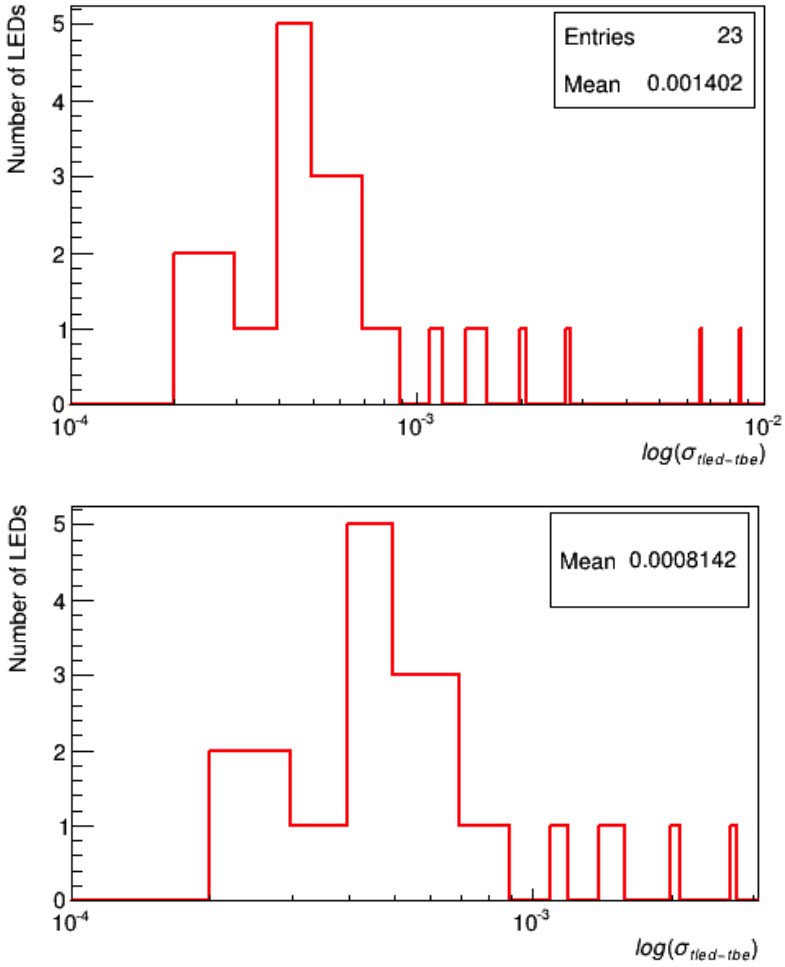

Figure 5.3: *The two histograms represent the distribution of dispersion for all 23 LEDs when we consider only the contribution from the temperature of LEDs T_{led} and the one from the backend electronics T_{be}. In the first one we considered all LEDs, while in the second one at the bottom, we eliminated the worst two LEDs: LED09 and LED24.*

suffers from a temperature dependence is already confirmed from measurements taken with the first generation of DICE, SnDICE.

Equation 5.1 contains only the T_{led} dependency of the LED flux. At first order, a simple way to study the backend temperature effect is to expand the relation 5.1 with a more complete model:

$$\phi^{mod}(T_{led}, T_{be}, V_{led}) = \phi_0 + a_0\Delta T_{led} + a_1\Delta T_{be} + a_2\Delta V_{led} \tag{5.2}$$

This last equation contains, all temperatures dependences T_{led}, T_{be}, and the voltage V_{led}, via the parameters ϕ_0 and a_0,a_1,a_2. As the previous model, we take into account not simply the parameter but its variations from the average measured value, so $\Delta T_{be} = T_{be} - \overline{T}_{be}$ and $\Delta V_{led} = V_{led} - \overline{V}_{led}$.

This new model 5.2 is fit on the data, minimising a standard χ^2 function, as follows:

$$\chi^2 = \sum_i \frac{[\phi_i^{NIST} - \phi^{mod}(T_{led}, T_{be}, V_{led})_i]^2}{\sigma_i^2} \tag{5.3}$$

where the sum is done over all the measurements. The ϕ_i^{NIST} are the NIST flux measurements, the ϕ^{mod} is the model describe in the equation 5.2, and σ is the error associated with measurements i. Minimise this sum is the goal of our test.

We divided the test in two steps: first, we only took into account the temperature variations, forgetting the voltage V_{led}. Then, we inserted both temperatures plus the voltage V_{led} into the fit.

5.2.2 T_{led} and T_{be} Fit

If we consider only the temperature read by the Lakeshore-probe, namely T_{led}, and the temperature of the backend electronics T_{be}, the equation above is simplified as follows:

$$\phi^{mod}(T_{led}, T_{be}) = \phi_0 + a_0 \Delta T_{led} + a_1 \Delta T_{be} \tag{5.4}$$

Figure 5.3 represents the stability obtained for each LED (i.e. the dispersion of the residuals around the law above). From the plot on the top of the figure we can see that 6 of the 23 LEDs are above the 10^{-3} limits with two, LED09 and LED24 almost at the 10^{-2}. We discuss just below the reason of that instability. If we discard this last two LEDs, we go down, from an average dispersion of 10^{-3} to a few 10^{-4}. To be more precise, we have a total of 17 LEDs with a value that is around the $5 \cdot 10^{-4}$ level.

5.2.3 T_{led}, T_{be} and V_{led} Fit

With the last result in mind we can go further and add the last parameter V_{led} in our model 5.2. Putting all parameters, T_{led}, T_{be} and V_{led} to see how better we can do from the value $\sim 8.1 \cdot 10^{-4}$ of the last fit.

Figure 5.4 shows the result of the χ^2 minimisation. As we can see, this time we get only 5 LEDs above the level of 10^{-3}, and if we eliminate the worst two (LED09 and LED24), we achieve an average value of $\sim 7 \cdot 10^{-4}$, which represent an improvement which is small if we consider the entire source, but is quite significant for a few LEDs.

5.2.4 The LED09 and LED24 instability

LED09 and LED24 display a different behaviour compared with the others LEDs. We decided to investigate this situation, in order to understand why these LEDs are significantly less stable than the others. reasons. We come out with two different possible explications.

The LED09 case

To understand what happens to the LED09 ($\langle \lambda_p \rangle = 763$ nm) we focus our attention on figure 5.5 that represents the time series of all monitored parameters during the run. What

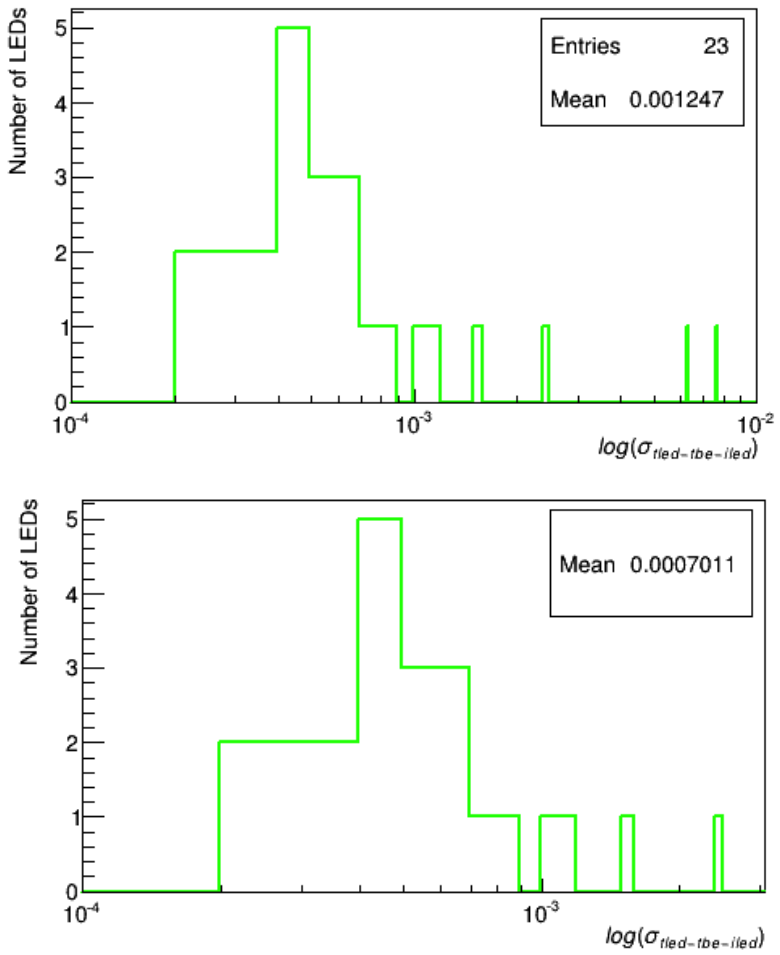

Figure 5.4: *The two figures show the distribution of the flux dispersion evaluated taking into account the temperatures T_{led}, T_{be} and the variations of the voltage V_{led}. In the figure on the top we put all LEDs where in the figure on the bottom we eliminated (as figure 5.3) the two worst LEDs, LED09 and LED24.*

is interesting is the unexpected jump of $\sim 2\%$ measured both by the NIST and the control photodiodes during the 4th day of measurements. This jump is not due to any variation of temperatures, nor to any backend control parameters (i.e., V_{ref} and V_{led}), as we can see from the plots on the centre of the figure where there is only a smooth decrease, the last bottom figures show where signals are only affected by an intrinsic fluctuation less than 10^{-5}. The only conclusion is that variation comes directly from the LED and probably is due to physical effects of the junction itself that constitutes the emission region.

A simple explanation could be a not perfect soldering between the LED and the circuit board, this latter causing a change of the parasitic resistance of the LED diode. Anyway, this kind of rapid LED variation is very rare, and moreover, as we can see from the next section §5.3, those variations are monitored by the off-axis control photodiode.

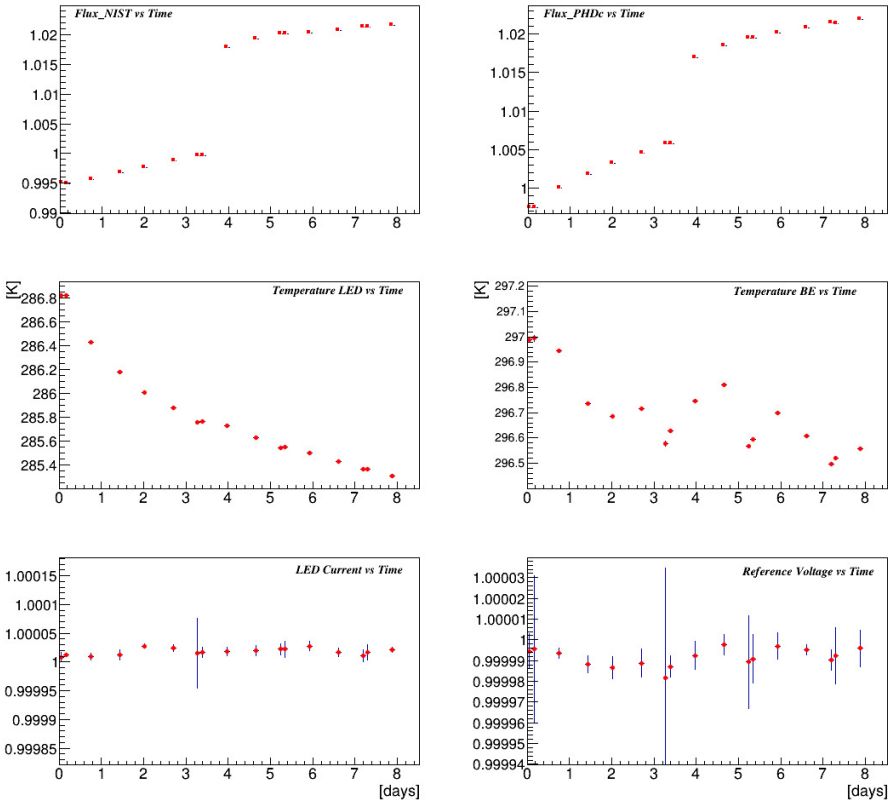

Figure 5.5: *Time series of all measured parameters of LED09. We can recognise the NIST flux, the photodiode flux, the LED and backend temperature and, finally, the LED current and the Voltage reference V_{ref} used to calculate the LED and backend temperature. All flux, current and voltage values are normalised to one.*

The LED24 case

The case of LED24 is different. To understand what happened we need again to take a look at figure 3.11. To explain the instability of the LED we need to show how the LED current generator works. Every LED has an input voltage V_{cc} of +7.5 V. When we set up a DAC value changing the I_{led} and hence the luminosity of the LED, we change the V_{led}. This value is applied at the boundaries of the load resistance R_L, but also affect the voltage applied on the transistor mounted between the LED and the R_L. The LED24 is an UV LED, with a $\lambda_{peak} = 342$ nm, and its threshold voltage is high being $\simeq 5$ V. Moreover, as its flux intensity is really faint, we need to impose an high voltage V_{led} to obtain a sufficient current LED flux. All these constrains lead to an instability of the I_{led} due to the fact that the transistor is not working in a saturated mode.

5.3 Flux Variations Control with Off-Axis Photodiodes

The linear model of the LED flux as a function of various temperatures gives good results for almost all LEDs. But we can also go one step forward, and use directly the LED flux measurements performed with the off-axis control photodiodes, in order to check directly the stability of LEDs flux. Mathematically, we model the LED flux variations as:

$$\phi^{mod}(V_{phd}, T_{be}) = \phi_0 + a_0 \Delta V_{phd} + a_1 \Delta T_{be} \tag{5.5}$$

This time we have only two parameters: the voltage V_{phd} related to the photodiode current I_{phd} by the simple law $V_{phd} = I_{led} \cdot R_L^{'}$ ($R_L^{'}$ is the load resistance for the current generator of the off-axis control photodiode), and the backend electronics temperature T_{be}. As discussed above, $\Delta V_{phd} = V_{phd} - \overline{V}_{phd}$, and $\Delta T_{be} = T_{be} - \overline{T}_{be}$.

Figure 5.6 shows the result obtained. The dispersion is around $5.8 \cdot 10^{-4}$ when we discard the worst three ones LED09, LED24 and this time LED08. This result is compatible with the one obtained using the LED model described in equation 5.2.

But what happened to LED08? Taking a look at its off-axis control photodiode we discovered no signal. Simply the photodiode was faulty and broken. For this LED we cannot use this model and we have to take the dispersion value computed with the LED source model 5.2.

5.3.1 Final Results

The final result from the flux analysis is well represented on figure 5.7. This plot shows flux dispersions σ_{flux} (computed over weeks of continuous data taking) for every LED, as a function of the wavelength.

In this figure we compare the raw dispersion (in black), with results coming from the two models discussed above (green is the LED model 5.2, and blue is the off-axis control photodiode model 5.5). We can see more clearly that for the majority of LEDs, the sigma is below the 10^{-3}. Moreover the best result coming from blue points where only three LEDs are expected to be above the 10^{-3} level. The behaviour of those three LEDs has been explained before in this chapter.

It important to say that these two different analysis paths represent also two completely different approach. The model described by the equation 5.2 is trying to directly model the LED source, using the dependence from the temperature and from the LED current, in the equation 5.5 we forget the source of light and we try to constrain the stability and so the uncertainties of the flux using instead the control photodiode current. However the two final results are totally in agreement showing that our DICE device is capable to achieve the stability level required for our calibration chain. Both approaches are complementary, and comparing them should even allow us to detect slow drifts of the source emission over the life of the instrument.

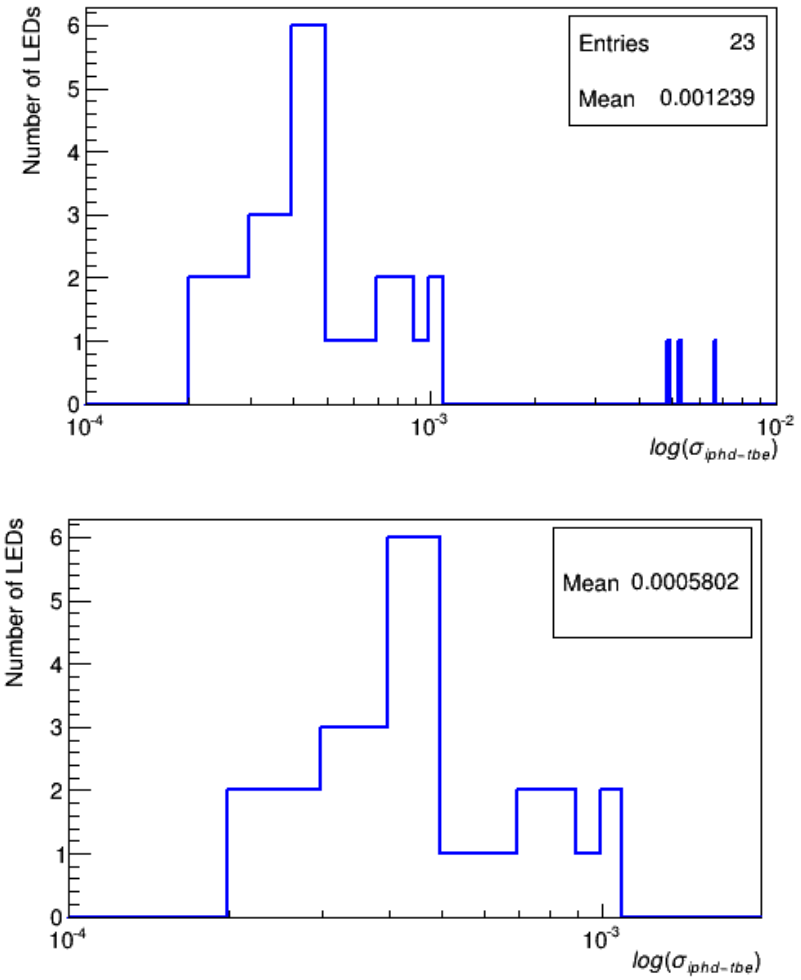

Figure 5.6: *Those two plots represent dispersion values calculated using the photodiode model 5.5. The plot at the bottom is the same distribution when we discarded the three worst LEDs: LED09, LED24 and LED08 because of its photodiode problem.*

5.4 Beam Uniformity Analysis

A last analysis was done to check the relative uniformity of LEDs beam in its central region. This kind of test is done using beam mini-maps collected during the stability run. Every maps contains only 9 points, with the central one chosen as a reference point. This central position is where we take different measurements at different time during the same run to check the stability of LEDs and of all the hardware set up used for the measurements.

The general method adopted to analyse this data is really simple: first of all we subtracted measured points from the NIST dark current. We normalise each single data point, using the average current obtained from the central position of every beam (this permits to absorb global variations of the LED flux). Finally, we histogram these normalised values. The RMS of that distribution represents an estimate of the map profile variation as a function

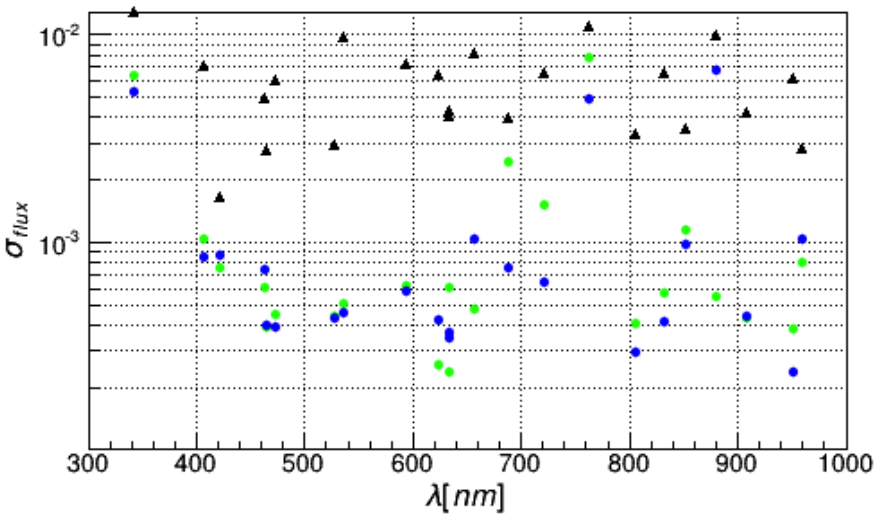

Figure 5.7: *This plot shows the final computed flux dispersion as a function of the wavelength. In particular we plotted the raw data (black diamond) versus the best result of the two different model. With green points the σ_{flux} using the LED source model describes by equation 5.2, and with blue points using the off-axis control photodiode model with equation 5.5.*

of temperature.

5.4.1 Results

Figure 5.8 shows the distribution of the relative flux dispersion for all the LEDs. In particular we obtained an average value below $3 \cdot 10^{-4}$ equivalent to results obtained with previous stability analysis in this chapter.

Finally, we have to stress in that case what we measured is not the absolute shape uniformity of the beam, but instead, it is a indicator of the relative uniformity of the beam shape during a typical run.

5.5 Conclusion

We have studied the stability of the source over very long durations. We have developed two different approaches to model and predict the LED flux variations as a function of time. Using both models, we have verified that we can control the source fluctuations with a precision of a few 10^{-4} for most LEDs. The beam maps also display an impressible stability of $\lesssim 5\ 10^{-4}$. As a conclusion, we believe we are well within the informal stability requirements that were drawn before DICE design studies were started.

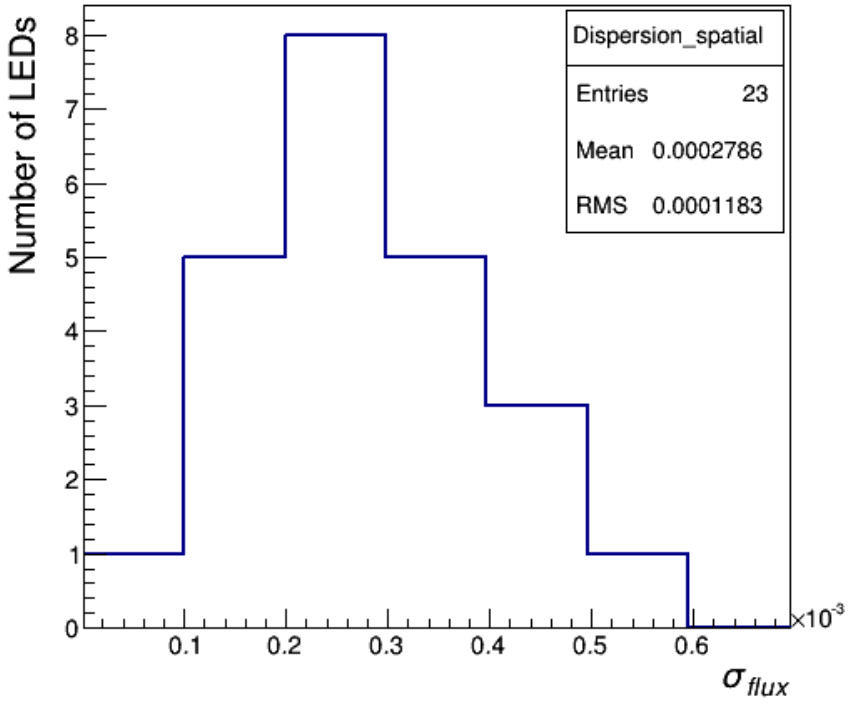

Figure 5.8: *This histogram shows the average flux dispersion for every LED beam map, normalised by its reference central point. Even in that case the distribution is centred around* $2.7 \cdot 10^{-4}$.

Chapter 6

Spectrophotometric Calibration of SkyDICE

Our goal is now to build a smooth model $\hat{S}(\lambda, T, \boldsymbol{u})$ of the LEDs true spectral intensity $\mathcal{S}(\lambda, T, \boldsymbol{u})$, valid at least in the temperature range $-5℃ < T < +10℃$, which is typical of what is measured in most telescope enclosures. Along with this model, we build an uncertainty model, that accounts for the finite precision of the test bench measurements and the finite stability of the source. These two ingredients will then allow us to predict, with a known accuracy, the amount of calibration light delivered by the source, for any real calibration exposure, taken under any condition.

In the following of this chapter, we describe how the test bench measurements are combined in to build such a model. The next section (§6.1) presents how we combine the test bench measurements presented in the last chapter to build the spectral intensity model $\hat{S}(\lambda, T)$ of each LED. We have tested the modelling technique on series of simulated test bench data on we present the results in §6.3. Then, we apply it on the SkyDICE calibration data and derive a spectrophotometric model of the source (§6.4). This dataset will be used in the last chapter to constrain the SkyMapper passbands. Finally, in §4.6, we say a word on how we will propagate the test bench systematics in the subsequent analyses.

6.1 Modelling Technique

We choose to develop the shape of the LED spectra on a basis of two-dimensional B-splines:

$$\hat{S}(\lambda, T) = \sum_p \theta_p B_p(\lambda, T) \tag{6.1}$$

where the $B_p(\lambda, T)$ functions are classically built as the product of one-dimensional-splines in the λ and T directions. For this work, we choose to use splines of order 3 to describe the wavelength variations, and splines of order 2 to model the temperature variations: $B_p(\lambda, T) \equiv B_{ij}(\lambda, T) = B_i^{(3)}(\lambda) \times B_j^{(2)}(T)$.

The model above is linear, and can easily be fit on the spectral data gathered on the spectroscopic test bench described in chapter 4. There is a complication, however, which is

that the absolute transmission of the monochromator is not known with a good precision. In chapter 4 we have determined its relative variations as a function of wavelength. However, we do not know its absolute scale with certainty. In fact, we suspect that it varies slightly with each spectrum, as there is a small uncertainty in the repositioning of the source with respect to the entrance slit of the monochromator. This uncertainty affects primarily the vertical direction, hence the absolute normalisation of the spectrum.

As a consequence, we would like to fit for the (unknown) normalisation f_s of each spectrum measurement s. This means that the only piece of information we extract from the spectroscopic measurements is the spectrum *shape*, and not the spectrum normalisation. Our model of the photodiode current (equation 4.3 in chapter 4) therefore becomes:

$$I_{|\text{spec}} = f_s \times \sum_p \theta_p \ [\eta(\lambda) \cdot T_m(\lambda) \cdot B_p \otimes W_m(\lambda, T)] \tag{6.2}$$

Since the θ_p's and the f_s's are degenerate, we impose that the absolute normalisation of the $\hat{S}$ models is determined by the photometric measurements (performed without a monochromator). In practice, this is done by adding the following term to the fit χ^2:

$$\sum_s w_i \cdot \left(\mathcal{J}\left(T_s\right) - \int \eta(\lambda) \cdot \hat{S}(\lambda, T_s)\ d\lambda \right)^2 \tag{6.3}$$

where $\mathcal{J}(T)$ is the photocurrent measured with the NIST photodiode at a reference position, as defined in chapter 4.

With this approach, the uncertainty affecting the monochromator transmission is entirely absorbed, and the normalisation of the LED spectral intensity models is set exclusively by the photometric measurements. We estimate of the LED spectral intensities by fitting the model above on the photodiode current measurements, and then marginalising on the f_s nuisance parameters.

6.2 Implementation Details

As described above, we develop the model on a basis of B-splines. In wavelength, we grid the space with one node every 2-nm, which corresponds to the resolution of the monochromator. In temperature, we use 2-order splines (i.e. piecewise linear functions) with 3 nodes on the $0℃ < T < 25℃$ temperature range. Depending on the extension of the spectrum, this means that the model is a function of about 500 parameters.

For each LED, we first fit the photometric data (i.e. the total flux variation as a function of T) with a linear law: $\mathcal{J}(T) = \alpha_{\text{led}}(T - T_0) + \beta_{\text{led}}$ (following the notations of chapter 4). Then, we fit the spectral model by minimising the χ^2:

$$\chi^2 = \sum_s \sum_i \left(I_{si|\text{spec}}(f_s, \theta) - y_{si} \right)^2 + \sum_s w_s \left(\mathcal{J}\left(T_s\right) - \int \eta(\lambda) \cdot \hat{S}(\lambda, T_s)\ d\lambda \right)^2 \tag{6.4}$$

as a function of the f_s and θ parameters. Here, the s index runs over the spectra, the i index, over the measurements for each spectrum s; the y_{si}'s are the flux measurements registered by

the bench, $I_{si|\mathrm{spec}}(f_s, \theta)$ is the corresponding prediction using the spectral intensity model. The second part of the χ^2 ensures that the normalisation of the spectral intensity model, $\hat{S}(\lambda, T)$, follows what is measured on the photometric test bench.

As the model is non-linear, the fit is linearised at each minimisation step. We use classically the Newton-Raphson method to predict the next minimisation direction, combined at each step with the Brent algorithm to check the amplitude of the minimisation step along that direction. The minimisation is stopped when the χ^2 has decreased by less than 0.01 points at the last iteration. On simulated data, the fit generally converges in a small number of steps (typically 5 steps). On real data, the procedure is about twice as long, as we use an outlier rejection procedure.

The model is implemented in `C++`, and uses some of the libraries developed for the SNLS project, in particular, easy-to-use bindings to the `BLAS` and `LAPACK` linear algebra libraries. On a standard laptop, a typical fit takes less than 30 seconds on simulated data, and less than 1 minute on real data.

6.3 Tests on Simulated Data

As the approach described above is somewhat complex, and relies on a non-linear fit, it has been tested on simulated data. These simulations will be used again in chapter 8 to test another method developed in this thesis, to constrain the telescope passbands from series of SkyDICE observations.

6.3.1 Simulated Dataset

In this simulation, we describe the LED spectra as gaussian functions of width $\sigma \sim 12$-nm. We simulate a linear evolution of the spectrum wavelength as a function of temperature, with a coefficient of $d\lambda_{\max}/dT \sim 1$Å/℃. This value corresponds to the highest coefficients observed for the SkyDICE LEDs. We also adopt a high value for the LED flux variation as a function of temperature (1% / ℃).

For the monochromator transmission, we adopt the model described in chapter 4 and the values determined for each grating, listed in table 4.7. The (normalised) transmissions of each grating are shown on figure 4.28. The monochromator spectral response is modelled as a triangle function of FWHM ~ 2 nm, and the simulated (gaussian) spectra are convolved into this window, following equation 4.3. To simulate the photocurrent measurements recorded on the bench, we use the efficiency curve of the NIST photodiode. For the noise level, we adopt a value typically observed on test bench measurements, of about ~ 0.03 pA.

For each LED, we simulate about 15 spectra and 10 mini-maps, taken in the temperature range $0℃ < T < 25℃$. This corresponds to the average number of spectra and maps actually gathered on the test bench during the April 2011 calibration runs. Typical simulated spectra are shown on figure 6.1.

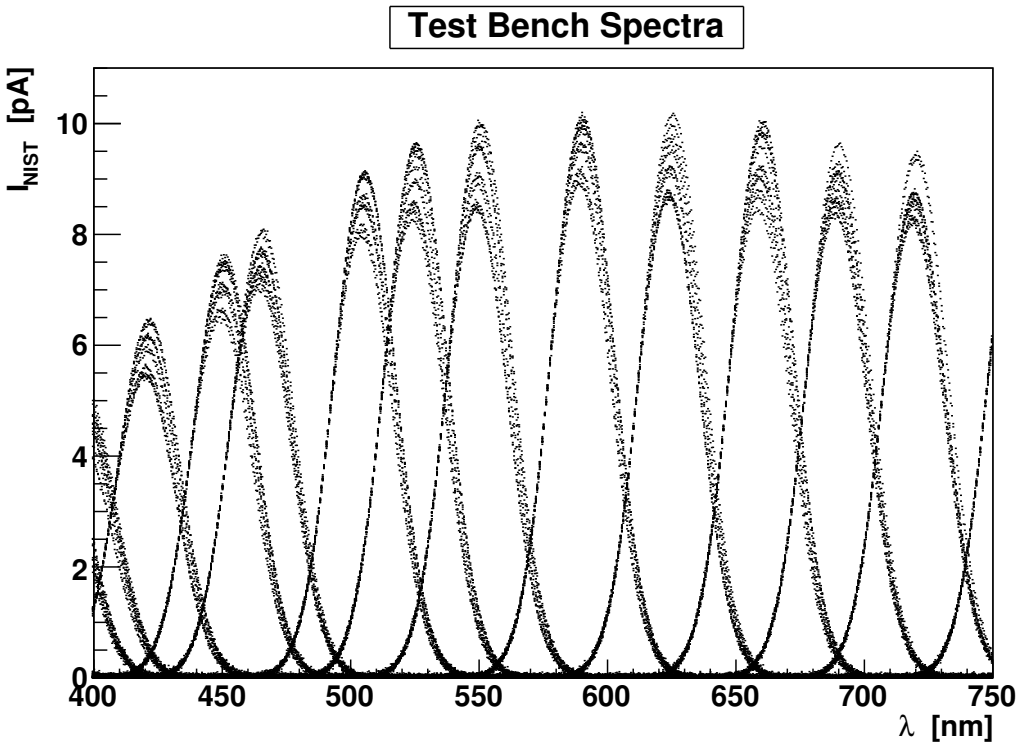

Figure 6.1: *Synthetic spectra taken as an input for the model.*

6.3.2 Fitting the Spectral Intensity Model on Simulated Data

Each LED data has been fit following the procedure described above. Figure 6.2 shows one model in the $T - \lambda$ plane, as well as the comparison with real data. Not surprisingly, the residuals do not show any significant feature.

A better check, is to see how the model does reproduce an independent spectral dataset for the same LED. The results are shown on figure (??). Again, we do not see any significant feature.

We also tried to see whether there is any bias affecting the recalibration parameters f. Indeed, this would affect the model normalisation, in a possibly temperature-dependent way, and this could affect the final normalisation of the LED head and the

We also tried to see whether there is any bias affecting the recalibration parameters f. Indeed, this would affect the model normalisation, in a possibly temperature-dependent way, and this could affect the final normalisation of the LED head and the telescope. Figure 6.3 shows the estimates of the f-parameters as a function of temperature. Again, the dispersion small, and no trend can be seen as a function of the temperature.

Finally, as we will see in chapter 8, these estimates of the LED spectral intensity $\hat{S}(\lambda, T)$ will be used to predict the broadband flux registered on the focal plane of the imager being calibration. A last important check is therefore to see how the true broadband flux, computed from the true spectral intensity compares with the synthetic broadband flux, computed from

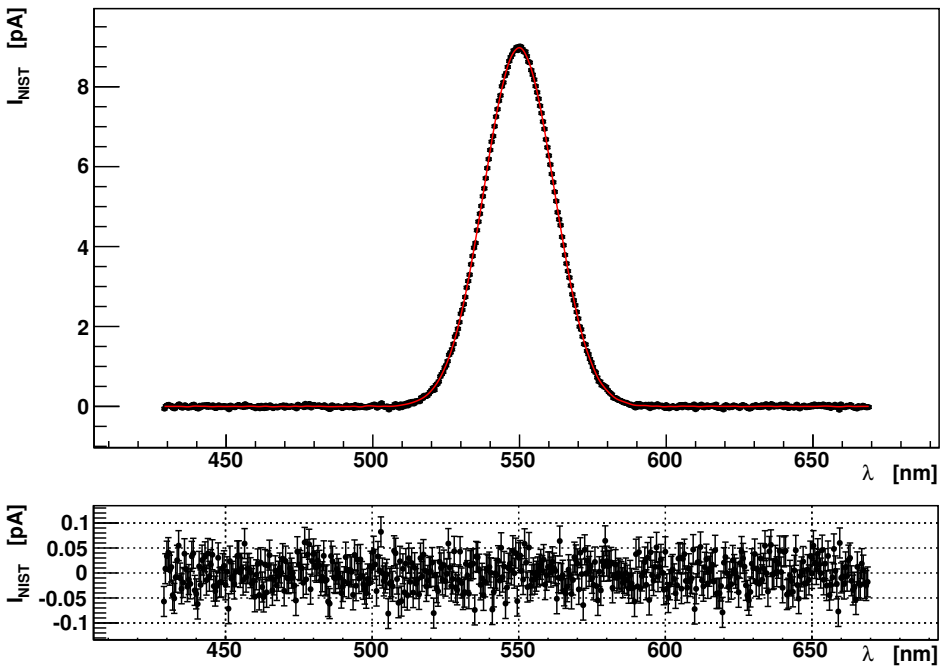

Figure 6.2: *Synthetic spectra taken as an input for the model.*

the estimated LED spectral intensity model. This is shown on figure (??). The error bars are the propagation of the model error estimates. As can be seen, the estimated spectral intensity models will allow us to estimate the broadband fluxes with typical uncertainties of about (xx %).

6.4 Spectrophotometric Calibration of SkyDICE

We calibrate the SkyDICE LEDs following the procedure that has been exposed above. The main difference between the real and simulated data, comes from the fact that due to the deficient shielding of the BNC connection between the NIST photodiode and the pico-ammeter, the level of noise affecting the data varies with time. One observes bursts of noise, as seen on figure 6.4, and also slow variations of the noise level, from one spectrum to another. We have not been able to locate the exact source of noise. However, its level has been very significantly reduced once we replaced the faulty connection between the photodiode and the pico-ammeter.

The noise level we infer from the repeated measurements performed with the pico-ammeter is smaller than what can be derived from the dispersion of nearby spectrum samples. As a consequence, the noise level was re-determined by fitting locally a 2-degree polynomial on a 20-nm wide sliding window, and by requesting that the local fit χ^2 be 1. Figure (??)

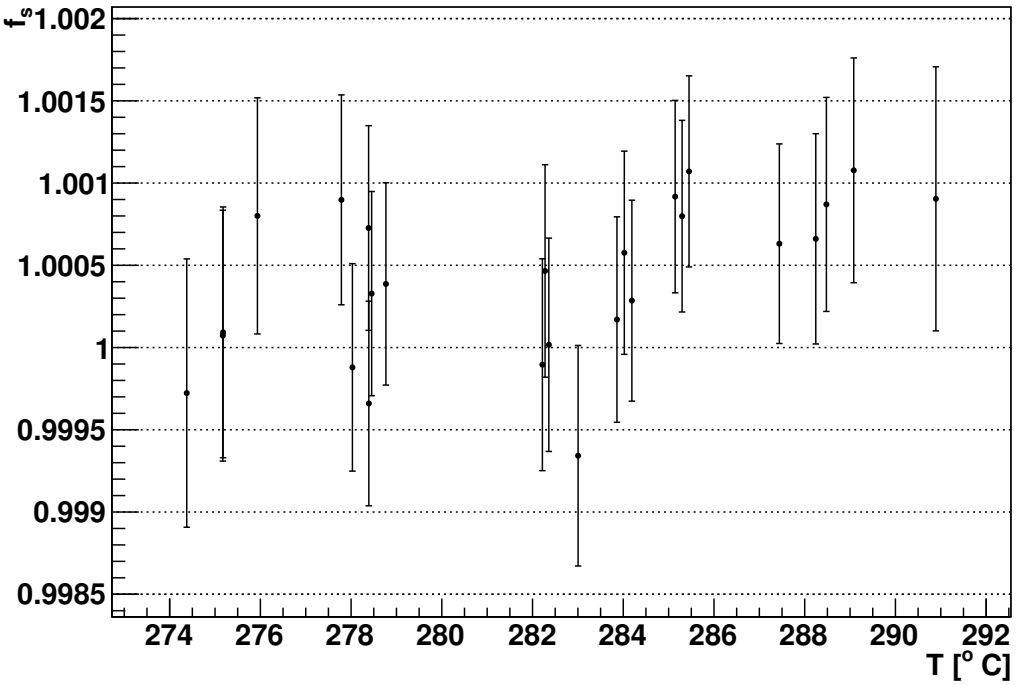

Figure 6.3: *Recalibration parameters f_s of all the spectra that were taken for one single LED. For some LEDs, such as this one, one can measure a small residual dependency as a function of temperature.*

shows the noise difference.

6.5 Systematics

The LED spectral intensity models $\hat{S}(\lambda, T)$ derived in this chapter are affected by the systematics related to the calibration of the test bench itself. These latter uncertainties are discussed in §4.6 of chapter 4. Obvious examples are the wavelength calibration of the monochromator, or the finite precision of our determination of the monochromator transmission. They are all listed in table 4.7. As any test bench error may affect our calibration of the SkyMapper passbands, we must propagate these systematics through the analysis.

To do so, we have to compute the impact of each systematic error on the estimated LED spectral intensity ($\hat{S}$). The most direct way to do so, is to compute the derivatives of the $\boldsymbol{\theta}_{\text{led}}$ parameters as a function of each test bench systematic $\boldsymbol{\eta}_b$:

$$\mathbf{H}_{\text{led}} \equiv \frac{\partial \boldsymbol{\theta}}{\partial \boldsymbol{\eta}_b} \tag{6.5}$$

and later use these derivatives to propagate the bench uncertainties to $\hat{S}$, using the standard

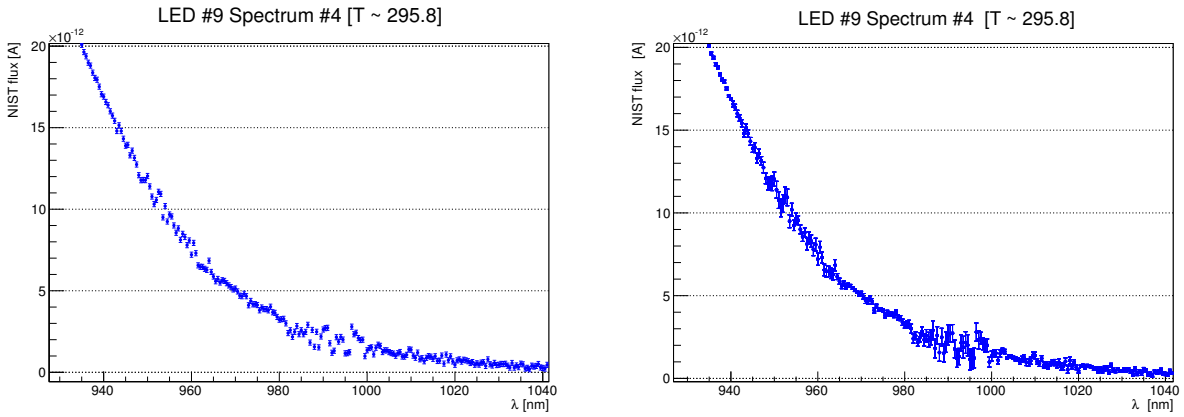

Figure 6.4: *A spectrum affected by a burst of noise. Before and after recomputing the errors.*

error propagation techniques.

In practice, the $\mathbf{H}_{\text{led}}$ matrix is determined in a straightforward way, by shifting in turn each bench systematic, refitting the model, and then computing numerically the corresponding derivatives $\partial\theta_p/\partial\eta_q$. Determining the model along with its derivatives is somewhat longer (5 to 7 minutes per LED), but this has to be done only once, after each recalibration.

As an illustration, we show the impact of a wavelength shift of 1-nm on the monochromator calibration (figure 6.6), and the impact of a small modification of the NIST response (figure 6.7), computed at first order, using the derivatives of the model: $\delta\hat{S} = \mathbf{H}_{\text{led}} \cdot \delta\boldsymbol{\eta}_b$.

Note that the bench systematics induce correlated uncertainties on the various spectral intensity estimates, $\hat{S}_{\text{led}}(\lambda, T)$. As a consequence they will also induce correlated uncertainties on our determinations of the imager passbands (see chapter 8). For example, a systematic error in the wavelength calibration of the monochromator will shift our determinations of the filter fronts; a systematic error in the NIST photodiode efficiency will bias the relative calibration of the passbands. This is the reason why we propagate these systematics as carefully as possible. As we will see in chapter 8 this technique allows us to account for all these correlations automatically.

6.6 Conclusion

We have shown that it is possible to build smooth models of the LED spectral intensities by combining in an optimal way the photometric and spectroscopic bench data. These models account for the LED spectral dependence as a function of temperature. They are normalised, in the sense that their integral is equal to the radiant intensity of the LEDs (in watt/sr). As we will see, these models will allow us to predict the broadband flux measured by the imager, in a large temperature range.

Along with each model, we determine a covariance matrix, that allows us to account for the finite precision of the bench measurements. We also compute the model derivatives as a function of the identified test bench systematics. All this material will be used in chapter 8

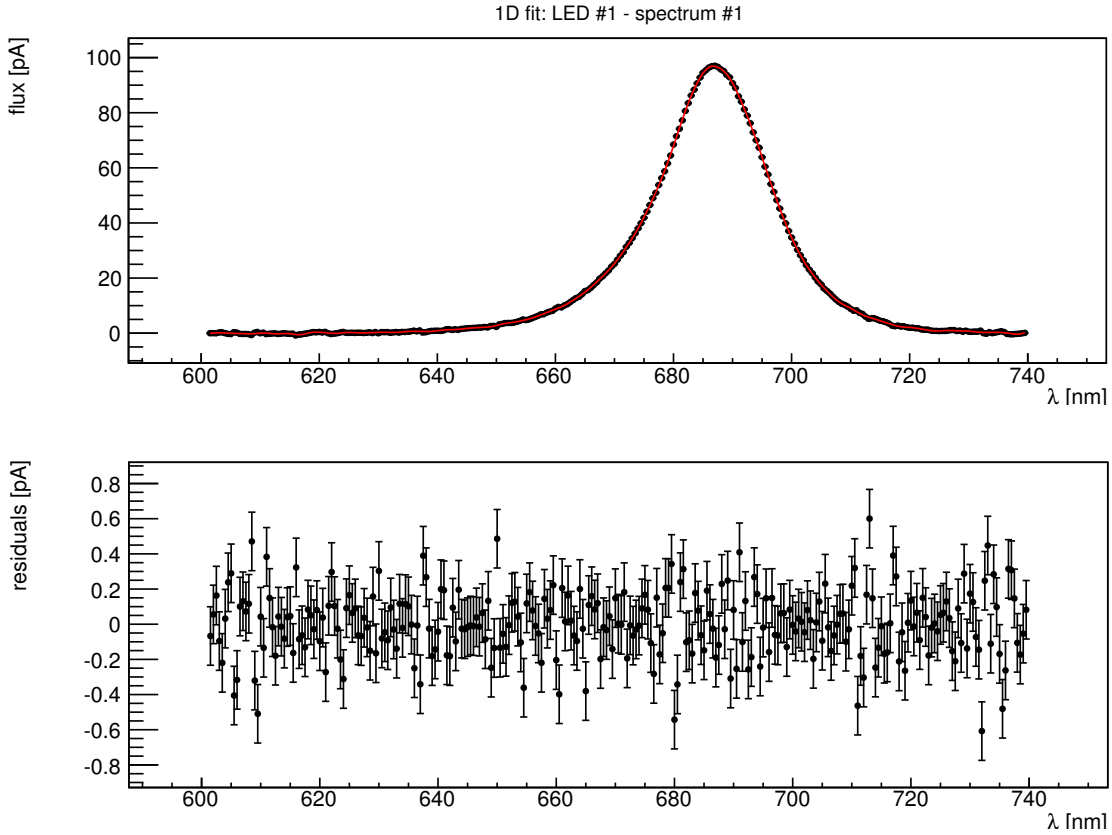

Figure 6.5: *Fit of a SkyDICE spectrum (+residuals).*

for the study of the SkyMapper passbands.s

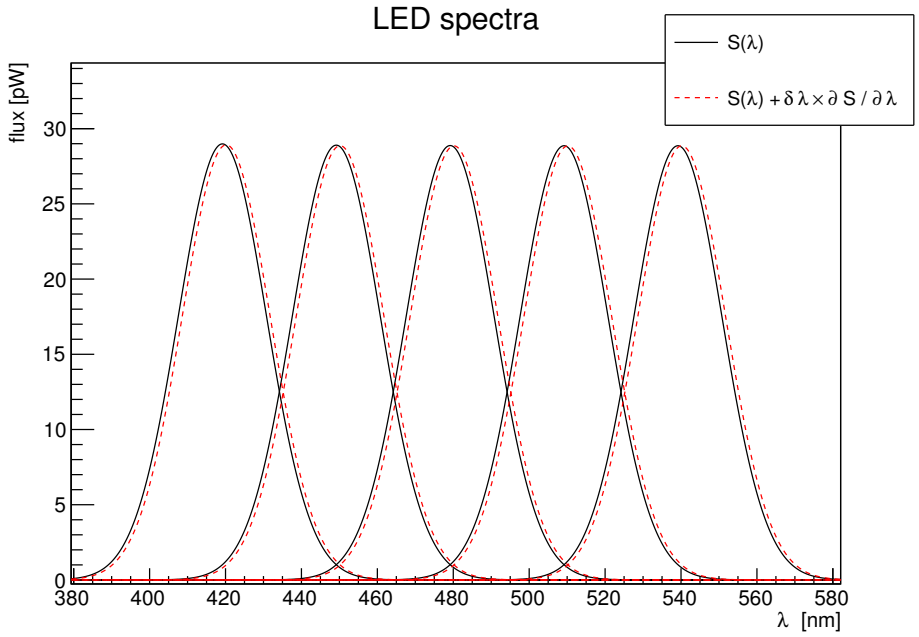

Figure 6.6: *Reconstructed LED spectra (from simulated data) (black). Effect of a 1-nm error on the monochromator calibration, computed using the model derivatives w.r.t. the bench calibration systematics (dashed red line).*

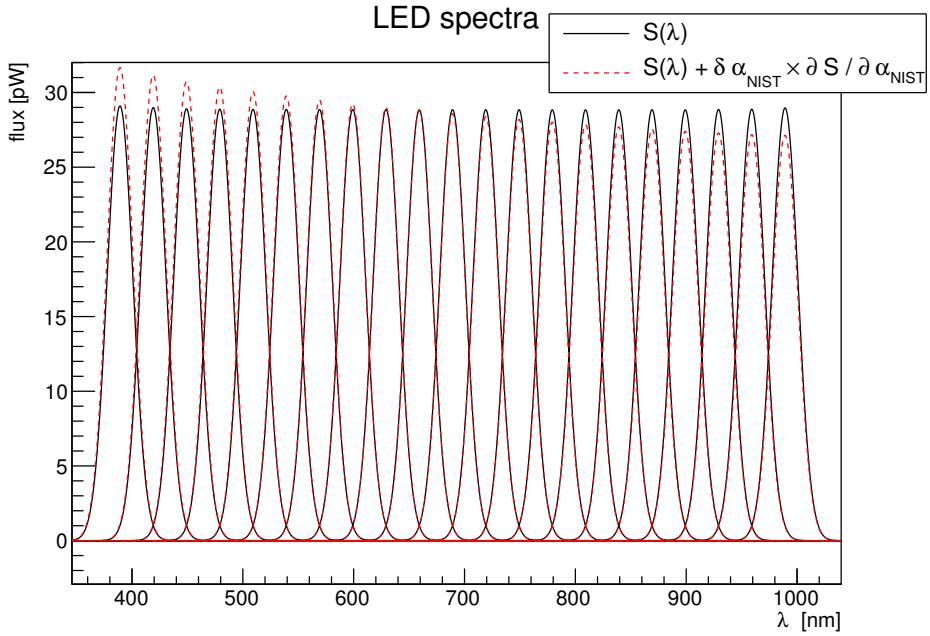

Figure 6.7: *Recomputed LED spectra (from simulated data) (black). Effect on the reconstructed spectra of a colour error in the determination of the NIST photodiode efficiency (dashed red).*

Chapter 7

SkyDICE Commissioning and First Data

In this chapter we discuss the first data obtained at the SkyMapper telescope. In section §7.1 and §7.2, we illustrate the physical installation of the SkyDICE calibrator inside the enclosure of the telescope, then in section §7.3 we describe the interface of the SkyDICE DAQ with the telescope DAQ. In section §7.4, we give details on the alignment protocol used to centre the SkyDICE beam in the focal plane of the telescope. Then, in section §7.5, we describe all the data taken during the June-July 2012. Finally, in sections §7.6.3, §7.6.4 and §7.6.2, we illustrate preliminary results of SkyMapper filters transmission, the study of the possible filter light leaks, and a study of the average illumination of the telescope enclosure.

7.1 *pre*-Test

During the summer 2012, the team went to the Siding Spring Observatory to install the SkyDICE system inside the enclosure of the SkyMapper telescope.

Before the installation, we needed to evaluate the integrity of the whole hardware and software components of the SkyDICE calibrator necessary to its installation after its arrival at the observatory. We mounted the whole system in a technical room close to the telescope following the installation plan shown on figure 7.1 and 7.4. The *pre*-test has been done during the first two days. We can divide it in four main checks:

- We tested the PC104 and software interface to the LED-head as well as the four motors.
- We checked all LED sources at different input current I_{led}.
- We mounted the LED-head on metallic support and we tested the correct functionality of xy motors, the artificial planet and the lens focus motors.
- We tested the alignment and the intensity of the artificial planet using a target put at different distances.

We repeated this test different times to ensure the repeatability of the whole system. After that we proceeded with the physical installation of the SkyDICE calibrator.

7.2 SkyDICE Installation

In this section we describe the installation of the SkyDICE LED-head, of the CLAP system and of the electronics of control necessary to interface the apparatus with the telescope. All aspects of installation had been discussed a few months earlier, with the team based at the Siding Spring Observatory and at the Stromlo Observatory (both observatories are part of the Australian National University[1]). Preliminary measurements of the dome and telescope dimensions had been taken during a previous visit to the observatory on 2011 by N. Regnault and R. Pain of the LPNHE laboratory.

7.2.1 LED-head Installation

The plan that our team followed is represented on figure 7.1. This diagram is divided in two main parts: the LED-head and motors, and the unit of control composed by the backend box, the PC104 and the RPC (remote power control), that interfaces the whole system with the local network of the observatory.

In agreement with the SkyMapper team, we decided to fix the LED-head support to one of the major metal arch of the telescope enclosure, close to the dome aperture. This is was the best solution to obtain a mechanical stability for the whole system and to maximise the clearance between the instrument and the telescope mount during standard operations. The device was fixed at 60° from the zenith, and about 2.3 meters from the ground. With this angle we have a distance between the telescope and the illumination system always larger than 0.2 meters. Furthermore, we may scan the whole mirror without having to push the telescope further than 75° from zenith. Finally, to fix the LED-head on the metal arch we used a set of modular ELCOM© bars, represented on the left side of figure 7.2. This permits to easily set the correct position and to ensure a stable installation. Figure 7.3 shows two pictures of the LED-head at the end of the installation process.

With this solution the average LED-head distance from the primary mirror is ~ 3 meters. Figure 7.2 on the right shows the CAD drawing of the LED-head and the telescope, and at the top of the LED-head we can recognise the backend box installed close to it.

Then, the motor controllers, the PC104 for the LED-head and the RPC unit (remote power control unit), have been mounted below the aperture of the dome (as shown on figure 7.2 on the right), in a secure position and covered with a black painted mask that eliminates any possible leakage of light from the control unit.

7.2.2 CLAP Installation

After the LED-head and its unit of control, we installed the CLAP device close to the primary mirror, as shown on the diagram of figure 7.4). As described in chapter 3, the CLAP is used

[1] see http://rsaa.anu.edu.au/

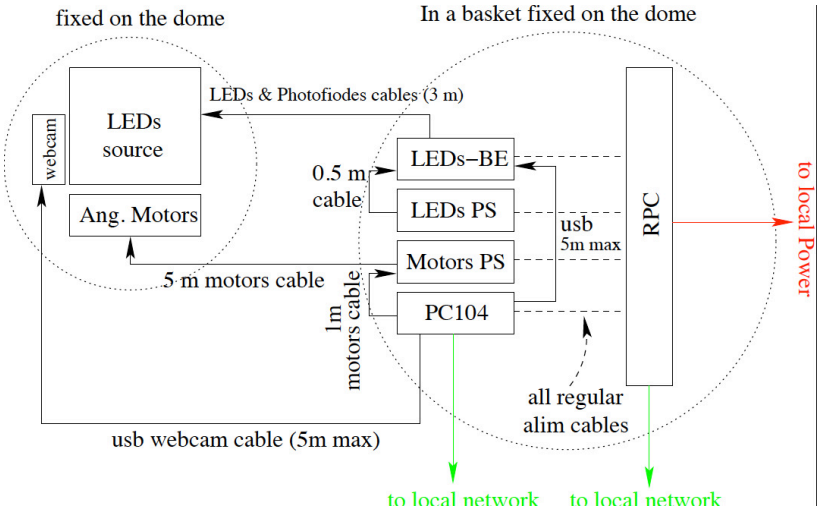

Figure 7.1: *The figure shows the SkyDICE installation diagram for the LED-head and the units of control.*

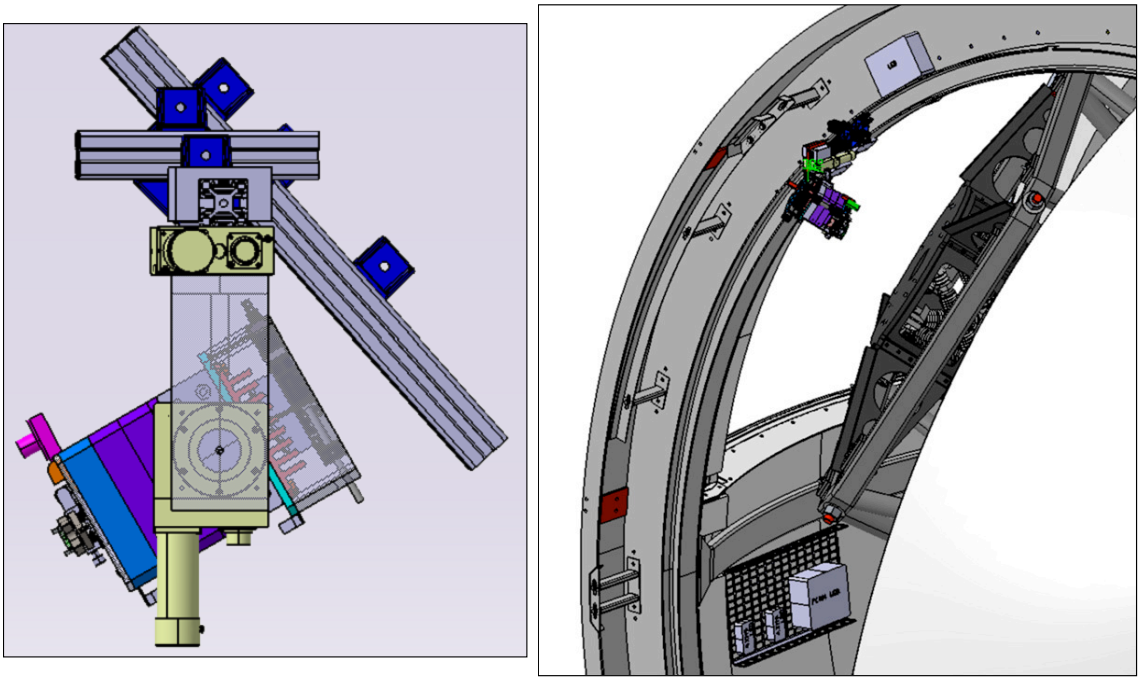

Figure 7.2: *(Left) - Particular of the SkyDICE mounting system used to fix the device on the telescope's enclosure. he mount is attached to a structure made of* 3 *ELCOM© bars, each of them fixed on three points. (Right) - SkyDICE is placed at* 60° *from zenith. We can recognise the backend box at the top of the device and all components mounted below the dome aperture.*

Figure 7.3: *The pictures show the SkyDICE LED-head attached to the main arch of the SkyMapper dome at the end of its installation in June 2012.*

as an external sensor to monitor the flux that hits the primary mirror. This allows one to have a strong feedback on our measurements and to inter-calibrate the beam flux.

The mirror CLAP has been placed at a distance of ~ 0.05 m from the primary mirror. Since the spot generated by the LED beams is $\sim 0.3 - 0.35$ m wide, at that distance from the primary we are able to illuminate simultaneously both the CLAP and the mirror of the telescope. We mounted the CLAP to a metallic support, made of two ELCOM bars fixed on the telescope mechanical structure. All support and CLAP height is lower than the mirror protection.

The backend unit box, the power supply, the PC104 and the RPC unit have been fixed inside one of the arms of the azimuthal mount as shown on the top of figure 7.5. This allow us to eliminate any problems coming from electronics interferences and from any kind of light pollution.

Originally the idea was also to install a twin CLAP close to filters box; this project has been postpone due to technical difficulties. Figure 7.5 on the bottom shows the CLAP after installation, we can recognise the photodiode window and, on the left side of the picture, a fraction of the primary mirror.

7.3 SkyDICE - SkyMapper DAQ interface

After these operations we went on to configure the remote control of the whole system and its DAQ with the CICADA/TAROS unit. This is used to control the telescope and to take

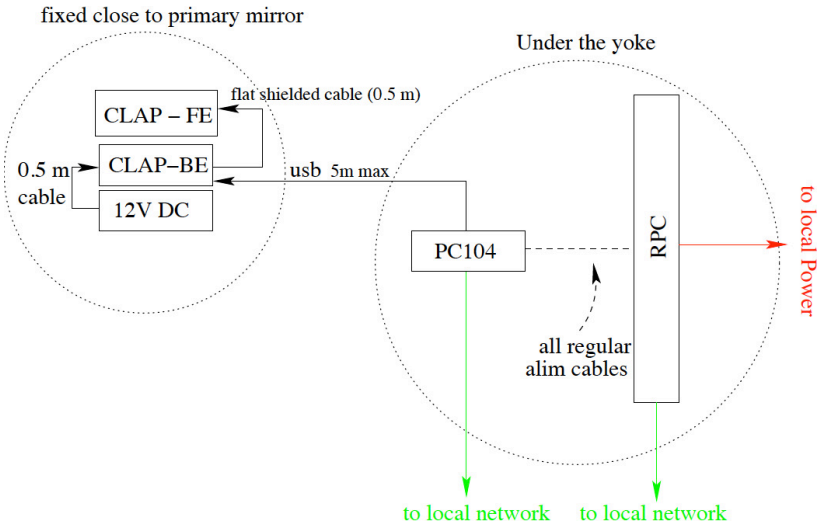

Figure 7.4: *The installation diagram for the CLAP system.*

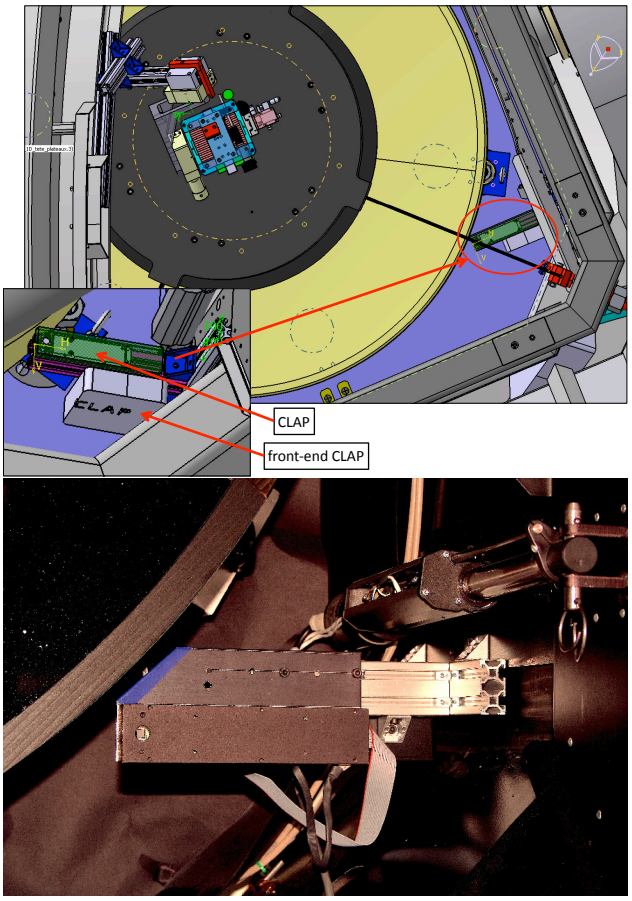

Figure 7.5: *A zoom of the CLAP installed in the mirror support system. We can recognise the small hole of the CLAP photodiode, and on the left a part of the primary mirror.*

images. This step is necessary to combine a reliable and stable calibration system with the possibility to monitor on real-time and for long durations the *telescope + camera*. To do that we needed a robust remote control interface to access the SkyDICE control system and the telescope functions during the operation.

First we installed the RPC system and the two PC104 ethernet interfaces within the main network of the observatory using fixed IPs. In a first attempt to install the network we adopted a wireless solution to eliminate problems with ethernet cable. This issue came out because all the dome is physically detached from the reinforced concrete where the telescope mount is fixed, that means every cable has to pass from the central column and has to have the proper length to avoid distortions during operations. The disadvantage of using wireless solutions is a narrower pass band that permits only $\sim 1,5-2$ MB/s.

After the network connection was established, we installed the software interface and the main command scripts, written mainly by L. Le Guillou and myself, on the PC104s and inside the main server of the Stromlo Observatory, where physically the computing and controlling centre is located. In that operation we have been remotely helped by the software team of the Stromlo Observatory. Once installed, we were able to control the system remotely, takes images and monitor all operations between the telescope and the SkyDICE device.

7.3.1 SkyDICE - SkyMapper Remote Protocol

The protocol used to communicate between SkyDICE, the CLAP and the SkyMapper DAQ is XML-RPC, a simple, open, text-based network protocol, implemented in many different open source libraries. Communication between devices and the CICADA/TAROS system works as follow: (1) - a request is initiated by the client (CICADA), which sends a message to the LED-head or the CLAP PC104s to execute a command. (2) - the PC104 executes the command. (3) - a return response is sent to the client; this can either be a status code or status code plus data. All commands are always initiated by the SkyMapper CICADA/TAROS system.

7.3.2 SkyDICE Operation Mode

During a typical session SkyDICE can be work in four mode:

Silent in that mode LEDs are off and the LED-head is in a fixed position. The SkyDICE control channels (LED, off-axis photodiodes, CLAP current and temperatures) are monitored. This mode is used to check the stability of the electronics, and to perform measurements of the control photodiodes and CLAP dark current.

Planet exposures are being taken with one of the planet LEDs on. This mode is used to align the optical axis between the SkyDICE and telescope. In this mode we can also perform ghosts study of the telescope optical elements.

Shutter the telescope is illuminated with one of the 24 LEDs. The a sequence of exposure of various durations are taken. In this mode, the duration of the CCD illumination is

determined with the telescope shutter. Taking data in shutter mode follows the time sequence describe on figure 7.6. Notice that the telescope and SkyDICE must be aligned.

E-shutter same of *shutter* except that the exposure time is determined by the illumination system. A specific LED is turned on just after the shutter has been opened, and turned off just before the shutter is closed. This mode contains a difficult because is not easy to keep the time interval between the shutter closure and the illumination as small as possible. The time sequence for this operation is describe on figure 7.6. The problem is then to minimise the time during which the shutter is open while no-illumination is delivered. The operation depends of how dark the dome is.

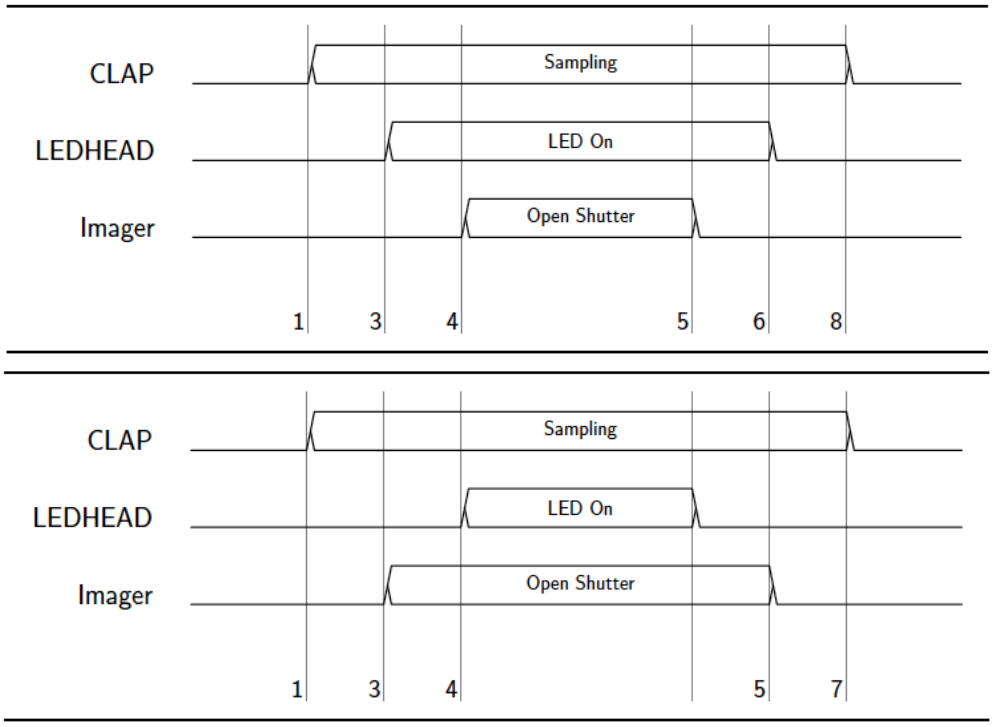

Figure 7.6: *(Top) - Shutter mode time sequence. (Bottom) - E-shutter mode time sequence.*

First Light

After the SkyDICE installation and the first configuration of the units of control and the DAQ, we manually aligned the *SkyDICE + Telescope* system to obtain a first image from the SkyMapper focal plane.

Because SkyMapper is an automated telescope, there is no control room inside the building of the telescope an to do all these operations we used the one inside the ANU 2.3 m telescope[2], close to SkyMapper.

[2] http://rsaa.anu.edu.au/observatories/siding-spring-observatory/telescopes/

We turned on the LED05 at the nominal current $I_{led} = 1000$ ADU, and we recorded the image on the SkyMapper server (file ccd00007.fits on the data archive). The alignment was not perfect. This was visible as the upper side of the FITS image was clearly vignetted; the average illumination of the focal plane was of about ~ 21954 ADU.

We repeated the operation for different LEDs and also using the artificial white planet LED29, to check the focal plane illumination and to focus the artificial planet LED using the lens system mounted on the LED-head. Then we pass to the alignment procedure and configuration.

7.4 Alignment Procedure

The final task before we could start taking science data was to secure a procedure to align the two main axes of both, SkyDICE and SkyMapper, to be parallel with an error of few dozen arcseconds. Because the LED-head is attached on the dome, first we checked the repeatability of motors those move the dome structure: we obtained a repeatability of ± 3 mm after several cycles, which is excellent for a dome. This means that we control the initial positioning of the head with respect to the telescope with a precision of $\lesssim 0.1°$. Then we tested again errors given by the two main xy motors of the LED-head mount, and we obtained a repeatability of ~ 10 µm (i.e. a few arcses).

After this operation we started tuning an alignment model, based on a geometrical model of the SkyDICE source and the telescope. Our starting point was a series of distance measurements, taken with a laser telemeter. Then, we refined this preliminary model with a series of planet exposures.

7.4.1 SkyDICE - Telescope Reference Frames

Before aligns both, SkyDICE and the telescope, we needed to choose a reference frame for the whole system. Because the DICE device, the telescope and the dome are totally independent, the first step is to obtain a reference frame for these three systems.

The first ones were the dome coordinates; as natural choice is the centre of the dome at the ground position. This set of coordinates, shown on figure 7.7, are represented by the vector:

$$\mathbf{R_D} = (O_D, \vec{E}, \vec{N}, \vec{Z})$$

where O_D is the origin, $\vec{E}$ is the east direction, $\vec{N}$ is the north and $\vec{Z}$ is the zenith of the dome. The next reference frame to choose was the one associated to the telescope mount/mirror. As illustrated on figure 7.7 this is a moving frame centred on the primary mirror and describe by the following set of coordinates:

$$\mathbf{R_T} = (O_{Al}, O_{Az}, \theta_{Al}, \theta_{Az}, \vec{Z})$$

`anu-23m-telescope`

where O_{Al} and O_{Az} are the origin respectively of the altitude and of the azimuth of the telescope mount, θ_{Al} and θ_{Az} the angle associated to the azimuthal mount, and $\vec{Z}$ the zenith of the telescope that corresponds at the zenith of the dome when the telescope is on is home position.

The last set to be choose were the one associated to the SkyDICE LED-head (see figure 7.8). As natural choice we decided to take as origin the interception of the xy motors, so we obtained:

$$\mathbf{R_{DICE}} = (O_{DICE}, \vec{X}_{DICE}, \vec{Y}_{DICE}, \vec{Z}_{DICE})$$

as usual, O_{DICE} is the origin of the reference frame, $\vec{X_{DICE}}$ and $\vec{Y_{DICE}}$ are the coordinates of the xy motors and finally, the $\vec{Z_{DICE}}$ is the z axis that points toward the primary mirror.

With this set of coordinates, we were able to find the perfect alignment positions before taking every images.

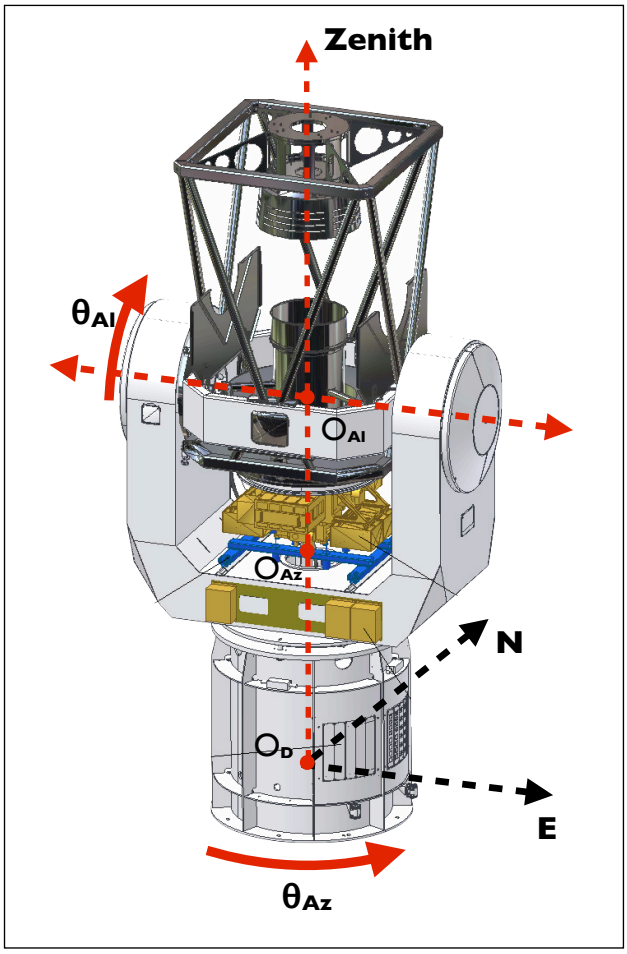

Figure 7.7: *Origins and main reference frames for the telescope mount and primary mirror (O_{Al}, O_{Az}), and for the dome position O_D.*

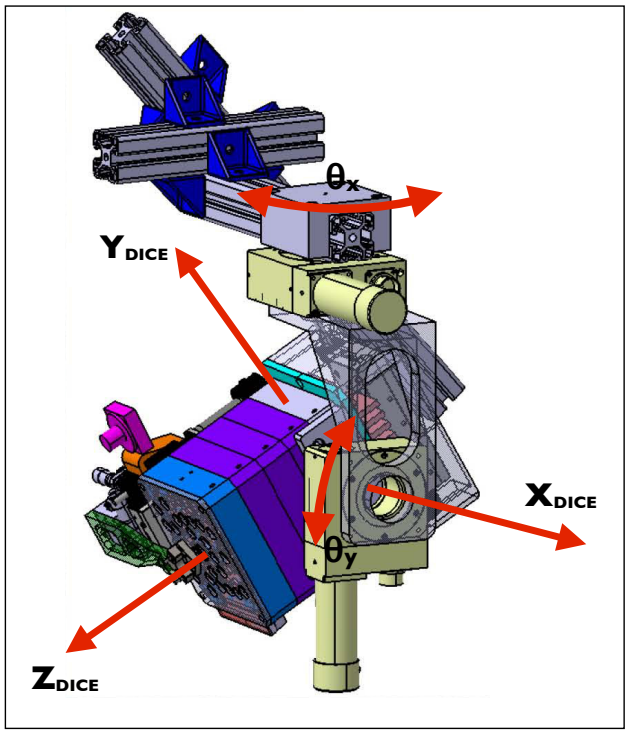

Figure 7.8: *Reference frame for the SkyDICE position. The origin O_{DICE} (invisible in this image), falls inside the device.*

7.4.2 Artificial Planet Alignment

Once obtained, the set of reference frames and dome measurements have been put inside a SkyDICE/SkyMapper model to align the two R_T and R_{DICE} frames. To do that we used a modify version of the software already tested with SnDICE/MegaCam system during different data runs (Villa 2012).

Before correctly set up the system, the software has been trained using different artificial planet session. This procedure is easily explain:

- We set the zero position of the telescope, usually the zenith coordinates.
- We set the zero position of the dome before moving the SkyDICE device.
- We set the zero positions of the SkyDICE motors, using the mechanical stops mounted on the LED-head.
- We move the telescope and then the LED-head to the positions given by the geometrical model.
- We take an image using the white artificial beam and we check the centring of the beam on the CCD focal plane.

- We calculate the xy displacement of the beam from the centre and we correct the software parameters.
- We repeat the loop until we obtained a good alignment of the artificial planet on the CCD focal plane.

This last procedure has been repeated for the four main positions of the LED beam on the primary mirror, illustrated on figure 7.9. These positions has been also used to take the first set of data from SkyMapper.

Once we have corrected the parameters of our geometrical model, the align procedure is generally reached only adjusting the SkyDICE xy axis, and it takes at maximum 4 exposures.

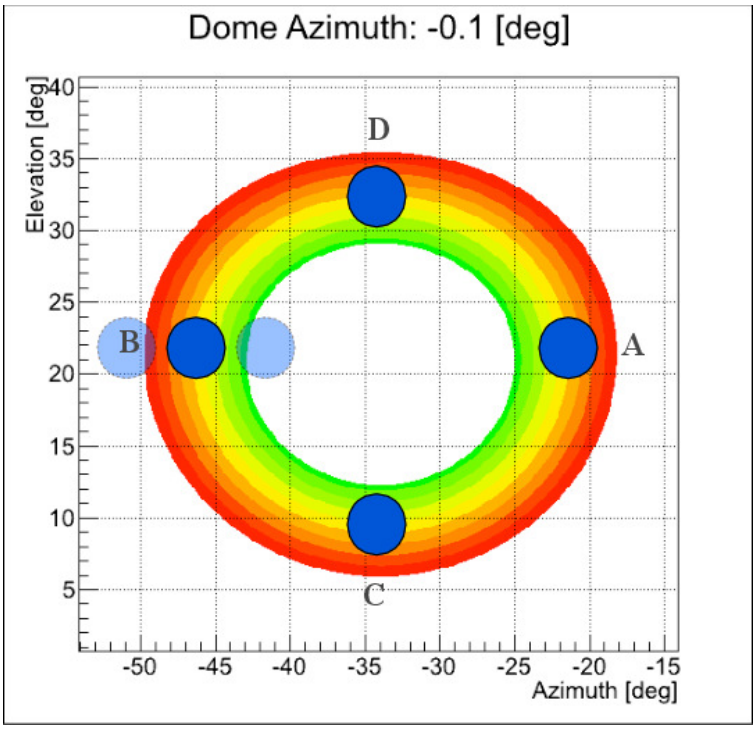

Figure 7.9: *Because we could not scan all the primary mirror, we chose 4 positions A,B,C,D. These represent 4 different configuration between the telescope, the dome and the SkyDICE LED-head. Once we set up the altitude and the azimuth of the telescope, we move the dome to the decided position, then we centre the beam of SkyDICE with the focal plane of the telescope using the xy motors mounted on the LED-head.*

7.5 First Data

During a typical run, SkyDICE is put into *silent* mode, and the electronics is monitored during a few minutes. The data taken is analysed in real time and we check that all parameters are nominal.

The system is then put into *planet* mode. On the telescope side, the dome and telescope are desynchronised, and the telescope put into a position, pointing roughly towards the LED-head. A series of planet images are then taken, each followed by a correction of the LED head orientation, in order to align the optical axes of both systems; few shoots are required to determine the dome position and get a good alignment. After this operation, SkyDICE - SkyMapper were able to take science data.

Almost all images in these first runs have been taken during the day light, when the telescope was not used for routine observations, expect for half of data taken the 2 of July, where, because of the bad weather, we used part of the night to take images for the position C and D of the mirror.

The full data sample is divided in different set of images, each one taken shooting the LED beam on a different position of the telescope's primary mirror; these positions are illustrated on figure 7.9. The real science data have been taken during the 23 June and the 30 June, 1-2 July run. We can divide these runs in two sub-set, a set of *flat-fields* images using the main 23 LEDs (30 of June and 1-2 of July data), and a second set of *planet* images using the artificial planet (23 of June data).

For data until 06/27/2012 we centred the artificial planet spot at the xy position (560, 510) of the focal plane. After we decided to slightly changed this with another position at the xy coordinates (432, 569) to obtain a better beam centring. This has suggested that the artificial planet beam is tilted by an angle of ~ 0.1 degree respect to LED-head z axis. Every exposure has been chosen to obtain a good signal to noise ratio but avoiding CCDs saturation. The typical average level for most of the images is in the range of $\sim 10000-20000$ ADU. A table contains summary informations about all the 2012 data sample is shown in 7.1.

Date	Img #	LED type	Filter	Dome/Position (°)	Azimuth (°)	Elevation (°)	Derotator (°)	Image type
17-21-22/06/2012	14+41+136	planets/LEDs	No/All	A	-	-	-	Alignment/Planet Focus/ LEDs centring
23/06/2012	64	planets	No/All	359,92 - A	-21 20	22 00	N/A	Planets study/ ghosts study
24-25/06/2012	14+14	planets	No	-	-	-	-	Dome reproducibility
26/06/2012	12	planets/LED05	No	359.91/A				CLAP alignment
27/06/2012	22+94	planet29/LEDs	No	359,92/A	-21 20	22 00	158 10 21	Flat Fields
28/06/2012	50	planets/LEDs	No	A/B/C/D	-	-	-	Position offsets
29/06/2012	14	planets/LEDs	No	A/B/C/D	-	-	-	Repeatability tests
30/06/2012	151	planet29/LEDs	No/All	359,91/A	-21 20	22 00	158 10 20	Flat Fields
01/07/2012	122	planet29/LEDs	No/All	359,91/A	-21 20	22 00	158 10 20	Flat Fields
02/07/2012	272	planet19-29/LEDs	No/All	359,90/B	-47 10	22 36	138 10 19	Flat Fields
		planet19-29/LEDs	No/All	359,90/C	-34 30	34 00	149 28 35	Flat Fields
		planet19-29/LEDs	No/All	359,90/D	-32 51	09 25	143 32 44	Flat Fields
04/07/2012	20+78+6	LEDs	No	-	-	-	-	Test sequence remote control

Table 7.1: *Here we represent the whole set of data taken during different data runs on summer 2012. Here the coordinates of azimuth, elevation and de-rotator are the reference values of the artificial planet used to centred the beam. During each run this value slightly changed to centre the LED.*

7.5.1 DICE Flat Fields and Filters Study

The 30 of June and 1 of July data samples have been taken using the whole set of 23 working LEDs of SkyDICE. For the position A on the mirror we have taken images with the complete set of 6 filters u, v, g, r, i, z for each LED. We have used this set of images to study the filter transmission for each passband. Preliminary results on the filter transmission analysis are reported on the last section of this chapter. Another reason of taking images using all filters is to monitor that filters works properly.

Figure 7.10 illustrates a set of 4 images taken using the LED05 ($\langle\lambda_p\rangle = 505$ nm). They have been taken using *no* filter, then g filter and r filter, then the v filter (to monitor the filter passband). For all images we have chosen different exposure time to obtain a similar signal level, expect for the last one where we used a long exposure of about 100 second, only to monitor the filter passband. We can see by eyes that level of each images is similar and the illumination is almost uniform expect for a small vignetting on the left side of the focal plane. This is created by the finite angular aperture of the LED beam and the fact that we cannot physically point the SkyDICE at some positions because of mechanical obstructions of the telescope such as the secondary mirror spiders. Finally, some interesting features that emerged from images, are the diffraction patterns created by the dust and small defects (such as scratches) on the mirror and the various optical surfaces along the path of light.

Another interesting image that introduce us on the reason to take a second subset of images using artificial planets, is presented on figure 7.11. This is a *flat field* image took using the near-IR LED12 ($\langle\lambda_p\rangle = 850$ nm) with 15 s of exposure with the filter z. The image is in false colour to highlight the pattern created by the reflection of the CCDs grid itself on the bottom side of z filter. It is clear that to analysis images like that is necessary to take into account this type of ghosts (reflections) created by the filter set and the optical lenses between the LED source and the focal plane of the telescope. The first step to reconstruct this ghosts is to create a model of the telescope optics and a simple ray-tracing system to analyse the path of the light source.

This has already been done, and the complete description of this model can be found on appendix A. The full analysis of this set of images and the reconstruction of ghosts is in progress and not yet finished. To understand how we reconstruct the direct and reflected lights from these images we can refer to the work ok the SnDICE team and F. Villa thesis (Villa 2012).

7.5.2 The Artificial Planet and Ghosts Study

Ghosts are a central problem on the way to analyse flat field images taken by SkyDICE and SnDICE. An interesting possibility to use these ghosts is represented on figure 7.12 and 7.13. These examples are taken from the 23 of June data set using the set of artificial planet LEDs built for the SkyDICE device. In particular these images have been taken with the white artificial planet LED29. The spot created is around 100 pixels. On figure 7.12 we did not used any filter, while on figure 7.13 we used the g filter.

For both images it is easy to see a set of small spots along a virtual line that passes through the main artificial planet spot. The direction of this virtual line depends in the

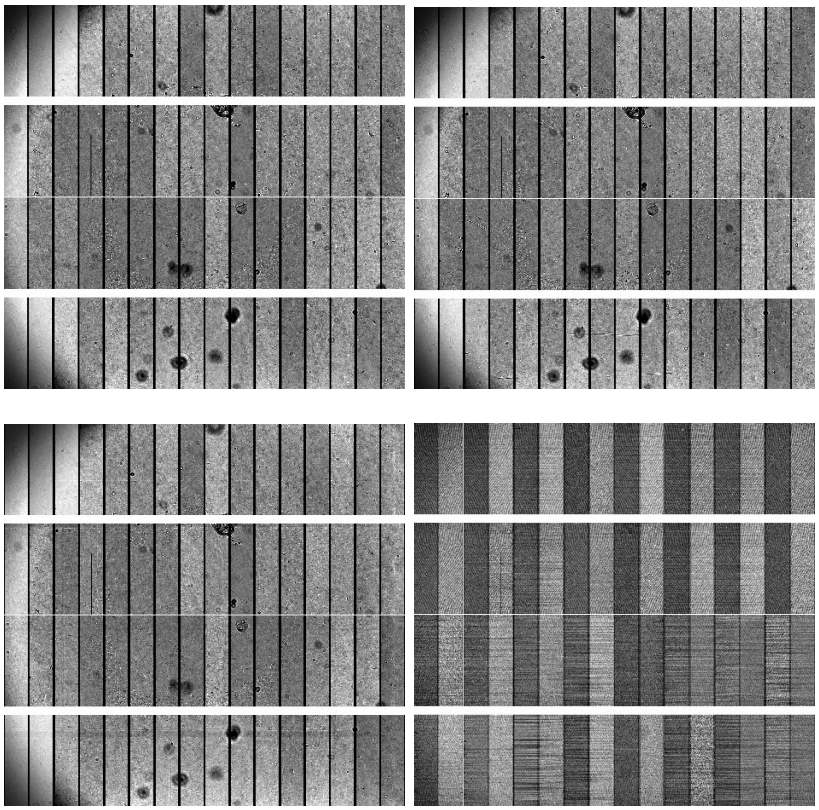

Figure 7.10: *These are a set of images took using the LED05 ($\langle\lambda_p\rangle = 505$ nm) with different exposures time. From top-left to bottom-right the filters used are: no filter with 3 s of exposure, g filter with 3 s, r filter with 15 s, and v filter with 100 s of exposure. Interesting features that emerged from images, are the diffraction patterns created by the dust and impurities on the CCDs focal plane and on the lens system.*

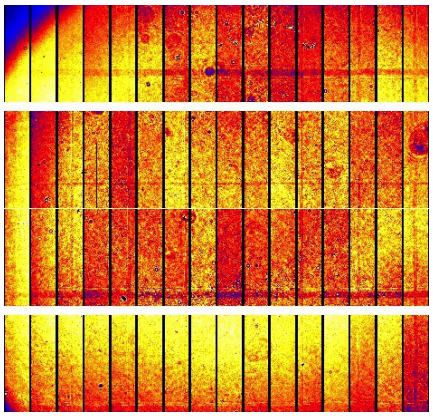

Figure 7.11: *This is another image in false colours took with LED12 ($\langle\lambda_p\rangle = 850$ nm) and 15 s of exposure. In that case the filter used was the z. We can notice the CCD grid reflected by the filter itself.*

position of the beam on the primary mirror. We can also see how the number and the intensity disappear as we modify the light path adding a filter between it. The analysis of these images is not yet completed but what we can already say is that every of that small spot represents a ghost created by a particular light path on the telescope optics. Again, to reconstruct those ghosts we need the help of the optical model created by the team and described on appendix A.

An interesting use of this is the study of the optics and filters reflectivity of the telescope. In particular once we know the intensity of each ghosts and we reconstruct its optical path, one is able to compute the reflectivity of each refracting elements in the telescope. This feature is extremely useful if we want to study the total transmission of the telescope and monitor the efficiency of lenses and filter coating system along their durations.

7.6 Preliminary Analysis

In this section we are going to describe first results of a preliminary analysis done using the whole set of images taken from 30 of June to the 2 of July 2012. First we illustrate a sample of the full data set, then in describe the study of the dark dome images, used to evaluate the average illumination of the dome during the shoots, then we pass to describe the first preliminary result of the filter transmission computed using SkyDICE data and finally, we briefly discuss some first result from filter leakage study.

7.6.1 Data Sample

In table 7.2 we report a small sample of the data taken during the whole session. In that case we use as an example the LED03 with the SkyDICE device aligned along the A position of the primary mirror (see figure 7.9).

The first eight images are the *dome dark* images. These images have been taken to obtain an average dark frame of the background light inside the enclosure of the telescope after we turned off every artificial light. This allow us to obtain not only the dark frame but also a preliminary study of the possible Because the dome is not completely dark and because images are taken during the day light, this effect slightly depends on the outside weather conditions. As general procedure, these images are subtracted from the real science images to take into account this tiny effect (the average intensity for images taken during the day was not bigger than 30 ADU).

After dark frames, we turned on the LED at the nominal current, and we shot the beam into the primary mirror to obtain an uniform illumination of the focal plane. For some LEDs we were not able to cover perfectly the focal plane due to the physical obstructions of the secondary mirror spiders: some images have small vignetting on the corners of the CCDs focal plane.

Furthermore, in the first position A of the mirror, for every LEDs we repeated the measurement using the whole set of filters. This allowed us to obtain a preliminary study of the possible filter leakages at different wavelength. For the remain position B,C,D, we took images using only filters associated with the correct wavelength of each LED.

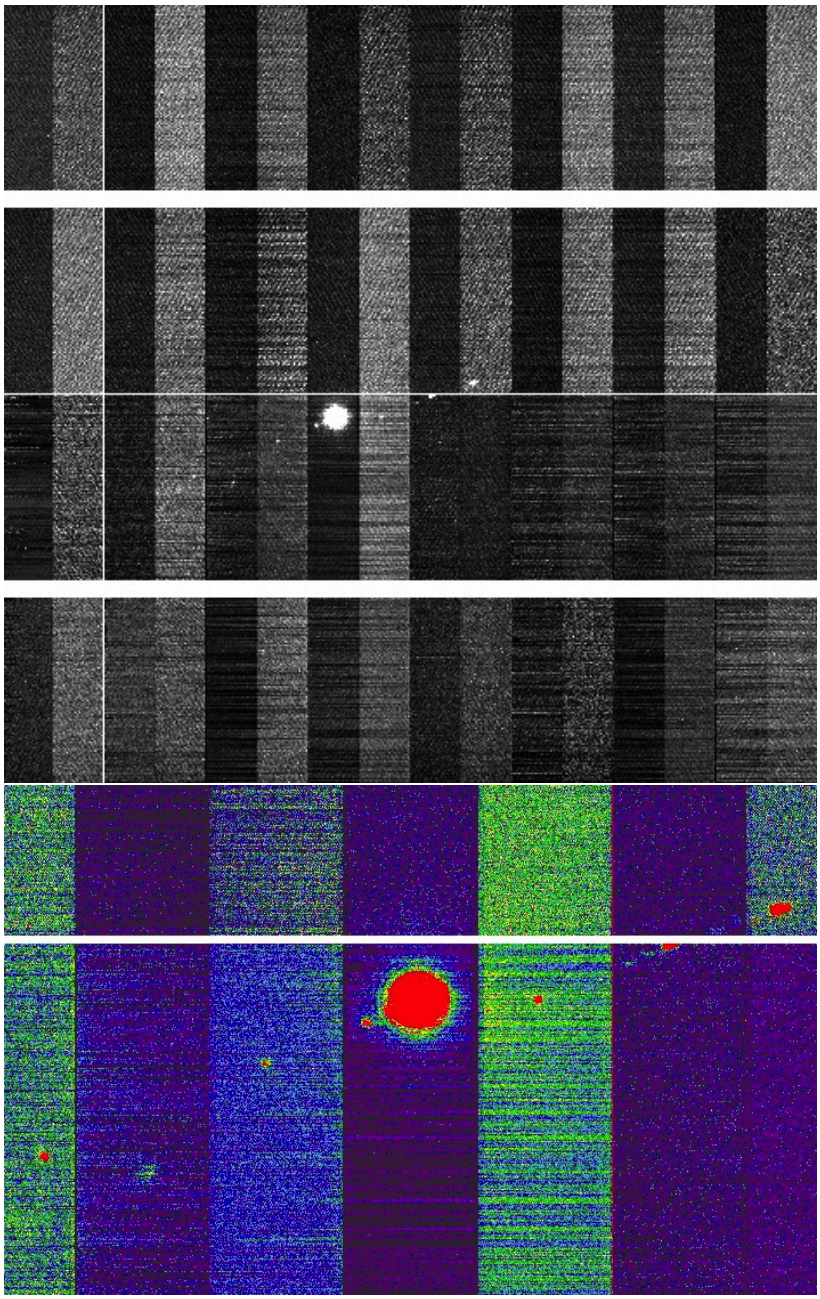

Figure 7.12: *Here we have the image of the focal plane illuminated by the artificial white planet with* 5 *s of exposure without using filter. It is clearly possible the sum of the ghosts created by the internal reflections of the filter and the correction lenses system between the secondary mirror and the focal plane.*

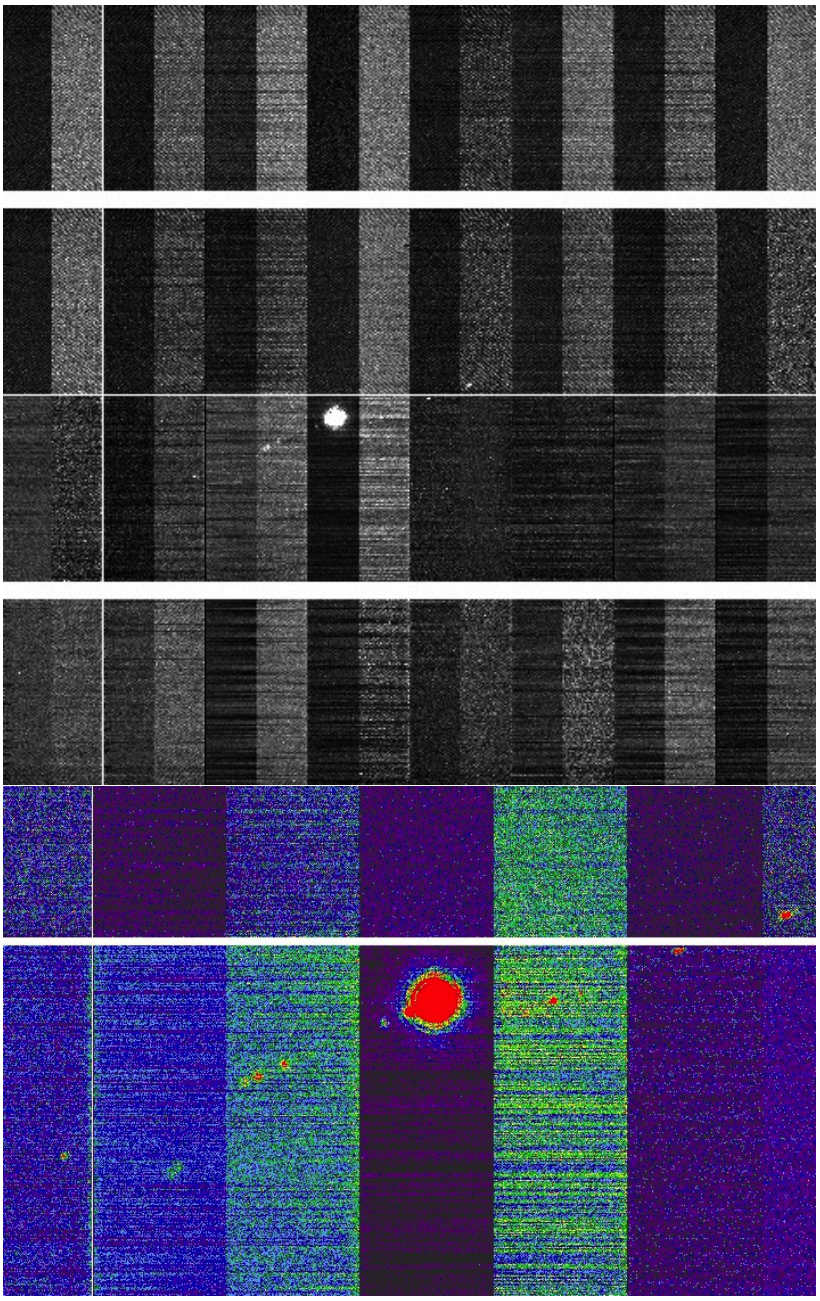

Figure 7.13: *The same picture but putting the filter g in front of the camera. Again the ghosts are created by the lenses correction system and the filter.*

This has permitted us to obtain a set of images to study the transmission of the SkyMapper passband and. Here we present the preliminary results of this study.

Img #	LED	I_{led} (ADU)	Filter	Exp (s)	Az. (°)	Elev. (°)	Derot. (°)	θ_x (step)	θ_y (step)	<Flux> (ADU)
6028	dark	NO	NO	100	-23:00:44	21:26:24	156:28:47	-22120	-7242	-1.7
6030	dark	NO	u	100		-	-	-	-	-
6031	dark	NO	v	100	-	-	-	-	-	-1.8
6032	dark	NO	g	100	-	-	-	-	-	-0.6
6033	dark	NO	r	100	-	-	-	-	-	2.8
6034	dark	NO	i	100	-	-	-	-	-	3.8
6035	dark	NO	z	100	-	-	-	-	-	8.1
6036	dark	NO	NO	100	-	-	-	-	-	27
6063	3	5000	NO	2	-23:00:48	22:14:24	156:40:52	-22120	-8040	9279
6064	3	5000	u	60	-	-	-	-	-	725
6065	3	5000	v	5	-	-	-	-	-	8349
6066	3	5000	g	100	-	-	-	-	-	850
6067	3	5000	r	100	-	-	-	-	-	89
6068	3	5000	i	100	-	-	-	-	-	5
6069	3	5000	z	100	-	-	-			3

Table 7.2: *This table is taken from the 30 June 2012 data sample. It shows the typical routine operation to take SkyDICE flat-fields for the UV LED03. The operation is repeated for all 23 LEDs. In particular because the dome is not perfectly dark, at the start and at the end of the sample, we record different dome dark images to take into account the background level of the dome.*

7.6.2 Dark Dome Study

Before we can study the filter transmissions, we need to take into account the effect due to the fact that our device is inside a dome which is not perfectly dark. As a consequence, we need to measure the count rate inside the dome, so that we can estimate the pollution of our calibration frames by the ambient luminosity. The typical procedure is to take a dark exposure before and after every images, but because of the lack of time at the telescope, for these first runs we decided to take only one dark (in the case of the A position for every filters) before and after a set of images using the same LED.

This method, even though not full correct, has permitted to obtain a good estimate of the level of background light, during the day and during the night (we expect to obtain different count rates and dispersion depending on whether the calibration frames are taken during the day or at night).

The analysis has been done as follows. We checked every dark dome exposures for bad centring of the beam and for bad illumination, and at the same time we estimated the average illumination (in ADU). After that we divided the exposures in the for mirror position A,B,C,D. For each of these images we created another subset of images taken during the day light and during the night. Because the winter season, the hour chosen as limit between day and night was the 5 : 00 pm (local time, 7:00 am UTC). The images is a mosaic of 32 CCDs each built with two amplifiers for a total of 64 CCDs sections. Each of these amplifiers have a physical overscan region made by 50×4096 pixels and a second virtual region (using the CCD pixels) of the same dimension. The dimension of the science data sector is 1024×4096.

For each of the 64 amplifiers we extracted the illumination level, in particular the mean, the median and the rms using a data pipeline created by the L. Le Guillou and his student R. Le Breton. The same data pipeline has been used for the whole set of images taken during the 30 June and the 1-2 July 2012.

To calculate a preliminary dark dome level we implemented a simple program that has taken into account only the contribution of the overscan regions in the science images. In particular, for each CCDs amplifier we subtracted the mean of the two overscan regions, the physical and the virtual one. We did that for the day and night dark dome and for every filter. Table 7.3 shows the result for the central region of the CCD mosaic, in the case of the amplifier #33 and #26. In particular these values are the mean of the whole set of usable images. The error associated with the dark dome illumination during the day is larger that one of the night values, as shown on figure 7.14, because of variability of illumination due to a really unstable weather conditions. As can be seen, the contamination we observe is small. In the worst case of a 10-second calibration exposure taken during the day, we obtain a contamination of ~ 2 ADU, i.e. less than 0.1% of the expected signal (a few thousand ADUs).

7.6.3 Measuring the Filters Transmission

The data used for this analysis is divided in 4 subsets, each one contained data taken at one of the chosen mirror position A,B,C,D. A typical session for one LED at one position is shown in table 7.2. The method is repeated for each of the 23 working LEDs.

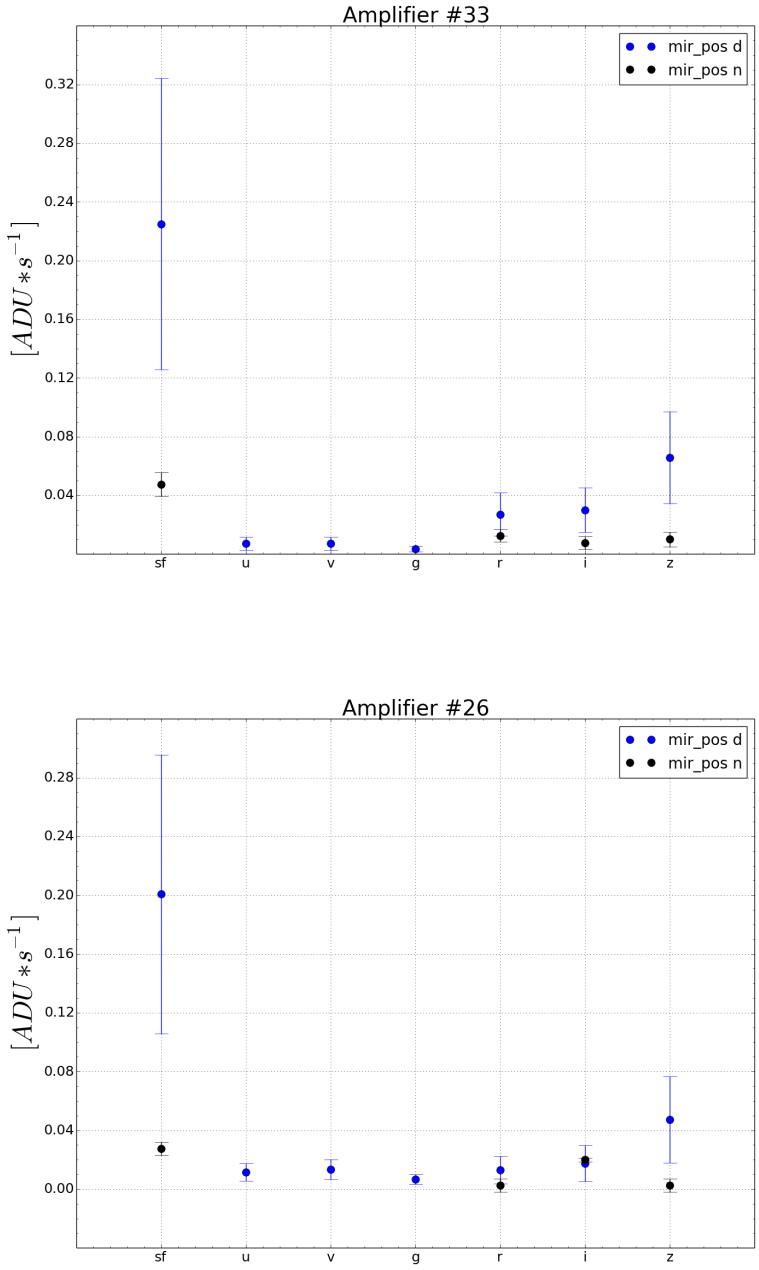

Figure 7.14: *Dark dome illumination in ADU/s for the CCD amplifiers* #33 *and* #26. *Without filter we can see that the contribution of the dome illumination is not trivial.*

Filter	Amplifier (#)	Night (ADU/s)	Day (ADU/s)
NO	33	0.047 ±0.008	0.22 ±0.09
	26	0.027 ±0.004	0.20 ±0.09
u	33	-	0.007 ±0.004
	26	-	0.012 ±0.006
v	33	-	0.007 ±0.004
	26	-	0.013 ±0.007
g	33	-	0.004 ±0.002
	26	-	0.007 ±0.003
r	33	0.012 ±0.004	0.03 ±0.01
	26	0.003 ±0.004	0.01 ±0.01
i	33	0.010 ±0.004	0.03 ±0.01
	26	0.020 ±0.002	0.02 ±0.01
z	33	0.010 ±0.005	0.06 ±0.03
	26	0.003 ±0.004	0.05 ±0.03

Table 7.3: *Dome dark study of night and daylight along all the filters set for* #33 *and* #26.

Analysis

As for the dark dome frames, we divided every FITS image in the 64 CCDs amplifier and using the same technique we extracted the mean, the median and the rms of the flux for the overscan regions and for the main science data. To avoid vignetting effects of the images, here we focus our analysis on two amplifiers, the #26 and the #33. These amplifier has chosen because mounted in the central region of the CCD mosaic. The data set used as reference measurement for our analysis is the one described on Bessell et al. (2011), of the SkyMapper team.

What we present here is an analysis that was done shortly after data taking, in order to check the quality (and completeness) of the dataset. The technique presented in the next chapter is more sophisticated and exact. Our goal here is to take the ratio of the flux level measured with a filter over the flux level measured without a filter, and to compare it to the expected filter transmissions.

As we said in chapter 3 and in the wavelength *pre*-analysis in chapter 4, LEDs wavelength depends on the temperature of the *pn* junction. The first step is to compute the real wavelength of each LEDs beam using the linear model described by the equation 4.9 and results from table 4.6. Because the computation of the filter transmission is a ratio of the flux of the same LEDs with and without filter it is not necessary to normalise the flux with the temperature. Moreover, from the SkyMapper monitor, we knew that inside the dome the average temperature was ~ 285 K. Putting this value inside the equation we were able to calculate the real λ_{peak} for every LED used in the data sample.

Once we get the real wavelength, next step is to calculate the real illumination of the focal

plane for each LEDs and filter set up. To do that we subtracted each images with the dark dome associated, then we subtracted to the result the mean of the overscan regions. Finally we normalise the flux with the exposure time of each images. We repeated the operation for images with filters and images without filters. To summarise in a simple relation the filter transmission computation. we can write all the operations as follows:

$$T = \left[\frac{[ccd_f - (prescan_f + overscan_f)/2) - dark_f]/t_f}{[ccd_{nf} - (prescan_{nf} + overscan_{nf})/2) - dark_{nf}]/t_{nf}} \right] \tag{7.1}$$

where ccd_f and ccd_{nf} are the flux values of the chosen amplifier respectively, with and without filter, $prescan_f$ and $overscan_f$) are the overscan regions, t_f and t_sf are the time of exposures and $dark_f$, $dark_{nf}$ are the dark dome estimations. This procedure has been repeated for every CCDs amplifiers and images for the four position A,B,C,D of the primary mirror.

All the results shown in this section have been calculated using the median of the flux for each amplifier rather than its mean value, because it represents better the real average flux of the signal.

Results

Preliminary results are shown on figure 7.15, 7.15, and 7.17. As we can see, for the u and v we have few points but in a good agreement with the reference filter transmission. The best result, even if it is a preliminary analysis, is with the g. The accordance of reference data versus calculated points is really strong. Note that we are comparing here integrated fluxes (ADU/s) with a differential transmission (ADU/nm/s) which explains the disagreement between the curves and the points. A more exact method will be presented in the next chapter.

7.6.4 Filters Leakage Study

Another that was performed shortly after data taking is the search for possible leakages and defects of the SkyMapper filters set. The study has been done only for the position A of the mirror and during the 30 June and 1 of July. Moreover all data set has been taken during the day when the telescope was not used for observations.

The procedure followed was the same of studying the transmission of filters, but this time using the whole set of LEDs outside the passband of each filter. As for the transmission analysis the method to reduct data was the same. Again, we took the mean, the median and RMS of both science exposures and overscan regions. Moreover, we calibrated the LED wavelength using the mean temperature and the equation 4.6.

Finally, using the same procedure describe in the relation 7.6.3, we were able to calculate the transmission of each filter. Preliminary results are shown on figures 7.18, 7.19, and 7.20.

In these plots the most important result is the one shown on figure 7.18 for the filter u. The green band it represents the transmission given by the SkyMapper team (Bessell et al. 2011) and the blue points are form SkyDICE data analysis. We can see that our device is

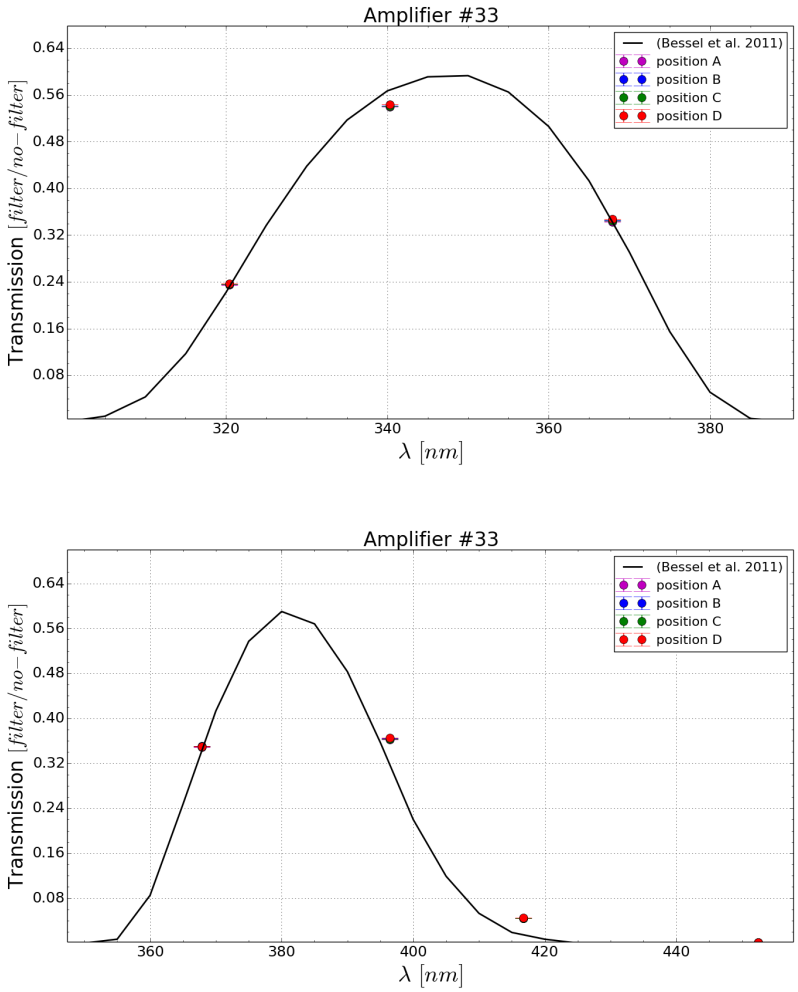

Figure 7.15: *The picture shows the preliminary result for the u, v filters transmission using the data taken from the 30 June to the 2 July 2012 with the SkyDICE system. The CCD amplifier is the #33.*

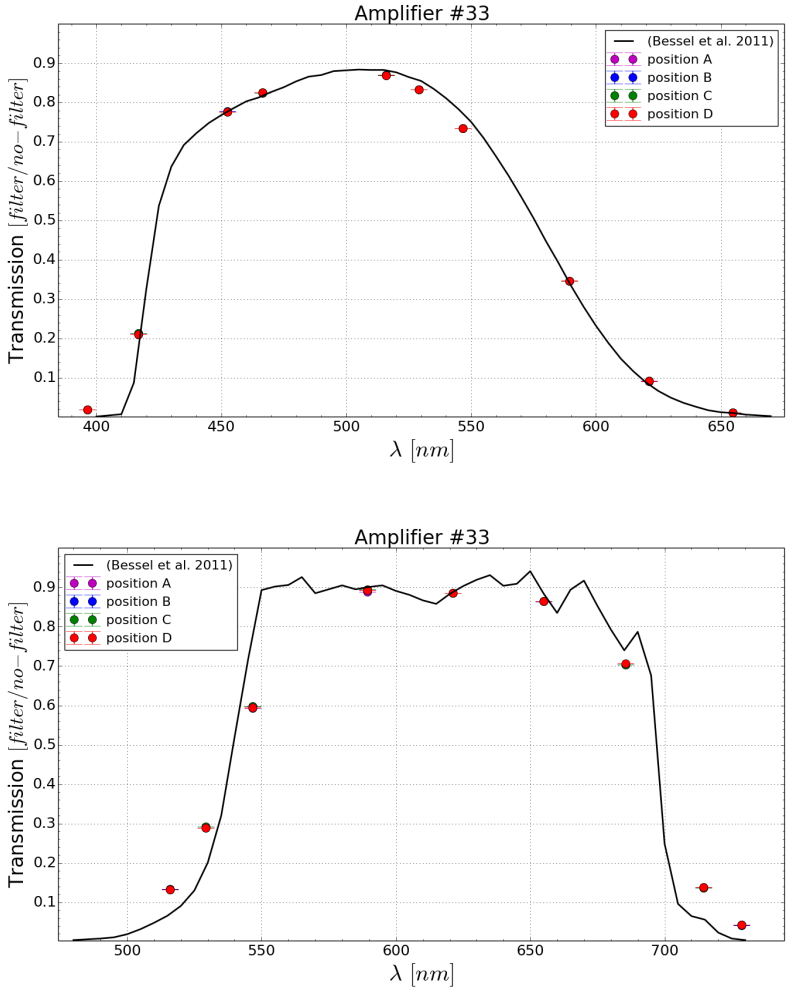

Figure 7.16: *The same analysis of figure 7.15 but for the g, r filters. The amplifier is the* #33..

able to reconstruct, even with only a preliminary analysis, the faint leakage on the near-IR of the u filter, where the transmission is lower than 4×10^{-2}. Again in the same figure for the v filter we see another small feature, probably linked to leakage on the near-IR. In that case because of the lack of data from the SkyMapper team, and because this analysis does not take into account systematics expect for the dark dome frames, we cannot discriminate at the moment from a real filter feature or from background noise.

For the others filters g,r,i,z the analysis does not reveal strange feature or strong leakage expect for some isolated points. More data and a more accurate analysis should be necessary to study in details those filter transmission.

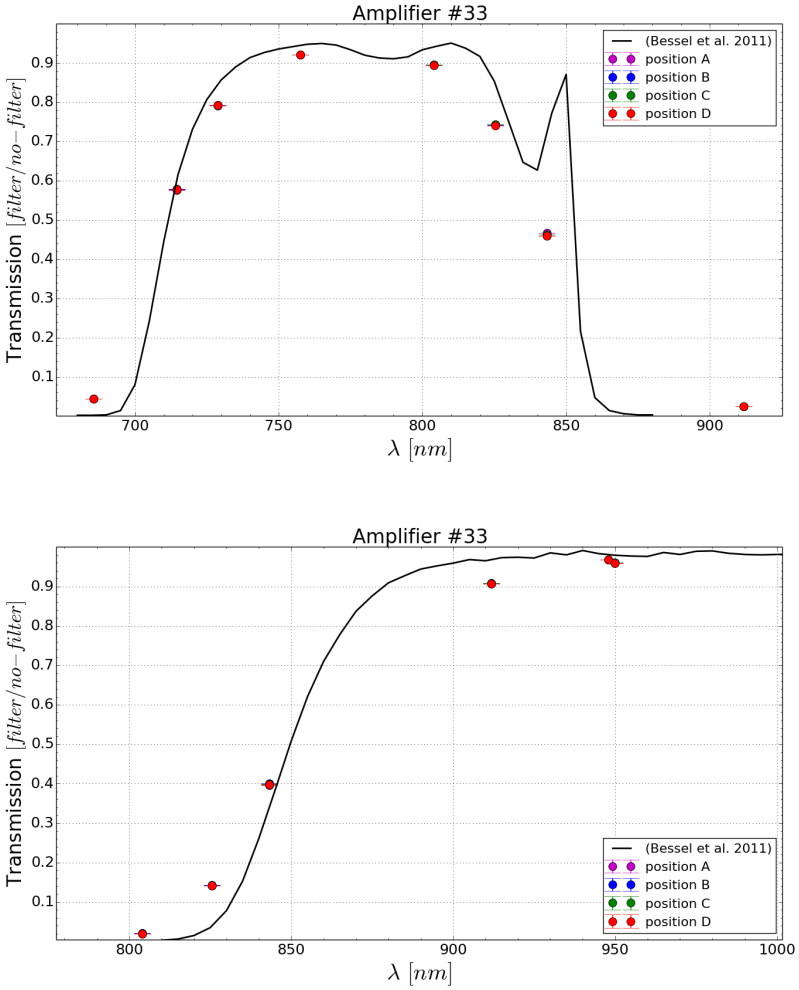

Figure 7.17: *The same analysis of figure 7.15 but for the i, z filters. Again the CCDs amplifier is the* #33.

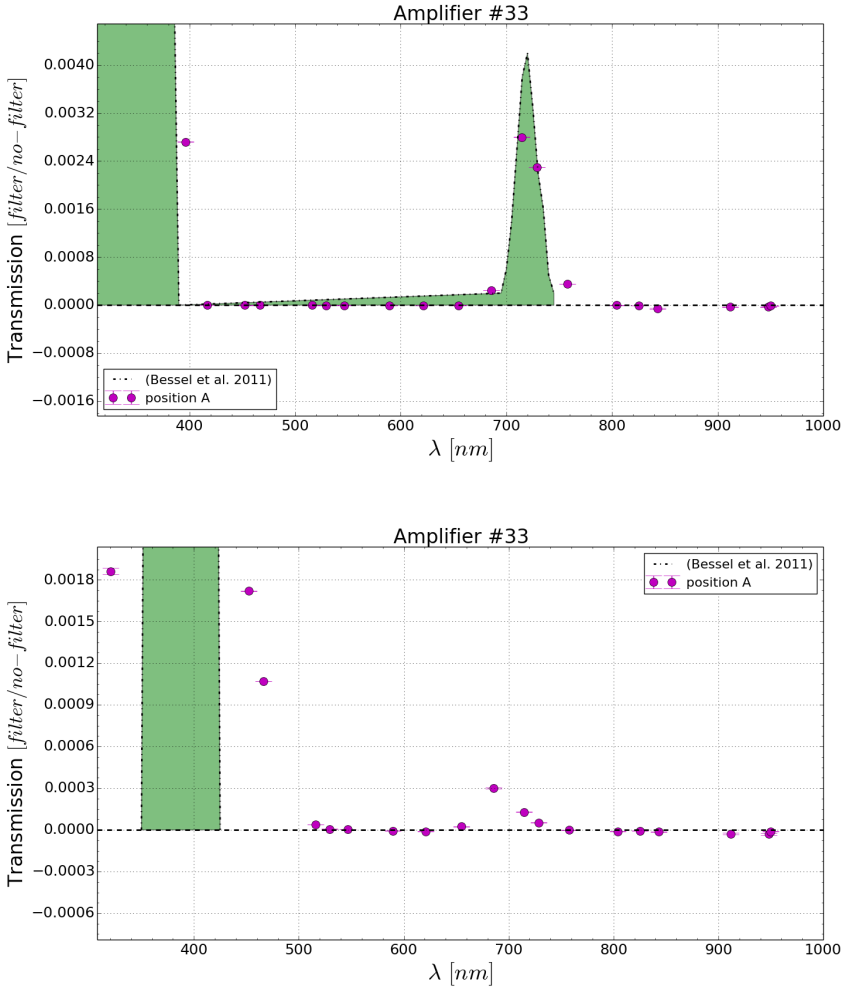

Figure 7.18: *Here we show the transmission parameters for the u, v filters outside the filters passband. Even in that case the CCDs amplifier was #33.*

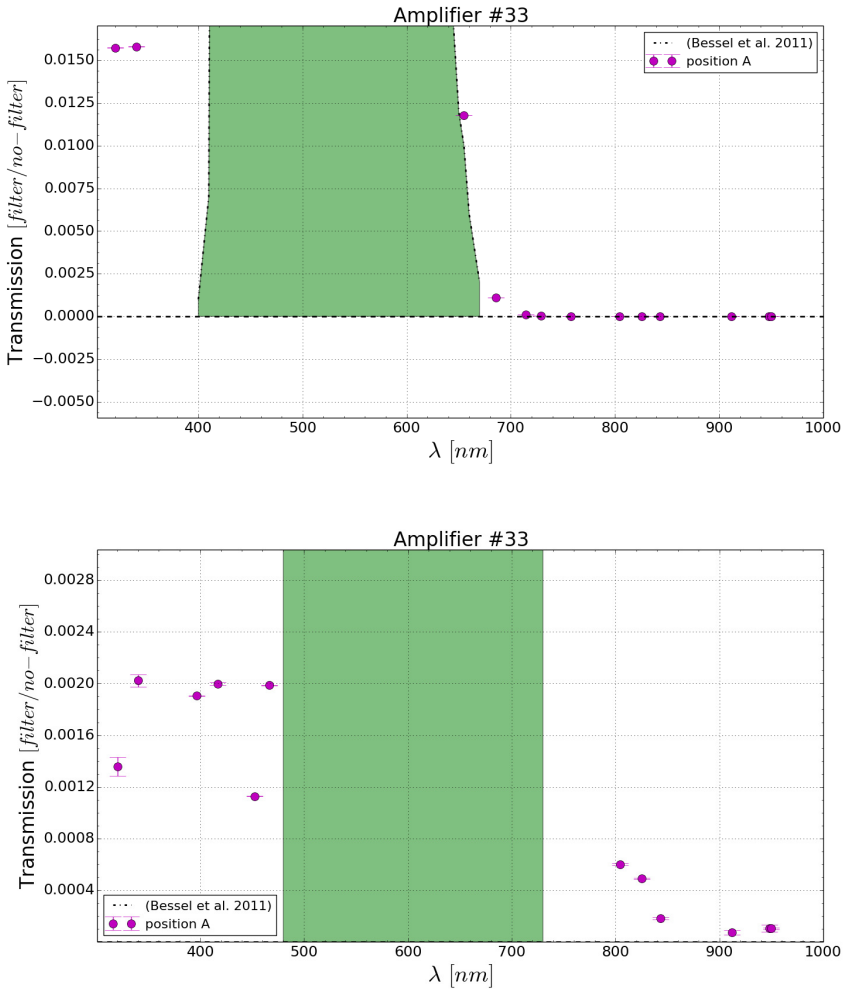

Figure 7.19: *Same plot of figure 7.18 but for the g and r filters.*

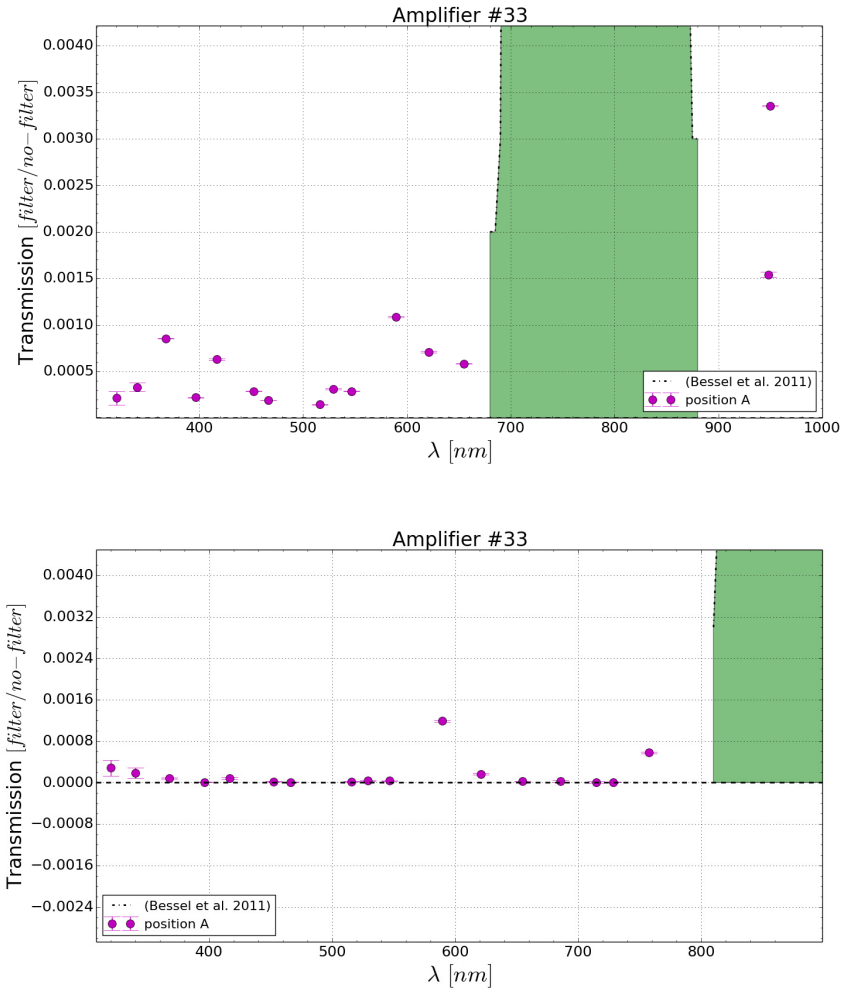

Figure 7.20: *Again the same plot for filters i and z.*

Chapter 8

Constraining the Passbands of SkyMapper

At first sight, no matter how stable and well calibrated the calibration source may be, the design of DICE seems sub-optimal, when it comes to measuring the passbands of a telescope. A quasi-monochromatic source, such as a tuneable laser, or a stabilised lamp coupled to a monochromator, seems to be a more judicious choice, as it permits to scan the telescope transmission every 1-nm or even less. This approach is costly, as it requires to acquire and process about O(100) exposures per filter, but permits to capture all the tiny features of the telescope passbands.

In this chapter we will show, that DICE is a very economical way to determine and follow precisely all the important features of broadband transmissions, and this, with about ten times less data ($\lesssim$ 10 exposures per filter). This makes it possible to implement a lightweight calibration program, that may be run several times a week, during daytime. As we will see, the calibration precision that can be obtained with this approach is well within the specifications that were issued for the next generation Dark Energy surveys.

In this last chapter, we present the method we have developed to derive constrains on the imager passbands, from a series of measurements taken with a device such as SkyDICE (§8.1 and §8.2). We discuss the propagation of the test bench systematics (§8.4). We test the method on a simulated dataset, built from the simulated test bench data presented in chapter 6 (§8.3). In particular, we discuss the precision that can be attained by the various DICE instruments on the MegaCam and SkyMapper passbands (§8.5).

8.1 Telescope Transmissions

In general, the shapes of the passbands are known long before the first star light hits the focal plane. The transmissions of all optical components, the quantum efficiency curves of the detectors are all carefully measured before assembly. One can therefore combine these measurements to build a synthetic model of the telescope passbands:

$$T(\lambda) = g \times \mathcal{A} \times R_{\rm mirror}(\lambda) \times T_{\rm optics}(\lambda) \times T_{\rm filter}(\lambda) \times \varepsilon(\lambda) \tag{8.1}$$

Here $\varepsilon(\lambda)$ is the quantum efficiency of the CCD, g is the gain of its readout chain, $\mathcal{A}$ is the area of the mirror and the other terms of the various transmissions and reflectivity of the optical elements. Note that $T(\lambda)$ is a dimensioned quantity: here it has units of $\mathrm{ADU}/\gamma/\mathrm{m}^2$.

Although the shape of $T(\lambda)$ is known *a priori*, its absolute normalisation varies with time and must be monitored: the gain g of the readout electronics may vary by a few per-mil over timescales of a few hours; also, alterations of the optical surfaces (dust deposits, ageing of the coatings ...) degrade slowly the transmission of the instrument, by as much as 5-10% per year. The resulting attenuation of the telescope transmission is slightly wavelength dependent. Therefore, the *relative* normalisation of the passbands with respect to each other may itself vary by a few percents per year. The main purpose of calibration is therefore to monitor the relative variations of the passband normalisation over time. In most applications, we need to measure in the evolution of the relative normalisation of the passbands, with respect to each other.

The *shape* of the passbands is not expected to vary very significantly over time. This is generally a design requirement. However, several studies have reported evidence for slow evolution of the passbands shape. For example, Doi et al. (2010) reports a significant evolution of the blue side of the SDSS 2.5-m u-band channels, probably due to ageing of the CCD antireflective coatings. Another example can be found in Betoule et al. (2013), who shows hints that the MegaCam r- and i-filters may be $2-3$-nm off, with respect to the scans provided by the manufacturer. In this case, it is not clear whether this evolution of the passbands took place in an early phase of the life of the instrument, or later. As a consequence, there is a strong incentive for future surveys to monitor the shape of their effective passbands.

8.2 Constraining Passbands with a DICE Source

The broadband flux of an astrophysical object is primarily sensitive to (1) the normalisation of the passband and (2) the position (in wavelength) of the blue and red filter cutoffs. These three quantities are therefore what should be monitored in the long run.

An alternative to a full transmission scan is to alter the synthetic passband model $T(\lambda)$ presented in equation 8.1, for example by allowing for a different normalisation, and for small variations of the filter blue and red cutoffs (called $\delta\lambda_b$, $\delta\lambda_r$ hereafter). Then, one would use the DICE calibration frames to constrain these alterations of the synthetic passbands. Shifting the filter fronts can be done by composing $T(\lambda)$ with a function $f(\lambda)$ which stretches (or dilates) the λ variable around the filter maximum:

$$f : \lambda \mapsto \lambda' = \alpha \times (\lambda - \lambda_{\max}) + \beta$$

In practice, we reparametrize the function above, so that it depends directly on $\delta\lambda_b$ and $\delta\lambda_r$. This way, one can shift easily each front essentially independently of the other, as shown on figure 8.1 for the SkyMapper g and r filters.

With such an approach, we reduce our problem to fitting only three parameters per filter: a normalisation, $\mathcal{N}$, and two filter front displacements, $\delta\lambda_{\mathrm{blue}}$ and $\delta\lambda_{\mathrm{red}}$. For an

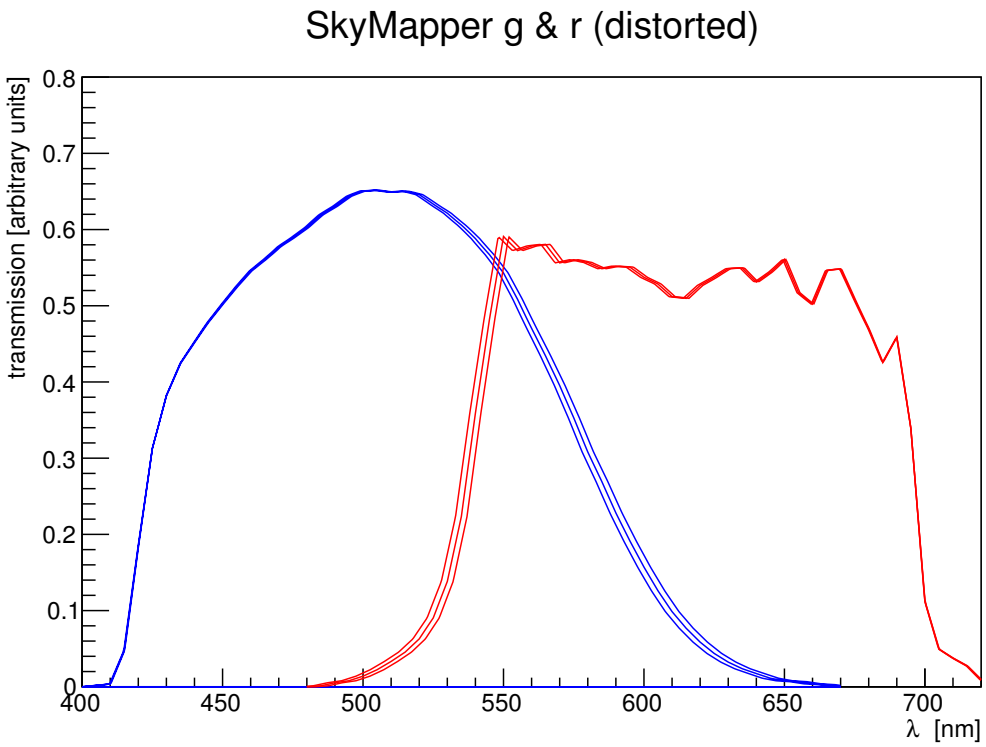

Figure 8.1: *Altered SkyMapper bands. Illustration of how we can alter the red front of the g-band and the blue front of the r-band, without displacing the other front.*

imager equipped with N (typically 5) filters, we end up with $3 \times N$ calibration parameters, which we group in a single vector, noted $\boldsymbol{\vartheta}_t$ hereafter:

$$\boldsymbol{\vartheta}_t = \begin{pmatrix} \mathcal{N}_u \\ \delta\lambda_{\mathrm{b}|u} \\ \delta\lambda_{\mathrm{r}|u} \\ \vdots \\ \mathcal{N}_z \\ \delta\lambda_{\mathrm{b}|z} \\ \delta\lambda_{\mathrm{r}|z} \end{pmatrix} \tag{8.2}$$

To constrain these unknowns, we compare measurements of the DICE calibration flux performed with the imager, with a *model* of the same measurements, built from the altered passband shapes described above, and the LED spectral intensity estimates presented in chapter 6. The model predictions depend on $\boldsymbol{\vartheta}_t$, and a least-square fit will yield estimates of the alterations.

More specifically, the model is built as follows. We implement a parameterized model of the shape of each passband ($b \equiv ugriz$): $T_b(\lambda; \boldsymbol{\vartheta}_t)$, as discussed above. From these parametrized passbands, and from the LED spectral intensity estimates, $\hat{S}_l(\lambda, T)$, we can

predict the flux registered on the focal plane for each band b and each LED l:

$$\varphi_{bl} = \delta\omega_p \times \int \hat{S}_l(\lambda, T)\ T_b(\lambda, \boldsymbol{\vartheta}_t)\ d\lambda \tag{8.3}$$

where $\delta\omega_p$ is the solid angle covered by the focal plane pixel or super-pixel where we measure the imager flux. It is useful to write the equation above in matrix form:

$$\varphi_{bl} = \delta\omega_p \times \boldsymbol{\theta}_{\hat{S}_l}^T \cdot \boldsymbol{\Sigma}_{b,\boldsymbol{\vartheta}_t} \tag{8.4}$$

$\boldsymbol{\theta}_{\hat{S}_l}$ are the parameters of the $\hat{S}_l$ model, and $\boldsymbol{\Sigma}$ is a vector whose components are the integrals of the basis functions $B_p(\lambda, T)$ defined in chapter 6, convolved with the telescope transmission $T_b(\lambda)$: $\boldsymbol{\Sigma}_p = \int B_p(\lambda, T)\ T_b(\lambda, \boldsymbol{\vartheta}_t)\ d\lambda$.

The calibration parameters are classically determined by minimising a χ^2 built from the measurements of the LED calibration light observed through the different telescope passbands, and from the corresponding predictions φ_{bl}. Since φ_{bl} is not a linear function of $\boldsymbol{\vartheta}_t$ we linearise it:

$$\varphi_{bl} = \delta\omega_p \times \boldsymbol{\theta}_{\hat{S}_l}^T \cdot (\boldsymbol{\Sigma}_0 + \boldsymbol{Y}\ \boldsymbol{\delta\vartheta}_t) \tag{8.5}$$

at each minimisation step. $\boldsymbol{\Sigma}_0$ is the the "current" value of the $\boldsymbol{\Sigma}$ vector at a given step, and $\boldsymbol{Y}$ is a matrix containing its derivatives with respect to the calibration parameters. Both are computed numerically, the full minimisation taking a little less than 5 seconds on a laptop.

8.3 Tests on Simulated Data – Statistical uncertainties

As the method described above involves a slightly non-linear fit, we test it on simulated data. A goal is to check that the problem is not degenerate, and that the fit is not biased. Another important output of this simulation work is the assessment of the quality of the constraints that may be obtained from typical 45-mn to 1 hour DICE calibration runs.

Simulated scenarios The precision obtained after a few runs is going to be a function of the precision of the flux measurements performed on site, but also of the wavelength coverage of each filter. For each imager (MegaCam and SkyMapper) and each calibration source (SnDICE and SkyDICE), we assess what can be done with the source already installed in the telescope enclosure (SnDICE for MegaCam and SkyDICE for SkyMapper respectively). We therefore study two different situations which are summarised in table 8.1.

Simulated datasets To emulate these situations, we run the simulation described in chapter 4 (ideal gaussian LED spectra) with three different possible wavelength coverages: the SnDICE-like coverage (as seen for example on figure 3.4a), the SkyDICE coverage (figure 3.4b). In table 8.1 we indicate, for each band, the number of LEDs that may be used to constrain the passband shape and normalisation. These numbers depend on the filter width and the density of LEDs in the corresponding wavelength range. We see in particular that for SkyMapper, the u- and v-filters which are quite narrow are not extremely well covered.

		u	v	g	r	i	z	Duration (mn)
1	MegaCam (SnDICE)	6	–	8	7	7	6	54
4	SkyMapper (SkyDICE)	3	3	8	7	5	6	52

Table 8.1: *Typical MegaCam and SkyMapper calibration runs.*

We then generate synthetic flux measurements by integrating the true (gaussian) spectral intensities of the LEDs into the (un-distorted) passbands of the imager under-study. For each measurement, the photon noise is negligible, as the flux is generally measured on large super-pixels (millions of photo-electrons). On the other hand, the main source of noise comes from the presence of diffraction patterns all over the calibration frame. This contribution to the noise is very significantly reduced to $\sim 0.1\%$ is we average the calibration flux over large enough super-pixels. It is further reduced by making sure that the relative position of the telescope with respect to the source varies slightly from one calibration run to another – this way, the position of each diffraction pattern changes. Another issue seems to be the estimate of contamination by ghosts (stray light), which is proportional to the flux. For SkyMapper, contamination by ghosts is small, as most filters are made of coloured glass. Given the repeatability observed on typical sequences, we simulate a relative uncertainty of 0.5% (i.e. the uncertainty affecting each measurement is proportional to the flux registered on the focal plane).

The calibration parameters $\boldsymbol{\vartheta}_t$ are reconstructed from these simulated datasets following the method in the previous section.

Typical calibration runs As can be seen from table 8.1 and figures 3.4a and 3.4b, each passband is covered by 3 to 9 LEDs, depending on the extension of the filter. In general, each filter front is sampled by one to two LEDs –except with SnDICE, the early prototype, which presented an under-sampled region around 700-nm, precisely at the location of the red front of the r-filter, and the blue front of the i-filter. In table 8.1 we estimate the number of exposures of typical MegaCam and SkyMapper calibration runs. We also give a (conservative) estimate of the run duration, assuming about one minute per exposure, plus 20-minutes of overheads (filter changing, telescope pointing...) per run.

DICE has been designed to be run in routine mode, every day or so. We expect the normalisation of the passbands to change slightly from one night to another. On the other hand, we do not expect the position of the filter fronts to move in a measurable way overnight. As a consequence, we will typically combine all the calibration data into one single fit, fitting for one normalisation per filter and per run, but only one position for each filter front. This allows us to improve sizeably the precision of all calibration parameters, at the price of a slightly more complex procedure, as we typically fit for $\sim N_{bands} \times N_{runs} + 2 \times N_{bands}$ (e.g. 72 parameters for 10 SkyMapper calibration runs).

8.4 Systematics

The calibration measurements are expected to be dominated by systematics after a short number of calibration runs. These systematics come predominantly from the test bench characterisation of the source. We have studied them in chapter 4 (see in particular table 4.7). They are described by seven parameters: two related to the NIST photodiode, and five to the monochromator (wavelength calibration and transmission). We group them into one single vector $\boldsymbol{\delta\eta}_b$, and we note $\boldsymbol{V}_{\mathbf{sys}}$ the associated (diagonal) covariance matrix, built from the uncertainty estimates listed in table 4.7.

Propagation In section 6.5 of chapter 6 we have discussed how we propagate the test bench systematics on our estimates of the LED spectral intensities $\hat{S}_{\rm led}(\lambda, T)$. What we do is that we compute numerically the derivatives $\boldsymbol{H}_{\hat{S}}$ of the spectral intensity models $\hat{S}(\lambda, T)$ as a function of $\boldsymbol{\delta\eta}_b$. The impact of the bench systematics on the value of $\hat{S}$ or on the associated broadband systematics is derived from there by a simple Taylor expansion.

We now detail how we compute their impact on the determinations of the calibration parameters, $\boldsymbol{\vartheta}_t$. There are several equivalent ways to go about it. What we do is that we include the $\boldsymbol{\delta\eta}_b$ parameters as nuisance parameters into the calibration fit described in the previous section, adding their uncertainty estimates $\boldsymbol{V}_{\rm sys}$ as priors in the χ^2. More specifically, the χ^2 to minimize is of the form:

$$\chi^2 = \sum_{bl} w_{bl} \left(\varphi_{bl}(\boldsymbol{\vartheta}_t, \boldsymbol{\delta\eta}_b) - \phi_{bl}\right)^2 + \boldsymbol{\delta\eta}_b^T \boldsymbol{V}_{\rm sys}^{-1} \boldsymbol{\delta\eta}_b \tag{8.6}$$

where the b and l run over the bands and the LEDs respectively, the φ_{bl} are the model predictions and the ϕ_{bl} are the flux measurements performed with the imager. The $\boldsymbol{\delta\eta}_b$ are fit along with the calibration parameters, and marginalised over. This is the most direct and exact way to compute their contribution to the total error budget.

Again, the fit is non linear, and the model is linearised at each step, as follows:

$$\varphi_{bl} = \delta\omega_p \times \left[\boldsymbol{\theta}_{\hat{S}_l}^T \cdot (\boldsymbol{\Sigma}_0 + \boldsymbol{Y}\ \boldsymbol{\delta\vartheta}_t) + \boldsymbol{\Sigma}_0^T \boldsymbol{H}_{\hat{s}}\ \boldsymbol{\delta\eta}_b\right] \tag{8.7}$$

which is the equivalent of equation 8.5, with the systematics. Our (un-optimised) implementation of the calibration fit with systematics is reasonably fast. On a standard laptop, is takes from 10 seconds for a single run, to 2-3 minutes if we combine 20 to 25 runs.

Covariances The test bench systematics are shared by all LEDs. Hence, we expect them to introduce sizeable off-diagonal terms in the covariance matrix of the calibration parameters. On figure 8.2, we show typical correlation matrices obtained from the fit of ten (simulated) calibration runs. The matrix elements labeled $\mathcal{N}_x$ are related to the filter normalisation (relative to the r-filter normalisation). The elements labeled $\delta\lambda_x$ are the filter front displacements.

The left panel shows what is obtained when we assume that the NIST uncertainty display wavelength-dependent correlations (worst case scenario), while the right panel shows what

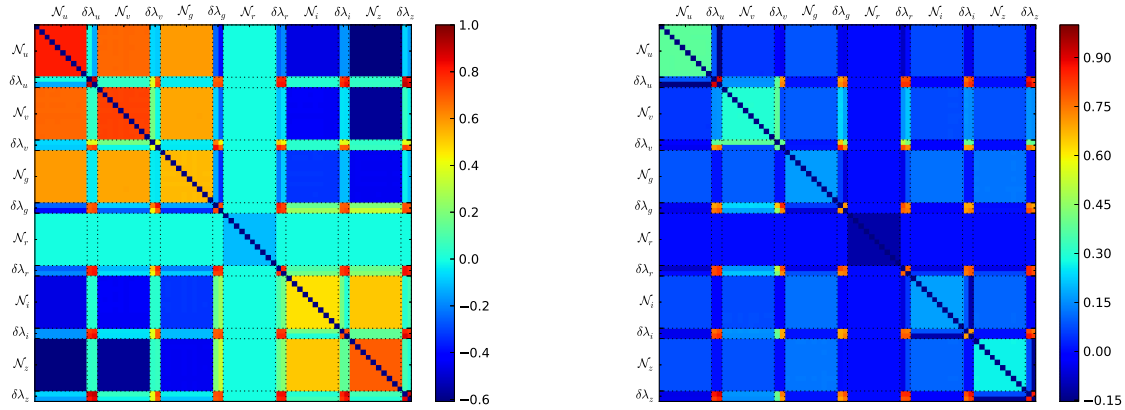

(a) α_{NIST} (worst case)

(b) No α_{NIST} (best case)

Figure 8.2: *Correlation matrix of the calibration parameters for two hypotheses of the NIST error budget. In both cases, the filter fronts are all positively correlated. This is because they all share the monochromator calibration uncertainty, which is the dominant contribution to the error budget.*

we get when assuming that the NIST uncertainties are all positively correlated (best case scenario). Not surprisingly, in the worst case scenario, the band-to-band correlations of the normalisation terms are sizeable, while they essentially vanish is the best case scenario. We also see that the filter front displacements are all positively correlated. Indeed, they all share the uncertainty on the monochromator wavelength calibration, which is the dominant contribution to their error budget.

In all cases, our method permits to compute exactly the stat+syst covariance matrix affecting all the calibration parameters. It can then be propagated into the subsequence cosmological analyses.

8.5 Expected Precision for SkyMapper

The scenarios discussed in section 8.3 have been explored with a series of simulations. The analysis of the commissioning data with the method described above is still ongoing, and we therefore present here the main results obtained from the simulated datasets. In all cases, we have found that the fits are well constrained, and do not display any sizeable bias (as shown for example on figure 8.3). Besides a series of checks of the method, the most valuable output of the simulations is a quantitative estimate of the statistical and systematic uncertainty budget. We present the main results of this study in the remaining of this section.

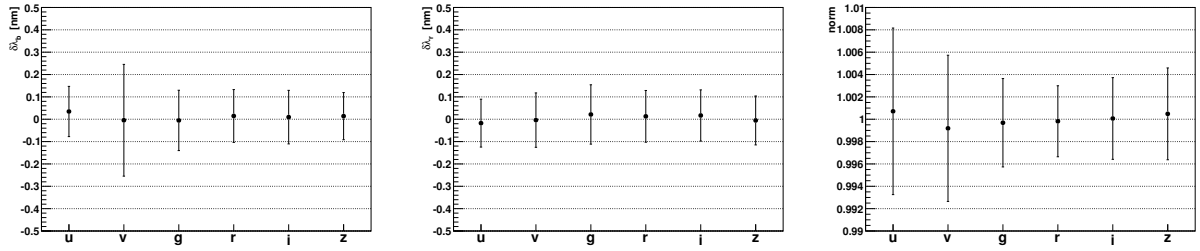

Figure 8.3: *Average of the calibration parameters reconstructed from 100 independent realisations. All the parameters are well constrained, and no significant bias can be detected on average. The error bars show the uncertainties as estimated from one single realisation.*

8.5.1 Filter Fronts

The statistical and systematic uncertainties affecting our estimates of the filter front displacements, after one calibration run, are displayed on figure 8.4. As expected, the statistical uncertainties are a close-to-linear function of the measurement noise. The total (stat+syst) uncertainty budget follows a similar law, expect that it is bounded from below by a systematics floor (which corresponds to the 1Å error on the monochromator wavelength calibration).

From our inspection of the commissioning dataset, we expect the measurement noise to be of about 0.5%. This means that in one single calibration run, we should be sensitive to filter front displacements of 1Å to 5Å (depending on the quality of the filter coverage). This is an important result, as it shows that we can get to high precisions despite the fact that we are measuring our filters with non-monochromatic sources. The key here is a good knowledge of the source spectrum, and some a-priori knowledge of the telescope effective passbands.

We show on figure 8.5 that the uncertainty budget decreases significantly as we increase the number of calibration runs. For an expected measurement noise of 0.5%, we reach the systematics floor after about 10 calibration runs.

For MegaCam, we find similar sub-nanometer uncertainty budgets, excepted for the red-cutoff of the r-band and the blue-cutoff of the i-band which are essentially unconstrained.

This is due to the poor quality of the filter coverage in this wavelength area. As noticed earlier in this manuscript, the large number of LEDs available today permits to obtain excellent constraints in the entire visible range.

8.5.2 Relative Normalisation of the Passbands

We now turn to the expected precision on the normalisation of the passbands. As noticed earlier, the cosmological measurements performed with SNe Ia are not sensitive to the absolute flux scale. For this reason, we are interested in assessing the uncertainties on the *relative* passband normalisations. In what follows, we will only consider the passband throughputs relative the the r-band throughput.

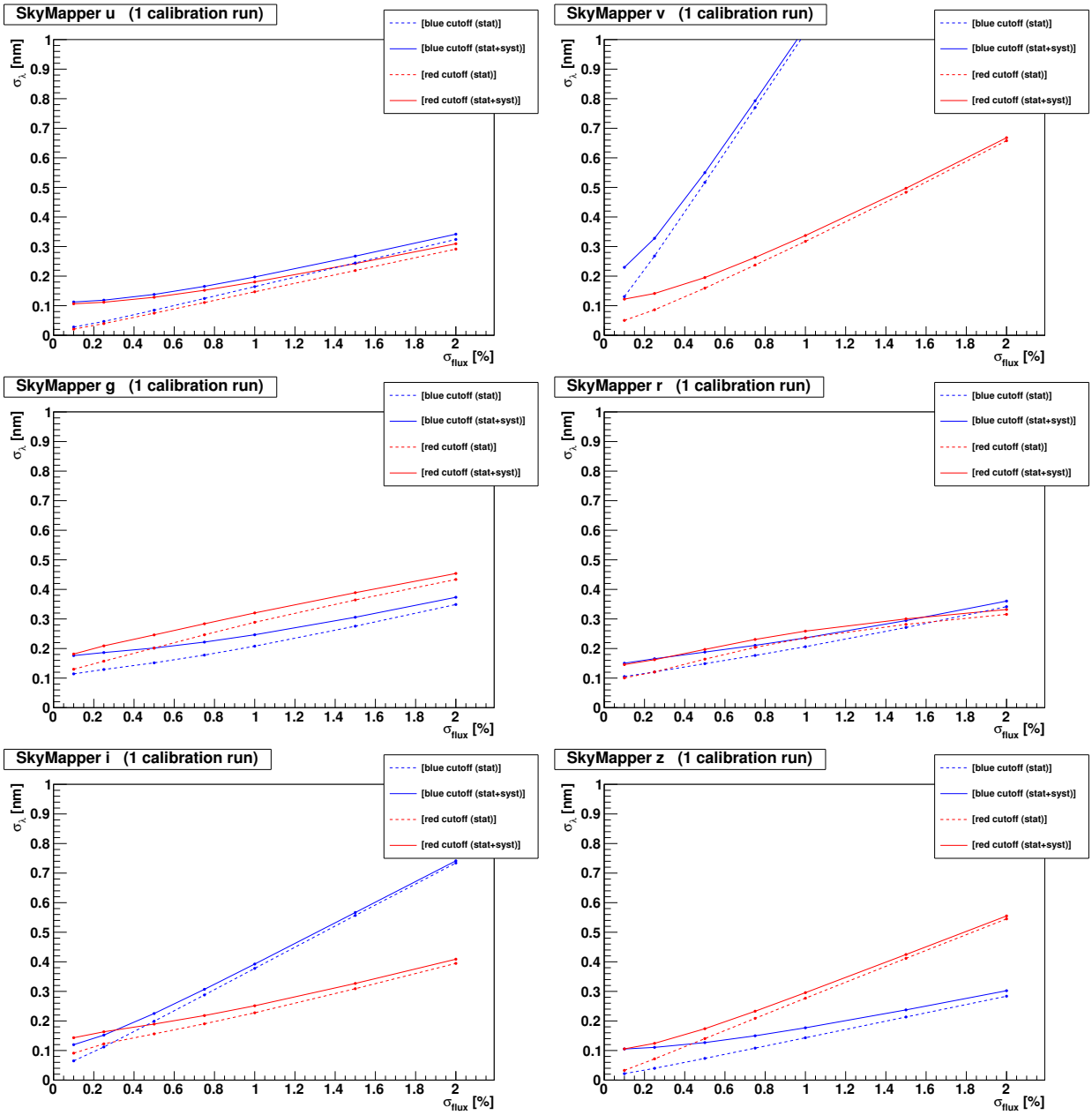

Figure 8.4: *Statistical and systematic uncertainties on the measurement of the SkyMapper filter front displacements with the SkyDICE source, as a function of the precision of the calibration flux measurements.*

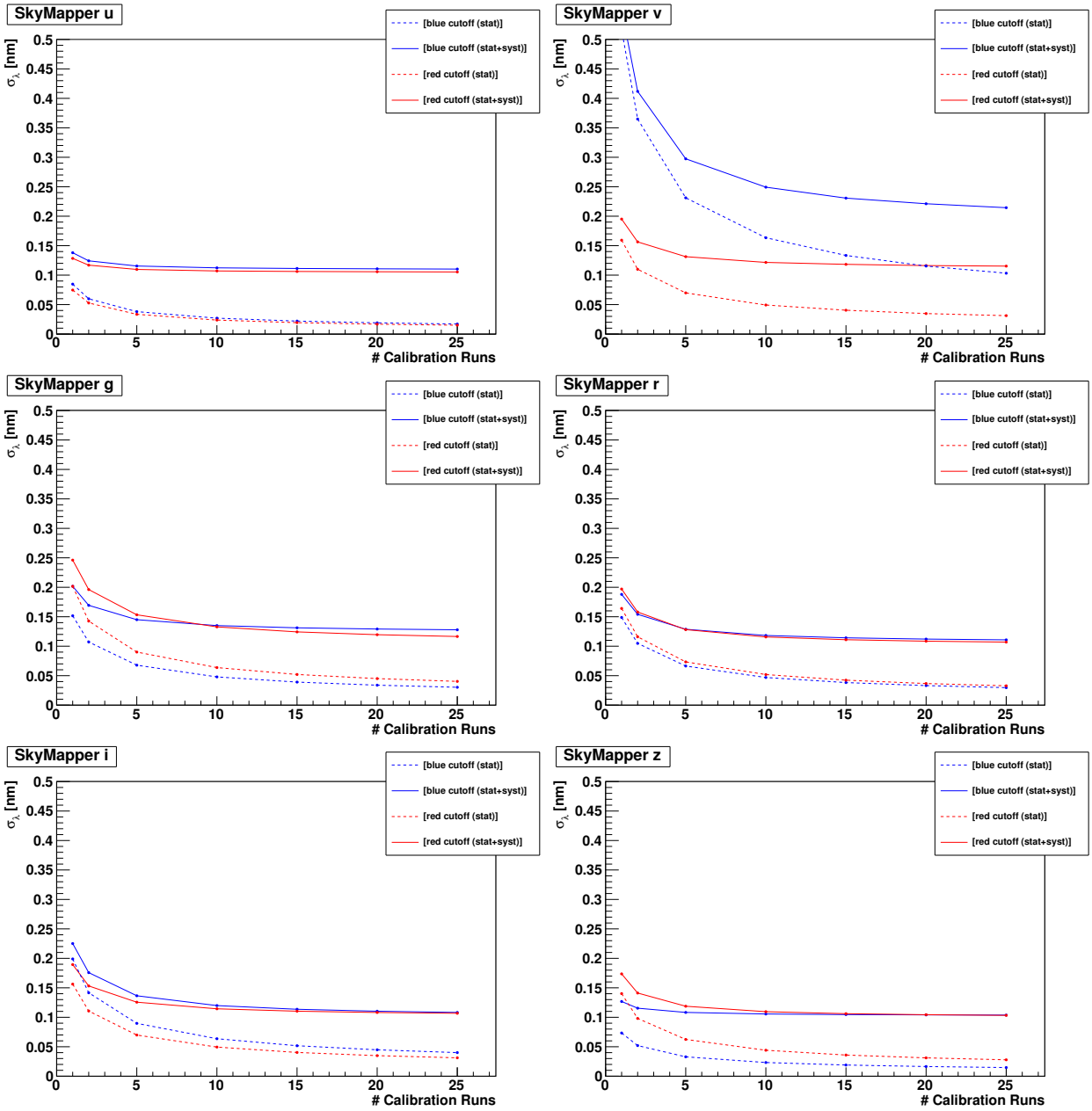

Figure 8.5: *Statistical and systematic uncertainties on the measurement of the SkyMapper filter front displacements with the SkyDICE source, as a function of the number of runs (assuming a precision of the flux measurements of 0.5%).*

We expect the NIST error budget to dominate the uncertainties on the passband normalisations. As discussed earlier, this budget is not well known, in the sense that the off-diagonal terms on the measurements on the photodiode efficiency $\eta(\lambda)$ are not known. In chapter 4 we have discussed two scenarios: an optimistic scenario, in which all the NIST uncertainties are positively correlated, hence, have essentially no impact on the relative normalisation of the passbands. We also discussed a "worst-case scenario", where the uncertainties at the extremes of the wavelength range are negatively correlated. In the first scale, the NIST error budget is assumed to affect only the absolute flux scale, while in the second case it almost entirely corresponds to a "colour uncertainty".

The correlation matrices displayed in figure 8.2 show that both hypotheses result in very different off-diagonal terms. In figures 8.6 and 8.7 we show the diagonal terms as a function of (respectively) the measurement noise and the number of runs, for both interpretations of the NIST errors.

Let's first have a look on figure 8.6. In the best case scenario (dashed red line), the total uncertainty is almost equal to the statistical error budget, which is a linear function of the input noise (with a slope that depends essentially on the number of LEDs used to constrain the filter. In the worst-case scenario (plain black line), the calibration error is slightly higher, due to the impact of the colour uncertainty affecting $\eta(\lambda)$. The true calibration error lies somewhere is the band defined by the two lines. For a measurement noise of $\sim 0.5\%$, the total uncertainty reached in a single calibration run is comprised between 0.5% and 1% (or slightly less), depending on how we interpret the NIST error budget.

On figure 8.7 we show how the error varies as a function of the number of runs. Again, the systematics floor is almost attained in 15 to 20 runs. This floor is comprised between 0.4% and 0.6% for the bluer bands and 0.3%-0.4% for the redder bands of the imager.

8.5.3 Relative impact of the Bench Systematics

The test bench systematics floor seems to be attained after a relatively small number of runs. Of course, we also have to consider the systematics affecting the imager measurements of the calibration flux (currently under investigation). These systematics will also play a role, and push the final error budget slightly higher. However, preliminary investigations let us think that these contributions will not be dominant, especially for SkyMapper.

The relative importance of each bench systematics is summarised in table 8.2. Regarding the filter positions, our main systematics is clearly the error on the wavelength calibration of the monochromator. This uncertainty affects simultaneously all estimates of the filter fronts, which are therefore (almost completely) positively correlated after a few runs.

On the flux calibration side, the dominant contribution seems to be the NIST error budget.

8.6 Conclusion

In this chapter, we have presented a method to constrain the passbands shapes are normalisations with series of SkyDICE exposures. This method combines results from the test bench

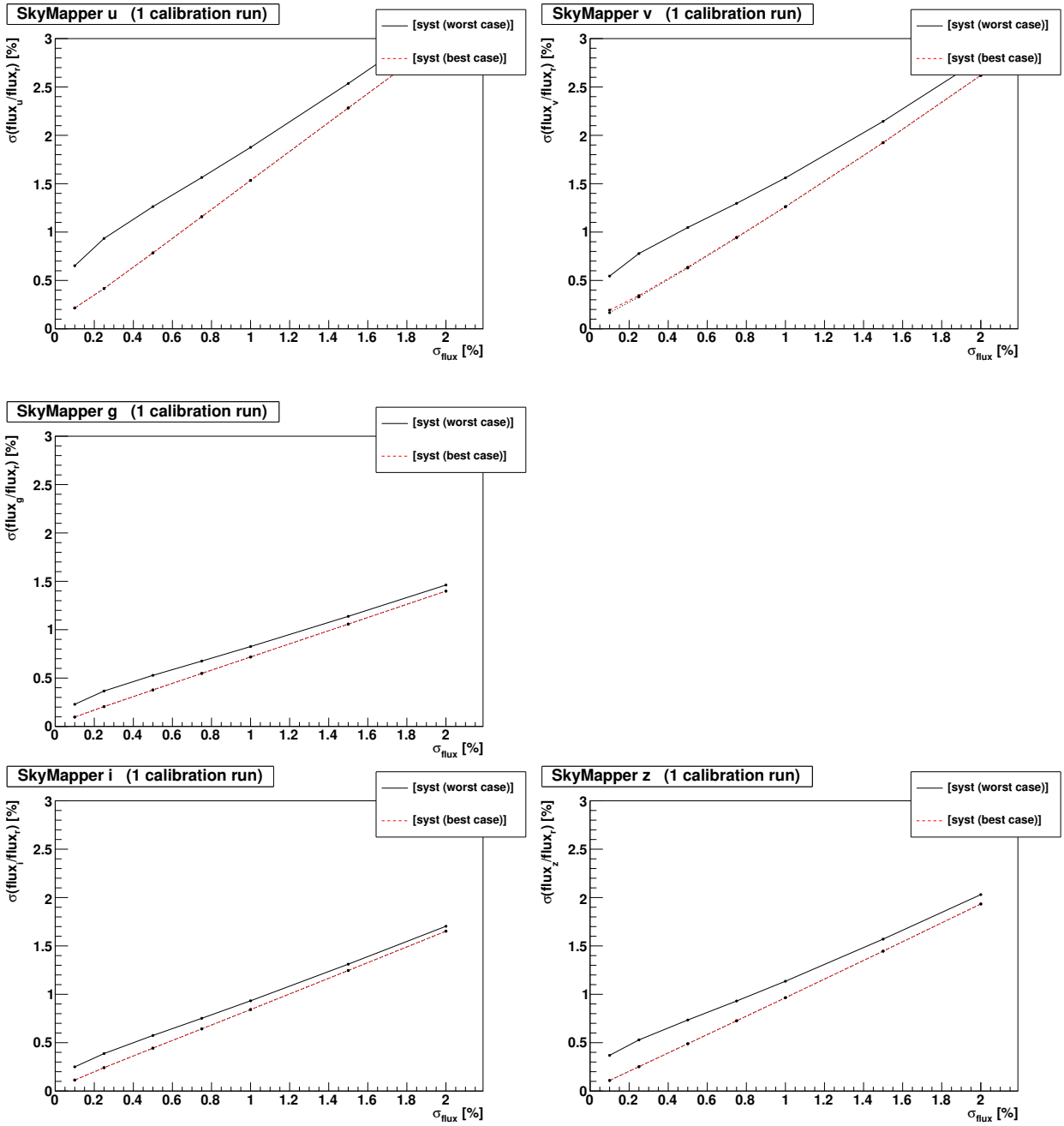

Figure 8.6: *Statistical and systematic uncertainties on the measurement of the SkyMapper filter normalisation (relative to the r-band) as a function of the precision of the imager flux measurements.*

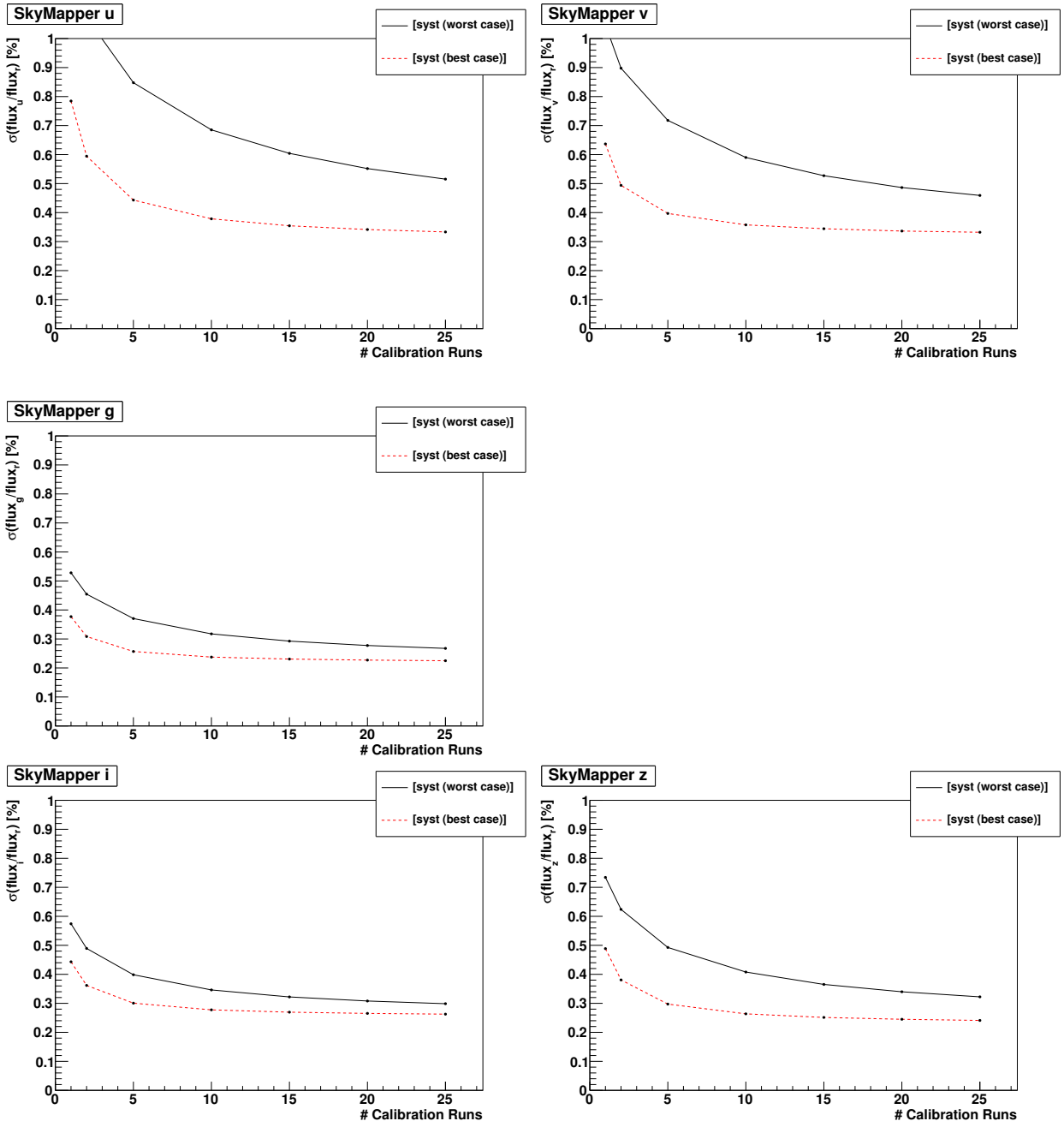

Figure 8.7: *Statistical and systematic uncertainties on the measurement of the SkyMapper filter normalisation (relative to the r-band) SkyDICE source, as a function of the number of calibration runs (assuming a precision of the imager flux measurements of 0.5%).*

	filter fronts (nm)	flux calibration (relative to r, %)
Wavelength calibration	0.1	< 0.2
Monochromator transmission	$\lesssim 0.1$	$\lesssim 0.2$
NIST photodiode calibration (best case)	< 0.1	$\lesssim 0.2$
NIST photodiode calibration (worst case)	< 0.1	$0.3 - 0.6$
Total	~ 0.1	$\sim 0.3 - 0.6$

Table 8.2: *Systematics affecting the final SED measurements.*

analysis presented in chapters 4 and 6 into a model that can predict the calibration flux, as a function of the passband shapes and normalisations. This model is compared to the calibration measurements performed with the telescope, in order to determine a series of calibration parameters, namely passband normalisations, and potential filter front displacements. The method yields the full (stat+syst) covariance matrix of the calibration parameters, which can then be propagated into any subsequence science analysis.

The DICE calibration source does not emit monochromatic light. As a consequence, it cannot constrain entirely the shape of the passbands. We have shown that it is nevertheless sensitive to ~ 1Å variations of the position of the filter cutoffs. A DICE calibration source is therefore a very sensitive monitoring tool that can be used to follow potential passband alterations at minimal cost (i.e. ~ 1 hour calibration runs).

Regarding the passband normalisations, DICE again seems to display an excellent constraining power. The systematics floor is of about 0.3%, and comes mostly from our knowledge of the NIST photodiode efficiency. In order to improve on this, a better knowledge of the NIST error budget seems to be essential.

The analysis of the commissioning data (chapter 7) using the method presented here is still ongoing, and first constraints on the SkyMapper passbands should be soon available.

Conclusion

A few months after SkyDICE was installed on site, Siding Spring Observatory was ravaged by a bush fire. Fortunately, no telescope was seriously damaged, except for ashes and smoke in the domes (especially on the optical surfaces). SkyMapper has resumed taking data a few weeks ago. It is possible that SkyDICE was affected by the smoke and the high temperatures that have been recorded in the enclosure of the telescope. Very likely, a recalibration of the device is in order.

The outcome of the project is nevertheless extremely positive. We have shown that it is possible to build a LED based light source that samples evenly the full visible wavelength range. The stability of the source is remarkable, ranging from a few $\sim 10^{-4}$ for a few of the LEDs, to 10^{-3} for the less stable channels. I have detailed the spectrophotometric characterisation of the device on our test bench at LPNHE. More importantly, I have shown that it is possible to build a smooth spectrophotometric model of each LED, that can predict the LED spectrum at any temperature (in a temperature range representative of what is measured in the telescope enclosure). Each of these models comes with an uncertainty budget that accounts for (1) the finite number of spectroscopic and photometric measurements and (2) the test bench uncertainties.

Finally, I have described a method to calibrate the effective passbands of the imager, and monitor their fronts from series of calibration frames taken with SkyDICE. This method takes into account all the test bench uncertainties and they are propagate as exactly as possible to the final result. It is currently being applied to the real SkyDICE dataset, and what has been presented here is a set of tests performed on (realistic) simulated datasets. A important result of this work is that, despite the fact that the LEDs are not monochromatic sources, we are able to control the position of the filter fronts with an accuracy well below 1-nm.

Regarding the passband inter-calibration, we have computed the expected uncertainties affecting our estimates of the passband normalisation, relative to the r-band. These uncertainties actually depend on how we interpret the uncertainties that affect the calibration of the NIST photodiode. In the "best case" scenario, where the NIST uncertainties are all positively correlated, we have shown that after a few calibration runs, we get down to a precision of $\sim 0.4\%$ in the u- and v-bands (near-UV) and of $\sim 0.3\%$ in the other bands.

Depending on how we estimate the CALSPEC uncertainties (which are themselves uncertain), this result is either a major improvement on CALSPEC, or on par with what can be obtained with CALSPEC. In any case, this means that by using routinely a DICE source to calibrate a survey telescope, we should be able to test the CALSPEC flux scale.

The analysis of the SkyDICE commissioning dataset is still ongoing. The main missing ingredient is the control of the relative positions of the telescope and the sources, as well as an estimate of the pollution of the calibration frames. These two aspects of the analysis are actively worked on, and the first constrains should be published soon.

Appendix A

SkyMapper Optical Model

A.1 Optical Model of SkyMapper Telescope

We have developed a simple model of SkyMapper optics, to predict the focal plane illumination for each SkyDICE exposure. This model is used as a tool to guide the design of the illumination system. It will also be used to interpret the SkyDICE exposures. The model is written in `C++` using the `ROOT`[1] framework software. In what follows, we summarise the characteristics of the optical surfaces and optical materials that were used into the model. Then we present in section §A.2, various tests of the optical model. Finally, we describe how we computed the focal plane illumination for any SkyDICE exposure in §A.3.

A.1.1 Strategy

The modelling strategy is very simple. SkyMapper and SkyDICE are implemented as a set of volumes. The position, orientation and shape of these volumes is defined with the help of `ROOT` framework.

The model actually comprises two main components. First, a set of geometrical routines that allow one to compute relative positions and orientations of the illumination device and the telescope, this for any exposure. Second, an optical model of SkyMapper, that permits to track any ray emitted from SkyDICE, and to predict the focal plane position of the resulting impacts, and this, for the direct light as well as for a selection of ghosts. To track the rays, we have written a very simple ray-tracer, implementing the snell-descartes law.

The intensity of rays (direct light or ghosts), that hits the focal plane depend on the reflectivity and transmissions of the optical surfaces. The goal of SkyDICE is to measure these quantities. Hence, the reflectivity and transmissions of each optical element are treated as parameters of the model. Knowing them a priori is not really important, since our goal is to measure them by comparing the model predictions with the SkyDICE data.

On the other hand, the position of the rays depend on the geometry of the optical surfaces. The SkyDICE planet channel will allow us to check the correctness of the model, but does not permit to measure them directly. Hence, it is crucial to ensure, that this simple optical

[1] CERN data analysis framework (`http://root.cern.ch`).

model is correct. In what follows, we summarise the characteristics of all the model elements, and we describe the tests we have performed on the model.

The information on the SkyMapper optics was extracted from a ZEMAX file sent to us by P. Tisserand. Some additional information was obtained from the published SkyMapper paper (Keller et al. 2007, Bessell et al. 2011).

A.1.2 Mirrors and Lenses

The optical design of SkyMapper has been optimised for wide-field observations in visible and near-IR. The main configuration is a modified Cassegrain (focal plane behind primary mirror), with hyperbolic primary and secondary mirrors completed by a set of three wide field corrector lenses.

The first lens, L1 is positioned between the primary and secondary mirrors, the other two (L2-L3), between the primary mirror and the focal plane. The front-face of L1 is an aspherical surface.

The optical system is baffled to ensure that no stray light reaches the CCD detector. We have modelled very carefully all the optical elements (mirrors, lenses, filters, cryostat window). For the baffling, we have included only the surfaces that might block the beam for some orientations of SkyDICE relative to the telescope. On figure A.1 we show a 3 dimensional visualisation of our model, along with a realistic representation of the SkyDICE beam.

The position and shapes of the optical elements included in the model are summarised in table A.1. The characteristics of the optical materials (refraction index) are summarised in table A.3.

At almost all wavelengths, the lens transmittance is greater than 88% (Keller et al. 2007). We do not know much about the internal absorption of these elements. At this point we assume that the transmission $\mathcal{T}$ is related to the reflectivity $\mathcal{R}$ by: $\mathcal{T} = 1 - \mathcal{R}$.

A.1.3 Filters

SkyMapper has a set of 6 filters *uvgriz* made by different manufacturers (Bessell et al. 2011). The characteristics of each filter are summarised in table A.2. The exact position of each filter along the optical path is not known with micro metric precision.

The u, v, g and z filters are made of coloured glass. Hence, their transmission is extremely uniform and does not depend on the incidence angle. r and i, on the other hand, are dielectric filters. Their uniformity is not as good and their effective transmissions are expected to depend on the incidence angle of the rays.

The angular dependence of interference filters transmissions can be approximated by:

$$T(\lambda, \theta) = T\left(\lambda\left[1 - \frac{\sin^2\theta}{n^2}\right]^{-1/2}, \theta = 0\right) \tag{A.1}$$

where n is the refracting index of the filter, and θ the incidence angle. This expression, exact for a single fabry-perrot layer, should be accurate enough to describe the angle depen-

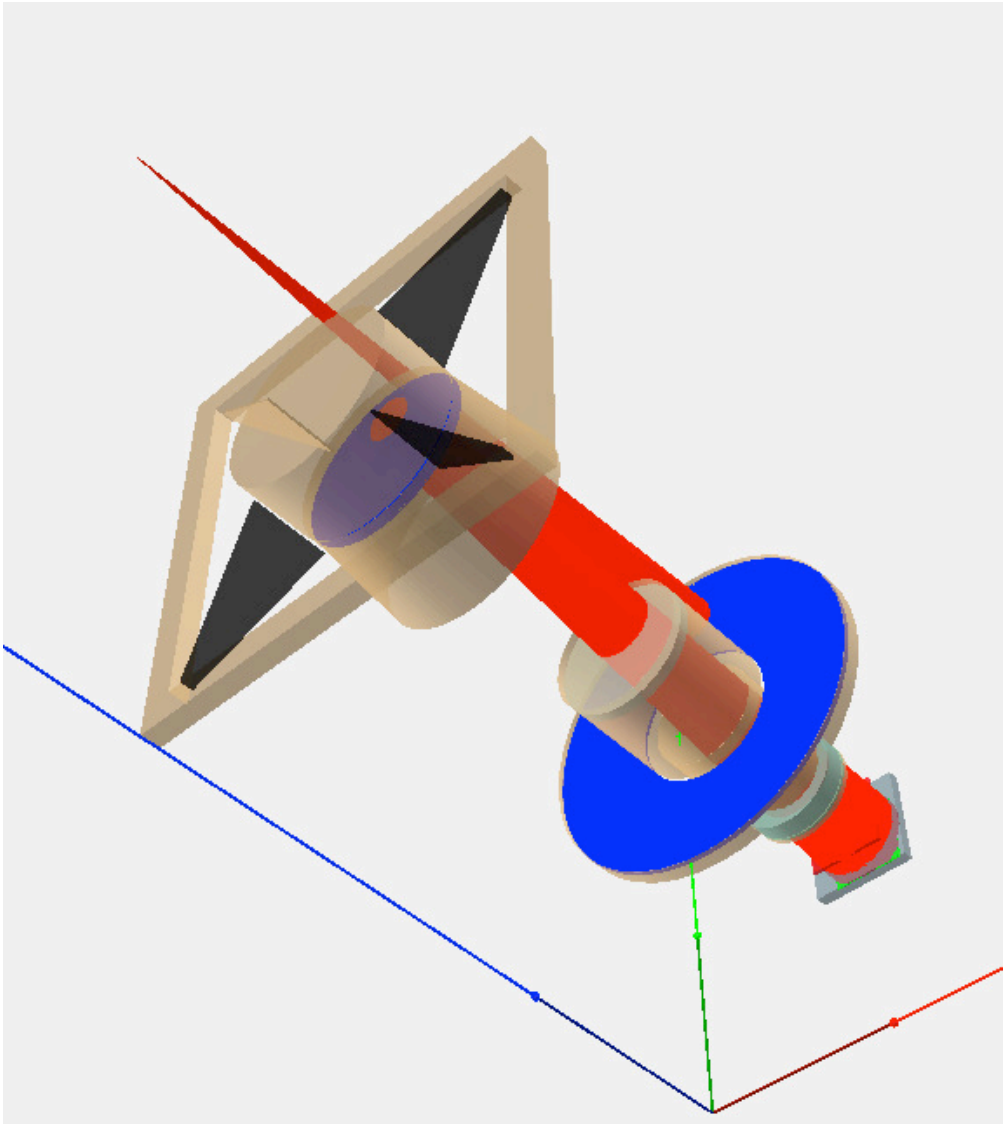

Figure A.1: *3-dimensional model of the SkyMapper optics. In red we have represented the SkyDICE beam used for our simulations.*

dance of the transmission. For these filters, we still have to measure n from transmission measurements performed at various angles by the SkyMapper team. In any case, these transmissions will be measured in situ from SkyDICE observations, so it is not crucial to known them *a priori*. The filters should have a uniformity of 1% across the entire surface. These variations are believed to be radial at first approximation. The transmission of each filter has been measured at normal incident angle, at various positions.

A.1.4 Detectors and Optical Materials

The SkyMapper focal plane is made by 32 CCDs. The exact spacing between all these CCDs is currently not known with precision. It will be possible later to measure it in situ, using a set of science exposures with well measured WCS transformations. There are significant disparities between detectors, that should be routinely measurable from SkyDICE exposures.

Element	R_1 (m)	K_1	R_2 (m)	K_2	Radius (m)	Thickness (m)	$z^{(d)}$ (m)	Material
M1	-	-	5.9120	-1.626	0.675	0.150	0.	ULE[b]+ Aluminum
M2	-	-	4.9810	-19.41	0.34985	0.070	$1.64645 + focus$	LE© + Aluminum
L1	7.9769	0.[a]	4.8207	0.	0.275	0.045	0.45181	HPFS 7980 Class AA
L2	0.5566	0.	1.0304	0.	0.2155	0.070	-0.5208	HPFS 7980 Class AA
L3	0.8261	0.	0.7747	0.	0.2155	0.0829	-0.538	HPFS 7980 Class AA

[a] - plus an a-sphericity correction: $-1.386\times10^{-16} \times y^6$, y in mm.
[b] - Ultra Low Expansion Glass
[c] - Low Expansion Glass
[d] - with respect to the vertex of the M1 mirror.

Table A.1: *SkyMapper main optical elements.*

	w (m)	l (m)	Thickness (m)	$z^{(a)}$ (m)	Type & Material
u	0.309	0.309	0.0145	-0.85585	6.2mm UVC2 + 8.3mm B270
v	0.309	0.309	0.0145	-0.85585	3mm yΦC1 + 6.5mm C3C23 + 5mm BC7
g	0.309	0.309	0.0147	-0.85585	4mm GG420 + 5mm C3C21 + 5.7mm BC4
r	0.309	0.309	0.015	-0.85585	15mm BK7 + LWP + SWP
i	0.309	0.309	0.0145	-0.85585	6mm KC19 + 8.5 mm
z	0.309	0.309	0.0146	-0.85585	4.5mm RG850 + 10.1mm B270
Window	0.378	0.378	0.025	13.65675	Fused Silica + BBAR-384
Focal Plane	0.300	0.300	0.000	13.68375	E2V CCDs Silicon

[(a)] - with respect to the vertex of the M1 mirror. Note that we do not know the exact position of each filter.

Table A.2: *SkyMapper focal plane elements.*

Optical Material	n
HPFS 7980 Class AA	1.465763
Filters[(a)]	1.531250
Fused Silica	1.458464
BBAR-384	1.459000

[(a)] - We have used the average value of the g filter.

Table A.3: *Materials and coating properties.*

A.1.5 Baffling System

Some non-optical surfaces have been added to the model, especially those which may block the SkyDICE beam. They are currently modelled as perfect absorbers. The most important ones are:

1. The baffles of M1 and M2: the most important is the one on the secondary mirror. The correct shape is a cone section with a length of 0.4518 m.
2. The baffles of L1 and L2/L3.
3. The spiders and the upper cap over the secondary mirror.

A.2 Checking the Model

The best way to check the model is to compare it with the SkyDICE exposures. Before SkyDICE is installed, we were able to perform simple checks. Among those:

- checking that a parallel beam is correctly focussed.
- checking with the SkyMapper team (using the original ZEMAX model) that we predict correctly the position of the ghosts for some relative orientations of SkyDICE and SkyMapper telescope.
- checking (with the ZEMAX model), that we can predict the correct plate scale variations.

In particular, we have checked the focus of the mirror and the pattern of direct and reflected lights. To evaluate that we have built a simple model of the SkyDICE source using `C++` language. Inside this model we have three different type of beams:

- The “single shot” source.
- The “random” beam.

- The “planet” beam.

For the “planet” beam we can also choose the width of the conical beam. We also set up two others different types of beam: “half-moon" (like the “planet" but with a semi-conical beam) and a “slit" beam (like a grating system).

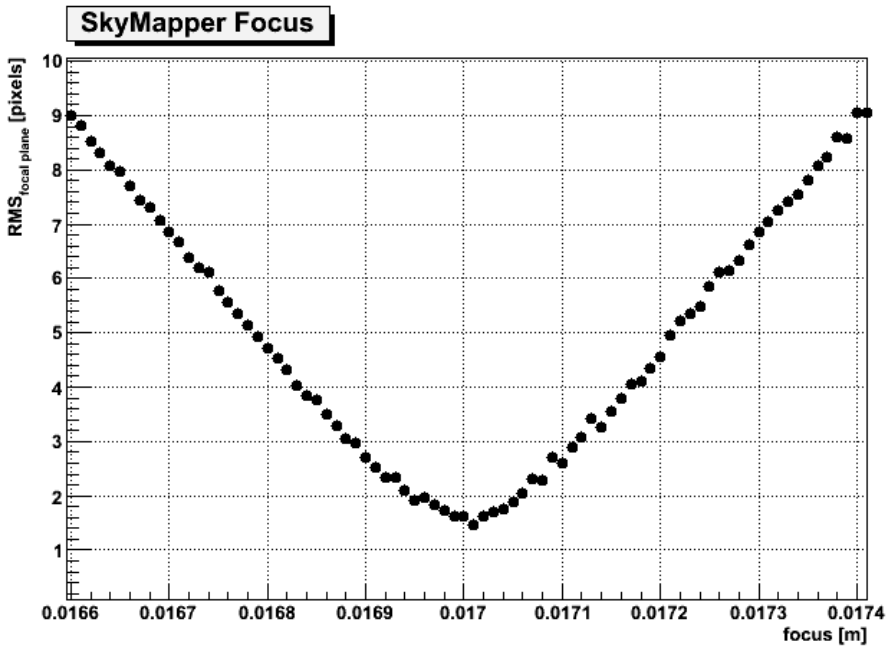

Figure A.2: *The plot represent the Root Mean Square (in pixel units) versus the position of the secondary mirror (focus of the telescope). We found a value of* ~ 1.5 *pixels (*$22.5\ \mu m$*) at a focus of* $+0.01702$ *m.*

A.2.1 Focus

The simplest test is the focus of the telescope. This test is fundamental because it tell us if we have set correctly the shapes and positions of optical surfaces. Figure A.2 shows the size (RMS in pixels) of the resulting spot when illuminating the telescope with a parallel beam ($\sim 100,000$ rays). The best focus is obtained by shifting the secondary mirror by $+0.01702$ m with respect to the original position (see tables above). The resulting spot has a RMS size of about 22.5 μ m, around 1.5 pixels.

Using a “random” source with $\approx 100,000$ rays perpendicular to the z axis of the telescope at a distance of 3 m from the main mirror. The final value of the average position of all rays inside a circle of 22.5 μm. The fact that each pixel of SkyMapper CCD camera is 15 μm, we have obtained a focus of ~ 9 pixels. This value is not acceptable for simulating real data, but is good enough for our purpose. The figure A.2 shows the result.

A.2.2 Model Prediction and ZEMAX Model

A second test is to check and predict accurately the focal plane position of the ghosts. This would tell us if our optical surfaces are accurately positioned along the optical path.

Table A.4 gives the position of a fews ghosts, when illuminating the telescope with a single ray defined as:

$$O \simeq \begin{pmatrix} 0.22 \\ 0.48 \\ 3. \end{pmatrix} \qquad \vec{u} = \begin{pmatrix} 0. \\ 0. \\ -1. \end{pmatrix} \tag{A.2}$$

For each ghost, we indicate the focal plane position.

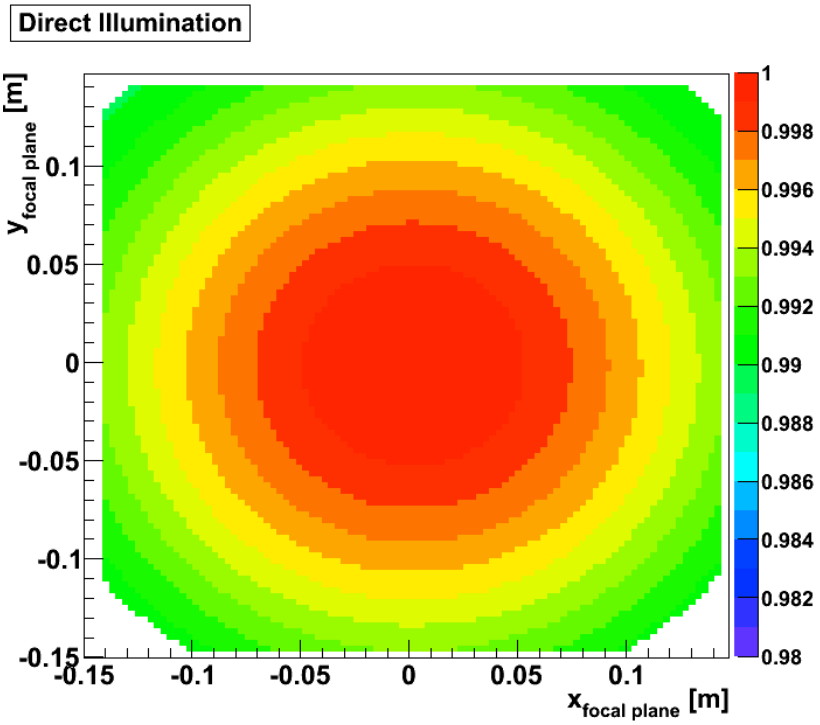

Figure A.3: *Direct light illumination on the focal plane. We can see a vignetting effect on borders on the focal plane.*

A.2.3 Plate Scale Variations

A last test is to check that we are predicting the plate scale variation across the focal plane well. Indeed, the flux recorded on the telescope focal plane is proportional to the solid angle subtended by each pixel. Figure A.3 shows the predicted plate scale variations. Our model predicts about 1%, centre-to-corner. Then on figure A.4 we show the ratio between the direct and the indirect (reflected) light in the focal plane of the camera model. The ratio is around 3%, acceptable for our purpose.

Ghost name	FP_x (m)	FP_y (m)
PrimaryMirror-SecondaryMirror	-0.002011182165	-0.004388033816
L3int-L3int L3int-L3int	-0.03932275974	-0.08579511216
L3int-L3int L2ext	-0.03746922209	-0.08175103002
L3int-L3int L2int-L2int	-0.009866133205	-0.02152610881
WINDOWint-WINDOWint WINDOWint-WINDOWint	-0.004453119919	-0.009715898005
WINDOWint-WINDOWint FILTERext	-0.01096399921	-0.02392145281
WINDOWint-WINDOWint FILTERint-FILTERint	-0.01166190422	-0.02544415466
WINDOWint-WINDOWint L3ext	-0.044206974	-0.09645157963
WINDOWint-WINDOWint L3int-L3int	0.0008832500757	0.001927091074
WINDOWint-WINDOWint L2ext	-0.00245442498	-0.005355109046
WINDOWint-WINDOWint L2int-L2int	-0.0612575745	-0.1336528898
FILTERint-FILTERint FILTERint-FILTERint	-0.00270908718	-0.005910735665
FILTERint-FILTERint L3ext	-0.02587750034	-0.05646000073
FILTERint-FILTERint L3int-L3int	-0.008148212183	-0.01777791749
FILTERint-FILTERint L2ext	-0.009667691117	-0.02109314425
FILTERint-FILTERint L2int-L2int	-0.03735389848	-0.08149941486
L1int-L1int L1int-L1int	-0.0236988068	-0.05170648757
CCDext WINDOWext	-0.003233016619	-0.007053854442
CCDext WINDOWint-WINDOWint	-0.005674954373	-0.01238171863
CCDext FILTERext	-0.01218583366	-0.02658727344
CCDext FILTERint-FILTERint	-0.01288373867	-0.02810997529
CCDext L3ext	-0.04673083695	-0.1019581897
CCDext L3int-L3int	0.002144467508	0.0046788382
CCDext L2ext	-0.001449741465	-0.003163072288
CCDext L2int-L2int	-0.06456548714	-0.1408701538
L3ext L2ext	0.0007562862785	0.001650079153
L3ext L2int-L2int	0.04915643275	0.1072503987
FILTERext L3ext	-0.02445889926	-0.0533648711
FILTERext L3int-L3int	-0.008844646513	-0.01929741057
FILTERext L2ext	-0.01022504185	-0.02230918222
FILTERext L2int-L2int	-0.03551172876	-0.07748013548
WINDOWext FILTERext	-0.008522061453	-0.01859358862
WINDOWext FILTERint-FILTERint	-0.009219966467	-0.02011629047
WINDOWext L3ext	-0.03918041164	-0.08548453449
WINDOWext L3int-L3int	-0.00161031173	-0.003513407412
WINDOWext L2ext	-0.004442901084	-0.009693602364
WINDOWext L2int-L2int	-0.05468211567	-0.1193064342
L2int-L2int L2int-L2int	0.04604744374	0.10046715

Table A.4: *Position on the focal plane of all reflections calculated using our ray-tracing model.*

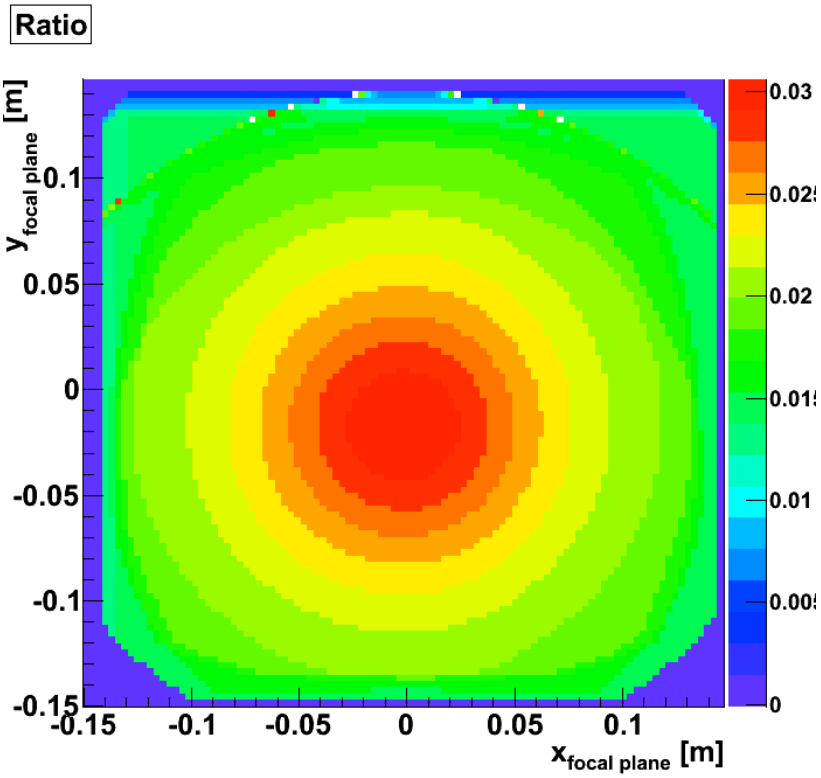

Figure A.4: *Ratio of reflected light over direct light on the focal plane. The max value is around* 3%*, acceptable for our purpose.*

A.3 Illumination by a Lambertian Beam

One of the nice aspects of the SkyDICE design, is that simulating the focal plane illumination is not computationally heavy, since there is a one-to-one relationship between the infinitesimal beam solid angles $\delta\Omega$ and the infinitesimal focal plane surfaces δS.

Simulating a SkyDICE flat field does not require computing an integral over the angles and/or the mirror positions. Then, it can be determined very quickly, without requiring expensive Monte-Carlo computations. The illumination recorded on a focal plane surface element δS at location (x, y) on the focal plane is given by:

$$\phi(x,y)\delta S = \sum_p \alpha_p \frac{\Phi}{J_p(xy)}\delta\Omega \tag{A.3}$$

where p runs over all possible paths (including at least two or more reflections within the optics), Φ is the emitted flux per unit solid angle and $J_p(x, y)$ is the Jacobian $\|\partial(xy)/\partial\Omega\|$.

Figure A.3 shows the resulting illumination for two SkyDICE orientations. As can be seen, there is a significant level of contamination by ghosts, at the level of $\sim 2-3\%$.

In table A.5 we also calculated the expected illumination in the focal plane for each LED installed in the SkyDICE source. In this calculus we used as reference current the nominal

I_{led} of every LED.

LED number	$\langle\lambda_p\rangle$ (nm)	I_{led} (ADU)	$\mathcal{B}$ W/sr/ADU	Beam (W)	E_γ (10^{-19} J)	N_{e^-}
8	320	5000	$8.394723\ 10^{-9}$	$1.174467\ 10^{-7}$	6.2076	$3.5241\ 10^{2}$
21	340	5000	$8.283531\ 10^{-9}$	$1.158911\ 10^{-7}$	5.8425	$3.6947\ 10^{2}$
2	365	5000	$4.163912\ 10^{-8}$	$5.825539\ 10^{-7}$	5.4423	$1.9938\ 10^{3}$
3	395	5000	$1.879078\ 10^{-7}$	$2.628932\ 10^{-6}$	5.0290	$9.7371\ 10^{3}$
22	420	1000	$3.017910\ 10^{-7}$	$8.444441\ 10^{-7}$	4.7296	$3.3256\ 10^{3}$
4	450	1000	$1.093368\ 10^{-6}$	$3.059363\ 10^{-6}$	4.4143	$1.2909\ 10^{4}$
17	465	1000	$1.579288\ 10^{-6}$	$4.419021\ 10^{-6}$	4.2719	$1.9268\ 10^{4}$
5	505	1000	$7.692614\ 10^{-7}$	$2.152477\ 10^{-6}$	3.9729	$1.0092\ 10^{4}$
24	528	1000	-	-	3.8201	$1.0092\ 10^{4}$
6	550	1000	$3.356951\ 10^{-7}$	$9.393113\ 10^{-7}$	3.6117	$4.8442\ 10^{3}$
20	590	5000	$6.680035\ 10^{-8}$	$9.345732\ 10^{-7}$	3.3669	$5.1703\ 10^{3}$
7	625	1000	$3.832214\ 10^{-7}$	$1.072295\ 10^{-6}$	3.1783	$6.2842\ 10^{3}$
18	660	1000	$1.017161\ 10^{-7}$	$2.846127\ 10^{-7}$	3.0098	$1.7614\ 10^{3}$
1	690	1000	$1.833168\ 10^{-7}$	$5.129403\ 10^{-7}$	2.8789	$3.3187\ 10^{3}$
16	720	1000	$2.451453\ 10^{-7}$	$6.859433\ 10^{-7}$	2.7590	$4.6310\ 10^{3}$
13	745	1000	$4.998257\ 10^{-7}$	$1.398567\ 10^{-6}$	2.6664	$9.7700\ 10^{3}$
15	760	1000	$2.585281\ 10^{-7}$	$7.233896\ 10^{-7}$	2.6137	$5.1551\ 10^{3}$
10	810	1000	$2.697023\ 10^{-7}$	$7.546563\ 10^{-7}$	2.4524	$5.7318\ 10^{3}$
19	830	1000	$3.191477\ 10^{-7}$	$8.930100\ 10^{-7}$	2.3933	$6.9500\ 10^{3}$
12	850	1000	$2.466564\ 10^{-7}$	$6.901713\ 10^{-7}$	2.3370	$5.5008\ 10^{3}$
9	905	1000	$1.772280\ 10^{-7}$	$4.959031\ 10^{-7}$	2.1950	$4.2082\ 10^{3}$
14	940	1000	$9.967060\ 10^{-8}$	$2.788892\ 10^{-7}$	2.1132	$2.4582\ 10^{3}$
11	970	1000	$1.614272\ 10^{-7}$	$4.516907\ 10^{-7}$	2.0479	$4.1083\ 10^{3}$

Table A.5: *Expected focal plane illumination for the whole set of SkyDICE LEDs.*

Salimmo sù, el primo e io secondo,
tanto ch'i' vidi de le cose belle
che porta 'l ciel, per un pertugio tondo.
E quindi uscimmo a riveder le stelle.
(D. Alighieri / Inferno - Canto XXXIV)

Everyone is a genius.
But if you judge a fish on its ability to climb a tree,
it will live its whole life believing that is stupid.
(G. H. Reavis / The Animal School)

Bibliography

D. J. Bacon, A. R. Refregier, and R. S. Ellis. Detection of weak gravitational lensing by large-scale structure. MNRAS, 318:625–640, October 2000. doi: 10.1046/j.1365-8711.2000.03851.x. 15

E. Barrelet and C. Juramy. Direct illumination LED calibration for telescope photometry. *Nuclear Instruments and Methods in Physics Research A*, 585:93–101, January 2008. doi: 10.1016/j.nima.2007.10.048. 2, 38

M. Bessell, G. Bloxham, B. Schmidt, S. Keller, P. Tisserand, and P. Francis. SkyMapper Filter Set: Design and Fabrication of Large-Scale Optical Filters. PASP, 123:789–798, July 2011. doi: 10.1086/660849. 29, 139, 140, 164

M. Betoule, J. Marriner, N. Regnault, J.-C. Cuillandre, P. Astier, J. Guy, C. Balland, P. El Hage, D. Hardin, R. Kessler, L. Le Guillou, J. Mosher, R. Pain, P.-F. Rocci, M. Sako, and K. Schahmaneche. Improved photometric calibration of the SNLS and the SDSS supernova surveys. *Astronomy & Astrophysics*, 552:A124, April 2013. doi: 10.1051/0004-6361/201220610. 1, 33, 34, 40, 148

Blanton M. and SDSS Collaboration, 2008. URL `http://www.sdss.org`. v, 4

S. W. Brown, G. P. Eppeldauer, and K. R. Lykke. Facility for spectral irradiance and radiance responsivity calibrations using uniform sources. Appl. Opt., 45:8218–8237, November 2006. doi: 10.1364/AO.45.008218. 35

R. R. Caldwell and E. V. Linder. Limits of Quintessence. *Physical Review Letters*, 95(14): 141301, September 2005. doi: 10.1103/PhysRevLett.95.141301. 23

M. Chevallier and D. Polarski. Accelerating Universes with Scaling Dark Matter. *International Journal of Modern Physics D*, 10:213–223, 2001. doi: 10.1142/S0218271801000822. 10

A. Conley, J. Guy, M. Sullivan, N. Regnault, P. Astier, C. Balland, S. Basa, R. G. Carlberg, D. Fouchez, D. Hardin, I. M. Hook, D. A. Howell, R. Pain, N. Palanque-Delabrouille, K. M. Perrett, C. J. Pritchet, J. Rich, V. Ruhlmann-Kleider, D. Balam, S. Baumont, R. S. Ellis, S. Fabbro, H. K. Fakhouri, N. Fourmanoit, S. González-Gaitán, M. L. Graham, M. J. Hudson, E. Hsiao, T. Kronborg, C. Lidman, A. M. Mourao, J. D. Neill, S. Perlmutter,

P. Ripoche, N. Suzuki, and E. S. Walker. Supernova Constraints and Systematic Uncertainties from the First Three Years of the Supernova Legacy Survey. ApJS, 192:1, January 2011. doi: 10.1088/0067-0049/192/1/1. v, 1, 19, 20, 31

P. de Bernardis, P. A. R. Ade, J. J. Bock, J. R. Bond, J. Borrill, A. Boscaleri, K. Coble, B. P. Crill, G. De Gasperis, P. C. Farese, P. G. Ferreira, K. Ganga, M. Giacometti, E. Hivon, V. V. Hristov, A. Iacoangeli, A. H. Jaffe, A. E. Lange, L. Martinis, S. Masi, P. V. Mason, P. D. Mauskopf, A. Melchiorri, L. Miglio, T. Montroy, C. B. Netterfield, E. Pascale, F. Piacentini, D. Pogosyan, S. Prunet, S. Rao, G. Romeo, J. E. Ruhl, F. Scaramuzzi, D. Sforna, and N. Vittorio. A flat Universe from high-resolution maps of the cosmic microwave background radiation. Nature, 404:955–959, April 2000. 1

C. Deffayet. Cosmology on a brane in Minkowski bulk. *Physics Letters B*, 502:199–208, March 2001. doi: 10.1016/S0370-2693(01)00160-5. 23

M. Doi, M. Tanaka, M. Fukugita, J. E. Gunn, N. Yasuda, Ž. Ivezić, J. Brinkmann, E. de Haars, S. J. Kleinman, J. Krzesinski, and R. French Leger. Photometric Response Functions of the Sloan Digital Sky Survey Imager. *Astronomical Journal*, 139:1628–1648, April 2010. doi: 10.1088/0004-6256/139/4/1628. 37, 40, 148

G. Dvali, G. Gabadadze, and M. Porrati. 4D gravity on a brane in 5D Minkowski space. *Physics Letters B*, 485:208–214, July 2000. doi: 10.1016/S0370-2693(00)00669-9. 23

A. Einstein. Die Feldgleichungen der Gravitation. *Sitzungsberichte der Königlich Preußischen Akademie der Wissenschaften (Berlin), Seite 844-847.*, pages 844–847, 1915. 6

A. Einstein. Kosmologische Betrachtungen zur allgemeinen Relativitätstheorie. *Sitzungsberichte der Königlich Preußischen Akademie der Wissenschaften (Berlin), Seite 142-152.*, pages 142–152, 1917. 3

A. Einstein and W. de Sitter. On the Relation between the Expansion and the Mean Density of the Universe. *Proceedings of the National Academy of Science*, 18:213–214, March 1932. doi: 10.1073/pnas.18.3.213. 3

D. J. Eisenstein, I. Zehavi, D. W. Hogg, R. Scoccimarro, M. R. Blanton, R. C. Nichol, R. Scranton, H.-J. Seo, M. Tegmark, Z. Zheng, S. F. Anderson, J. Annis, N. Bahcall, J. Brinkmann, S. Burles, F. J. Castander, A. Connolly, I. Csabai, M. Doi, M. Fukugita, J. A. Frieman, K. Glazebrook, J. E. Gunn, J. S. Hendry, G. Hennessy, Z. Ivezić, S. Kent, G. R. Knapp, H. Lin, Y.-S. Loh, R. H. Lupton, B. Margon, T. A. McKay, A. Meiksin, J. A. Munn, A. Pope, M. W. Richmond, D. Schlegel, D. P. Schneider, K. Shimasaku, C. Stoughton, M. A. Strauss, M. SubbaRao, A. S. Szalay, I. Szapudi, D. L. Tucker, B. Yanny, and D. G. York. Detection of the Baryon Acoustic Peak in the Large-Scale Correlation Function of SDSS Luminous Red Galaxies. ApJ, 633:560–574, November 2005. doi: 10.1086/466512. v, 13

ESA/Planck Collaboration, 2013. URL http://arstechnica.com/science/2013/03/first-planck-results-the-universe-is-still-weird-and-interesting/. vi, 22

A. V. Filippenko. Optical Spectra of Supernovae. ARA&A, 35:309–355, 1997. doi: 10.1146/annurev.astro.35.1.309. 15

D. S. Finley and D. Koester. Hot DA White Dwarfs as Ultraviolet Absolute Flux Standards. In *Bulletin of the American Astronomical Society*, volume 23 of *Bulletin of the American Astronomical Society*, page 907, March 1991. 33

D. J. Fixsen. The Temperature of the Cosmic Microwave Background. ApJ, 707:916–920, December 2009. doi: 10.1088/0004-637X/707/2/916. 5

W. L. Freedman, B. F. Madore, B. K. Gibson, L. Ferrarese, D. D. Kelson, S. Sakai, J. R. Mould, R. C. Kennicutt, Jr., H. C. Ford, J. A. Graham, J. P. Huchra, S. M. G. Hughes, G. D. Illingworth, L. M. Macri, and P. B. Stetson. Final Results from the Hubble Space Telescope Key Project to Measure the Hubble Constant. ApJ, 553:47–72, May 2001. doi: 10.1086/320638. 1

A. Friedmann. Über die Krümmung des Raumes. *Zeitschrift fur Physik*, 10:377–386, 1922. doi: 10.1007/BF01332580. 3

J. A. Frieman, C. T. Hill, A. Stebbins, and I. Waga. Cosmology with Ultralight Pseudo Nambu-Goldstone Bosons. *Physical Review Letters*, 75:2077–2080, September 1995. doi: 10.1103/PhysRevLett.75.2077. 22

J. A. Frieman, M. S. Turner, and D. Huterer. Dark Energy and the Accelerating Universe. ARA&A, 46:385–432, September 2008. doi: 10.1146/annurev.astro.46.060407.145243. 24

L. Fu, E. Semboloni, H. Hoekstra, M. Kilbinger, L. van Waerbeke, I. Tereno, Y. Mellier, C. Heymans, J. Coupon, K. Benabed, J. Benjamin, E. Bertin, O. Doré, M. J. Hudson, O. Ilbert, R. Maoli, C. Marmo, H. J. McCracken, and B. Ménard. Very weak lensing in the CFHTLS wide: cosmology from cosmic shear in the linear regime. *Astronomy & Astrophysics*, 479:9–25, February 2008. doi: 10.1051/0004-6361:20078522. 15

G. Goldhaber, D. E. Groom, A. Kim, G. Aldering, P. Astier, A. Conley, S. E. Deustua, R. Ellis, S. Fabbro, A. S. Fruchter, A. Goobar, I. Hook, M. Irwin, M. Kim, R. A. Knop, C. Lidman, R. McMahon, P. E. Nugent, R. Pain, N. Panagia, C. R. Pennypacker, S. Perlmutter, P. Ruiz-Lapuente, B. Schaefer, N. A. Walton, and T. York. Timescale Stretch Parameterization of Type Ia Supernova B-Band Light Curves. ApJ, 558:359–368, September 2001. doi: 10.1086/322460. 16

A. Granlund, P. G. Conroy, S. C. Keller, A. P. Oates, B. Schmidt, M. F. Waterson, E. Kowald, and M. I. Dawson. A large-format imager for the SkyMapper Survey Telescope. In *Society of Photo-Optical Instrumentation Engineers (SPIE) Conference Series*, volume 6269 of *Society of Photo-Optical Instrumentation Engineers (SPIE) Conference Series*, July 2006. doi: 10.1117/12.670121. 29

R. Gregory, N. Kaloper, R. C. Myers, and A. Padilla. A new perspective on DGP gravity. *Journal of High Energy Physics*, 10:069, October 2007. doi: 10.1088/1126-6708/2007/10/069. 23

A. H. Guth. Inflation. *Measuring and Modeling the Universe*, page 31, 2004. 23

J. Guy, P. Astier, S. Nobili, N. Regnault, and R. Pain. SALT: a spectral adaptive light curve template for type Ia supernovae. *Astronomy & Astrophysics*, 443:781–791, December 2005. doi: 10.1051/0004-6361:20053025. 16

J. Guy, P. Astier, S. Baumont, D. Hardin, R. Pain, N. Regnault, S. Basa, R. G. Carlberg, A. Conley, S. Fabbro, D. Fouchez, I. M. Hook, D. A. Howell, K. Perrett, C. J. Pritchet, J. Rich, M. Sullivan, P. Antilogus, E. Aubourg, G. Bazin, J. Bronder, M. Filiol, N. Palanque-Delabrouille, P. Ripoche, and V. Ruhlmann-Kleider. SALT2: using distant supernovae to improve the use of type Ia supernovae as distance indicators. *Astronomy & Astrophysics*, 466:11–21, April 2007. doi: 10.1051/0004-6361:20066930. 16, 18

A. Guyonnet. *Etalonnage Photometrique des Imageurs Grand Champ par Illumination Directe*. PhD thesis, UPMC - LPNHE, 2012. viii, xiii, 39, 44, 51, 58, 65, 68, 69, 71, 72, 73

M. Hamuy, M. M. Phillips, N. B. Suntzeff, R. A. Schommer, J. Maza, and R. Aviles. The Absolute Luminosities of the Calan/Tololo Type IA Supernovae. *Astronomical Journal*, 112:2391, December 1996. doi: 10.1086/118190. 16

P. H. Hauschildt and E. Baron. Non-LTE treatment of Fe II in astrophysical plasmas. J. Quant. Spec. Radiat. Transf., 54:987–999, December 1995. doi: 10.1016/0022-4073(95)00118-5. 33

D. S. Hayes. Stellar absolute fluxes and energy distributions from 0.32 to 4.0 microns. In D. S. Hayes, L. E. Pasinetti, and A. G. D. Philip, editors, *Calibration of Fundamental Stellar Quantities*, volume 111 of *IAU Symposium*, pages 225–249, 1985. 32

G. Hinshaw, D. Larson, E. Komatsu, D. N. Spergel, C. L. Bennett, J. Dunkley, M. R. Nolta, M. Halpern, R. S. Hill, N. Odegard, L. Page, K. M. Smith, J. L. Weiland, B. Gold, N. Jarosik, A. Kogut, M. Limon, S. S. Meyer, G. S. Tucker, E. Wollack, and E. L. Wright. Nine-Year Wilkinson Microwave Anisotropy Probe (WMAP) Observations: Cosmological Parameter Results. *ArXiv e-prints*, December 2012. 6, 13

H. Hoekstra, Y. Mellier, L. van Waerbeke, E. Semboloni, L. Fu, M. J. Hudson, L. C. Parker, I. Tereno, and K. Benabed. First Cosmic Shear Results from the Canada-France-Hawaii Telescope Wide Synoptic Legacy Survey. ApJ, 647:116–127, August 2006. doi: 10.1086/503249. 15

J. A. Holtzman, J. Marriner, R. Kessler, M. Sako, B. Dilday, J. A. Frieman, D. P. Schneider, B. Bassett, A. Becker, D. Cinabro, F. DeJongh, D. L. Depoy, M. Doi, P. M. Garnavich,

C. J. Hogan, S. Jha, K. Konishi, H. Lampeitl, J. L. Marshall, D. McGinnis, G. Miknaitis, R. C. Nichol, J. L. Prieto, A. G. Riess, M. W. Richmond, R. Romani, M. Smith, N. Takanashi, K. Tokita, K. van der Heyden, N. Yasuda, and C. Zheng. The Sloan Digital Sky Survey-II: Photometry and Supernova IA Light Curves from the 2005 Data. *Astronomical Journal*, 136:2306–2320, December 2008. doi: 10.1088/0004-6256/136/6/2306. 34

J. M. Houston and J. P. Rice. NIST reference cryogenic radiometer designed for versatile performance. *Metrologia*, 43:31, April 2006. doi: 10.1088/0026-1394/43/2/S07. 35

D. A. Howell, A. Conley, M. Della Valle, P. E. Nugent, S. Perlmutter, G. H. Marion, K. Krisciunas, C. Badenes, P. Mazzali, G. Aldering, P. Antilogus, E. Baron, A. Becker, C. Baltay, S. Benetti, S. Blondin, D. Branch, E. F. Brown, S. Deustua, A. Ealet, R. S. Ellis, D. Fouchez, W. Freedman, A. Gal-Yam, S. Jha, D. Kasen, R. Kessler, A. G. Kim, D. C. Leonard, W. Li, M. Livio, D. Maoz, F. Mannucci, T. Matheson, J. D. Neill, K. Nomoto, N. Panagia, K. Perrett, M. Phillips, D. Poznanski, R. Quimby, A. Rest, A. Riess, M. Sako, A. M. Soderberg, L. Strolger, R. Thomas, M. Turatto, S. van Dyk, and W. M. Wood-Vasey. Type Ia supernova science 2010-2020. *ArXiv e-prints*, March 2009. 1

W. Hu and I. Sawicki. Models of f(R) cosmic acceleration that evade solar system tests. Phys. Rev. D, 76(6):064004, September 2007. doi: 10.1103/PhysRevD.76.064004. 23

E. Hubble. A Relation between Distance and Radial Velocity among Extra-Galactic Nebulae. *Proceedings of the National Academy of Science*, 15:168–173, March 1929. doi: 10.1073/pnas.15.3.168. 3, 7

I. Hubeny and T. Lanz. Non-LTE line-blanketed model atmospheres of hot stars. 1: Hybrid complete linearization/accelerated lambda iteration method. ApJ, 439:875–904, February 1995. doi: 10.1086/175226. 33

S. Jha, A. G. Riess, and R. P. Kirshner. Improved Distances to Type Ia Supernovae with Multicolor Light-Curve Shapes: MLCS2k2. ApJ, 659:122–148, April 2007. doi: 10.1086/512054. 16

H. L. Johnson and W. W. Morgan. Fundamental stellar photometry for standards of spectral type on the revised system of the Yerkes spectral atlas. ApJ, 117:313, May 1953. doi: 10.1086/145697. 33

M. E. Kaiser, J. W. Kruk, S. R. McCandliss, D. J. Sahnow, R. H. Barkhouser, W. Van Dixon, P. D. Feldman, H. W. Moos, J. Orndorff, R. Pelton, A. G. Riess, B. J. Rauscher, R. A. Kimble, D. J. Benford, J. P. Gardner, R. J. Hill, B. E. Woodgate, R. C. Bohlin, S. E. Deustua, R. Kurucz, M. Lampton, S. Perlmutter, and E. L. Wright. ACCESS: Enabling an Improved Flux Scale for Astrophysics. *ArXiv e-prints*, January 2010. 35

E. A. Kazin, M. R. Blanton, R. Scoccimarro, C. K. McBride, A. A. Berlind, N. A. Bahcall, J. Brinkmann, P. Czarapata, J. A. Frieman, S. M. Kent, D. P. Schneider, and A. S.

Szalay. The Baryonic Acoustic Feature and Large-Scale Clustering in the Sloan Digital Sky Survey Luminous Red Galaxy Sample. ApJ, 710:1444–1461, February 2010. doi: 10.1088/0004-637X/710/2/1444. 14

S. C. Keller, B. P. Schmidt, M. S. Bessell, P. G. Conroy, P. Francis, A. Granlund, E. Kowald, A. P. Oates, T. Martin-Jones, T. Preston, P. Tisserand, A. Vaccarella, and M. F. Waterson. The SkyMapper Telescope and The Southern Sky Survey. PASA, 24:1–12, May 2007. doi: 10.1071/AS07001. vi, 29, 31, 164

R. L. Kurucz. Model Atmospheres (Kurucz, 1979). *VizieR Online Data Catalog*, 6039:0, October 1993. 33

A. U. Landolt. UBV photoelectric sequences in the celestial equatorial Selected Areas 92-115. *Astronomical Journal*, 78:959–+, November 1973. 33

A. U. Landolt. UBVRI photometric standard stars around the celestial equator. *Astronomical Journal*, 88:439–460, March 1983. doi: 10.1086/113329. 33

A. U. Landolt. UBVRI photometric standard stars in the magnitude range 11.5-16.0 around the celestial equator. *Astronomical Journal*, 104:340–371, July 1992. doi: 10.1086/116242. 33

T. C. Larason and J. M. Houston. Spectroradiometric Detector Measurements: Ultraviolet, Visible, and Near-Infrared Detectors for Spectral Power . 2008. URL `http://www.nist.gov/calibrations/upload/sp250-41a.pdf`. 34

G. Lemaître. Un Univers homogène de masse constante et de rayon croissant rendant compte de la vitesse radiale des nébuleuses extra-galactiques. *Annales de la Societe Scietifique de Bruxelles*, 47:49–59, 1927. 3

A. Liddle and J. Loveday. *Companion of Cosmology*. 2009. 6

E. V. Linder. Exploring the Expansion History of the Universe. *Physical Review Letters*, 90 (9):091301, March 2003. doi: 10.1103/PhysRevLett.90.091301. 10

A. Mantz, S. W. Allen, H. Ebeling, and D. Rapetti. New constraints on dark energy from the observed growth of the most X-ray luminous galaxy clusters. MNRAS, 387:1179–1192, July 2008. doi: 10.1111/j.1365-2966.2008.13311.x. 14

J. C. Mather, E. S. Cheng, R. E. Eplee, Jr., R. B. Isaacman, S. S. Meyer, R. A. Shafer, R. Weiss, E. L. Wright, C. L. Bennett, N. W. Boggess, E. Dwek, S. Gulkis, M. G. Hauser, M. Janssen, T. Kelsall, P. M. Lubin, S. H. Moseley, Jr., T. L. Murdock, R. F. Silverberg, G. F. Smoot, and D. T. Wilkinson. A preliminary measurement of the cosmic microwave background spectrum by the Cosmic Background Explorer (COBE) satellite. ApJ, 354: L37–L40, May 1990. doi: 10.1086/185717. 5

J. C. Mather, E. S. Cheng, D. A. Cottingham, R. E. Eplee, Jr., D. J. Fixsen, T. Hewagama, R. B. Isaacman, K. A. Jensen, S. S. Meyer, P. D. Noerdlinger, S. M. Read, L. P. Rosen, R. A. Shafer, E. L. Wright, C. L. Bennett, N. W. Boggess, M. G. Hauser, T. Kelsall, S. H. Moseley, Jr., R. F. Silverberg, G. F. Smoot, R. Weiss, and D. T. Wilkinson. Measurement of the cosmic microwave background spectrum by the COBE FIRAS instrument. ApJ, 420:439–444, January 1994. doi: 10.1086/173574. 5

J. T. McGraw, P. C. Zimmer, D. C. Zirzow, J. T. Woodward, K. R. Lykke, C. E. Cramer, S. E. Deustua, and D. C. Hines. Near-field calibration of an objective spectrophotometer to NIST radiometric standards for the creation and maintenance of standard stars for ground- and space-based applications. In *Society of Photo-Optical Instrumentation Engineers (SPIE) Conference Series*, volume 8450 of *Society of Photo-Optical Instrumentation Engineers (SPIE) Conference Series*, September 2012. doi: 10.1117/12.927296. 36

R. Minkowski. Spectra of Supernovae. PASP, 53:224, August 1941. doi: 10.1086/125315. 15

P. Onaka, J. Tonry, S. Isani, A. Lee, R. Uyeshiro, C. Rae, L. Robertson, and G. Ching. Pan-STARRS PS1 STARGRASP Controller. In *The Advanced Maui Optical and Space Surveillance Technologies Conference*, 2006. 30

A. A. Penzias and R. W. Wilson. A Measurement of Excess Antenna Temperature at 4080 Mc/s. ApJ, 142:419–421, July 1965. doi: 10.1086/148307. 11

S. Perlmutter, S. Gabi, G. Goldhaber, A. Goobar, D. E. Groom, I. M. Hook, A. G. Kim, M. Y. Kim, J. C. Lee, R. Pain, C. R. Pennypacker, I. A. Small, R. S. Ellis, R. G. McMahon, B. J. Boyle, P. S. Bunclark, D. Carter, M. J. Irwin, K. Glazebrook, H. J. M. Newberg, A. V. Filippenko, T. Matheson, M. Dopita, W. J. Couch, and Supernova Cosmology Project. Measurements of the Cosmological Parameters Omega and Lambda from the First Seven Supernovae at Z $>$ 0.35. ApJ, 483:565, July 1997. doi: 10.1086/304265. 16

S. Perlmutter, G. Aldering, M. della Valle, S. Deustua, R. S. Ellis, S. Fabbro, A. Fruchter, G. Goldhaber, D. E. Groom, I. M. Hook, A. G. Kim, M. Y. Kim, R. A. Knop, C. Lidman, R. G. McMahon, P. Nugent, R. Pain, N. Panagia, C. R. Pennypacker, P. Ruiz-Lapuente, B. Schaefer, and N. Walton. Discovery of a supernova explosion at half the age of the universe. Nature, 391:51, January 1998. doi: 10.1038/34124. 1, 9

S. Perlmutter, G. Aldering, G. Goldhaber, R. A. Knop, P. Nugent, P. G. Castro, S. Deustua, S. Fabbro, A. Goobar, D. E. Groom, I. M. Hook, A. G. Kim, M. Y. Kim, J. C. Lee, N. J. Nunes, R. Pain, C. R. Pennypacker, R. Quimby, C. Lidman, R. S. Ellis, M. Irwin, R. G. McMahon, P. Ruiz-Lapuente, N. Walton, B. Schaefer, B. J. Boyle, A. V. Filippenko, T. Matheson, A. S. Fruchter, N. Panagia, H. J. M. Newberg, W. J. Couch, and Supernova Cosmology Project. Measurements of Omega and Lambda from 42 High-Redshift Supernovae. ApJ, 517:565–586, June 1999. doi: 10.1086/307221. v, 1, 3, 9, 10

M. M. Phillips. The absolute magnitudes of Type IA supernovae. ApJ, 413:L105–L108, August 1993. doi: 10.1086/186970. 16

Planck Collaboration, P. A. R. Ade, N. Aghanim, C. Armitage-Caplan, M. Arnaud, M. Ashdown, F. Atrio-Barandela, J. Aumont, C. Baccigalupi, A. J. Banday, and et al. Planck 2013 results. I. Overview of products and scientific results. *ArXiv e-prints*, March 2013a. v, 5

Planck Collaboration, P. A. R. Ade, N. Aghanim, C. Armitage-Caplan, M. Arnaud, M. Ashdown, F. Atrio-Barandela, J. Aumont, C. Baccigalupi, A. J. Banday, and et al. Planck 2013 results. XVI. Cosmological parameters. *ArXiv e-prints*, March 2013b. v, 1, 6, 8, 10, 11, 12

N. Regnault. Photometric calibration of wide field imagers, 2013. vi, 32, 36

N. Regnault, A. Conley, J. Guy, M. Sullivan, J.-C. Cuillandre, P. Astier, C. Balland, S. Basa, R. G. Carlberg, D. Fouchez, D. Hardin, I. M. Hook, D. A. Howell, R. Pain, K. Perrett, and C. J. Pritchet. Photometric calibration of the Supernova Legacy Survey fields. *Astronomy & Astrophysics*, 506:999–1042, November 2009. doi: 10.1051/0004-6361/200912446. 33, 34

N. Regnault, E. Barrelet, A. Guyonnet, C. Juramy, P.-F. Rocci, L. Le Guillou, K. Schahmanèche, and F. Villa. (Sn)DICE: A Calibration System Designed for Wide Field Imagers. *ArXiv e-prints*, August 2012. vi, 42

K. Reif, G. Klink, P. Müller, and H. Poschmann. The OmegaCam Shutter. In P. Amico, J. W. Beletic, and J. E. Belectic, editors, *Scientific Detectors for Astronomy, The Beginning of a New Era*, volume 300 of *Astrophysics and Space Science Library*, pages 367–370, 2004. 29

J.-P. Rheault, D. L. Depoy, T. W. Behm, E. W. Kylberg, K. Cabral, R. Allen, and J. L. Marshall. Spectrophotometric calibration system for DECam. In *Society of Photo-Optical Instrumentation Engineers (SPIE) Conference Series*, volume 7735 of *Society of Photo-Optical Instrumentation Engineers (SPIE) Conference Series*, July 2010. doi: 10.1117/12.857411. 38, 42

A. G. Riess, W. H. Press, and R. P. Kirshner. A Precise Distance Indicator: Type IA Supernova Multicolor Light-Curve Shapes. ApJ, 473:88, December 1996. doi: 10.1086/178129. 16

A. G. Riess, A. V. Filippenko, P. Challis, A. Clocchiatti, A. Diercks, P. M. Garnavich, R. L. Gilliland, C. J. Hogan, S. Jha, R. P. Kirshner, B. Leibundgut, M. M. Phillips, D. Reiss, B. P. Schmidt, R. A. Schommer, R. C. Smith, J. Spyromilio, C. Stubbs, N. B. Suntzeff, and J. Tonry. Observational Evidence from Supernovae for an Accelerating Universe and a Cosmological Constant. *Astronomical Journal*, 116:1009–1038, September 1998. doi: 10.1086/300499. 1, 3, 9

A. G. Riess, L. Macri, S. Casertano, M. Sosey, H. Lampeitl, H. C. Ferguson, A. V. Filippenko, S. W. Jha, W. Li, R. Chornock, and D. Sarkar. A Redetermination of the Hubble Constant

with the Hubble Space Telescope from a Differential Distance Ladder. ApJ, 699:539–563, July 2009. doi: 10.1088/0004-637X/699/1/539. 13

M. Rowan-Robinson. Cosmology. 1996. 4

B. P. Schmidt, N. B. Suntzeff, M. M. Phillips, R. A. Schommer, A. Clocchiatti, R. P. Kirshner, P. Garnavich, P. Challis, B. Leibundgut, J. Spyromilio, A. G. Riess, A. V. Filippenko, M. Hamuy, R. C. Smith, C. Hogan, C. Stubbs, A. Diercks, D. Reiss, R. Gilliland, J. Tonry, J. Maza, A. Dressler, J. Walsh, and R. Ciardullo. The High-Z Supernova Search: Measuring Cosmic Deceleration and Global Curvature of the Universe Using Type IA Supernovae. ApJ, 507:46–63, November 1998. doi: 10.1086/306308. 1, 9

F. Schubert. *Light-Emitting Diodes*. 2007. vi, 43

Siding Spring Observatory, 2012. URL http://rsaa.anu.edu.au/observatories/siding-spring-observatory. vi, 28, 30

V. M. Slipher. Nebulae. *Proceedings of the American Philosophical Society*, 56:403–409, 1917. 7

G. F. Smoot, C. L. Bennett, A. Kogut, E. L. Wright, J. Aymon, N. W. Boggess, E. S. Cheng, G. de Amici, S. Gulkis, M. G. Hauser, G. Hinshaw, P. D. Jackson, M. Janssen, E. Kaita, T. Kelsall, P. Keegstra, C. Lineweaver, K. Loewenstein, P. Lubin, J. Mather, S. S. Meyer, S. H. Moseley, T. Murdock, L. Rokke, R. F. Silverberg, L. Tenorio, R. Weiss, and D. T. Wilkinson. Structure in the COBE differential microwave radiometer first-year maps. ApJ, 396:L1–L5, September 1992. doi: 10.1086/186504. 11

C. W. Stubbs, P. Doherty, C. Cramer, G. Narayan, Y. J. Brown, K. R. Lykke, J. T. Woodward, and J. L. Tonry. Precise Throughput Determination of the PanSTARRS Telescope and the Gigapixel Imager Using a Calibrated Silicon Photodiode and a Tunable Laser: Initial Results. ApJS, 191:376–388, December 2010. doi: 10.1088/0067-0049/191/2/376. 37, 42

M. Sullivan, J. Guy, A. Conley, N. Regnault, P. Astier, C. Balland, S. Basa, R. G. Carlberg, D. Fouchez, D. Hardin, I. M. Hook, D. A. Howell, R. Pain, N. Palanque-Delabrouille, K. M. Perrett, C. J. Pritchet, J. Rich, V. Ruhlmann-Kleider, D. Balam, S. Baumont, R. S. Ellis, S. Fabbro, H. K. Fakhouri, N. Fourmanoit, S. González-Gaitán, M. L. Graham, M. J. Hudson, E. Hsiao, T. Kronborg, C. Lidman, A. M. Mourao, J. D. Neill, S. Perlmutter, P. Ripoche, N. Suzuki, and E. S. Walker. SNLS3: Constraints on Dark Energy Combining the Supernova Legacy Survey Three-year Data with Other Probes. ApJ, 737:102, August 2011. doi: 10.1088/0004-637X/737/2/102. v, 1, 19, 20, 31

M. Turatto. Classification of Supernovae. In K. Weiler, editor, *Supernovae and Gamma-Ray Bursters*, volume 598 of *Lecture Notes in Physics, Berlin Springer Verlag*, pages 21–36, 2003. v, 15, 16

F. Villa. *Calibration photometrique de l'Imaguer MegaCam. Analyse des données SnDICE.* PhD thesis, UPMC - LPNHE, 2012. vii, 39, 44, 51, 52, 65, 126, 130

X. Wang, L. Wang, X. Zhou, Y.-Q. Lou, and Z. Li. A Novel Color Parameter as a Luminosity Calibrator for Type Ia Supernovae. ApJ, 620:L87–L90, February 2005. doi: 10.1086/428774. 16

S. Weinberg. The cosmological constant problem. *Reviews of Modern Physics*, 61:1–23, January 1989. doi: 10.1103/RevModPhys.61.1. 22

C. Wetterich. Cosmology and the fate of dilatation symmetry. *Nuclear Physics B*, 302: 668–696, June 1988. doi: 10.1016/0550-3213(88)90193-9. 22

S. D. M. White, J. F. Navarro, A. E. Evrard, and C. S. Frenk. The baryon content of galaxy clusters: a challenge to cosmological orthodoxy. Nature, 366:429–433, December 1993. doi: 10.1038/366429a0. 14

G. Wilson, A. Czezowski, G. R. Hovey, M. A. Jarnyk, J. Nielsen, B. Roberts, K. Sebo, D. Smith, A. Vaccarella, and P. Young. Telescope Automation and Remote Observing System (TAROS). In P. Shopbell, M. Britton, and R. Ebert, editors, *Astronomical Data Analysis Software and Systems XIV*, volume 347 of *Astronomical Society of the Pacific Conference Series*, page 563, December 2005. 30

R. W. Wilson and A. A. Penzias. Isotropy of Cosmic Background Radiation at 4080 Megahertz. *Science*, 156:1100–1101, May 1967. doi: 10.1126/science.156.3778.1100. 11

P. J. Young, W. H. Roberts, and K. M. Sebo. CICADA – Configurable Instrument Control and Data Acquisition. In D. M. Mehringer, R. L. Plante, and D. A. Roberts, editors, *Astronomical Data Analysis Software and Systems VIII*, volume 172 of *Astronomical Society of the Pacific Conference Series*, page 115, 1999. 30, 55

I. Zlatev, L. Wang, and P. J. Steinhardt. Quintessence, Cosmic Coincidence, and the Cosmological Constant. *Physical Review Letters*, 82:896–899, February 1999. doi: 10.1103/PhysRevLett.82.896. 22

F. Zwicky. On the Masses of Nebulae and of Clusters of Nebulae. ApJ, 86:217, October 1937. doi: 10.1086/143864. 3, 14